Levitated Optomechanics in a hybrid electro-optical trap

Piergiacomo Zucconi Galli Fonseca

A thesis submitted to University College London
in partial fulfilment of the requirements for the
degree of Doctor of Philosophy

Department of Physics and Astronomy
University College London
May 2017

I, Piergiacomo Zucconi Galli Fonseca, confirm that the work presented in this thesis is my own. Where information has been derived from other sources, I confirm that this has been indicated in the thesis.

Signed ..... Date .....

Abstract

This thesis describes the progress made in trapping and cooling silica nanoscale particles, levitating in a hybrid electro-optical trap. The light field of a high finesse Fabry-Perot cavity and the quadrupole field generated by an rf Paul trap are used for the first time to both trap and cool naturally charged 209 nm dielectric nanospheres in high vacuum. Particles are first loaded into the Paul trap at pressures of $\sim 10^{-1}$ mbar, after which their centre-of-mass motion is damped via optomechanical cooling, as the pressure is lowered to $\sim 10^{-6}$ mbar. The combined ion trap-optical cavity set-up exposes an interesting interplay between the ion trap dynamics and the cavity mode which lead to a novel optomechanical cooling mechanism of a cyclic nature. This eliminates the need for a second, dedicated cooling mode from the cavity, or feedback cooling in order to cool the levitated particles to the ground state. At the same time, we identify a previously unobserved shift of the Paul trap secular frequencies due to the optical cavity, which enables readout of key parameters, such as the nanoparticles charge and the mean number of photons in the cavity.

The dynamical features of the levitated particle, driven by linear and nonlinear optomechanical coupling, are observed through the cavity output, as well as the light scattered by the particle. As the background pressure is lowered, we observe greater than 1000 fold reduction in the centre-of-mass temperature of particles, before temperatures fall below the read-out sensitivity of the set-up.

Contents

Introduction **7**

1 Cavity Optomechanics: an overview **12**
1.1 Principles of optomechanical interaction . . . 12
1.2 Limits . . . 17
1.3 Experimental realizations . . . 18

2 Optomechanics with levitated dielectric particles **21**
2.1 Motivations . . . 22
2.2 Optical Trapping . . . 26
2.3 Interaction with a cavity . . . 29
2.4 Limits . . . 30
2.4.1 Particles loss . . . 31

3 Optomechanical coupling **34**
3.1 Mechanical Harmonic Oscillator . . . 34
3.1.1 Energy Levels . . . 35
3.1.2 Coupling to the environment . . . 36
3.1.3 Dynamics of the oscillator . . . 38
3.2 Optical cavity . . . 40
3.3 Optomechanical coupling . . . 41
3.4 Quadratic coupling in Optomechanics . . . 45

4 The Hybrid electro-optical trap **48**
4.1 Nanoparticles in an Paul trap . . . 48
4.2 Nanoparticles in an optical cavity . . . 51
4.3 Hybrid electro-optical trap . . . 53
4.4 Introducing quadratic coupling . . . 58
4.4.1 Cooling rate . . . 60

5 Experimental apparatus **62**
5.1 Optical setup . . . 62
5.2 Laser system . . . 64
5.3 Laser detuning . . . 65
5.4 Optical cavity . . . 67
5.4.1 Cavity stability . . . 68
5.4.2 Cavity coupling . . . 70
5.4.3 Thermal instabilities . . . 71
5.4.4 Finesse measurements . . . 72
5.4.4.1 Sidebands technique . . . 72
5.4.4.2 Ringdown . . . 73

5.4.4.3 Scanning technique . . . 75
5.5 Paul trap structure . . . 76
5.5.1 Paul trap components . . . 78
5.5.2 Loading the Paul trap . . . 79
5.5.3 Positioning the trap . . . 81
5.6 Vacuum system and stability . . . 82
5.6.1 Air breakdown . . . 83
5.7 Particles detection . . . 86
5.7.1 Secular and micromotion . . . 86
5.7.1.1 Secular frequencies vs Voltage . . . 89
5.7.1.2 Secular frequencies vs Driving frequency . . . 90
5.8 Heating rates of particle's motion . . . 91
5.9 Mechanical damping rates of particle's motion . . . 93

6 Cavity cooling in the hybrid trap 96
6.1 Particle's motion via scattered light . . . 96
6.2 Blue detuning . . . 98
6.3 Red detuning and cooling . . . 99
6.4 Analysis of the experiment . . . 101

7 Nonlinear dynamics and strong cavity cooling 104
7.1 New cavity . . . 104
7.1.1 Cavity finesse . . . 107
7.2 Heterodyne detection of cavity output . . . 108
7.2.1 Estimating N from sideband structure . . . 111
7.3 Cooling . . . 112
7.4 The cavity shift . . . 117

8 Experimental tests for future improvements 120
8.1 Side locking . . . 120
8.1.1 Balanced detection . . . 124
8.2 Second laser . . . 126
8.3 Optical phase locking . . . 129
8.4 Mirror cleaning . . . 134
8.5 Future perspectives . . . 136

Summary and conclusions 138

Appendix A: Modulated Optomechanics 142

Appendix B: The AOMs drivers 148

Appendix C: The Fabry-Perot cavity 151

Appendix D: The Pound-Drever-Hall method 159

Bibliography 163

Acknowledgments

I will always be grateful to Professor Peter Barker for giving me the opportunity to work at UCL and shape myself as a scientist, while meeting wonderful people in the process.

My deepest thanks go to Dr. James Millen, for teaching me so much in the lab and trusting me enough to put such a promising experiment into my hands. I was lucky to have the company of Lia and Manish since the start of my PhD, always ready to give me support, inside and outside the lab. All members of the UCL optomechanics group that I had the pleasure to meet during the last four years have my sincere gratitude and esteem.

All the friends I made in the physics department couldn't contribute any better to this great experience.

A big thanks goes to my family, for always supporting my choices and believing in me.

Publications

1. J. Millen, P. Z. G. Fonseca, T. Mavrogordatos, T. S. Monteiro, P. F. Barker, "Cavity cooling a single charged levitated nanosphere", Physical Review Letter **114**, 123602 (2015)

2. P. Z. G. Fonseca, E. B. Aranas, J. Millen, T. S. Monteiro, P. F. Barker, "Nonlinear dynamics and strong cavity cooling of levitated nanoparticles", Physical Review Letter **117**, 173602 (2016)

3. E. B. Aranas, P. Z. G. Fonseca, P. F. Barker and T. S. Monteiro, "Split-sideband spectroscopy in slowly modulated optomechanics", New Journal of Physics **18**, 113021 (2016)

4. E. B. Aranas, P. Z. G. Fonseca, P. F. Barker and T. S. Monteiro, "Thermometry of levitated nanoparticles in a hybrid electro-optical trap", Journal of Optics **19**, 3 (2017)

Introduction

On the 11th of February 2016 many of us at UCL stopped working and gathered together to watch a live press conference from the National Science Foundation, announcing the first direct detection of gravitational waves. 100 years after Einstein's predictions [1], scientists at LIGO laboratory were able to observe for the first time distortions in space-time caused by passing gravitational waves, generated by two colliding black holes 1.3 billion light years away [2]. Besides the historical scientific achievement, what I was truly impressed about was the fact that LIGO's interferometer was actually able to sense a displacement that was thousands of times smaller than the nucleus of an atom. In order to do that, one of the most precise and sophisticated tools was employed: light. By propagating two high-power light beams over a long distance (4 km in the case of LIGO), and recombining them to create an interference pattern, allows one to detect changes in the length of one of the two interferometer's arms, which can be of the order of 10^{-19} m. Such sensitivity in the LIGO experiment is actually achieved by including two optical cavities along the optical paths of the interferometer, that continually reflect parts of each laser beam back and forth within the 4 km long arms, about 300 times, before they are merged together again. This makes LIGO's interferometer arms effectively much longer, boosting its sensitivity. Of course, to achieve such precision, one needs to refine the experiment in order to remove any unwanted vibration that the test masses of the interferometer might pick up (from a truck driving on nearby roads to earthquakes on the other side of the world), that would inevitably hide a, much weaker, gravitational wave signal. At this point, one should ask themselves how precise such types of measurements can get, once the surrounding noise has been, ideally, completely eliminated. The answer is that, even if the best isolation and damping systems are used, there will be an ultimate limit in the measurement precision achievable, a limit given by the nature of light itself. To understand why, we need to remember that, as already observed by Kepler looking at comet tails [3], and theoretically explained by Maxwell later on [4], electromagnetic radiation can exert forces on material objects, due to the momentum transfer given by the reflection of photons. As a matter of fact, at the beginning of the seventies, in the context of interferometric gravitational wave experiments, it was

observed that monochromatic light trapped in a high-finesse optical cavity exerts radiation pressure on the end mirrors, coupling their oscillatory motion to the light. Now, this fact imposes an insurmountable sensitivity limit in displacement measurements of the mirrors, since quantum fluctuations of the radiation pressure force induce a random motion that masks the displacements to be detected [5]. This effect is now referred to as quantum back action. Besides, it was also understood that radiation pressure could effectively influence the dynamics of a mirror, adding an optically induced viscous damping to its motion. This classical phenomenon is instead called dynamical back action, and can be used in principle to amplify or cool the motion of a mechanical resonator [6].

The effect of optical forces on material objects soon suggested the idea of controlling the dynamics of mechanical degrees of freedom using light, something that has been revealed to be possible in a surprisingly flexible and precise way. The use of radiation pressure forces associated with focused laser beams brought important achievements, from trapping single atoms [7] to optical tweezing of organic cells [8]. In parallel, the use of the strong enhancement provided by resonant light scattering led to the laser cooling of ions and neutral atoms [9, 10, 11], and the production of the atomic Bose-Einstein condensate in 1995 [12], allowing the exploration of quantum-degenerate atomic systems. Resonant enhancement of the light-matter interaction soon also became the key requirement in the attempt to control the motion of bigger and more complex systems, which can range from nanometer-sized devices to centimeter-sized mirrors used in gravitational wave detectors. In these cases, rather than considering the internal structure of materials, researchers started pointing their attention to high quality cavity resonators, which offer at the same time the advantage to achieve optomechanical effects for a broad range of wavelengths, from the microwave to the optical regime, and to give a very large enhancement of the interaction through an engineered resonant structure.

The intersection of two subjects, optical cavities and mechanical resonators, based on the presence, and on the effects, of optical forces, gave rise to the burgeoning field of cavity optomechanics, which explores and exploits the interactions between optical and nano- or micro-mechanical resonators, and it has now been investigated for over three decades [13, 14, 15]. At the beginning, many theoretical works have been published proposing to use optomechanical systems to explore quantum effects: quantum non demolition measurements of the light intensity [16], generation of non-classical states of motion [17], generation of squeezed light [18], and generation of entangled states of the light field and the mechanics [19]. In particular, it has been suggested to cool the mechanical mode of an oscillator to its quantum ground state using dynamical back action, in order to reach and observe the zero-point fluctuations of its motion. Such engineered systems are seen as a new frontier in

quantum physics as they offer a route to determine and control the quantum state of truly macroscopic objects, and paves the way to experiments that study the classical-quantum boundary and decoherence mechanisms in an unexplored regime [20, 21]. From the point of view of applications, quantum optomechanical techniques will provide motion and force detection near the fundamental limit imposed by quantum mechanics [21].

First experimental results did not arrive until the early 2000s, when the latest progress in micro and nano-fabrication technologies made it possible to overcome the main experimental challenges in this field. Namely, the very feeble effect that each reflected photon has on massive objects usually lead to a very weak optomechanical coupling. At the same time, the oscillator displacements associated with quantum effects are easily masked by noise. Nonetheless, using devices with higher and higher mechanical and optical quality factors made it possible to observe static and dynamic manifestations of radiation pressure forces on micro and nano-mechanical oscillators, like the modification of mechanical oscillator stiffness, parametric instability and back action cooling [22, 23, 24]. The coexistence of high-Q optical and mechanical modes has been achieved in a large variety of optomechanical geometries and setups, involving cantilevers, micro-mirrors, microtoroidal cavities, nanomembranes, as well as microelectromechanical systems (MEMS) and nanoelectromechanical systems (NEMS) [14]. In recent years, these efforts have culminated in the cooling of the center-of-mass motion of several micromechanical systems to the quantum ground state (i.e. a mean thermal occupation $\langle n_{th} \rangle < 1$) [25, 26]. In the first case [25], the mechanical resonator was a suspended circular aluminum membrane tightly coupled to a superconducting lithographic microwave cavity. The cavity was pre-cooled to 20mK, corresponding to an initial occupation of 40 phonons, and then further cooled by radiation pressure forces to an average phonon occupancy of $\langle n_{th} \rangle \approx 0.3$. In reference [26] instead, they utilized an optomechanical structure with co-located photonic and phononic band gaps in a suspended on-chip waveguide. The structure was pre-cooled to 20K, corresponding to about 100 thermal quanta, and then cooled via radiation pressure to $\langle n_{th} \rangle \approx 0.85$.

Following the work done by Arthur Ashkin and co-workers in the 70's on optical levitation of glass microspheres [93, 94], recently the idea of levitating mechanical objects within an optical cavity, either by an additional optical dipole trap or in the standing wave trap formed by the cavity field, has been suggested [27, 28, 29]. This scheme is particularly attractive as it offers the prospect of mesoscopic and even macroscopic quantum oscillators with extremely high quality factors and largely decoupled from environmental heating and decoherence: a mechanical oscillator such as a nanosphere that is oscillating in vacuum minimized the coupling to the environment, and the lack of clamping minimizes mechanical dissipation [30]. Achieving a high mechanical quality factor, while maintaining low mechan-

ical frequencies and comparatively high masses, would make levitated schemes useful for cat-state preparation [31], matter-wave interferometry [32], tests of collapse theories [33, 34] and ultra-sensitive short-range force sensing [35].

In this thesis, we present a new method for cavity cooling charged nanoparticles, utilizing both the optical field of a cavity and the electric field of a Paul trap [36, 37]. As it will be extensively described in the next chapters, the hybrid nature of our combined Paul trap-optical cavity set up gives rise to a peculiar and rich mechanical dynamics, which can be read either via the light scattered from the nanoparticle, or the output light of the cavity, and which reveals an interesting interplay between the two traps. The Paul trap crucially drives the cavity cooling dynamics by introducing a cyclic displacement of the equilibrium point of the mechanical oscillations in the optical field. At the same time, the optical field provides a cavity field shift to the Paul trap secular frequencies and stability parameters. In addition, the deep Paul trap potential avoids instabilities that have been observed in all-optical traps at low pressures, and allows us to operate in vacuum. This system has allowed us to stably trap 200 nm silica nanoparticles at pressures of 10^{-6} mbar, and observe the cooling dynamics via both linear and non-linear optomechanical coupling. As the background gas pressure was lowered, we observed greater than 1000 fold reduction in temperature, before temperatures fell below the read-out sensitivity of the setup. This work opens the way to strongly-coupled quantum dynamics between a cavity and a nanoparticle largely decoupled from its environment.

The thesis is structured as follows: in the first chapter I will summarize the main features of cavity optomechanics. A qualitative description of the principles of interaction between an optical cavity and a mechanical resonator is given, in order to understand the mechanisms of cooling and heating of the mechanical motion. This is done by taking into consideration a standard setup, where one of the end mirrors of the cavity is free to oscillate, and it represents the mechanical moving part, subjected to radiation pressure.

In chapter 2, the discussion is extended to levitated optomechanics, where a levitating dielectric object is optically trapped in the middle of the cavity with fixed mirrors, and whose motion is coupled to the cavity mode via dipole forces. The main advantages and limitations of levitated setups will be discussed, to better understand the innovative role of the hybrid trap presented in this thesis.

Chapter 3 is dedicated to a more detailed description of the optomechanical coupling, starting with a separate picture of quantum harmonic oscillators and optical cavities. After that, the two elements are combined to derive the equations of motion of a general optomechanical system, and to gain an understanding on the origins of the optomechanical cooling. Such results are relevant as they will introduce to the specific case of a levitated nanoparticle.

In chapter 4 we will start to study the hybrid system used in our experiment. First, we analyze the typical behavior of a charged particle in a quadrupole Paul trap. Then, the behavior of a particle trapped inside an optical cavity is presented. After that, we use the concepts expressed previously to mathematically describe the combined dynamics of a charged nanoparticle in the hybrid electro-optical trap. Here we set all the relevant aspects that will allow the reader to understand the experimental results presented further in the thesis.

Chapter 5 is devoted to the description of the experimental apparatus, in all its components. This will include the discussion on calibrations, and the main methods of measurements used to obtain important experimental parameters, for both the cavity and the Paul trap, with and without particles trapped.

In chapter 6 and 7, we present the cooling results. Two different setups, with cavities of different finesse and volume, have been presented separately in the two chapters. In the first case (chapter 6), in order to observe the particle's dynamics and estimate the cooling of its centre of mass motion, we analyze the light scattered from the nanoparticle. In the second case (chapter 7), a new cavity of higher finesse allows the modulation of the light field, driven by linear and nonlinear couplings with the particle, to be visible through the light transmitted by the cavity. Here, we observe an improvement in the cooling performances, given by the higher finesse cavity, and realize the limits of our setup.

Finally, chapter 8 presents some of the most recent modifications to the experimental apparatus, implemented in the attempt of improving the detection sensitivity and cooling performances of our setup. Future perspectives and conclusions will end the dissertation.

Chapter 1

Cavity Optomechanics: an overview

In this first chapter I give a qualitative overview of the main working principles in cavity optomechanics. The mutual coupling of optical and mechanical degrees of freedom will be described for the case of a general optomechanical system, formed by a laser-driven optical cavity and a vibrating end mirror. All the features discussed for such a commonly used experimental setup can then be extended to the large range of systems that are now available, including the levitated system described in this thesis.

1.1 Principles of optomechanical interaction

We can define a cavity optomechanical system as an optical cavity that contains a mechanical moving part. Consider a cavity where one of the end mirrors is free to oscillate, as if attached to a spring, as represented in figure 1.1.

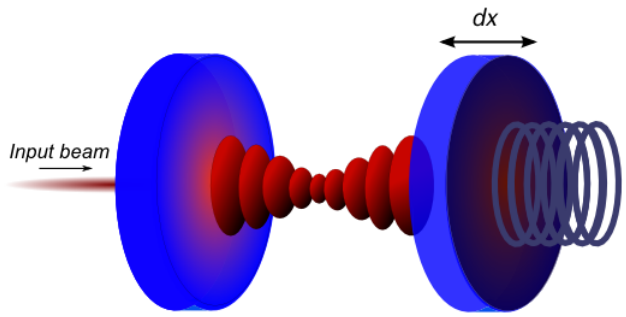

Figure 1.1: Schematic of a standard optomechanical system, formed by an optical cavity with a fixed, partially reflective input mirror, and a movable end mirror, whose oscillatory motion is coupled to the intracavity light.

The force F exerted by a light beam of power P retroreflecting from a mirror is $\mathrm{F} = 2P/c$ [15], and it is typically extremely small since the speed of light is very large. Hence, the importance of using an optical cavity, which is able to increase this effect by many orders of magnitude, as it makes photons bounce around hundreds of thousands of times, each time transferring a small momentum kick to the end mirrors. The harmonically bound mirror then will start moving under the effect of a light-induced force, and this will change the length L of the cavity. As proved in Appendix C, when the distance between the two mirrors is an integer multiple of half of the incident beam wavelength (resonance condition) the intracavity intensity shows a maximum; so, when L changes around that resonant value, the intensity changes according to a Lorentzian peak, whose height is proportional to the incident intensity. Furthermore, the phase of the reflected field is also sensitive to length changes (see figure 1.2); if the moving mirror experiences a displacement dx from the resonance position, the modulation in phase $d\varphi$ will be given by the relation [23]:

$$d\varphi \propto \mathcal{F}\frac{dx}{\lambda},$$

where the proportionality factor $\mathcal{F}$ is called cavity finesse. If dx is of the order of the full width at half maximum of the intensity peak, the phase will undergo a variation equal to 2π.

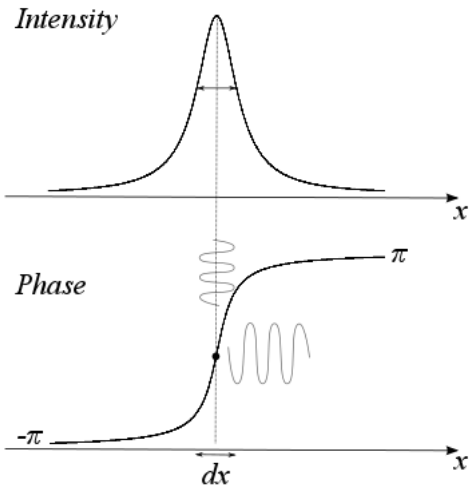

Figure 1.2: Transduction mechanism for the light beam resonantly probing the cavity. A small change in dx around resonance induces a large change in the phase [23, 55].

It is interesting to note that the high number of roundtrips that the light undergoes between the two mirrors enhances the effect that the displacement has on the light, by the factor $\mathcal{F} = 2\pi b$, with b number of roundtrips, with respect to the equivalent phase shift that one

could measure with a simple Michelson interferometer [38]. This shows that the sensitivity of a Fabry-Perot cavity is much higher than two-wave interferometers, as long as we work near the optical resonance of the cavity. In the end, a Fourier analysis of the light field reflected by the cavity is able to reveal the mechanical spectrum of the mirror motion, allowing one to estimate the values of dx [47].

Besides the ability to measure with high sensitivity the position of a mechanical oscillator, this kind of setup gives the possibility of exploiting radiation forces to manipulate the center-of-mass motion of the mechanical oscillator. Optomechanical coupling arises when the mechanical motion changes not only the phase, but also the intracavity field intensity, which in turn will change the radiation pressure force experienced by the mirror. The latter acts as an additional elastic force on the oscillator, which changes the mirror's spring constant, creating the so called "optical spring effect". This can be used to increase or decrease the frequency of an oscillating mirror [48]. We note that this mechanism can not take place at resonance, where the intensity function's slope is null. We need then to move away from the resonance position, and this can be done either by changing the cavity length, or by detuning the laser with respect to the characteristic frequency ω_c of the cavity.

However, this picture is incomplete, as it does not take into account the fact the radiation forces respond to the motion of the mirror only after some time delay. This is due to the ring-down time of the cavity, i.e., the time needed for photons to leak out (proportional to the cavity finesse $\mathcal{F}$). The radiation force as a function of mirror position is itself a simple Lorentzian; so, if we assume the equilibrium position of the mirror to be somewhere on the rising slope of the resonance, on approaching resonance, the force will be smaller than expected, due to the time lag, and it remains larger when the mirror retracts (figure 1.3).

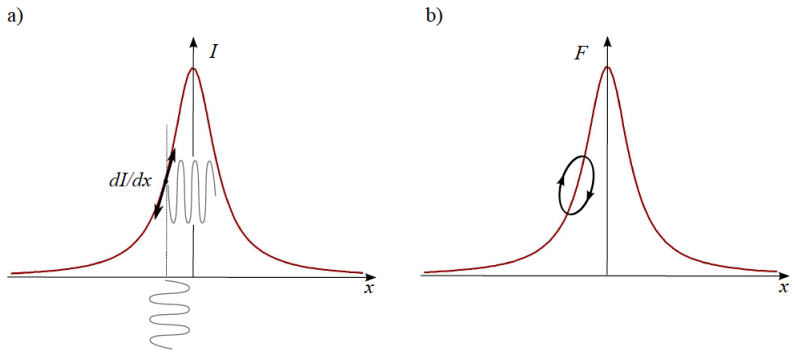

Figure 1.3: a) Intracavity intensity vs mirror position: moving on one side of the resonance the intracavity intensity changes with position fluctuations. b) Radiation pressure force vs position: As the mirror oscillates the system moves up and down the slope of resonance leading to damping of the mirror fluctuations [14, 54].

Overall, the radiation force F extracts work from the mirror:

$$\oint \mathrm{F} dx < 0.$$

This amounts to an extra damping, which will cool down the centre-of-mass motion of the mirror by reducing thermal fluctuations. Clearly, positioning the mirror on the opposite side of the resonance leads to a negative effective damping constant, and hence to an amplification of the mirror's oscillations. The mechanism just described is referred to as "dynamical back action effect" [22], so called because it involves the light field acting back on the mechanical motion after having been perturbed by the mirror. Like quantum back action, this effect modifies the motion of the object being measured. While quantum back action causes the mirror to be subjected to a stochastic force, effectively setting a measurement precision, dynamical back action modifies the dynamical behavior of the mirror in a predictable manner.

We could describe the coupling mechanism with a feedback loop ([54]).

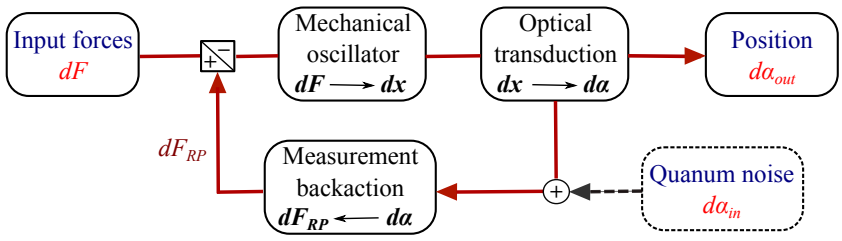

Figure 1.4: Feedback loop describing the measurement process and its back-action on the movable mirror. The elements of this loop include the mechanical and optical oscillators coupled through two distinct paths. Along the upper path, a force acting on the mechanical oscillator causes a mechanical displacement, which (for a detuned laser) changes the cavity field due to the optomechanical coupling. However, the amplitude fluctuations, which contain information on the mirror position, are also coupled back to the mechanical oscillator via radiation pressure (lower path), resulting in a back-action. A blue detuned pump wave sets up positive feedback (the instability), whereas red detuning introduces negative feedback. Resonant optical probing (where the excitation frequency equals the cavity resonance frequency) interrupts the feedback loop because changes in position only change the phase, not the amplitude, of the field (figure from [54]).

The mechanical oscillator is initially acted on by a force dF, caused by thermal coupling with the environment or by an externally applied signal, which induces a mechanical response dx. Such displacement creates a change in the optical field, either in amplitude $d\alpha$ or in phase $d\varphi$, depending on the detuning, which allows the measurement of the mechanical position; but it does that with a time delay given by the finite cavity lifetime. For a detuned laser, the amplitude change feeds back to the mechanical oscillator through the radiation pressure force, closing the feedback loop. The sign of the feedback depends on the cavity detuning and can produce either damping or amplification. In a quantum description, this feedback

branch is not noiseless but is subjected to the quantum noise of the optical field ($d\alpha_{in}$) causing quantum back action. Although dynamic back action can be prevented by probing the cavity on resonance ($d\alpha = 0$) the quantum back action nevertheless feeds into the mechanical oscillator's input, reinforcing the standard quantum limit, as further explained in next section.

Another way of understanding the origins of cooling and mechanical amplification in the optomechanical system described is the motional sideband approach. In this description it is convenient to switch from the time domain to the frequency domain; in this way we can intuitively understand that periodic motion of the mechanical system at frequency ω_{M} will modulate the reflected beam laser frequency, creating sidebands at frequencies $\omega_l \pm \omega_{\mathrm{M}}$, which are generally referred to as Stokes (red) and anti-Stokes (blue) signals. The latter is a result of pump-laser photons acquiring energy by annihilating thermal phonons in the mechanical element; the former instead results from photons depositing phonons and shedding energy. By carefully detuning of the frequency of the pump field relative to a specific cavity resonance ω_c (i.e. $\Delta_0 \equiv \omega_l - \omega_c \neq 0$), one can resonantly enhance one of these processes. In particular, red detuning from the cavity resonance enhances the upper sideband and promotes extraction of energy from the mechanical element. Because the scattered photons leak out of the cavity, energy is dissipated from the optomechanical system, and the process can cool the motion of the mechanical element well below the temperature of its surroundings. On the other hand, by blue-detuning the laser, one is able to amplify the mirror oscillations (see figure 1.5).

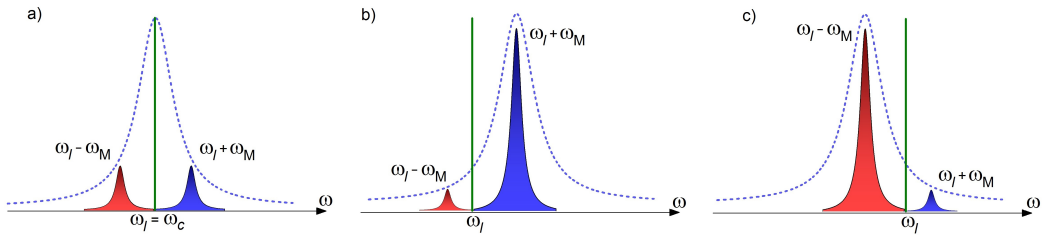

Figure 1.5: Optomechanical interaction in terms of motional sidebands. a) With the pump beam (green) tuned to a cavity resonance, sidebands are of equal amplitude. b) By red-detuning the laser ($\Delta_0 = \omega_l - \omega_c = -\omega_{\mathrm{M}}$) the anti-Stokes sideband (blue peak) will be enhanced, resulting in cooling of the mechanical oscillator. c) Blue-detuning instead ($\Delta_0 = \omega_l - \omega_c = \omega_{\mathrm{M}}$) will favor Stokes sideband (red peak), giving mechanical amplification [14, 54, 67].

The sideband scheme, which also explains how to achieve cooling, makes us see that we cannot approach the quantum ground state unless the Stokes intensity is close to zero. This is reasonable since the Stokes process excites the mechanical system to higher energy levels. To reach large Stokes/anti-Stokes asymmetry, the cavity resonance linewidth κ, represented by the full with at half maximum (FWHM) of the Lorentzian, has to be smaller than the

sideband spacing (set by the mechanical frequency of the oscillator, ω_{M}). In literature, this is referred to as good cavity limit, or resolved sideband regime [49, 50, 51], represented by the condition $\kappa < \omega_{\mathrm{M}}$.

1.2 Limits

A key feature in optomechanical systems is the use of highly coherent optical beams, as the ones given by a laser source, which enhance the sensitivity in the measurements of mechanical displacement, since they are able to offer noise performances that are limited only by quantum noise. This consideration brings us to the problem of fluctuations, both thermal and quantum, that set ultimate limits to sensitive force and displacement detection. In terms of mirror-displacement measurement, two fundamental sources of imprecision exist. First, there is shot noise [52], which is related to the detection of light. When a photodetector is illuminated by a laser beam, the resulting photocurrent is not perfectly steady, and this comes directly from the probabilistic distribution of the number of photons in laser emitted coherent states, which makes the photocurrent not uniform. The magnitude of shot noise increases according to the square root of the number of signal electrons N, which depends on the intensity of the incoming light beam, and so the signal-to-noise ratio can be written as:

$$\mathrm{SNR} = \frac{N}{\sqrt{N}}.$$

To increase this ratio, and improve the measurement precision, we can simply increase the laser power.

Increasing power, however, means also enhancing the quantum back action effect, feeding additional noise to the movable mirror. This is the second source of imprecision: the fluctuating number of momentum kicks of reflected photons creates mirror displacement noise. The higher the intracavity intensity, the stronger this effect will be.

In conclusion, for low-input laser power, detector noise due to the quantum shot noise of the laser field dominates, whereas at high laser power the quantum fluctuations of the light field cause the mirror to undergo random fluctuations. At the optimum power, the two sources of fluctuation contribute equally to the measurement imprecision, constituting the so called standard quantum limit (SQL) [53]. Here, detector noise and quantum back-action noise each contribute a position uncertainty equal to half of zero-point motion (ZPF) of the mirror, where the ZPF is given by:

$$x_{\mathrm{ZPF}} = \sqrt{\frac{\hbar}{2\mathrm{M}\omega_{\mathrm{M}}}}, \tag{1.1}$$

where M is the mass of the mirror, and ω_{M} its harmonic frequency. Another way to see this, is through the Heisenberg's Uncertainty Principle, which does not allow one to follow the mirror motion over time with arbitrary precision, revealing the mirror trajectory, and ultimately sets a measurement limit. Furthermore, as one can see from figure 1.6, the displacement sensitivity can reach the zero-point motion only when the mechanical oscillator temperature is absolute zero.

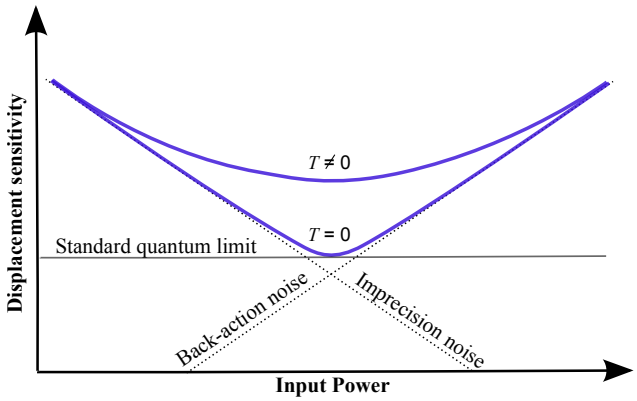

Figure 1.6: Measurement sensitivity in the case of a zero-temperature mechanical oscillator mirror and for finite temperature T [54].

At finite temperature the radiation pressure quantum back action is masked by thermal noise. This temperature-related noise is something that strictly concerns the mechanical oscillator and its coupling to the environment. The thermal phonon number n_{th} of a mechanical mode is set by the mode frequency ω_{M} and the device temperature T, and it follows the Bose-Einstein distribution [55]:

$$n_{th} = \frac{1}{e^{\hbar\omega_{\mathrm{M}}/k_B T} - 1}.$$

For high temperatures this expression reduces to the classical equipartition of energy: each mode carries $k_B T$ of energy. But to enter the regime where quantum fluctuations become dominant and observable requires that the mechanical mode's temperature satisfies $k_B T < \hbar\omega_{\mathrm{M}}$, equivalently an average thermal occupation less than unity.

1.3 Experimental realizations

Satisfying the condition $k_B T < \hbar\omega_{\mathrm{M}}$ is the main challenge with observing quantum phenomena in optomechanical systems. This is difficult to overcome just by using cryogenic cooling, since even mechanical frequencies of 1MHz correspond to temperatures of $\sim 10^{-5}$ K (although we note that in 2010 O'Connell *et al.* demonstrated cooling of a microwave-frequency mechanical resonator to $\langle n_{th} \rangle < 0.07$ just by using a conventional dilution re-

frigerator that can reach temperatures of 25 mK, thanks to the resonator's high frequency, of about 6 GHz, [56]). However, a combination of cryogenic pre-cooling and back-action laser cooling demonstrated that reaching an occupancy of a few thermal quanta is already possible [57].

The choice of the mechanical elements to use is also of crucial importance. We need high mechanical frequencies, not only because ω_M sets the ground state temperature of the mechanical mode, but also because we need a high mechanical quality factor Q, given by:

$$Q = \frac{\omega_M}{\Gamma_M}, \tag{1.2}$$

where Γ_M represents the damping rate of the oscillator. High Q means that the devices will be less coupled to the environment, and so optomechanical cooling will be more effective.

During the last few years many different setups have been realized, demonstrating the working principles of cavity optomechanics (see figure 1.7).

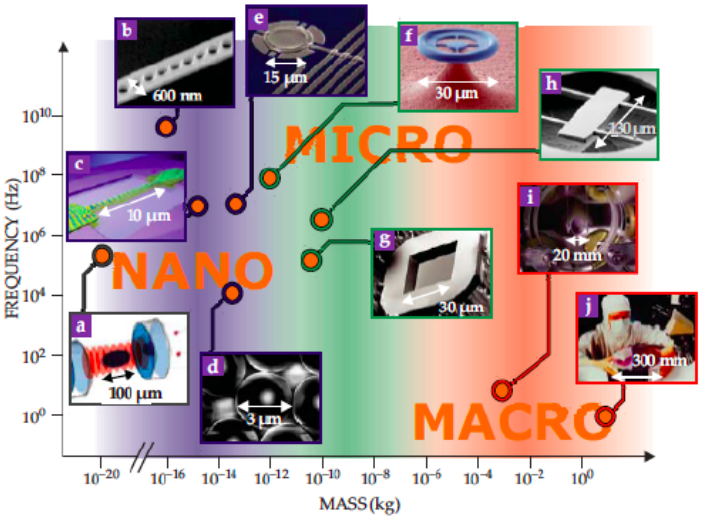

Figure 1.7: Different optomechanical possibilities involving cantilevers, micro-mirrors, waveguides, nano-membranes, ultracold atoms and macroscopic mirrors, at their typical frequencies $\omega_M/2\pi$ and masses M (figure taken from [67]).

They mostly involve harmonically suspended end mirrors with high reflectivity coatings, whose masses can range from 10^{-3} to 10^{-15} kg, while frequencies typically go from the kHz to the MHz regime. These end mirrors have been realized in multiple ways, such as from an etched, high-reflectivity mirror substrate [23, 58], a miniaturized and harmonically suspended gram-scale mirror [59], or an atomic force cantilever on which a high-reflectivity and micron-sized mirror coating has been transferred [60]. A rather different approach is based on microtoroid and microsphere resonators, where light is injected and coupled into an optical whispering gallery mode to exert a radiation pressure that couples to a mechanical breathing mode [61]. Their small size allows one to achieve large light-matter coupling

rates, and to access mechanical frequencies from several MHz to up to some GHz. Another interesting scheme involves a membrane of very low thickness, with masses of the order of nanograms, placed between two macroscopic, rigid, high finesse mirrors. This circumvents the problem of integrating small, light and sensitive micromechanical elements into cavities, which are typically much more rigid and massive, without compromising the mechanical or optical properties of either, since it segregates optical functionality to physically distinct structures [62]. In 2017, nanomechanical resonators consisting of a silicon nitride membrane patterned with a phononic crystal structure [63], have been shown to strongly suppress mechanical dissipation via "soft" clamping and dissipation diluition, yielding the highest mechanical $Q \cdot \omega_M$ products ($> 10^{14}$ Hz) yet reported at room temperature. Other interesting setups involve waveguides and photonic crystal cavities, [64], ultra-cold atom clouds [65], microwave resonators [25, 66], and levitated nano-objects. The latter is the subject of this thesis, and it will be introduced in next chapter.

Chapter 2

Optomechanics with levitated dielectric particles

The idea of using particles that are levitated in a vacuum as the mechanical elements of an optomechanical system has recently attracted much interest [68]. To reach a regime where the quantum behavior of mechanical devices emerges, it is critical that the thermalization and decoherence rates of these systems are minimized, by reducing the coupling to thermal reservoirs. In most experimental realizations, this had necessitated the use of cryogenic operating environments. From an engineering standpoint, it is also desirable to reduce the dissipation and thermalization rates of these systems through their clamping and material supports. Barker and Shneider [27], Chang *et al.* [28] and Romero-Isart *et al.* [29] in 2010, where among the first to propose to completely eliminate material supports by optically levitating the nano-mechanical system inside a Fabry-Perot optical cavity. Knowing that levitation under good vacuum conditions can lead to extremely low mechanical damping rates, they show that such an approach can also facilitate the emergence of quantum behavior even in room-temperature environments, when the polarizability of the particles (as defined in section 2.3) is such that noise effects from optical scattering become negligible. In their illustration, these systems constitute an extreme example of environmental isolation, as the centre-of-mass motion is naturally decoupled from the internal degrees of freedom (as the sphere effectively has no internal structure) in addition to the external isolation provided by levitation.

The damping rate from the background gas can be approximated as [28]:

$$\Gamma_{\mathrm{M}} \simeq \frac{16p}{\pi \bar{\mathrm{v}} \rho \mathrm{R}}, \tag{2.1}$$

where p and $\bar{\mathrm{v}}$ are the background gas pressure and mean speed respectively (with $\bar{\mathrm{v}} \simeq$

500 m/s at room temperature), R is the sphere radius, and ρ its mass density. The number of coherent oscillations of the particle before the energy increases by a single phonon is defined as $N_{osc} \equiv \omega_{\mathrm{M}}\tau_{\mathrm{M}}/2\pi$, where $\tau_{\mathrm{M}} \sim \hbar\omega_{\mathrm{M}}/\Gamma_{\mathrm{M}}k_BT$ is the characteristic time for the system to heat by one photon starting from the ground state. For a sphere of radius $\mathrm{R} = 50\,\mathrm{nm}$, $\omega_{\mathrm{M}}/2\pi = 1\,\mathrm{MHz}$ and a room temperature gas with $p = 10^{-10}\,\mathrm{mbar}$ one finds $\Gamma_{\mathrm{M}} \sim 10^{-6}\,\mathrm{s}^{-1}$, a mechanical quality factor $\mathrm{Q} \sim 10^{12}$ and $N_{osc} \sim 10^5$. This indicates that the levitated sphere can be essentially de-coupled from its thermal environment, and it can coherently evolve for many oscillation periods. This makes this system a promising candidate for observing coherent quantum phenomena. In [28], besides the dominant heating mechanisms of background gas collisions and photon recoil kicks, contributions from shot noise, blackbody radiation and sphere anisotropy have been accounted for and shown to be negligible.

Another advantage of this implementation is that oscillation frequencies are fully tunable, since they are not an intrinsic feature of the resonator, but they are determined by the optical field [69, 70]. The mechanical frequency of a polarizable particle trapped near an anti-node of a standing wave $E(x) = E_0 \cos kx$, (with optical wave number $k \equiv 2\pi/\lambda$), can be expressed as [28]:

$$\omega_{\mathrm{M}} = \left(\frac{6k^2 I_0}{\rho c}\mathrm{Re}\frac{\epsilon - 1}{\epsilon + 2}\right)^{1/2}, \tag{2.2}$$

where ϵ is the electric permittivity and I_0 is the field intensity.

2.1 Motivations

As discussed in the previous chapter, cooling a mechanical resonator to its ground state of motion is an essential step in eliminating the thermal fluctuations that normally mask quantum features. However, by itself that state is not particularly interesting, so the next challenge is to prepare, manipulate and characterize quantum states of the mechanical resonator required for a specific science or engineering goal. Levitated nanoparticles offer the chance of developing protocols to prepare and observe genuine quantum features. As an example, once the ground state is achieved, it is possible to exploit the coherent coupling of the levitating particles with single photons or qubits to create quantum superpositions [29, 71]. We can illuminate the cavity with a single-photon state, sent on top of the driving field, from parametric down conversion followed by a detection of a single photon [72]. When entering the cavity, part of the field will be reflected and part transmitted. In the presence of the cooling laser, the optomechanical coupling will swap the photon state into the centre of mass phonon state of the nanoparticle, yielding the entangled state $|0\rangle_r |1\rangle_m + |1\rangle_r |0\rangle_m$, where r denotes the reflecting photon mode, and m denotes the center of mass phonon mode. The

motional state collapses into the superposition state $|\Psi\rangle = c_0 |0\rangle_m + c_1 |1\rangle_m$, by performing a balanced homodyne measurement of the output mode and by switching off the driving field. Here the coefficients $c_{0(1)}$ depend on the measurement result. The superposition state can be detected by either transferring it back to a new driving field and then performing tomography on the output field, or by monitoring the quantum mechanical oscillation caused by the harmonic trap. One could even modify this protocol to circumvent the challenging step of measuring the displaced output mode that generates the superposition, namely the fact that the signal-to-noise ratio in the balanced homodyne measurement will be too low. The possibility to time-modulate the laser intensity, and consequently the optomechanical coupling, can be exploited to obtain a perfect absorption of the light pulse by the oscillator, such that the non-Gaussian state of the light is transferred to the mechanical oscillator [29].

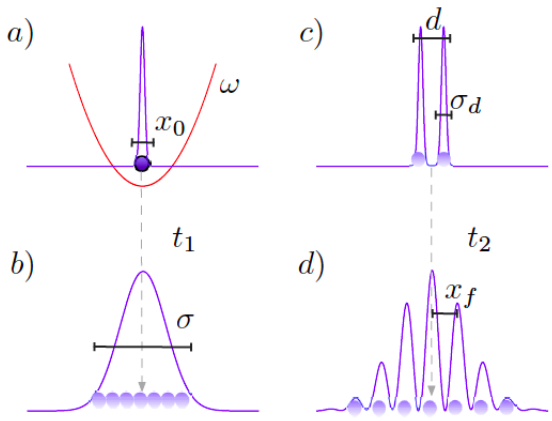

Figure 2.1: Schematic illustration of MERID. a) An harmonically trapped sphere is cooled to its ground state, giving a zero point motion x_0. b) The trap is switched off and the wave function expands during some time t_1. c) A squared position measurement is performed such that the wave function collapses into a superposition of two wavepackets, conditional on the measurement outcome. d) The particle falls during a time t_2 until its centre of mass position is measured, which after repetition unveils an interference pattern (figure taken from [73]).

In a superposition of the mechanical motion state of the form $|0\rangle + |1\rangle$, where $|0\rangle$ and $|1\rangle$ are respectively the ground state and the first excited state of the particle's motion, the position is delocalized over distances of the order of the zero point motion (eq. 1.1). A different proposal [31, 73], to coherently delocalize an harmonically trapped sphere over distances much larger than its zero point motion and to generate superpositions, is based on matter-wave interferometry. The proposed protocol, called Mechanical Resonator Interference in a Double slit (MERID), consists of cooling the nanoparticle to the ground state and then switching off the harmonic trap to let the wavefunction expand freely during some time of flight t_1. After the wave packet is sufficiently dispersed, the sphere enters a small cavity driven by a pulse of light and ideally aligned such that the mean position $\langle \hat{x} \rangle$ of the sphere along the cavity axis is at a node of the cavity mode. In this configuration the optomechanical coupling is quadratic

with $\hat{x}$. This implies that the output light of the cavity contains information about $\hat{x}^2$, and therefore, this can be measured by homodyning the output light. This measurement acts as a Young's double slit since, given the outcome x^2, the state collapses into a superposition of being $+x$ and $-x$. The mechanical resonator is then prepared in a spatial superposition separated by a distance $d = 2|x|$. The system freely evolves for a second time of flight t_2 until the two wave packets overlap, and an interference pattern should then be visible after many repetitions of the experiment, by correlating the detected positions with the results of the homodyne meaurements.

The overall performance of this challenging experiment is mainly limited by the quality of the cavity used in the measurement and the vacuum and temperature conditions required for the environment. In particular, very good vacuum conditions ($\lesssim 10^{-13}$mbar) are needed to keep the coherence of these fragile states. Standard sources of decoherence given by scattering of air molecules and emission, absorption and scattering of blackbody radiation, always need to be taken into account as they all contribute to a localization rate that imposes a series of constrains in the experimental parameters [73].

Being able to perform matter-wave interferometry experiments like MERID would allow one to unveil the validity of several collapse models, which predict an objective fast localization of the wave function for sufficiently large masses and sizes [73, 74]. In essence, when applying standard quantum theory to macroscopic systems, one predicts the existence of superpositions of different macroscopic states (Schrodinger's cat being dead + alive). However such superpositions do not match with the world as we perceive it. The lack of observations of macroscopically distinguishable superposition states of macroscopic objects allows us to conjecture that quantum mechanics should be modified at large scales. The modifications have been developed to explain the collapse of the wave function at the macroscopic level and also to solve the quantum measurement problem [75]. Various attempts have been made in this direction, including the Ghirardi-Rimini-Weber approach [76], Continuos Spontaneous Localization [77], and gravitationally-induced collapse models by Dionisi-Penrose [78]. These models modify the Schrödinger equation by introducing appropriate stochastic non-linear terms, which resolve the problems at macroscopic scales, while reproducing the same results as quantum theory at microscopic scales. In doing this, collapse models explain the quantum-to-classical transition, how the probabilistic and wave nature of atoms and molecules gives rise to the world of classical physics as we experience it, when objects become larger. Levitated nanoparticles are promising candidates for collapse tests as, in proposed experiments, the superposition states have to be associated to a large mass, have a large spatial separation between the positions where the particle is delocalised, and a long lifetime of the spatial superposition states (low decoherence rates) [79]. Unfortunately, the

experimental state-of-the-art is still far from allowing for a conclusive test. For instance the leading matter-wave experiments are still two orders of magnitude in mass away from testing a collapse model at interesting regimes [80, 81]. Alternatively, different approaches have been proposed, where non-interferometric tests can be explored, bypassing the need for the preparation of quantum superposition states, and even the need of cooling to the particle's motion to ground state [82, 83, 84].

Another possibility to be explored with levitated nanoparticle setups is non-linear coupling to position. As already demonstrated for other setups, such as the membrane-in-the middle scheme [85, 86], the optical frequency shift may no longer be linear but rather quadratic in the mechanical displacement, depending on the precise equilibrium position of the object. This is also a prominent feature of levitated systems, and it will be one of the subjects of chapter 3. Quadratic coupling opens up a number of interesting possibilities, such as quantum non demolition (QND) readout of the mechanical eigenstate [87, 88]. This would take optomechanics beyond the milestone of demonstrating phonon occupancies less than one, to actually allowing one in principle to observe quantum jumps in the mechanical state. This goal has, to date, not been realized but is receiving continuing attention and effort.

Ultrasensitive force detection with optically levitated sensors has been also investigated [35]. Unlike conventional sensors consisting of solid state mechanical resonators, e.g. cantilevers or membranes, the center of mass motion of optically trapped dielectric objects is immune to the chief sources of dissipation in these devices at low pressures, consisting of lossy internal flexural and vibrational modes, surface imperfections, and clamping mechanisms. The result is sub-attonewton force sensitivity that may have a number of applications ranging from Casimir force measurements [89], search for non-Newtonian gravity forces [90], and detection of gravitational waves [91]. It is important to emphasize that, given the large mechanical quality factors Q of these resonators, some form of oscillator damping is necessary to reduce Q to a value such that measurements can be made in a reasonable timescale. For example, a resonator with a quality factor of $\approx 10^{12}$ and an oscillation frequency of 100 kHz takes on the order of 10^6 s to equilibrate upon perturbation by a force. Optical cooling can therefore be used here to both damp the Q factor so that perturbations to the system ring down within reasonably short periods of time, and to localize the sphere by reducing the amplitude of the thermal motion. Nonetheless, for the aim of experiments proposed in references [35, 91], reaching the ground state is not required. This kind of applications represent an alternative to the use of levitated systems for the study of quantum coherence at the mesoscopic scale.

2.2 Optical Trapping

In 1970, Arthur Ashkin first demonstrated the possibility of accelerating and trapping micrometer-sized transparent particles in a fluid, using focused laser beams [92]. A few years later, levitation of glass microspheres in air [93] and high vacuum [94] was also achieved. Initially, setups involved the use of an upward-propagating beam, exploiting radiation pressure to counteract the gravitational force acting on the particle, while lateral confinement was provided by its non-uniform transverse intensity profile. In subsequent works, complete three-dimensional trapping was demonstrated in fluid [95] and air [96] even with downward-directed beams. By using focuses tight enough, the longitudinal forces acting on the particle, and given by the rapid divergence of the beam away from the focal spot, could overcome radiation pressure and gravity. These forces are generally called gradient (or dipole) forces, and form a trapping potential that attracts the object along the gradient of the laser intensity, into the region of strongest field.

When describing the gradient force, it is useful to distinguish between the case where the size of the object is much larger than the wavelength of the trapping light, and the one where its size is much smaller than the wavelength. In the former scenario the optical forces, generated by the exchange in momentum between the light and the object, can be described using ray optics. If the particle moves away from the center of the beam axis, it will deflect the beam, increasing the momentum of photons in the same direction as the displacement (figure 2.2). This imparts a force on the object which pulls it back towards the beam axis. Similarly, if the particle is displaced axially from the focus of the beam, the resulting refraction generates a force pushing it back towards the focal point. If we also include in this picture surface reflection, effectively corresponding to the action of radiation pressure force (also known as scattering force), the particles will also be subject to a push along the beam direction of propagation. If this force is larger than the restoring force due to refraction, the object will be pushed out of the trap. It is clear that, in order to trap a particle stably, the condition $\mathrm{F_{grad}} > \mathrm{F_{scat}}$ must be verified. This condition depends mainly on the ability to focus a laser beam strongly enough (i.e. using high numerical aperture objective lens) and on the relative index of refraction $\mathrm{p} = n_p/n_{md}$ (with n_p refractive index of the particle, and n_{md} refractive index of the medium) [97, 100].

If we consider a dielectric particle whose size is much smaller than the wavelength of the trapping laser beam, the object can be approximated as a dipole. As the electric field oscillates harmonically in time, the induced dipole follows synchronously and the particle acts as an oscillating electric dipole, scattering light coherently, with a radiation pattern that depends on the light polarization [98].

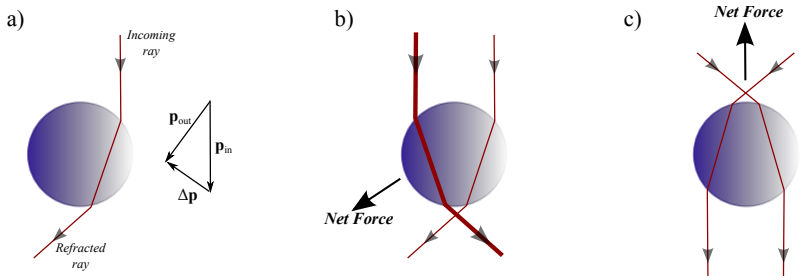

Figure 2.2: Ray-optics picture for an optically trapped particle of size $\mathrm{R} \gg \lambda$, as demonstrated in [98]. (a) Refraction of light on the particle generates a light momentum change $\mathbf{\Delta p}$ that is transferred to the particle with opposite sign. (b) Net force felt by the particle when two rays of different intensities are refracted, where the particle is pulled towards the higher intensity. (c) Net force resulting from a single-beam trap pulling the particle towards the focal point in the axial direction.

The corresponding momentum transfer will result in a scattering force proportional to the Poynting vector, therefore pointing in the direction of light propagation (see figure 2.3), which can be written as in [99]:

$$\vec{F}_{\mathrm{scat}}(\vec{r}) = \hat{x}\frac{128\pi^5 n_{md}\mathrm{R}^6}{3\lambda_0^4 c}\left(\frac{\mathrm{p}^2-1}{\mathrm{p}^2+2}\right)^2 n_{md}^5 I(\vec{r}), \tag{2.3}$$

with $\vec{r} = (x, y, z)$. R is the radius of the particle, λ_0 is the wavelength in vacuum, and $I(\vec{r})$ is the intensity distribution of a tightly focused trapping laser, in the form of a Gaussian beam:

$$I(x, y, z) = \frac{2P}{\pi w^2(x)}\left(\frac{w_0}{w(x)}\right)^2 e^{-2\frac{\left(y^2+z^2\right)}{w^2(x)}}, \tag{2.4}$$

where P is the power of the laser beam, w_0 the beam's waist size, and $w(x)$ the spot size at x (see Appendix C for definitions).

The gradient force is instead due to the Lorentz force acting on the dipole induced by the electromagnetic field. In contrast to the scattering force of equation (2.3), the gradient force is proportional to the gradient of the laser intensity:

$$\vec{F}_{\mathrm{grad}}(\vec{r}) = \frac{2\pi n_{md}\mathrm{R}^3}{c}\left(\frac{\mathrm{p}^2-1}{\mathrm{p}^2+2}\right)\nabla I(\vec{r}). \tag{2.5}$$

Inserting equation (2.4) into (2.5) we realize that each space component of the gradient force is negative, for $\mathrm{p} > 1$, which is indicative of the restoring nature of this force. That is, it acts to return the particle to the a region of high intensity. It is also interesting to note that, due to the different dependence on R of (2.3) and (2.5), the trapping stability will also depend on the size of the particle. Nanometer sized particles that are trapped in optical tweezers are typically confined by forces of some tens of piconewtons, using trapping powers of tens of milliwatts.

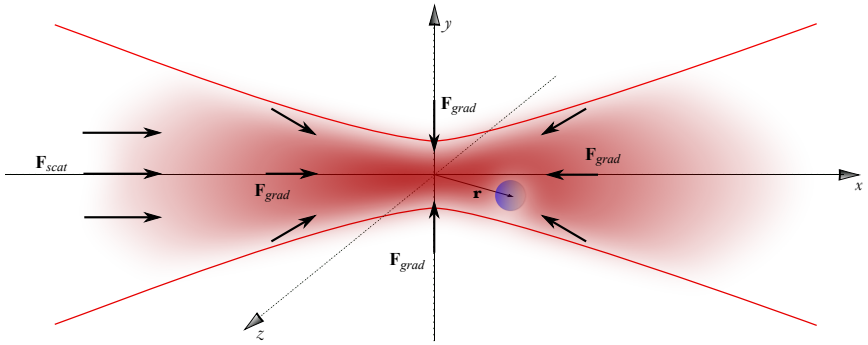

Figure 2.3: Schematic of a particle of size R $\ll \lambda$, trapped near the focal point of a laser beam. The particle can be approximated as a point dipole reacting to an electric field gradient. The scattering force acts to push the sphere along the beam axis, out of the trapping region, while the gradient force forms a stable 3D trap around the beam waist.

One clever way of reducing the destabilizing effect of the scattering force, especially if working with large particles, is to use two counter propagating beams, overlapped and focused down to the same waist point. In this way the scattering forces from the two beams cancel out and the gradient force forms a stable three-dimensional trap. In 2010 Li *et al.* employed such a setup to measure the instantaneous velocity of the Brownian motion of a 4.7μm diameter silica sphere [113].

A natural extension to using counter-propagating beams is to levitate particles inside an optical cavity, as light travels in both directions bouncing off the mirrors, so that the time average of the scattering force is zero. In this case though, the intracavity light field is represented by a standing wave with a Gaussian transverse profile (Appendix C), and the gradient force will keep particles trapped at the stationary antinodes (figure 2.4). Cavity traps have very strong axial confinement but poor radial confinement, due to the relatively large cavity waists, as it will be shown in section 4.2.

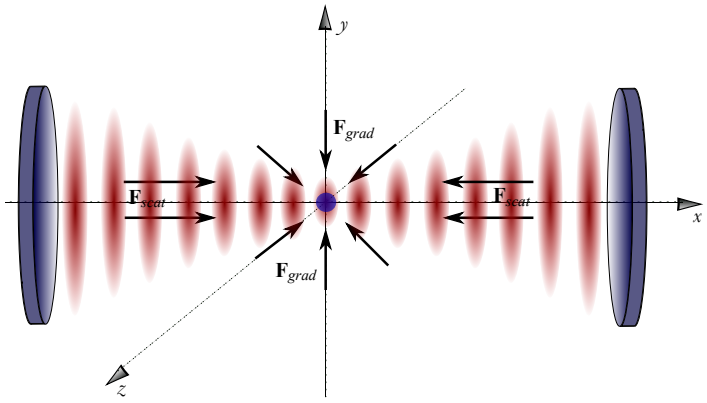

Figure 2.4: Forces acting on the particle in the light field of an optical cavity. Scattering forces cancel out and gradient forces form a stable 3D trap for the sphere.

2.3 Interaction with a cavity

The cooling process that takes place in the case of a nanoscale particle trapped at the center of a high finesse optical cavity can still be explained by considering the cavity resonance frequency shift as a function of displacement. The particle will scatter a fraction of the trapping light into the cavity mode, inducing a change in the effective path length of the intracavity field, due to the phase change in the scattered light. This results in a shift in the cavity resonance which is sensitive to the particle's volume and position.

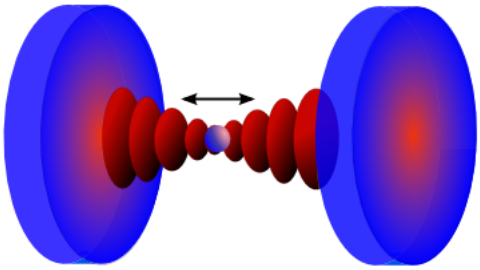

Figure 2.5: Schematic of an optical cavity with fixed mirrors and a particle levitating within the intracavity field.

When a particle moves into a high intensity region (antinode), as it oscillates, there will be a slight increase in the optical path length of the cavity. This corresponds to an increase in the position-dependent frequency shift $U(x)$ [27]:

$$U(x) = \frac{\alpha\omega_l \cos^2 kx}{\epsilon_0 V_c}, \tag{2.6}$$

where $\alpha = 4\pi\epsilon_0 \frac{n^2-1}{n^2+2}\mathrm{R}^3$ is the polarizability of the particle, n is the refractive index, and V_c is the volume of the cavity mode (as obtained in section 4.2). For an input field that is red-detuned from the cavity resonance, this effect brings the input field closer into resonance, acting to increase the intracavity intensity and thus also the dipole force on the particle. The finite time required for the intracavity intensity to increase results in an additional frictional force that slows down the motion of the sphere as it passes through the antinode. In summary, the mechanism of dynamical backaction is analogous to the standard movable mirror setup, but unlike the latter, which utilizes radiation pressure, the levitated nanoparticle scheme uses the dipole force. In the same way as discussed before, we can use the sideband approach to describe the cooling mechanism. The axial motion of the particle means that light scattered into the cavity mode undergoes a Doppler shift, with scattered photons being blue or red shifted. This scattered spectrum is convolved with the cavity

spectrum, as it limits the available optical states. The result is that the presence of the cavity will enhance or suppress scattering of the shifted frequency components. If the laser is red-detuned from the cavity mode, the scattering of blue-shifted photons is enhanced, resulting in removal of energy from the particle, and in the damping of its motion.

We finally note that such a scheme is essentially analogous to atomic laser cooling by coherent scattering inside optical resonators [101, 102, 103]. Here the advantage, with respect to other laser cooling techniques, is that a cooling force is generated that is determined exclusively by the atom's motion and does not depend on its internal structure. As such a mechanism does not require atomic excitation, it follows that the lowest attainable temperatures are not limited by the atomic linewidth as for free-space Doppler cooling [104], but by the linewidth of the cavity, which can be much smaller. Furthermore, this technique is applicable to atomic species where lasers matching the transition frequencies are not readily available, or to complex molecules and more massive particles. Although larger nanoscale particles usually do not have discrete internal energy levels, they do have large static polarizabilities, which scale with particle volume. It is precisely this feature that allows a single nanoscale particle to be cooled in high-finesse cavities using fields that are not near resonance.

2.4 Limits

The levitated system that has been described suffers from a few important issues that can limit the cooling performance. We need to point them out in order to better understand the different implementations that have been proposed and realized, including the hybrid electro-optical trap, presented in this thesis.

As already explained, nanospheres levitating in an optical cavity driven by a red detuned laser will be cooled by light towards the bottom of a local standing wave potential well (center of an antinode). In this region though, cooling is ineffective since the nanosphere's motion doesn't significantly modulate the cavity length. As a matter of fact, it has been clearly shown [27] that best damping occurs when the particle is located in the largest gradient of the field, where the intensity varies as a function of the particle position. One way to achieve this is to use one additional field to trap and position the particle in this location of the cavity field for maximum cooling. This can be done optically either by using an optical tweezers [71], or a second cavity mode [28, 69]. In the latter case, the use of two near-resonant cavity fields that both act to trap and cool the particle offers much higher cooling rates over a wider range of cavity field detunings when compared with the use of a single cooling and single trapping field [69]. Some experimental results in this sense have been achieved recently by operating the optical cavity with two longitudinal Gaussian modes with different frequency

and intensity, allowing the particle to oscillate within a region where the intensity of one of the two beams varies with the particle position [105]. The cooling performance in this last case (an effective temperature of $\simeq$ 64K, starting from room temperature) was limited by the modest vacuum (4mbar) the particle was trapped in, resulting in a low mechanical quality factor.

2.4.1 Particles loss

The last consideration brings us to a second problem that levitated systems exhibit, related to the surrounding gas pressure. Since the earliest experiments [92], it has been observed that optically levitated particles tend to escape from the trap when pressures lower than a few millibar are reached. This known, yet not fully explained phenomenon was initially attributed to the radiometric forces which, although negligible at atmospheric pressure, grow in magnitude as the pressure is reduced, where they compare to, or can exceed, radiation pressure. The temperature gradients responsible for the destabilizing radiometric forces arise from residual and uneven optical absorption in the particle (photophoresis) [106, 107]. For highly absorbing particles the front face of the particle is heated much more than the rear face; the integrated effect of gas molecules rebounding asymmetrically from the surface of the particle gives rise to a force on the particle center of mass, pointing towards the direction of light propagation. For weakly absorbing particles, the light refracted through the particle is focused on the back surface, giving a backward directed force. In both cases, when gas pressures is decreased down to a point where the mean free path of an air molecule is comparable to the particle size, trapping becomes too unstable and particles escape from the beam. This was partially overcome in [94], where, using lower absorption particles, they could observe levitation in high vacuum (10^{-6} mbar), where radiometric forces are completely negligible.

In more recent works [108], it has been proved that other causes, related to heating and not, are responsible for particle loss. Here, a counter-propagating dual-beam optical trap was employed, which suggests a more evenly heated surface for the trapped particles, that would exclude the effect described before (although the lens-like character of the sphere along the beam axis was still considered). Nevertheless, impinging gas particles do not necessarily equilibrate to the same temperature as the sphere surface (depending on the value of the pressure) but can emerge with a different temperature, effectively generating two non-interacting baths that bring a modified Brownian motion for the particle, and a non equilibrium centre-of-mass motion. From the latter parameter, the surface temperature of the particle can be evaluated. It has been observed that at high enough intensities of the trapping beams, the surface temperature of silica micro-sized particles can reach

values of $\approx$ 2000 K even via a small light absorption; this is if the heat transfer to the surrounding gas is poor, which happens more at lower and lower pressures. For this reason, also depending on their size, spheres can undergo phase changes eventually evaporating and vanishing from the trap. For certain (smaller) particle sizes, the minimum attainable pressure for stable trapping becomes independent on the beam intensity, suggesting that there are also temperature-independent loss mechanisms, such as parametric heating that results from any source of noise in the system around the mechanical frequency, and, even at low laser intensities, contributes to render the trap unstable.

In other experimental works [109], it has been found that optical traps are also sensitive to air currents and vacuum pump vibrations while evacuating the chamber. In these cases, the pumping rate to pressures down to a few millibars can be controlled by slowly pumping the air molecules away using mechanical valves, which at the same time isolate vibrations from mechanical rotatory pumps.

One possibility that has been demonstrated to overcome the problem of particle escape is the use of additional damping, applying an active optical feedback to modulate the intensity of the trapping beam to counteract the nanoparticle's oscillation. This method is especially good for correcting parametric heating, and it is also a different way of cooling, not based on the passive, self-sustained mechanism given by the optical cavity, but obtained by applying an external force proportional to the velocity of the particle (but with opposite sign). Li *et al.* [112] used three orthogonal sets of counter-propagating beams, one set for each component of motion, to cool the motion of 3.0 μm SiO_2 spheres to a final center-of-mass temperature of 1.5 mK. The cooling beams were weakly focused and relied on the scattering force to slow the motion. The electronic feedback system modulated the intensity of each cooling beam so that a beam was strong when the particle was moving upstream, but weak when it was moving in the propagation direction. This ensured that the cooling beams would only reduce the particle velocity, without speeding it back up. This technique successfully reduced the centre-of-mass temperature of the micro-scale particle by five orders of magnitude, however it required a total of eight beams. One year later, Gieseler *et al.* [110] demonstrated a similar active cooling technique which used the trap laser itself to cool a particle's motion in all three dimensions. Here a feedback signal is generated and fed into a single electro-optic modulator which modulates the intensity of the trapping beam, in such a way that the trap stiffness is increased whenever the particle moves away from the trap centre, and it is reduced when the particle falls back towards the trap. Effective temperatures as low as 50 mK were reported, using 70 nm SiO_2 nanoparticles. In a more recent work [111], with same technique a phonon occupancy of $n_{th} \simeq 63$ was measured, corresponding to microkelvin temperatures. Active feedback though, requires parametric modulation of the trap power, based on the

real-time behavior of the particle. Even if quantum ground state cooling seems achievable for both cavity cooling and feedback cooling [114], the latter would be limited by electronic noise coming from detection system and feedback circuits. In a Fabry-Perot cavity instead, a particle can be passively self-cooled through dynamical backaction simply by introducing a second detuned laser.

We finally report that in 2013 cavity cooling was achieved for silicon nanoparticles in a high-vacuum environment (10^{-8} mbar), but without providing any trapping [119]. Particles were created and launched by directing a pulsed focused laser on a pristine silicon wafer, and they then traveled through the optical cavity interacting with its light field for $\sim 200\,\mu$s. A reduction in the transverse kinetic energy by a factor of 30 was measured for each particle.

In order to circumvent loss and instability problems due to the trapping lasers, we make use of a Paul trap to levitate the nanoparticles, exploiting their residual surface charge. In this way, we can keep a nanoparticle stably trapped while reducing ambient pressure down to ultra-high vacuum, as the optomechanical interaction between the nanosphere and the optical cavity field takes place. We will describe in chapters 4 and 5 the details of such a setup, which presents itself as a new method for cavity cooling charged nanoparticles, in a combined (hybrid) trap. Before that, in the next chapter we want to describe the basic principles of harmonic oscillators and optical cavities, to better understand the origins, and the consequences, of the standard optomechanical interaction. We will then introduce the key features of Paul traps, to finally put all the elements composing the hybrid trap system together.

Chapter 3

Optomechanical coupling

In this chapter I describe in more detail the dynamical behavior of a mechanical oscillator coupled to an optical cavity. A quantum mechanical description of the mechanical oscillator, and the optical cavity field is provided. These two elements will be combined to study the origins of the optomechanical coupling, and to obtain the equations of motion for the combined system, which explain effects such as the optomechanical damping.

As in the following discussion the results obtained are quite general, the levitated hybrid system treated in later chapters will present itself as a special case, to which the optomechanical theory can be restricted.

3.1 Mechanical Harmonic Oscillator

One of the main components in an optomechanical system is the mechanical resonator. It has a mass M and resonance frequency ω_{M}, and couples to the light inside the cavity via the radiation pressure force. It can be described as a damped harmonic oscillator subject to external (optical) forces, as well as an external thermal bath. In this section, I briefly review the features of the quantum harmonic oscillator, and introduce some of the nomenclature that will be used throughout this thesis.

A lot of physical systems in nature, from microscopic objects such as molecules up to the biggest found in our universe including neutron stars, can be described as harmonic oscillators, since their motion is characterized by repetitive oscillations around an equilibrium position. Oscillations have constant amplitude and frequency as long as the system stays decoupled from its environment and only the restoring force proportional to its displacement acts. On the contrary, if a frictional force proportional to velocity is also present, the harmonic oscillator is described as a damped oscillator, whose amplitude decays in time until the system reaches the equilibrium position and momentum.

3.1.1 Energy Levels

The harmonic oscillator is one of the simplest examples of a quantum mechanical system that is analytically solvable. At the same time, it shows some of the peculiar quantum features that make it so distinct from a classical oscillator. The usual starting point is the classical Hamiltonian function $\hat{H}_{\mathrm{M}}$, which describes the total energy of the system. For the one-dimensional problem of an oscillator with mass M moving in an harmonic potential we can write [39]:

$$\hat{H}_{\mathrm{M}} = \frac{\hat{p}^2}{2\mathrm{M}} + \frac{1}{2}k\hat{x}^2, \tag{3.1}$$

where $\hat{x}$ and $\hat{p}$ represent respectively position and momentum of the oscillator, and they satisfy the commutation relation $[\hat{x}, \hat{p}] = i\hbar$. The spring constant k is related to the mechanical frequency and mass by:

$$\omega_{\mathrm{M}} = \sqrt{\frac{k}{\mathrm{M}}},$$

while the amplitude depends on the initial conditions. One can introduce the creation, $\hat{b}^\dagger$, and annihilation $\hat{b}$, operators as linear combinations of $\hat{x}$ and $\hat{p}$:

$$\hat{b} = \sqrt{\frac{\mathrm{M}\omega_{\mathrm{M}}}{2\hbar}}\left(\hat{x} + i\frac{\hat{p}}{\mathrm{M}\omega_{\mathrm{M}}}\right), \qquad \hat{b}^\dagger = \sqrt{\frac{\mathrm{M}\omega_{\mathrm{M}}}{2\hbar}}\left(\hat{x} - i\frac{\hat{p}}{\mathrm{M}\omega_{\mathrm{M}}}\right) \tag{3.2}$$

These operators fulfill the commutation relation $\left[\hat{b}, \hat{b}^\dagger\right] = 1$ and $[b, b] = \left[b^\dagger, b^\dagger\right] = 0$, and allow us to write the Hamiltonian in its canonical form:

$$\hat{H}_{\mathrm{M}} = \hbar\omega_{\mathrm{M}}\left(\hat{b}^\dagger\hat{b} + \frac{1}{2}\right). \tag{3.3}$$

The corresponding Schrödinger equation reads:

$$b^\dagger b\psi = \left(\frac{E}{\hbar\omega_{\mathrm{M}}} - \frac{1}{2}\right)\psi. \tag{3.4}$$

This is an eigenvalue equation for the operator $b^\dagger b$, called the number operator. The eigenfunctions of the eigenvalue equations are solutions of the Schrodinger equation. The lower eigenfunction ψ_0 is the ground state of the harmonic oscillator:

$$\psi_0(x) = \left(\frac{\mathrm{M}\omega_{\mathrm{M}}}{\pi\hbar}\right)^{1/4} e^{\left(-\frac{\mathrm{M}\omega_{\mathrm{M}}}{2\hbar}x^2\right)}, \tag{3.5}$$

and the eigenfunction for the n^{th} energy eigenstate is:

$$\psi_n(x) = \sqrt{\frac{1}{2^n n!}}\left(b^\dagger\right)^n \psi_0(x). \tag{3.6}$$

The energy spectrum for the harmonic oscillator can be found by simply writing down the eigenvalue equation for the Hamiltonian operator, $\hat{H}\,|n\rangle = E_n\,|n\rangle$, whose eigenstates are called Fock states. It is a discrete spectrum with equidistant energy levels:

$$E_n = \hbar\omega_{\mathrm{M}}\left(n + \frac{1}{2}\right)$$

each one separated from the other by a constant factor $\hbar\omega_{\mathrm{M}}$ (figure 3.1).

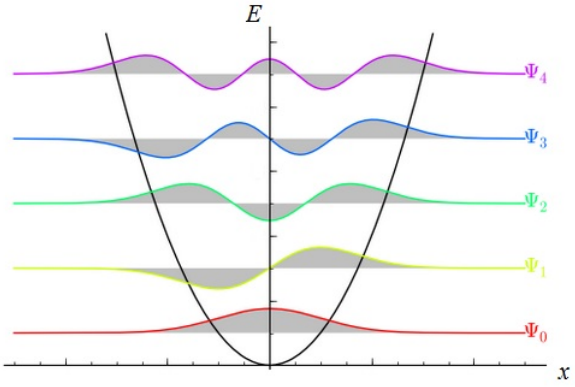

Figure 3.1: The first energy levels of an harmonic oscillator, all separated by a distance $\hbar\omega_{\mathrm{M}}$, and the respective wavefunction representations.

Thus, while in the classical framework the lowest state is normally characterized by the system localized at the equilibrium position with null energy, quantum description shows that at its fundamental state, without any force applied, the system has a non zero energy $E_0 = \hbar\omega_{\mathrm{M}}/2$. This fact can also be interpreted as a consequence of Heisenberg Uncertainty Principle, which prevents the oscillator to settle on the classical state with $x = 0$ and $p = 0$. The probability density of the position, described by the wave function corresponding to the ground state, is a Gaussian where the expectation value of $\hat{x}$ is $\langle\hat{x}\rangle = 0$ and mean square deviation is:

$$\langle\hat{x}^2\rangle = \frac{\hbar}{2\mathrm{M}\omega_{\mathrm{M}}}$$

These are the zero-point fluctuations whose extension, $x_{\mathrm{ZPF}} = \sqrt{\langle\hat{x}^2\rangle - \langle\hat{x}\rangle^2}$, is expressed in equation (1.1).

3.1.2 Coupling to the environment

In the treatment of any real harmonic oscillator, one should always include the effect of dissipation and the action of external forces. The most relevant dissipation mechanisms include: clamping losses [40] (which are due to the absorption of elastic energy by the substrate through the supports of the oscillator), fundamental anharmonic effects such as thermoelastic damping [41] and phonon-phonon interactions [42], material-induced losses

(due to intrinsic or extrinsic defects in the bulk or the surface of the oscillator), and viscous damping (given by the collision with residual gas particles surrounding the resonator). For the levitated systems that we are interested in, this last effect is the one we mostly need to take into account. In this case, the Hamiltonian of the global system must be written as the sum of three terms:

$$\hat{H}_{\rm tot} = \hat{H}_{\rm M} + \hat{H}_{\rm env} + \hat{H}_{\rm int} = \hbar\omega_{\rm M}\left(\hat{b}^\dagger\hat{b} + \frac{1}{2}\right) + \sum_i \hbar\omega_i(\hat{c}_i^\dagger\hat{c}_i + \frac{1}{2}) + \sum_i \hbar k_i\hat{c}_i^\dagger\hat{b} + h.c. \quad (3.7)$$

where $\hat{H}_{\rm env}$ describes the environment as an infinite ensemble of harmonic oscillators, representing the degrees of freedom of the reservoir. The third term $\hat{H}_{\rm int}$ denotes the coupling between environment and oscillator, and it contributes to modify the system so that its eigenstates cannot be written simply as those of the free oscillator. In this case, usually a statistical treatment is used, since it is experimentally impossible to study all the possible interactions, and so, to know the full evolution of the system. The latter is then considered to be in a state of thermodynamical equilibrium described by the density operator:

$$\rho = \frac{1}{Z}e^{-\frac{\hat{H}}{k_B T}}, \quad (3.8)$$

with partition function Z :

$$Z = \frac{e^{-\hbar\omega_{\rm M}/2k_B T}}{1 - e^{-\hbar\omega_{\rm M}/k_B T}}. \quad (3.9)$$

Thus, the mean energy of the oscillator is found to be:

$$\left\langle \hat{H}_{\rm M} \right\rangle = {\rm Tr}(\hat{H}_{\rm M}\rho) = \hbar\omega_{\rm M}(n_{th} + \frac{1}{2}), \quad (3.10)$$

where:

$$n_{th} = \frac{1}{e^{\hbar\omega_{\rm M}/k_B T} - 1}, \quad (3.11)$$

is the mean number of thermal phonons of the oscillator, as already mentioned in the first chapter. For $k_B T \gg \hbar\omega_{\rm M}$ it's easy to see that the energy reduces to the classical form: $\langle H\rangle_{\rm class} = k_B T$, that is the result of the energy equipartition theorem [43], according to which at thermal equilibrium each quadratic degree of freedom (p^2 and x^2) in the Hamiltonian contributes with a factor $\frac{1}{2}k_B T$.

3.1.3 Dynamics of the oscillator

In order to study the dynamics of an harmonic oscillator we need to follow its position in time, and this means to solve a differential equation of the type:

$$\ddot{x}(t) + \Gamma_{\mathrm{M}}\dot{x}(t) + \omega_{\mathrm{M}}^2 x(t) = \frac{F_T(t)}{\mathrm{M}}, \tag{3.12}$$

where the interaction with the environment is expressed by means of the damping rate Γ_{M}, which determines how fast the oscillation decays, and by an external driving force $F_T(t)$. For an oscillator subjected to Brownian noise, i.e. coupled to a thermal bath of temperature T, $F_T(t)$ represents the Langevin force [51], describing the unceasing impacts of the bath's particles on the oscillator. The general form of $x(t)$ in Fourier space is:

$$x(\omega) = \frac{F_T(\omega)}{\mathrm{M}} \cdot \frac{1}{\omega_{\mathrm{M}}^2 - \omega^2 - i\omega\Gamma_{\mathrm{M}}} = F_T(\omega) \cdot \chi(\omega),$$

where the last term $\chi(\omega)$ is the mechanical susceptibility, which is simply the response of the system to the applied force $F_T(\omega)$.

The spectral density function S_{xx}^T, which describes how the power associated to the signal $x(t)$ is distributed over the different frequencies, is the Fourier transform of the signal autocorrelation function (Wiener-Khinchin theorem):

$$S_{xx}^T(\omega) = \langle x(\omega)x(\omega')\rangle = |\chi(\omega)|^2 \, S_T(\omega), \tag{3.13}$$

where $S_T(\omega)$ is the spectrum of the Langevin force, and it takes the form [43]:

$$S_T(\omega) = \hbar \left| \mathrm{Im}\frac{1}{\chi(\omega)} \right| \coth\frac{\hbar|\omega|}{2k_B T} = \hbar \mathrm{M}\Gamma_{\mathrm{M}} |\omega| \coth\frac{\hbar|\omega|}{2k_B T}. \tag{3.14}$$

This last expression relates the dissipation of the system, described by the imaginary part of the mechanical susceptibility, to the spectrum of the Langevin force which accounts for the system's fluctuations.

For sufficiently high mechanical quality factor $Q = \omega_{\mathrm{M}}/\Gamma_{\mathrm{M}}$ the position spectrum $S_{xx}^T(\omega)$ is more and more peaked around the mechanical frequency ω_{M}, and we can approximate the spectrum of the Langevin force with its value taken at $\omega = \omega_{\mathrm{M}}$. One then obtains:

$$S_{xx}^T(\omega) = \frac{2\Gamma_{\mathrm{M}}}{\mathrm{M}\left[(\omega_{\mathrm{M}}^2 - \omega^2)^2 + \Gamma_{\mathrm{M}}^2\omega^2\right]} \hbar\omega_{\mathrm{M}}(n_{th} + \frac{1}{2}), \tag{3.15}$$

where n_{th} is the mean number of thermal phonons as expressed in equation (3.11).

$S_{xx}^T(\omega)$ is an experimentally measurable quantity, since one can measure the position of the

system over time and send this signal to a spectrum analyzer, which performs the Fourier transform of the autocorrelation function $\langle x(t)x(t+\tau)\rangle$. One can also see that the mean square deviation is related to the position spectrum by:

$$\langle x^2 \rangle = \frac{1}{2\pi} \int_{-\infty}^{+\infty} d\omega S_{xx}^T(\omega), \tag{3.16}$$

which corresponds to the area of the measured power spectrum.

For high temperatures ($k_B T \gg \hbar\Omega_{\mathrm{M}}$) equation (3.15) is simplified to:

$$S_{xx}^T(\omega) = \frac{2\Gamma_{\mathrm{M}}}{\mathrm{M}\left[(\omega_{\mathrm{M}}^2 - \omega^2)^2 + \Gamma_{\mathrm{M}}^2\omega^2\right]} k_B T. \tag{3.17}$$

This function has a Lorentzian shape with FWHM equal to Γ_{M}, and it is very peaked around the mechanical frequency ω_{M} (figure 3.2).

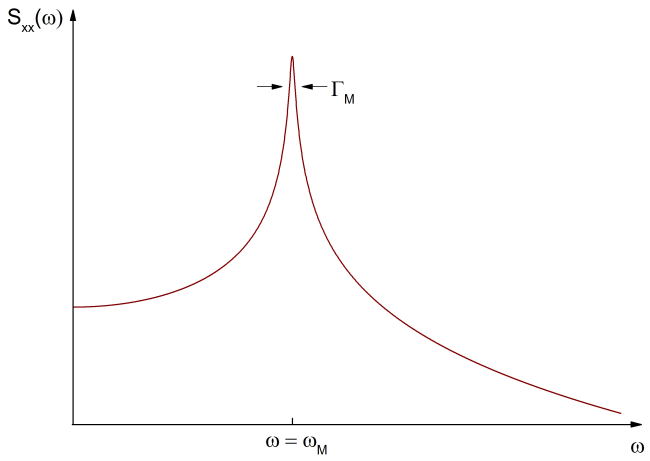

Figure 3.2: Typical noise spectrum curve for a harmonic oscillator (plotted on a logarithmic scale) with resonance frequency ω_{M} and damping rate Γ_{M}.

The height of the peak varies linearly with temperature,

$$S_{xx}^T(\omega_{\mathrm{M}}) = \frac{2k_B T}{\mathrm{M}\omega_{\mathrm{M}}^2 \Gamma_{\mathrm{M}}}, \tag{3.18}$$

and the area under the curve can be found by inserting equation (3.17) in (3.16):

$$\langle x^2 \rangle = \frac{k_B T}{\mathrm{M}\omega_{\mathrm{M}}^2}. \tag{3.19}$$

Thus, one can measure the area under the curve to find the value of the temperature T, and thus evaluate the number of thermal phonons for the oscillator. As soon as the temperature approaches a level such that $k_B T \simeq \hbar\omega_{\mathrm{M}}$, the noise spectrum reaches a limit corresponding

to the zero point fluctuations:

$$S_{xx}^{SQL}(\omega_{\mathrm{M}}) = \frac{\hbar}{\mathrm{M}\omega_{\mathrm{M}}\Gamma_{\mathrm{M}}} = \frac{\hbar \mathrm{Q}}{\mathrm{M}\omega_{\mathrm{M}}^2},$$

where Q is the quality factor of the resonator, which has to be as high as possible in order to see the quantum fluctuations of an oscillator.

3.2 Optical cavity

In quantum optics, the electromagnetic field can be decomposed into a sum of independent harmonic oscillators, describing independent optical modes [44, 45]. For an optical cavity, if we consider a single cavity mode, the Hamiltonian of the light field can be written as:

$$\hat{H}_C = \hbar\omega_c \left(\hat{a}^\dagger \hat{a} + \frac{1}{2}\right). \tag{3.20}$$

As for a single harmonic oscillator, the cavity mode is characterized by a frequency of oscillation ω_c, and by the two operators $\hat{a}^\dagger$ (creation) and $\hat{a}$ (annihilation), which satisfy the same commutation relations, appropriate for bosons, expressed for the harmonic oscillator in previous section. The operator $\hat{a}$ reduces the number of photons in the cavity mode by one, while the operator $\hat{a}^\dagger$ increases the number of photons by one. We can then define an operator $\hat{N} = \hat{a}^\dagger \hat{a}$, as the number operator representing the total number of photons in the cavity mode. The eigenstates of the Hamiltonian in equation (3.20) are the number or Fock states $|n\rangle$, which satisfy

$$\begin{aligned}
\hat{N}\,|n\rangle &= n\,|n\rangle \\
\hat{a}\,|n\rangle &= \sqrt{n}\,|n-1\rangle \\
\hat{a}\,|n\rangle &= 0 \\
\hat{a}^\dagger\,|n\rangle &= \sqrt{n+1}\,|n+1\rangle\,.
\end{aligned}$$

The vacuum state $|0\rangle$ is the ground state of radiation, and its energy takes the familiar form $E = \hbar\omega_c/2$.

In analogy with the mechanical harmonic oscillator, one needs to take into account the coupling with the environment. In particular in this case, a quantum mechanical description of a cavity which is coupled to the outside electromagnetic environment should be used. This can be provided by a framework known as input-output theory [14], which allows access to the light field being emitted (or reflected from) the cavity, and it allows us to model the quantum fluctuations injected from any coupling port (such as the input mirror) into the

cavity. In addition, it takes into account any coherent laser drive that may be present. As we won't go into details about this theory, the reader can refer to [44, 46]. Here we only state that input-output theory is formulated on the level of Heisenberg equations of motion, describing the time evolution of the field amplitude inside the cavity. The latter will be reported in next section, where we write the complete Hamiltonian for an optomechanical system and discuss the combined optomechanical equations of motion.

3.3 Optomechanical coupling

In the quantum framework, the radiation pressure interaction can be analyzed starting from the Hamiltonian of the optomechanical system [14, 114, 115] :

$$\begin{aligned} \hat{H} &= \hat{H}_c + \hat{H}_{\mathrm{M}} + \hat{H}_{int} + \hat{H}_L \\ &= \hbar\omega_c \hat{a}^\dagger \hat{a} + \hbar\omega_{\mathrm{M}} \hat{b}^\dagger \hat{b} - \hbar g_0 \hat{a}^\dagger \hat{a}(\hat{b} + \hat{b}^\dagger) + i\hbar\varepsilon(\hat{a}^\dagger e^{-i\omega_l t} + \hat{a} e^{i\omega_l t}), \end{aligned} \tag{3.21}$$

where $\hat{H}_c$ ($\hat{H}_{\mathrm{M}}$) is the free Hamiltonian of the cavity (mechanical oscillator) mode, $\hat{H}_{int}$ is the radiation pressure interaction term, and $\hat{H}_L$ describes the input driving by a laser with frequency ω_l, where ε is related to the input laser power P_{in} by $|\varepsilon| = \sqrt{P_{\mathrm{in}}\kappa/\hbar\omega_l}$. In this description we have assumed that we detect a single mechanical mode only and that couplings between the different vibrational modes can be neglected. We also consider a single cavity mode, supposing that the mechanical frequency is much smaller than the cavity free spectral range ($\omega_{\mathrm{M}} \ll c/2L$), so that scattering of photons from the driven mode into other cavity modes is negligible [116].

The two terms $\hat{H}_c = \hbar\omega_c \hat{a}^\dagger \hat{a}$ and $\hat{H}_{int} = -\hbar g_0 \hat{a}^\dagger \hat{a}(\hat{b} + \hat{b}^\dagger)$ in equation (3.21) come from the same Hamiltonian operator $\hat{H}_c(x) = \hbar\omega_c(x)\hat{a}^\dagger \hat{a}$ describing the cavity, which includes a general dependence of the optical resonance frequency on the displacement x of the oscillator. For small values of x though, we can expand $\omega_c(x)$:

$$\omega_c(x) = \omega_c + x\frac{\partial\omega(x)}{\partial x} + ...$$

Furthermore, from the resonance condition in the case of a simple optical cavity of length L, as expressed in equation (8.24) of Appendix C, we obtain:

$$\omega_c(x) = \omega_c\left(1 - \frac{x}{L} + ...\right). \tag{3.22}$$

The zero-order term ω_c in the expansion is the optical resonance frequency for $x = 0$, which brings to the first term $\hat{H}_c$ of equation (3.21). By definition the position operator

is $\hat{x} = \sqrt{\hbar/2\mathrm{M}\omega_\mathrm{M}}(\hat{b} + \hat{b}^\dagger)$, so from the first-order term of the expansion one derives the interaction Hamiltonian $\hat{H}_{int} = -\hbar g_0 \hat{a}^\dagger \hat{a}(\hat{b} + \hat{b}^\dagger)$, with:

$$g_0 = \frac{\omega_c}{L} \cdot \sqrt{\frac{\hbar}{2\mathrm{M}\omega_\mathrm{M}}}, \tag{3.23}$$

defined as the vacuum optomechanical coupling rate ($^{\mathrm{rad}}/_{\mathrm{sec}}$), and representing the frequency shift of the cavity due to a mechanical displacement x_{ZPF} .

Since the cavity frequencies ω_c are much larger then the mechanical frequency and decay rates of the system, it is normally convenient to move to a frame rotating at the laser frequency ω_l, thereby removing the fast oscillations and making the driving terms time independent. Applying the unitary transformation $\hat{U} = \exp\left(i\omega_l \hat{a}^\dagger \hat{a} t\right)$ we generate a new Hamiltonian $\hat{H} = \hat{U}\hat{H}_{old}\hat{U}^\dagger + i\hbar\partial\hat{U}/\partial t$ (where $\hat{H}_{old}$ would be Hamiltonian expressed in equation (3.21)) of the form:

$$\hat{H} = -\hbar\Delta_0 \hat{a}^\dagger \hat{a} + \hbar\omega_\mathrm{M} \hat{b}^\dagger \hat{b} - \hbar g_0 \hat{a}^\dagger \hat{a}(\hat{b} + \hat{b}^\dagger) + \hbar\varepsilon(\hat{a}^\dagger + \hat{a}), \tag{3.24}$$

where we have introduced the cavity detuning $\Delta_0 = \omega_l - \omega_c$. The system we are considering is intrinsically open as both the mechanical and optical mode are affected by fluctuation-dissipation processes. In order to account for the complete dynamics of the subsystems involved in this problem an adequate choice is to use the formalism of the Quantum Langevin Equations (QLEs) [117], which for an operator $\hat{O}$ is given by $\partial\hat{O}/\partial t = (i/\hbar)\left[\hat{H}, \hat{O}\right] + \hat{N}$, where $\hat{N}$ is the corresponding noise operator of $\hat{O}$.

If we consider the mechanical harmonic oscillator alone, from the Hamiltonian in equation (3.7) one obtains the complete QLEs [118]:

$$\begin{aligned}
\dot{\hat{x}} &= \omega_\mathrm{M}\hat{p} \\
\dot{\hat{p}} &= -\omega_\mathrm{M}\hat{x} - \Gamma_\mathrm{M}\hat{p} + \hat{\xi} \\
\left\langle \hat{\xi}(t) \right\rangle &= 0 \\
\left\langle \hat{\xi}(t)\hat{\xi}(t') \right\rangle &= \frac{\Gamma_\mathrm{M}}{\omega_\mathrm{M}} \int \frac{d\omega}{2\pi} e^{-i\omega(t-t')}\omega \left[\coth\left(\frac{\hbar\omega}{2k_B T}\right) + 1\right],
\end{aligned} \tag{3.25}$$

which retain the familiar form of the classical counterpart, associating a stochastic thermal force to a viscous damping force proportional to the velocity. Here, $\hat{\xi}(t)$ is a Gaussian quantum stochastic process, and its correlation function is given by the quantum fluctuation-dissipation theorem [43].

The same approach, in terms of QLEs, can be used to derive the dynamical equation of a single cavity mode. It's easier in this case to describe the cavity dynamics in terms of the

operators $\hat{a}$ and $\hat{a}^\dagger$, to obtain the time evolution of the intracavity field amplitude:

$$\dot{\hat{a}} = -\frac{\kappa}{2}\hat{a} + i\Delta_0\hat{a} - i\varepsilon + \sqrt{\kappa_{ext}}\hat{a}_{in} + \sqrt{\kappa_0}\hat{f}_{in} \tag{3.26}$$

and correlation functions

$$\begin{aligned}
\langle \hat{a}_{in}(t)\hat{a}_{in}(t')\rangle &= \left\langle \hat{a}^\dagger_{in}(t)\hat{a}^\dagger_{in}(t')\right\rangle = \left\langle \hat{a}^\dagger_{in}(t)\hat{a}_{in}(t')\right\rangle = 0 \\
\left\langle \hat{f}_{in}(t)\hat{f}_{in}(t')\right\rangle &= \left\langle \hat{f}^\dagger_{in}(t)\hat{f}^\dagger_{in}(t')\right\rangle = \left\langle \hat{f}^\dagger_{in}(t)\hat{f}_{in}(t')\right\rangle = 0 \\
\left\langle \hat{a}_{in}(t)\hat{a}^\dagger_{in}(t')\right\rangle &= \delta(t-t') \\
\left\langle \hat{f}_{in}(t)\hat{f}^\dagger_{in}(t')\right\rangle &= \delta(t-t').
\end{aligned}$$

Here $\hat{a}_{in}$ are quantum fluctuations coupled to the cavity mode through the input mirror, while $\hat{f}_{in}$ is the vacuum input noise describing optical internal losses and transmission losses. In the same way, κ_{ext} and κ_0 are the two cavity decay rate contributions related to input coupling losses and all remaining losses, respectively, so that $\kappa = \kappa_{ext} + \kappa_0$. Note here that the input field is normalized in such a way that the rate of photons arriving at the cavity is $\left\langle \hat{a}^\dagger_{in}\hat{a}_{in}\right\rangle = P/\hbar\omega_l$, while for the intracavity field $\left\langle \hat{a}^\dagger\hat{a}\right\rangle = n_c$, where n_c is the number of photons in the cavity at a given time.

At this point, to obtain the equations of motion for the combined system we just need to add to the separate sets of equations (3.25) and (3.26) the coupling term $\hat{H}_{int}$, and we have the coupled equations of motion:

$$\begin{aligned}
\dot{\hat{x}} &= \omega_{\mathrm{M}}\hat{p} \\
\dot{\hat{p}} &= -\omega_{\mathrm{M}}\hat{x} - \Gamma_{\mathrm{M}}\hat{p} + G\hat{a}^\dagger\hat{a} + \hat{\xi} \\
\dot{\hat{a}} &= -\frac{\kappa}{2}\hat{a} + i\left(\Delta_0 + G\hat{x}\right)\hat{a} - i\varepsilon + \sqrt{\kappa_{ext}}\hat{a}_{in} + \sqrt{\kappa_0}\hat{f}_{in},
\end{aligned} \tag{3.27}$$

where we have defined $G \equiv \omega_c/L = g_0\sqrt{2\mathrm{M}\omega_{\mathrm{M}}/\hbar}$. A considerable simplification to this analytical approach comes if we consider a very intense intracavity field (a limit which is often desirable as it brings to a stronger optomechanical coupling). This is the case for high finesse cavities and enough driving power, so that the system can be characterized by a semi-classical steady state defined by a stable amplitude of the intracavity field $|\alpha_s| \gg 1$ and a new equilibrium position of the cantilever, displaced by x_s:

$$\hat{x} = x_s + \hat{x}, \quad \hat{p} = p_s + \hat{p} \quad , \hat{a} = \alpha_s + \delta\hat{a}, \tag{3.28}$$

which bring the steady-state solutions for equations (3.27):

$$p_s = 0, \quad x_s = \tfrac{g_0}{\omega_{\rm M}} \left|\alpha_s\right|^2, \quad \left|\alpha_s\right|^2 = \frac{\varepsilon^2}{(\kappa/2)^2 + \Delta^2},$$

with an effective cavity detuning $\Delta = \Delta_0 + g_0^2 \left|\alpha_s\right|^2 / \omega_{\rm M}$. Using the relations (3.28) one easily obtains the linearized interaction Hamiltonian [14]:

$$\hat{H}_{int}^{(lin)} = -\hbar g_0 \sqrt{\bar{n}_c} \left(\delta\hat{a} + \delta\hat{a}^\dagger\right) \left(\hat{b} + \hat{b}^\dagger\right), \tag{3.29}$$

where we assume $\bar{n}_c = \left|\alpha_s\right|^2 = \varepsilon^2 / \left(\Delta^2 + \kappa^2/4\right)$ as the steady-state cavity population, i.e. the average number of photons circulating inside the cavity; and without loss of generality we also assumed α_s is real-valued.

From here, we can get the linearized QLEs of the system:

$$\begin{aligned}
\dot{\hat{x}} &= \omega_{\rm M}\hat{p} \\
\dot{\hat{p}} &= -\omega_{\rm M}\hat{x} - \Gamma_{\rm M}\hat{p} + G\sqrt{\bar{n}_c}\left(\delta\hat{a} + \delta\hat{a}^\dagger\right) + \hat{\xi} \\
\delta\dot{\hat{a}} &= \left(i\Delta - \frac{\kappa}{2}\right)\delta\hat{a} + iG\sqrt{\bar{n}_c}\hat{x} + \sqrt{\kappa_{ext}}\hat{a}_{in} + \sqrt{\kappa_0}\hat{f}_{in}.
\end{aligned} \tag{3.30}$$

The equations of motion (3.27) are inherently nonlinear as they contain the product of the mechanical oscillator $\hat{x}$ amplitude and the cavity field $\hat{a}$, or the radiation pressure force $\propto \hat{a}^\dagger\hat{a}$ that is quadratic in photon operators, and they cannot be solved exactly in the quantum regime, neither analytically nor numerically. Instead, the linearized coupled equations of motion (3.30) can be solved analytically, which is best performed in the frequency domain, to find the mechanical response of the oscillator to an external force, which is now not only given by its coupling to the thermal bath, but also by its coupling to the optical field of the cavity. The result is an effective mechanical susceptibility which can be written as [14]:

$$\chi_{\rm eff}(\omega) = \frac{1}{\mathrm{M}\left[\omega_{\rm M}^2 + 2\omega\delta\omega_{\rm M}(\omega) - \omega^2 - i\omega\left(\Gamma_{\rm M} + \Gamma_{\rm opt}(\omega)\right)\right]}, \tag{3.31}$$

where

$$\delta\omega_{\rm M}(\omega) = g_0^2\bar{n}_c\frac{\omega_{\rm M}}{\omega}\left[\frac{\Delta+\omega}{(\Delta+\omega)^2 + \kappa^2/4} + \frac{\Delta-\omega}{(\Delta-\omega)^2 + \kappa^2/4}\right] \tag{3.32}$$

represents a frequency-dependent mechanical frequency shift, and:

$$\Gamma_{\rm opt}(\Omega) = g_0^2\bar{n}_c\frac{\omega_{\rm M}}{\Omega}\left[\frac{\kappa}{(\Delta+\Omega)^2 + \kappa^2/4} - \frac{\kappa}{(\Delta-\Omega)^2 + \kappa^2/4}\right], \tag{3.33}$$

is a frequency-dependent optomechanical damping rate. In the limit $g_0\sqrt{\bar{n}_c} \ll \kappa$, generally referred to as "weak coupling regime" we can evaluate $\delta\omega_{\rm M}(\omega)$ and $\Gamma_{\rm opt}(\omega)$ at the original

oscillation frequency $\omega = \omega_{\mathrm{M}}$:

$$\delta\omega_{\mathrm{M}} = g_0^2\bar{n}_c\left[\frac{\Delta+\omega_{\mathrm{M}}}{\left(\Delta+\omega_{\mathrm{M}}\right)^2+\kappa^2/4}+\frac{\Delta-\omega_{\mathrm{M}}}{\left(\Delta-\omega_{\mathrm{M}}\right)^2+\kappa^2/4}\right] \tag{3.34}$$

$$\Gamma_{\mathrm{opt}} = g_0^2\bar{n}_c\left[\frac{\kappa}{\left(\Delta+\omega_{\mathrm{M}}\right)^2+\kappa^2/4}-\frac{\kappa}{\left(\Delta-\omega_{\mathrm{M}}\right)^2+\kappa^2/4}\right], \tag{3.35}$$

simply leading to a shifted and broadened mechanical resonance. Specifically, equation (3.34) describes the optical spring effect, while equation (3.35) represents the optomechanical damping, for which the full effective mechanical damping rate $\Gamma_{\mathrm{eff}} = \Gamma_{\mathrm{M}} + \Gamma_{\mathrm{opt}}$ can increase or decrease according to the sign of Γ_{opt} , which in turn depends on the sign of the detuning. Namely, for $\Delta < 0$ (red detuning), $\Gamma_{\mathrm{opt}} > 0$ and the effecting damping rate increases, leading to cooling of the mechanical oscillations, while $\Delta > 0$ (blue detuning) leads to optomechanical heating.

Finally, we want to note that from a thermodynamical point of view, the cavity mode acts as an effective additional reservoir for the oscillator, such that the effective temperature of the mechanical mode will be between the initial reservoir temperature and that of the effective optical bath. In the classical limit, we can simply define the final equilibrium temperature of the oscillator as:

$$T_{\mathrm{eq}} = T_{\mathrm{in}}\frac{\Gamma_{\mathrm{M}}}{\Gamma_{\mathrm{M}}+\Gamma_{\mathrm{opt}}}, \tag{3.36}$$

and, in analogy to the harmonic oscillator only subject to thermal Brownian driving force, we can find:

$$\left\langle x^2\right\rangle = \frac{k_B T_{\mathrm{eq}}}{\mathrm{M}\omega_{\mathrm{M}}^2}. \tag{3.37}$$

3.4 Quadratic coupling in Optomechanics

The optomechanical interaction term $\hat{H}_{int} = -\hbar g_0 \hat{a}^\dagger \hat{a}(\hat{b}+\hat{b}^\dagger)$, as it appears in equation (3.21), has been derived by expanding the cavity resonance frequency $\omega_c(x)$ for small values of the mechanical displacement x (equation (3.22)). Retaining only the linear term, we can define the optical frequency shift per displacement as $G = -\partial\omega_c/\partial x = \omega_c/L$, from which we can also write the vacuum optomechanical coupling rate of equation (3.23) as $g_0 = G x_{\mathrm{ZPF}}$. The interaction Hamiltonian $\hat{H}_{int}$ though, is cubic in the optical field operators, which means the corresponding Heisenberg equations of motion are nonlinear. However, in experiments this nonlinearity so far has only played a role in the classical regime of large amplitude oscillations, both mechanical and with regard to the light field [120, 121]. In the quantum regime, we have thus far resorted to the "linearized" description, both in the mechanical displacement x as well as the optical field amplitude operator $\hat{a}$, with an interaction Hamiltonian of the type $\hat{H}_{int}^{(lin)} = -\hbar g_0\sqrt{\bar{n}_c}(\delta\hat{a}^\dagger + \delta\hat{a})(\hat{b}+\hat{b}^\dagger)$ (equation (3.29)),

which is still quadratic in the operators, but it leads to linear equations of motion. This linearized approach is good enough to understand many facets of cavity optomechanics, like the displacement detection down to the SQL, and the theory of optomechanical ground-state cooling. The experimental advantage of the linearized interaction is that its strength $g = g_0\sqrt{\bar{n}_c}$ can be tuned at will by the incoming laser power. In this way, a small value of g_0 (fixed by the setup) may be compensated for by a stronger laser drive, until technical constraints become important.

Taking the optomechanical interaction one step further than the linear approximation opens up a new range of applications which are so far largely unexplored. Generally speaking, non-linear optomechanical interactions allow quantum non demolition (QND) measurements of energy eigenstates of the mechanical element, rather than the position detection characteristic of the linear coupling. This would bring to the possibility of monitoring quantum jumps in a macroscopic system [85]. They also offer the prospect of observing phonon quantum shot noise [122], nonlinear OMIT [123, 124], and the preparation of macroscopic nonclassical states [125]. To achieve a nonlinear interaction one can use optical means, which require strong single-photon coupling to the mechanical system [123, 124], but are a considerable experimental challenge. Besides, nonlinearities can also arise from spatial, mechanical effects, by engineering, for example, a light-matter interaction of the form $\left(\hat{a}+\hat{a}^\dagger\right)\left(G_1\hat{x}+G_2\hat{x}^2+...\right)$, where $\hat{a}$ and $\hat{a}^\dagger$ are the photon creation and annihilation operators and G_1 and G_2 are the linear and non-linear couplings between the field and the motion. In this sense, pioneering studies using membrane-in-the-middle set-ups [85, 86] investigated the shift in the cavity resonant frequency with membrane position inside the cavity, showing the ability to realize either linear or quadratic optomechanical couplings depending on the precise equilibrium position of the membrane. In case the membrane is located at an extremum of $\omega_c(x)$, so that $G = -\partial\omega_c/\partial x = 0$, we have to lowest order:

$$\omega_c(x) \approx \omega_c + \frac{x^2}{2}\frac{\partial^2\omega_c}{\partial x^2}, \tag{3.38}$$

so that the optomechanical Hamiltonian becomes:

$$\hat{H} = -\hbar\Delta_0\hat{a}^\dagger\hat{a} + \hbar\omega_{\mathrm{M}}\hat{b}^\dagger\hat{b} + \frac{1}{2}\hbar\frac{\partial^2\omega_c}{\partial x^2}x_{\mathrm{ZPF}}^2\left(\hat{b}+\hat{b}^\dagger\right)^2\sqrt{\bar{n}_c}\left(\delta\hat{a}^\dagger+\delta\hat{a}\right), \tag{3.39}$$

where we can define:

$$g_0^{(2)} \equiv \frac{\partial^2\omega_c}{\partial x^2}x_{\mathrm{ZPF}}^2. \tag{3.40}$$

The important result is that, in the sideband resolved regime, a rotating wave approximation

(RWA) [126] is possible, and the quadratic coupling reduces to:

$$\left(\hat{b}+\hat{b}^{\dagger}\right)^{2} \rightarrow \hat{b}^{\dagger}\hat{b}+1,$$

and since this commutes with the Hamiltonian (excluding dissipative terms):

$$\left[\hat{H},\hat{N}\right]=\left[\hat{H},\hat{b}^{\dagger}\hat{b}\right]=0,$$

a measurement of the eigenstate (phonon number) is possible. The key challenge is then to detect the dynamical effects of the quadratic coupling term. A proposal is to cool to the ground state, then to switch off the cooling and, by measuring the behavior for pure quadratic coupling, to observe quantum jumps in the mechanical eigenstates, from the ground state upwards. This is an outstanding challenge in the field of optomechanics.

Chapter 4

The Hybrid electro-optical trap

This chapter is devoted to the description of the hybrid trap used in our experiment. The field from an optical cavity is overlapped with the electric field generated by a Paul trap, and the nanoparticles are confined in a combination of optical and Paul trap potentials. We will first describe the dynamics of a charged particle inside a Paul trap, and within an optical standing wave of a cavity, separately. In the last two sections we combine the features of both, to understand the hybrid dynamics proper of our system.

4.1 Nanoparticles in an Paul trap

Since their discovery by Wolfgang Paul in 1950s, ion traps of different shapes and sizes have been employed by several researchers as levitators of micrometer sized spherical particles [127, 128]. The dynamics and stability properties of quadrupole ion traps have been extensively studied, given their importance for scientific research as well as applications such as ion mass spectroscopy [129, 130].

The usual starting point is to assume a binding force for the three-dimensional confinement of a charged particle to be harmonic, since this simplifies the analytical description of its motion:

$$F_u = -k_u u,\ u = x, y, z. \tag{4.1}$$

It follows from $\mathbf{F} = -\boldsymbol{\nabla}\Phi$, where $\Phi = QV$ is the potential energy, that the applied ion trap potential varies quadratically in the three coordinates x, y, z :

$$V = \phi_0(Ax^2 + By^2 + Cz^2), \tag{4.2}$$

where A, B, C are constants, and ϕ_0 can be a time-dependent function. Using an electrostatic field that acts on a particle of charge Q, we find that to satisfy Laplace's equation $\boldsymbol{\nabla}^2 V = 0$,

the coefficients must satisfy $A + B + C = 0$. Using $A = B = 1$ and $C = -2$ we obtain an hyperbolic equipotential surface with a saddle point at the origin (figure 4.1).

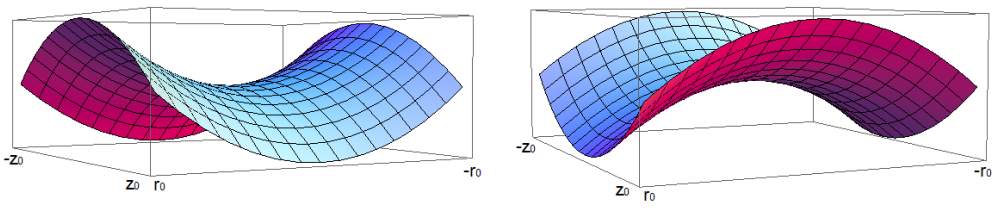

Figure 4.1: Paul's equipotential saddle-shaped surface in cylindrical coordinates, with $r^2 = x^2 + y^2$, oscillating with period $T = 2\pi/\omega_{\rm d}$. A particle is accelerated away from the trap centre in the axial or radial dimensions according to the rf phase. Inverting the field at an appropriate rate will provide stable trapping.

Given the shape of the potential, the only way to obtain three-dimensional confinement is to use a time-dependent electric field. This is the main idea behind the ideal Paul trap, which combines a DC static field with an AC component oscillating with a drive frequency $\omega_{\rm d}/2\pi$. The hyperbolic potential $V_{\rm ion}(x, y, z, \omega_{\rm d}t) = V^{\rm AC}(x, y, z, \omega_{\rm d}t) + V^{\rm DC}(x, y, z)$ can then be written in the form:

$$V_{\rm ion} = \phi_0^{\rm AC}(x^2 + y^2 - 2z^2)\sin\omega_{\rm d}t - \phi_0^{\rm DC}(x^2 + y^2 - 2z^2), \tag{4.3}$$

where we define $\phi_0^{\rm AC(DC)} = QV_0(U_0)/r_0^2$, with $V_0(U_0)$ the applied AC(DC) voltage, and r_0 a parameter that sets the length scale of the Paul trap potential. The AC component represents the rf signal used to periodically invert the field, such that the particle will always be trapped both in the radial and axial directions at the minimum of the potential (see figure 4.1). The resulting motion is separable; taking $u \equiv x, y, z$, the force $F_u = -\partial V_{\rm ion}/\partial u$ yields three equations of motion, one for each degree of freedom:

$$\begin{aligned}
{\rm M}\ddot{x} &= -\frac{QV_0}{r_0^2}2x\sin\omega_{\rm d}t + \frac{QU_0}{r_0^2}2x, \\
{\rm M}\ddot{y} &= -\frac{QV_0}{r_0^2}2y\sin\omega_{\rm d}t + \frac{QU_0}{r_0^2}2y, \\
{\rm M}\ddot{z} &= \frac{QV_0}{r_0^2}4z\sin\omega_{\rm d}t - \frac{QU_0}{r_0^2}4z.
\end{aligned} \tag{4.4}$$

These can be recast and summarized in the form:

$${\rm M}\ddot{u} = \frac{{\rm M}\omega_{\rm d}^2}{4}[a_u - 2q_u\sin\omega_{\rm d}t]u, \tag{4.5}$$

where the DC and AC stability parameters are respectively $a_{x,y} = 8QU_0/{\rm M}\omega_{\rm d}^2 r_0^2$ and $q_{x,y} = 4QV_0/{\rm M}\omega_{\rm d}^2 r_0^2$, while $a_z = -2a_x$ and $q_z = -2q_x$. The above equations are in the form of Mathieu equations, whose stability properties depend on the values of a_u and q_u. For a 3D

quadrupole trap and zero applied DC voltage ($U_0, a_u = 0$), the ion trap motion becomes unstable for $q_u \gtrsim 0.908$ (see figure 4.2).

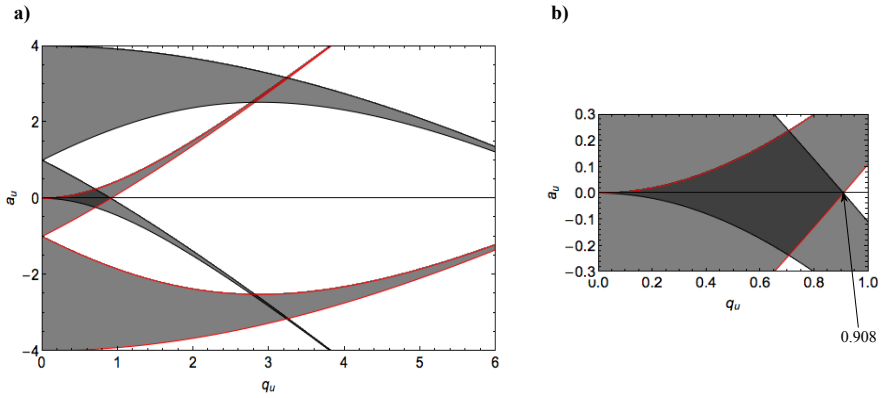

Figure 4.2: Symmetrized stability diagram for a quadrupole ion trap. The grey regions delimited by the black lines correspond to stable solutions of the Mathieu equation in the z direction, while the regions delimited by the red curves denote stability in the x, y degrees of freedom. The overlap regions represent the values of a and q for which solutions are stable simultaneously for the axial and radial directions, leading to three-dimensional confinement. b) Lowest stability domain of the Paul trap, for simultaneous storage of positive and negative ions of the same mass.

For nonzero a, the onset of instability occurs at lower values of q. This behavior underpins the operation of ion mass spectrometers. The key point is that both $a, q \propto Q/\mathrm{M}$ thus the trap potentials are adjusted to selectively eject the smallest masses (or highest Q/M ratios). Although there are techniques for absolute determination of masses, the basic spectrometer determines only the ratio Q/M as it ejects specific Q/M values from the trap, an accurate but "destructive" method of measurement. There are also "non-destructive" spectroscopic methods [131] which retain the sample in the trap and instead image the stable trajectories; in the stable regime, particles trace out Lissajous-type motions in the three degrees of freedom [132]. In particular, for $q_u \lesssim 0.2$ analytic methods are increasingly accurate: for small q, the timescale of motion in the harmonic well of the trap (i.e. excluding the $\sin \omega_\mathrm{d} t$ drive) is far longer than the period of the drive. In this adiabatic limit, the motion may be decomposed into a fast micromotion and a slower secular motion; the corresponding trajectories are given by:

$$u(t) = u_0 \sin \omega_\mathrm{s} t - u_0 \frac{q}{2} \sin \omega_\mathrm{s} t \sin \omega_\mathrm{d} t, \tag{4.6}$$

where u_0 is an initial amplitude. The first term on the left is the slow secular motion, while the second term is termed the micromotion and is characterized by a smaller amplitude oscillation dominated by $\omega_\mathrm{d} \gg \omega_\mathrm{s}$. For $q_u \lesssim 0.2$, the lowest harmonics of the secular motion appear at $\omega_\mathrm{s} = \beta \frac{\omega_\mathrm{d}}{2}$ and where:

$$\beta_u = \sqrt{a_u + \frac{q_u^2}{2}}. \tag{4.7}$$

We recall that the parameter a arises from the DC offset of the trap field and note that it regulates not only the stability but also the secular frequencies of the motion.

4.2 Nanoparticles in an optical cavity

It has been well established that a dielectric nanoparticle in an a optical cavity is levitated by the optical gradient force resulting from the interaction of its induced electric dipole and the electromagnetic field in the cavity. This has been recently investigated [28, 70, 105] in the specific context of optomechanical cooling of levitated particles but the underlying principles of the trapping have been very well-known for decades [92]. The resulting potential experienced by the nanoparticle, for a single (fundamental mode in the transverse direction) cavity mode takes the form:

$$V_{\rm opt}(x,y,z) = A\hbar\left|a_j\right|^2\cos^2(kx)e^{-2(y^2+z^2)/w^2}, \tag{4.8}$$

and thus combines a standing wave along the axial (x) direction and a Gaussian envelope in the transverse directions. w is the laser beam waist, while $a_j = \langle\hat{a}_j\rangle$ is the fluctuating cavity photon field amplitude for the j-th optical mode in the cavity (hence $\left|a(t)\right|^2$ is the photon number): it is these fluctuations which lead to temporal variations in radiation pressure which either cool or heat the particle in the cavity. For simplicity, below, we leave out the j label. The parameter A (dependent on the particle polarisability), determines the depth of the optical standing-wave potential in the cavity. For a dielectric of polarisability α [28, 70],

$$A\hbar = \frac{\hbar\omega_l}{2V_c\epsilon_0}\alpha. \tag{4.9}$$

$V_c = \pi w_0^2 L$ is the cavity volume, where L is the cavity length, while ω_l is the angular frequency of the laser driving the cavity. For a dielectric nanosphere of radius R, the polarisability:

$$\alpha = 3V_s\epsilon_0\frac{\epsilon-1}{\epsilon+2}. \tag{4.10}$$

$V_s = \frac{4}{3}\pi\mathrm{R}^3$ is the sphere volume (and hence $\mathrm{M} = V_s\rho$, where the density $\rho = 2198\,\mathrm{kg\,m^{-3}}$ for the case of a silica nanosphere), while $\epsilon_0 \simeq 8.854\times10^{-12}\,\mathrm{F/m}$ is the vacuum permittivity, and $\epsilon \simeq 3.8$ is the dielectric constant for silica. For the ideal case where the nanosphere radius R is small [28], i.e. $\mathrm{R} \ll \lambda$, then $A(\mathrm{R}\ll\lambda) \equiv A_0(\mathrm{R})$ where the small nanosphere coupling takes the form of equation (4.9), while for larger nanospheres, size-dependent corrections must be applied $A(\mathrm{R}) \equiv A_0(\mathrm{R})f^2(\mathrm{R})$. In previous works [69, 70] size dependent effects on the dynamics of the corresponding optomechanical system have been investigated; in particular experimental measurements of mechanical frequencies suggested that for lasers of

wavelength $\lambda = 1064\,\mathrm{nm}$, if $\mathrm{R} \lesssim 200\,\mathrm{nm}$, then $f(\mathrm{R}) \sim 1$ and $A(\mathrm{R}) \simeq A_0(\mathrm{R})$.

Formally equation (4.8) is not separable; however as the beam waist w is typically much larger than the nanospheres, a particle confined within one well of the optical standing wave experiences a large disparity between the axial frequencies $\omega_{\mathrm{M}}/2\pi$, along the laser beam $\equiv x$, and the transverse frequencies $\omega_{\mathrm{M}}^{(y,z)}/2\pi$ (y, z degrees of freedom, arising from the Gaussian form of the mode), with a ratio $\omega_{\mathrm{M}}/\omega_{\mathrm{M}}^{(y,z)} = kw/\sqrt{2}$, as verified in [70]. We will see that in our experiment typically the axial frequencies are of the order $\omega_{\mathrm{M}}/2\pi \sim 100\,\mathrm{kHz}$ and the transverse frequencies $\omega_{\mathrm{M}}^{(y,z)}/2\pi \sim 100\,\mathrm{Hz}$. Thus it is not unreasonable to neglect coupling to the transverse degrees of freedom in optomechanical set-ups and to analyze the trapping and cooling of the axial coordinates as an approximate 1D system. In this case one obtains coupled mechanical and optical Heisenberg equations of motion [28, 69, 70] for the quantum operators:

$$\begin{aligned} \ddot{\hat{x}} &= -\frac{\hbar k A}{\mathrm{M}}\hat{a}^\dagger\hat{a}\sin 2(k\hat{x}) - \Gamma_{\mathrm{M}}\dot{\hat{x}}, \\ \dot{\hat{a}} &= i\Delta_0\hat{a} - i\varepsilon + iA\hat{a}\cos^2(k\hat{x}) - \frac{\kappa}{2}\hat{a}, \end{aligned} \tag{4.11}$$

where $\Delta_0 = (\omega_l - \omega_c)$ is the detuning between the laser frequency and the selected cavity resonant frequency: for optomechanical cooling $\Delta_0 < 0$, corresponding to red-detuning; κ and Γ_{M} are the damping rates for the optical and mechanical systems respectively. ε is the driving amplitude for the optical mode.

If we are far from the quantum regime (i.e. far from the ground state) of the optomechanical system, we replace the operators by their expectation values $\hat{x} \to \langle\hat{x}(t)\rangle \equiv x(t)$ and $\hat{a} \to \langle\hat{a}(t)\rangle \equiv a(t)$ and simply solve the corresponding semiclassical equations of motion for the scalar complex variables. A comparison between solutions of quantum and semiclassical equations is found in [70] and it is only very near the ground state that the non-commuting character of $\hat{a}^\dagger$ and $\hat{a}$ becomes important and the quantum/semiclassical solutions begin to differ.

It is easy to see that for small oscillations, ($\sin 2kx \sim 2kx$) the equations for the mechanical degree of freedom correspond to a damped harmonic oscillator, i.e.,

$$\ddot{x}(t) = -\omega_{\mathrm{M}}^2 x - \Gamma_{\mathrm{M}}\dot{x} = -\frac{2\hbar k^2 A}{\mathrm{M}}\left|\bar{a}\right|^2 x - \Gamma_{\mathrm{M}}\dot{x} \tag{4.12}$$

where we neglect fluctuations in the cavity photon number. These fluctuations are associated with the retarded radiation pressure force which leads to optomechanical cooling. However, they do not significantly affect the value of the mechanical oscillation frequency, ω_{M}.

4.3 Hybrid electro-optical trap

We can now move to a new description of the nanoparticles motion inside our hybrid electro-optical trap, that utilizes both the optical field of a cavity and the electric field of a Paul trap. Combining the mathematical aspects of optomechanical interaction, and the nanoparticles dynamics inside the Paul trap and the optical cavity, presented separately in previous sections, here we are interested in giving a mathematical derivation of the nanoparticles motion that will help the analysis of the experimental results, presented in chapters 6 and 7. We will also go into the details of our experimental apparatus in chapter 5 , while in the following we only need a schematic representation to better visualize the theoretical concepts.

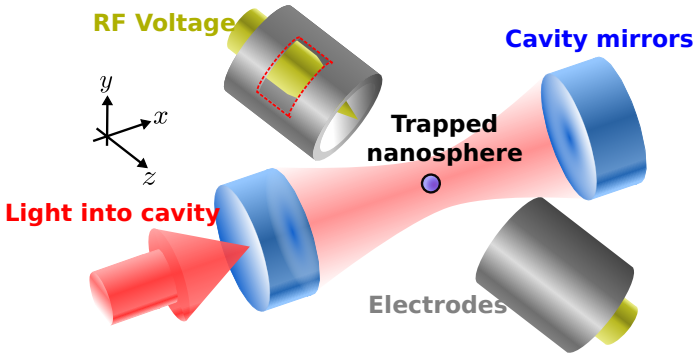

Figure 4.3: A schematic of the hybrid electro-optical trap, consisting of a Paul trap and standing wave optical cavity potential. The Paul trap is formed by two rounded electrodes separated by 1 mm which are enclosed by grounded cylindrical shield. The intracavity field of an optical cavity passes through the middle of the Paul trap (image from [36]).

A schematic of the hybrid electro-optical trap is shown in figure 4.3. In our experiment the Paul trap electric field is obtained by applying an RF voltage $V_0 \sin \omega_{\mathrm{d}} t$ (and zero DC voltage, $U_0, a_u = 0$) to two rounded electrodes placed perpendicularly to the cavity axis, and kept at a constant distance of 1 mm (see chapter 5).

We can redefine the ion trap potential in terms of a characteristic frequency $\omega_{\mathrm{T}}^2 = 2QV_0/\mathrm{M}r_0^2$, typically of the same order as ω_{s} :

$$V_{\mathrm{ion}}(x, y, z, t) = \frac{1}{2}\mathrm{M}\omega_{\mathrm{T}}^2(x^2 + y^2 - 2z^2)\sin \omega_{\mathrm{d}} t. \tag{4.13}$$

The combined dynamics in the hybrid cavity and Paul trap potentials requires the solution of coupled equations of motion for the mechanical degrees of freedom $\hat{x}, \hat{y}, \hat{z}$ as well as the cavity light mode $\hat{a}$. The equations of motion can be obtained from the total Hamiltonian of the hybrid trap. In a frame rotating at the laser frequency ω_l, the corresponding quantum

Hamiltonian may be written:

$$\hat{H} = \frac{\hat{p}^2}{2\mathrm{M}} - \hbar\Delta_0\hat{a}^\dagger\hat{a} + \hbar\varepsilon\left(\hat{a}^\dagger + \hat{a}\right) - V_{\mathrm{opt}}(\hat{x},\hat{y},\hat{z}) - V_{\mathrm{ion}}(\hat{x},\hat{y},\hat{z},t) - g\hat{y}. \tag{4.14}$$

The effects of gravitational acceleration g are included in the simulations; for the strongest values of the input power P_{in}, the effects are comparatively minor.

In the experimental regimes under consideration it is reasonable to assume semiclassical behavior and hence the equations of motion for the axial degree of freedom (along the cavity axis) can be written:

$$\ddot{x} = -\frac{\hbar k A}{\mathrm{M}}|a(t)|^2\sin(2kx)\mathcal{L}(y,z) - \Gamma_{\mathrm{M}}\dot{x} - \omega_{\mathrm{T}}^2 x\sin(\omega_{\mathrm{d}}t) - \zeta_x(t). \tag{4.15}$$

For the transverse motion:

$$\begin{aligned}\ddot{y} &= -\frac{4y}{w^2}\frac{\hbar A}{\mathrm{M}}|a(t)|^2\cos^2(kx)\mathcal{L}(y,z) - \Gamma_{\mathrm{M}}\dot{y} - \omega_{\mathrm{T}}^2 y\sin(\omega_{\mathrm{d}}t) - gy,\\ \dot{z} &= -\frac{4z}{w^2}\frac{\hbar A}{\mathrm{M}}|a(t)|^2\cos^2(kx)\mathcal{L}(y,z) - \Gamma_{\mathrm{M}}\dot{z} + 2\omega_{\mathrm{T}}^2 z\sin(\omega_{\mathrm{d}}t),\end{aligned} \tag{4.16}$$

and for the cavity field:

$$\dot{a} = i\Delta_0 a - i\varepsilon + iAa\cos^2(kx)\mathcal{L}(y,z) - \frac{\kappa}{2}a - \eta(t), \tag{4.17}$$

with transverse envelope of the light beam $\mathcal{L}(y,z) = e^{-2(y^2+z^2)/w^2}$. Here we have explicitly included noise terms $\zeta_x(t)$, which arises from the background bath of gas at room temperature, and $\eta(t)$, which is assumed to be photon shot noise. These allow a realistic description not only of the optical trapping and particle loss processes, but also of the final steady-state dynamics of the system (and hence the final equilibrium temperature). They satisfy the relations:

$$\begin{aligned}\langle\zeta_x(t')\zeta_x(t)\rangle &\simeq \Gamma_{\mathrm{M}}2n_B\frac{\hbar\omega_{\mathrm{M}}}{\mathrm{M}}\delta(t-t'),\\ \langle\eta(t')\eta(t)\rangle &= \kappa\delta(t-t'),\end{aligned} \tag{4.18}$$

where $n_B = k_B T/(\hbar\omega_{\mathrm{M}})$, with $T_B = 300\,\mathrm{K}$ and k_B is Boltzmann's constant. ζ_x and $\eta(t)$ are modeled as Gaussian random noise and the resulting Langevin equations are propagated numerically by a stochastic Runge-Kutta method [133]. In the absence of optomechanical damping, the resulting stochastic dynamics lead to a steady state temperature of $\approx 300\,\mathrm{K}$, corresponding to thermal mechanical oscillations at ω_{M}, superposed on much slower (and adiabatically separable) Paul trap micro motions and secular motions. Although noise terms

$\zeta_y(t)$ and $\zeta_z(t)$ may be also added for the transverse motions of equations (4.16), in practice their effects are of less significance; the amplitude of the transverse modes is not limited by noise and is largely set by other dynamical effects (such as gravity). In the present set-up, although there is slow mixing of the x, y, z motions and the transverse modes exhibit some optomechanical damping, only the axial mode is strongly cooled.

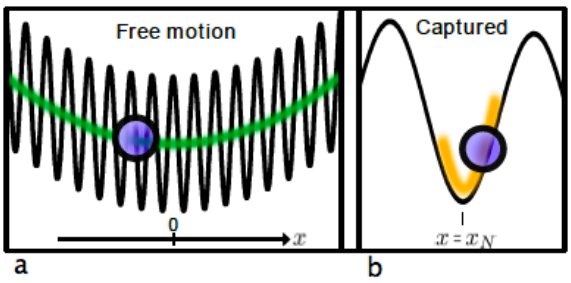

Figure 4.4: a) The sphere is trapped by the Paul trap and driven across the standing wave formed by the light in the cavity. b) Intermittently the sphere is trapped by the optical field and confined to one fringe of the standing wave [36].

We can define two regimes of motion within the hybrid trap: free motion, that refers to when the particle is driven across the optical standing wave potential by the Paul trap (see figure 4.4a), and captured motion, which corresponds to when the nanosphere is confined and oscillates within a single well of the standing wave (figure 4.4b), where most of the cooling takes place. Near turning points of the Paul trap motion (where the speed of the nanoparticle is a minimum) a small amount of damping can lead to the nanoparticle loosing enough energy to be captured by the optical potential within a well, at $x = x_{\mathrm{N}}$. The combined Paul trap and cavity mode potential is shown in figure 4.5.

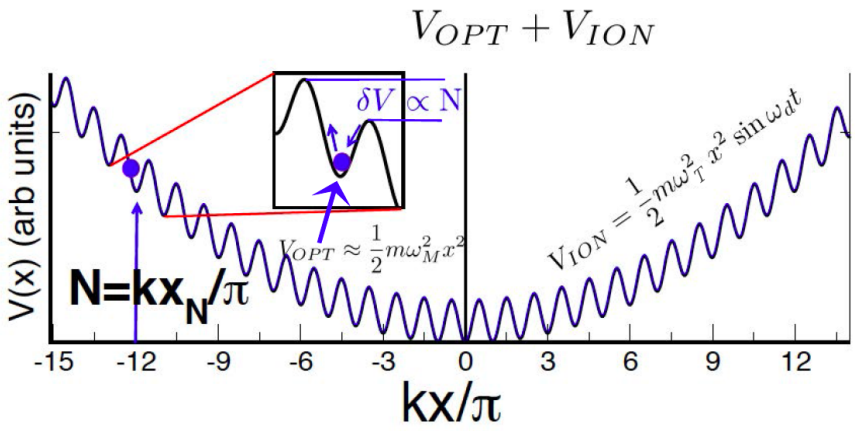

Figure 4.5: The hybrid trap potential combines the Paul trap (large scale) potential V_{ion}, of dimension $\sim 1\,\mathrm{mm}$, much larger than the wavelength $\lambda = 1064\,\mathrm{nm}$ of the standing wave potential of the cavity mode V_{opt}. The optical potential is approximately harmonic close to the bottom of each individual well. The dynamics, including the cooling rates, depend on N, the index number which labels the capture well [37].

Considering the mechanical motion given within a single optical well to be much larger than the motion in the Paul trap potential ($\omega_{\rm M} \gg \omega_{\rm T}$), we have many optical wells ($\sim 10^3$) within the Paul trap field. The key step in the experiment is capture of the nanoparticle in a single optical well, indexed by the label $\mathrm{N} \in [-\mathrm{N}_{max}, +\mathrm{N}_{max}]$, with $\mathrm{N}_{max} \simeq 1000$. After capture the particle remains confined to the vicinity of $x \sim x_{\rm N} = \mathrm{N}\lambda/2$, where the wavelength $\lambda = 1064\,\mathrm{nm}$.

Now, for a particle which has been trapped at the N-th optical well, it is most convenient to employ a coordinate frame with the origin at the antinode; hence, we transform the axial coordinates to $x' = x - x_{\rm N}$ and obtain for the axial motion:

$$\ddot{x}' = -\frac{\hbar k A}{\mathrm{M}}|a(t)|^2 \sin(2kx')\mathcal{L}(y,z) - \Gamma_{\rm M}\dot{x}' - \omega_{\rm T}^2\,(x' + x_{\rm N})\sin(\omega_{\rm d}t) - \zeta_{x'}(t) \tag{4.19}$$

For optically levitated particles, consideration of small oscillations about a point $x' = x_0$ determines a mechanical frequency $\omega_{\rm M}/2\pi$ where typically $\omega_{\rm M} \gg \omega_{\rm d}, \omega_{\rm s}$. Thus we assume that the fast oscillations near the antinode are adiabatically separable from the slower timescales associated with the quadrupole trap. We write $x'(t) = x_0(t) + x(t)$, where we assume that the amplitude of the (fast varying) $x(t)$ is small with respect to the slower oscillations $x_0(t)$. In the first instance, we assume a quasi-static position $x_0(t) \simeq x_0$ and obtain for the axial motion:

$$\begin{aligned} \ddot{x}_0 + \ddot{x} &= -\frac{\hbar k A}{\mathrm{M}}|a(t)|^2\mathcal{L}(y,z)\cos(2kx_0)\left[\sin(2kx) + \tan(2kx_0)\cos(2kx)\right] \\ &- \omega_{\rm T}^2 x_{\rm N}\sin(\omega_{\rm d}t), \end{aligned} \tag{4.20}$$

where we neglect damping due to the presence of the gas, and assume that the particle is caught in a well such that $x_{\rm N} \gg x'$.

Similarly, if we assume temporal fluctuations in the cavity field are small, we can also transform to shifted values for the field amplitudes hence $a(t) \to \bar{\alpha} + \delta a(t)$, where $\bar{\alpha}^2 \equiv \mathrm{n}$ represents the mean cavity photon number, and $\delta a(t)$ are now small fluctuations about the mean. Keeping only zero-th order terms in equation (4.20) and assuming that $|\ddot{x}_0| \ll |\ddot{x}|$ we obtain:

$$\omega_{\rm M}^2 \tan(2kx_0) \approx -2kx_{\rm N}\omega_{\rm T}^2 \sin(\omega_{\rm d}t)\,, \tag{4.21}$$

where we write $\omega_{\rm M}^2 \simeq \left(2\hbar k^2 A\mathcal{L}(y,z)\,|\bar{\alpha}|^2/\mathrm{M}\right)\cos(2kx_0)$ (and we show below that $\omega_{\rm M}$ is in fact the mechanical frequency of our optical system).

Recalling that $x_0(t)$ is time-dependent and is oscillating (albeit slowly), the above can be recast in the form:

$$\sin(2kx_0(t)) \approx -\frac{\omega_{\rm T}^2}{\bar{\omega}_{\rm M}^2}\,(2kx_{\rm N})\sin(\omega_{\rm d}t)\,, \tag{4.22}$$

where we have defined $\bar{\omega}_{\mathrm{M}}^2 \equiv \frac{2\hbar k^2 A}{\mathrm{M}} |\bar{\alpha}|^2$. Hence if x_0 remains small for all t then $x_0 \approx -\frac{\omega_{\mathrm{T}}^2}{\bar{\omega}_{\mathrm{M}}^2} x_{\mathrm{N}} \sin(\omega_{\mathrm{d}} t)$; however, we do not need to assume this: the excursion in x_0 can in fact span a significant fraction of the well; in that case, the mechanical frequency $\omega_{\mathrm{M}}(t)$ varies within the range $\omega_{\mathrm{M}} \left[1 - \sqrt{\cos\left(2k\frac{\omega_{\mathrm{T}}^2}{\bar{\omega}_{\mathrm{M}}^2} x_{\mathrm{N}}\right)}\right]$, which is approximately 15% of ω_{M} for an oscillation about a distance of $\lambda/4$ from the bottom of the optical potential well. As we will see in the analysis of experimental results (chapters 6 and 7) this variability in ω_{M} leads to an atypical structure in the cavity output spectrum, of different form from the displacement spectrum $S_{xx}^T(\omega)$ associated to the particles motion, and which depends on the optical well N at which the particle localizes.

For simplicity, we assume in the analysis below (but not in our numerical simulations) that the transverse excursions are small and thus $\mathcal{L}(y,z) \simeq 1$. However, in fact these excursions remain detectable and even for the trapped particle (see experimental data in chapters 6 and 7), we can detect oscillations at one or both transverse secular frequencies $\omega_{\mathrm{s}}^{(y,z)} = \left[\omega_{\mathrm{d}}/\left(2\sqrt{2}\right)\right] q_{y,z}$. The transverse oscillations are important for sensing the full 3-dimensional particle trajectories; as they are only weakly affected by the optical potential they provide a reliable measurement of the nanoparticle's charge, Q. If the transverse motions become significant, they lead to further variability in ω_{M} and more importantly, to escape from the optical well.

The zero-th order terms in the equation for the optical field yield a value for the mean intracavity fields:

$$|\bar{\alpha}|^2 = \frac{\varepsilon^2}{\kappa^2/4 + \Delta_{x_0}^2}, \tag{4.23}$$

where $\Delta_{x_0} = \Delta_0 + A\cos^2(kx_0)$ is an effective cavity detuning, which includes a small correction from the optical field [70]. The optomechanical coupling which leads to optical damping is contained in the first order equations for $x(t)$:

$$\ddot{x} = -\omega_{\mathrm{M}}^2 x - \frac{\hbar}{\mathrm{M}} (\delta a + \delta a^*) G - \Gamma_{\mathrm{M}} \dot{x}, \tag{4.24}$$

where $G = kA\bar{\alpha}\sin(2kx_0)$, and where, without loss of generality, we have assumed that $\bar{\alpha}$ is real. (e.g. in the Hamiltonian, by means of the transformation $\bar{\alpha} \to \bar{\alpha}e^{-i\theta}$ and $\hat{\alpha} \to \hat{\alpha}e^{-i\theta}$ we can restrict ourselves to real $\bar{\alpha}$).

For $\delta a(t)$ we obtain:

$$(\dot{\delta a}) = i\Delta_{x_0}\delta a - iGx - \frac{\kappa}{2}\delta a. \tag{4.25}$$

For red-detuning ($\Delta_{x_0} < 0$) the $x(t)$ motion is damped such that $x(t) \simeq X_{\mathrm{M}} e^{-\Gamma_{\mathrm{opt}} t}\cos(\omega_{\mathrm{M}} t)$ where X_{M} is the initial amplitude for mechanical oscillations (soon after capture by an optical well). Thus the mechanical motion cools until a steady state is achieved whereby

heating rates due to residual gas collisions or technical noise equals the cooling rate [70], and hence $X_{\mathrm{M}}e^{-\Gamma_{\mathrm{opt}}t} \rightarrow X_{\mathrm{M}}^{\infty}$ where X_{M}^{∞} is a steady state amplitude which may fluctuate in time due to background noise; in effect $\left\langle (X_{\mathrm{M}}^{\infty})^2 \right\rangle$ represents a good estimate of the variance of the mechanical motion and hence provides an estimate of the effective temperature of our system, as expressed in equation (3.19).

Finally, we combine the mechanical oscillations with the slower excursion in the equilibrium point to model the axial motion of the captured nanoparticle:

$$x'(t) \approx X_{\mathrm{d}} \sin(\omega_{\mathrm{d}} t) + X_{\mathrm{M}}^{\infty} \cos(\omega_{\mathrm{M}} t). \tag{4.26}$$

Here, $X_{\mathrm{d}} \approx \frac{\omega_{\mathrm{T}}^2}{\omega_{\mathrm{M}}^2} x_{\mathrm{N}}$ is the drive amplitude, which accounts for a cyclic displacement of the equilibrium point $x = x_{\mathrm{N}}$ of the mechanical oscillations in the optical field. In practice, the additional force on the charged nanosphere by the Paul trap acts to periodically pull the particle away from the antinode. This effect demonstrates that the Paul trap plays an important role in the optomechanical cooling dynamics, essentially eliminating the need for a second, dedicated optical beam [28, 69].

4.4 Introducing quadratic coupling

Quadratic coupling emerges naturally with the dipole force arising from an optical standing wave; although the goal of showing quantization of the mechanical motion is challenging, levitated systems offer certain advantages, not least almost complete environmental decoupling. One important advantage over membrane in the middle set-ups as [85] is that a leading cause of error in measurements of the mechanical eigenstate arises from imperfect positioning of the membrane; residual linear coupling introduces a back-action noise which provides a key limitation. However, unlike tethered membranes, levitated systems are self-trapping. When the second cooling mode or Paul trap which pulls the particle from the antinode is switched off, the particle will position itself at the antinode where the coupling is purely quadratic.

To describe the nature of linear/nonlinear coupling in our system (see diagram of figure 4.6), we can look again at the equations of motion, obtained from the total Hamiltonian of the hybrid trap, represented by equation (4.14), and extend the description carried out in previous section. The quadratic nature of the optomechanical coupling arises from small angle approximations made to obtain the linearized equations, thus $\cos 2k(x + x_0) \simeq (1 - 2k^2x^2)\cos 2kx_0 - 2kx \sin 2kx_0$ and $\sin 2k(x + x_0) \simeq (1 - 2k^2x^2)\sin 2kx_0 + 2kx \cos 2kx_0$ for small oscillations.

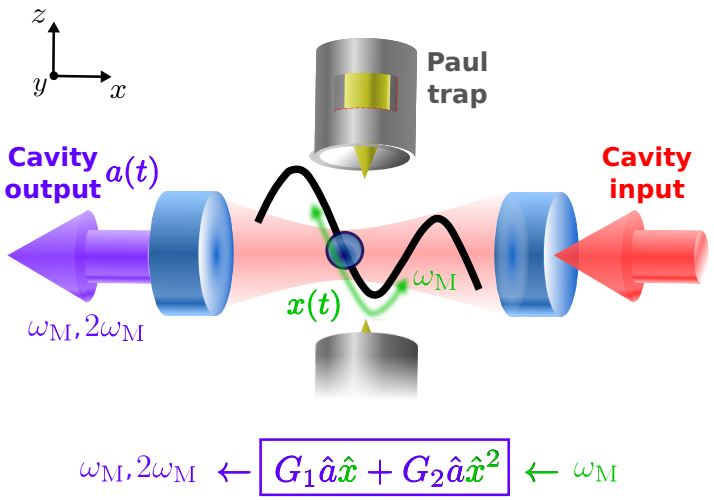

Figure 4.6: A particle trapped in an optical well of the hybrid trap oscillates at mechanical frequency $\omega_{\rm M}$. The cavity field is modulated by linear and quadratic coupling terms of variable strength (image from [37]) .

In contrast, no higher order terms in $a(t)$ are retained as the single-photon coupling strengths are too weak. We thus obtain:

$$\mathrm{M}\ddot{x} \simeq -\mathrm{M}\omega_{\rm M}^2\left[x-\epsilon x^2\right] - \hbar\left(\delta a+\delta a^*\right)\left(G_1+2xG_2\right) - \Gamma_{\rm M}\dot{x}, \tag{4.27}$$

and, for $\delta a(t)$, we have:

$$\dot{(\delta a)} \simeq i\Delta_{x_0}\delta a - i\left(G_1 x + G_2 x^2\right) - \frac{\kappa}{2}\delta a. \tag{4.28}$$

The other parameters are:

$$\begin{aligned} \mathrm{M}\omega_{\rm M}^2 &= 2\hbar k^2 A\left|\bar{\alpha}\right|^2\cos\left(2kx_0\right) \\ \epsilon &= k\tan\left(2kx_0\right) \\ G_1 &= kA\bar{\alpha}\sin\left(2kx_0\right) \\ G_2 &= k^2 A\bar{\alpha}\cos\left(2kx_0\right). \end{aligned} \tag{4.29}$$

All parameters above are scaled by $\mathcal{L}(y,z)\simeq 1$ but for convenience, this envelope is not included. Since, typically $\cos\left(2kx_0\right) \gg \sin\left(2kx_0\right)$, for an uncooled particle, the effects of the G_2 nonlinear term is comparatively large. However, as the particle cools, nonlinear effects are rapidly suppressed. This is most apparent if one compares one-photon coupling strengths (appropriately scaled for equations in terms of the usual phonon creation/annihilation op-

erators) such that:

$$\begin{aligned} g_1 &= kx_{\mathrm{ZPF}} A \sin(2kx_0) \\ g_2 &= (kx_{\mathrm{ZPF}})^2 A \cos(2kx_0) . \end{aligned} \tag{4.30}$$

Here $x_{\mathrm{ZPF}} = \sqrt{\hbar/2\mathrm{M}\omega_{\mathrm{M}}}$ gives the scale of the oscillator ground state (zero-point fluctuations). For a mechanical frequency $\omega_{\mathrm{M}} \sim 2\pi \times 10\,\mathrm{kHz}$, $kx_{\mathrm{ZPF}} = k\sqrt{\hbar/(2\mathrm{M}\omega_{\mathrm{M}})} \sim 10^{-5}$ and $A \simeq 26\,\mathrm{kHz}$, hence $g_2 \sim 10^{-5} g_1$ unless $x_0 \simeq 0$.

4.4.1 Cooling rate

The separation of the nanoparticle's motion into small oscillations about equilibrium, means that we can adapt optomechanical cooling theory for the hybrid trap system. The linear coupling G_1 drives the cooling. The optomechanical phonon damping has been already shown in section 3.3 to be given by:

$$\Gamma_{\mathrm{opt}} = G_1^2 \kappa \left[S(\omega_{\mathrm{M}}) - S(-\omega_{\mathrm{M}}) \right], \tag{4.31}$$

where $S(\omega) = \left[(\Delta_{x_0} - \omega)^2 + \frac{\kappa^2}{4} \right]^{-1}$. Thus if $kx_0 = 0$, then $G_1 = 0$ and there is no cooling (note though that G_2 is maximal at $x_0 = 0$). However, the effect of the oscillating Paul trap is to force a periodic excursion of the equilibrium point x_0, with a period which is slow compared with the mechanical oscillations since $\omega_{\mathrm{M}} \gg \omega_{\mathrm{d}}$. By consideration of the zero-th order terms in the linearization we obtain:

$$\sin(2kx_0(t)) \approx -\frac{\omega_{\mathrm{T}}^2}{\bar{\omega}_{\mathrm{M}}^2} 2\pi \mathrm{N} \sin(\omega_{\mathrm{d}} t) , \tag{4.32}$$

In effect, due to the Paul trap excursion, $G_1 \equiv G_1(t)$ so the optomechanical coupling strength is itself time-dependent:

$$G_1^2(t) \approx \chi \mathrm{n} \mathrm{N}^2 \sin^2(\omega_{\mathrm{d}} t) , \tag{4.33}$$

where we set $\chi = \frac{\omega_{\mathrm{T}}^4}{\bar{\omega}_{\mathrm{M}}^4} 4\pi^2 k^2 A^2$. But since $\omega_{\mathrm{d}} \ll \omega_{\mathrm{M}}$, we can average over one period of the micromotion $T_{\mathrm{d}} = 2\pi/\omega_{\mathrm{d}}$, thus here we use the averaged value $\bar{G_1^2} = \frac{\chi}{2} \mathrm{n} \mathrm{N}^2$ to obtain the cooling.

Hence, the cooling depends on both the photon number as well as the number of the capture well. However, although large N leads to strong cooling, it also introduces anharmonicity in the motion, via the term in ϵ and also on the dependence of $\omega_{\mathrm{M}} \propto \sqrt{\cos(2kx_0)}$. To minimize these, $kx_0 \lesssim \pi/10$, preferably. Fortunately, a very large excursion also makes optical capture more difficult, as the nanoparticle will not remain trapped in a single well.

Although in the present setup it is not possible to directly image N even to the nearest ≈ 100 wells (the precision required to simply obtain a good estimate of cooling), we will see in the results of chapter 7 that there is a rich sideband structure arising from the cavity field modulation, that can provide a characteristic fingerprint which enable one to estimate N.

Finally, we note that Γ_{opt} depends also on particle charge, since $\omega_{\mathrm{T}}^4 \propto Q^2$. However, we show in section 7.4 that the hybrid trap offers a unique way of simultaneously estimating the intra-cavity phonon number n, as well as Q, via the secular frequencies.

Chapter 5

Experimental apparatus

This chapter is devoted to the description of the experimental setup. I start from a general outline of the optical scheme, and then move to the presentation of some of the key experimental equipment. After that, a detailed description of the optical cavity and the Paul trap is reported. This will be accompanied by a description of the methods used for measuring experimental parameters such as cavity finesse, the breakdown voltage between the Paul trap electrodes, and the particle's charge.

5.1 Optical setup

The light field inside the optical cavity is formed by two beams entering from opposite directions. Light from a solid state 1064nm laser (Nd:YAG Mephisto Innolight) is split into a weak and a strong beam by a 10:90 beamsplitter (Figure 5.1).

The weak beam is used to keep the laser locked to the fundamental TEM_{00} cavity mode of resonance, via the Pound-Drever-Hall technique (Appendix D) . To this purpose, we use a $LiTaO_3$ electro-optic crystal (EOM), driven by a sinusoidal signal at $26.6 \pm 0.2\,\mathrm{MHz}$ coming from a custom-made Pound-Drever-Hall box (PDH). The same box receives the modulated signal reflected by the cavity and picked up by a fast photodetector (PD_1), and generates the error signal to be fed back to the laser via a high-speed servo controller (Newport LB1005).

The strong beam is used for optical trapping and cooling the nanoparticles and it can be arbitrarily shifted in frequency with respect to the cavity resonance to achieve the desired detuning. This is obtained by using two acousto-optic modulators (AOMs), placed in sequence at a distance of $\simeq 50\,\mathrm{mm}$.

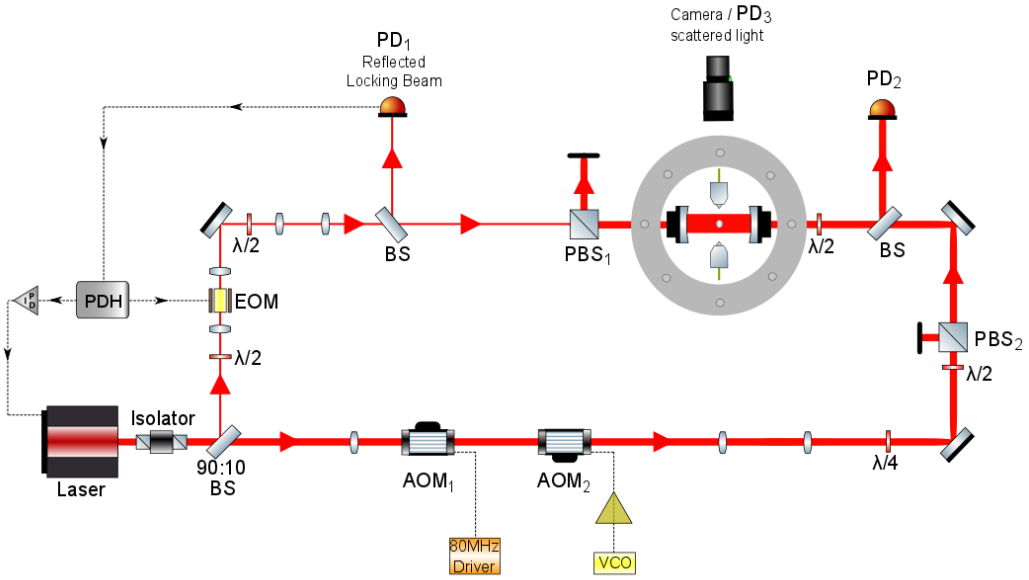

Figure 5.1: Optical layout of the experiment. A weak beam resonant with the optical cavity is used to stabilize the cavity through Pound-drever-Hall locking. A 9× stronger beam which can be detuned from the cavity resonance is used for trapping and cooling. The light that the nanosphere scatters as it moves through the optical cavity is collected and used to characterize its motion.

The reason for this is, first of all, that when a laser frequency is scanned with an AOM, the angle of the first-order diffracted beam shifts as well, since the beam diffraction angle is a function of modulation frequency (see section 5.3). This deviation can be corrected using a second modulator, working in the opposite way, to form a cascade structure. Secondly, the modulators we use have been optimized for operation at an acoustic frequency $\rho = 80 \pm 10\,\mathrm{MHz}$. In our experiment though we need to work with much lower detuning values (of the order of the cavity linewidth), so we take the difference between the two frequency shifts given by the AOMs. AOM_1 (Isle Optics LM080) is driven by an RF driver (Crystal Technology 1080-AF AIFO 2.0) with central frequency $80\,\mathrm{MHz} \pm 0.1\%$, while AOM_2 can be tuned around the same central frequency by a voltage-controlled oscillator (VCO) (ZX95-100-S+). As a result, the strong beam will be locked at any desired frequency around the TEM_{00} resonance, within $\sim 5\,\mathrm{MHz}$.

Both beams are mode-matched to the cavity and coupled to a fundamental longitudinal mode of resonance, and the choice of the series of lenses to be used in both beams before entering the cavity has been made using the laws of mode-matching (Appendix C), by means of MatLab and Labview simulators of Gaussian beams. The polarization of the two beams can be rotated by means of half waveplates ($\lambda/2$) and split accordingly by polarizing beamsplitters (PBS). This is particularly useful to isolate the reflected weak beam from the

transmitted strong one at PBS_1, before detection at PD_1. Having the two beams orthogonally polarized inside the cavity is also important as interference effects at the frequency difference between the two beams (detuning) will be minimized, resulting in a more stable locking and, consequently, a more stable trapping. The combination of $\lambda/2$ and PBS_2 instead is used as a control over the cavity input power for the strong beam, which we can range from a maximum of $\simeq 500\,\mathrm{mW}$ to a few μW. The weak beam input power is instead kept fixed at $0.2\,\mathrm{mW}$.

A lens placed above the cavity is used to collect scattered light from the nanosphere as it moves through the cavity field. This light is directed onto an amplified photodiode and is used to monitor the position of the nanosphere in time. The scattered light S and the PDH locking signal are recorded as a function of time using an oscilloscope.

5.2 Laser system

In all our measurements we have used a Nd:YAG laser (Innolight Mephisto). This is a diode-pumped, yttrium aluminum garnet solid state laser, with a linewidth of $\sim 1\,\mathrm{kHz}$, a tuning range of $30\,\mathrm{GHz}$, and nominal output power of approximately $2\,\mathrm{W}$, at $1064\,\mathrm{nm}$ wavelength [134]. An important characteristic of this device consists in the possibility of modulating the emitted frequency, something that can be done in two ways:

- a first control is possible through the fast frequency tuning port, located on the back of the laser head, with a response bandwidth of $100\,\mathrm{kHz}$, and a maximum input voltage of $100\,\mathrm{V}$. Here we can change the laser cavity length acting on a piezoelectric element, with the result that the frequency undergoes a variation of $\simeq 1\,\mathrm{MHz/V}$.

- the second control consists on a slow frequency tuning port, with a response bandwidth of $1\,\mathrm{Hz}$, through which the temperature of the crystal can be modified by $1\,\mathrm{K/V}$, using an input voltage of $\pm 10\,\mathrm{V}$. The thermal tuning coefficient is reported to be $-3\,\mathrm{GHz/V}$.

The correction signal from the PDH used to lock the laser to the cavity resonance, via the weak beam, is fed back to the PZT fast tuning port of the laser. Before closing the feedback loop, the laser receives a voltage ramp through the same tuning port, in order to center the laser frequency around the TEM_{00} cavity mode of resonance. To find the cavity mode in the first place, we can employ the temperature tuning port of the laser, which is simply controlled manually with a signal generator. Alternatively, we can tune the cavity length for the same purpose, by using a piezoelectric ring which one of the cavity mirrors is attached to, as described in section 5.4.

5.3 Laser detuning

As explained in section 5.1 , we use two cascaded acousto-optic modulators [135] along the strong beam path (see figure 5.2). In this way, we are able to detune its frequency respect to the weak beam (and to the cavity resonance) by the AOMs frequency difference $\Delta_0/2\pi = \rho_1 - \rho_2$, such that the laser frequency after going through the AOMs can be written:

$$f = f_{\mathrm{L}} + (\rho_1 - \rho_2)\,, \tag{5.1}$$

where f_{L} is the laser frequency before AOM_1. Only when both AOMs are driven at the same frequency, $\rho_1 = \rho_2$, $f = f_{\mathrm{L}}$ and the strong beam is in resonance with the cavity.

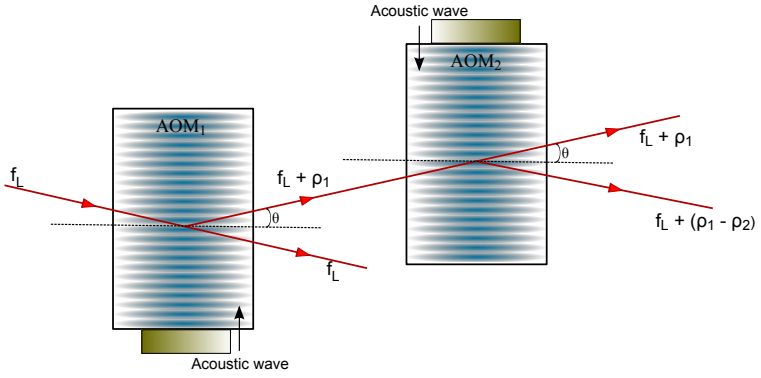

Figure 5.2: Schematic of two cascaded acousto-optic modulators. After the laser beam of frequency f_{L} passes through AOM_1 the first diffracted order gets a frequency $f_{\mathrm{L}} + \rho_1$, where ρ_1 is the frequency of the acoustic wave in AOM_1. When the latter goes through AOM_2 the frequency becomes $f_{\mathrm{L}} + (\rho_1 - \rho_2)$, where the difference $(\rho_1 - \rho_2)$ represents the value of detuning in our experiment.

AOM_1 is driven at a fixed frequency $\rho_1 = 79.98 \pm 0.01\,\mathrm{MHz}$, measured with a frequency counter, while AOM_2 frequency can be tuned using a VCO, from 50 to 100 MHz. To check the VCO response and evaluate its tuning sensitivity we change the tuning voltage applied and read the output frequency with the counter. Values are plotted in figure 5.3. The VCO has a linear response, with slope, given by a linear fit, of $(3.69 \pm 0.01)\,{}^{\mathrm{MHz}}/_{\mathrm{V}}$.

We need to be able to control the input voltage of the VCO, driving AOM_2, with a higher precision around the central values of figure 5.3 (i.e. $\sim 10\,\mathrm{V}$). In this way we can move the output frequency by smaller steps near the fixed value of AOM_1, and gain finer control over the laser detuning, around the cavity resonance. To this purpose, we employ a voltage divider [135, 136], where one of the two resistors (R_2) is variable and represented by a potentiometer (Bourns, 5K-3590S-2-502L).

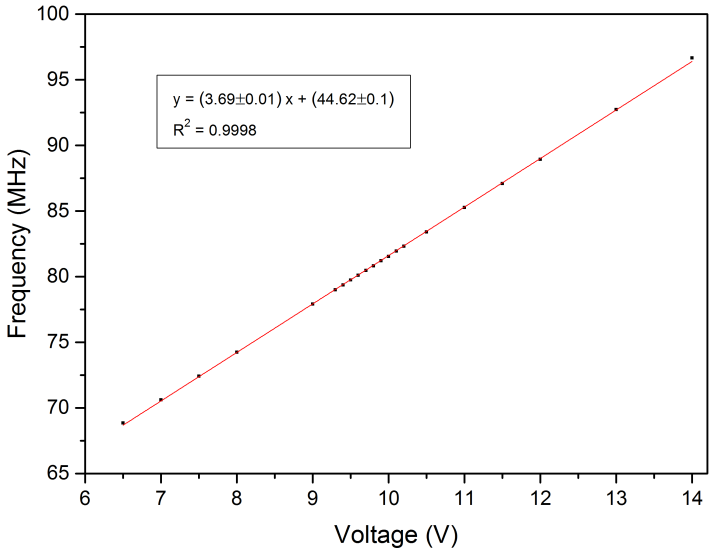

Figure 5.3: Linear fit of VCO output frequency vs tuning voltage. The resulting VCO tune sensitivity is $(3.69 \pm 0.01)\,{}^{\mathrm{MHz}}/_{\mathrm{V}}$.

The resistive divider ([136]) is such that, if we input a voltage of 10 V we obtain an output voltage ranging from 0 to 1.315 V. Considering the VCO tune sensitivity, we have now a frequency range around resonance of 4.85 ± 0.01 MHz, which means we can move by $\simeq$ 485 kHz every turn of the potentiometer. To calibrate the voltage divider, we plot in figure 5.4 the different values of the detuning obtained by changing the value of R_2, using as a reference the scale placed around the potentiometer's knob, with values going from 0 to 10, in steps of 0.10. Fixing resonance at potentiometer's setting = 5 (offset), we can span from red $(0-5)$ to blue detuning $(5-10)$.

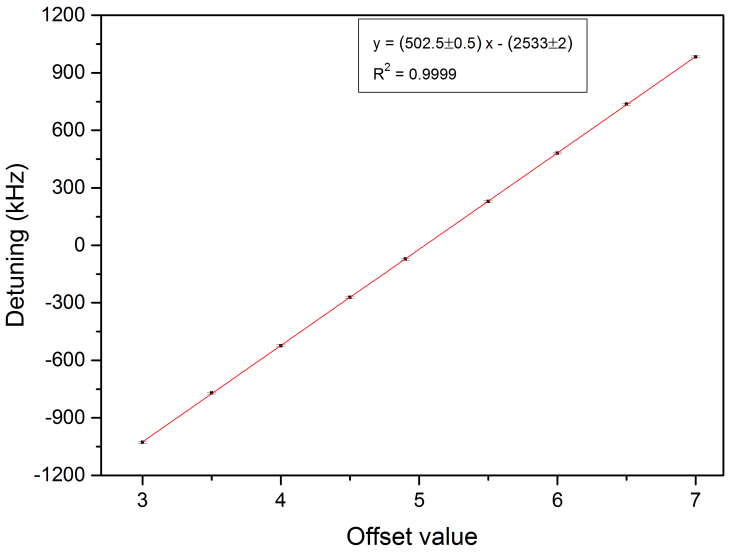

Figure 5.4: Detuning vs offset setting on the potentiometer, showing linear behavior.

The potentiometer shows an excellent linear behavior, with a fitting function:

$$y = 502.5x - 2533, \tag{5.2}$$

which we can now use to convert the offset values into values of detuning.

5.4 Optical cavity

The optical cavity is represented in figure 5.5. Mirrors are glued at the centre of two 48×48 mm (± 0.1 mm), 6 ± 0.1mm thick invar sheets, connected together by four 59 ± 0.1 mm long invar rods. One of the mirrors is attached to a 3mm thick piezoelectric ring, 15 mm in diameter (Piezomechanik HPCh 150), which is connected to a piezo controller (Thorlabs MDT 694A), allowing one to change the cavity length and tune the cavity resonance by applying a DC voltage that ranges between 0 and 100 V.

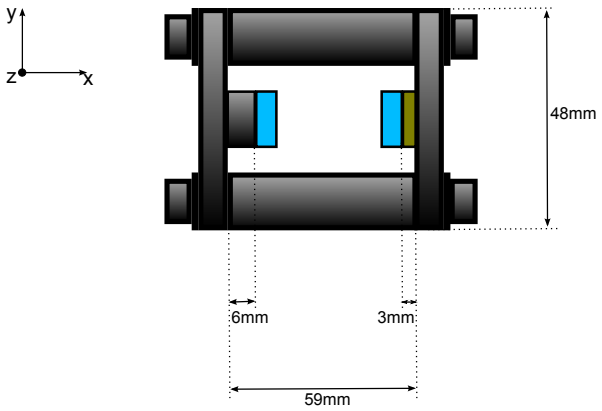

Figure 5.5: Representation of the optical cavity in the experiment. The mirrors are centered on two invar sheets, connected by four invar roads. The right-hand mirror is attached to a piezo ring to control the cavity length, while the left-hand one is glued to a 6 mm thick metallic ring.

The whole glueing process is carried out in several steps, and requires a few hours of our time for each mirror. We use high vacuum epoxy (Torr Seal) to glue the piezo ring onto one of the invar sheets first, and then one of the mirrors onto the piezo, around its edge. The second mirror instead, is glued to a 6.0 ± 0.1 mm thick metal ring and it's not attached to the second invar sheet until the whole cavity structure is assembled and placed inside the chamber. In this way we can position the second mirror from the top, holding it by the metal ring with tweezers, using a translation stage to optimize its position, maximizing the cavity alignment by looking directly at the laser light transmitted, before gluing it *in situ*. The Paul trap is normally kept outside the chamber during this delicate process, and it can be reinserted once the cavity is ready.

The mirrors have a plano-concave form, with diameter $12.7 \pm 0.1\,\text{mm}$ and thickness $6.35 \pm 0.1\,\text{mm}$, and same radius of curvature, $r_c = 200\,\text{mm}$, with a nominal reflectivity of 99.98% (Layertec 100337). Considering the size of all the cavity components, the distance between the two mirrors (i.e. cavity length) is $L = 37.3 \pm 0.2\,\text{mm}$. According to equation (8.25), the free spectral range $\text{FSR} = 4.02 \pm 0.02\,\text{GHz}$. Finally, we can estimate the nominal cavity finesse from the given mirror's reflectivity (see Appendix C):

$$\mathcal{F} = \frac{\pi\sqrt{R}}{1-R} = 15,700 \tag{5.3}$$

5.4.1 Cavity stability

The reason for using a spherical-mirror resonator, where the two mirrors have a certain radius of curvature r_c, is to provide a stable configuration for the confinement of light. A configuration with planar mirrors ($r_c \to \infty$), similar to the theoretical case treated in Appendix C to explain multiple-beam interference, is in fact high sensitive to misalignments. If the mirrors are not perfectly parallel, or the rays are not perfectly normal to the mirror surfaces, they undergo a sequence of lateral displacements that eventually causes them to wander out of the resonator.

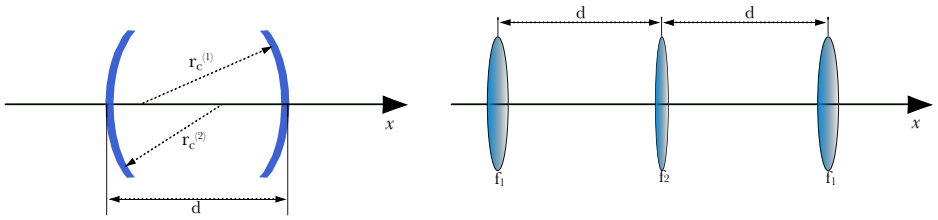

Figure 5.6: Spherical mirror resonator and equivalent sequence of lenses. The sequence is periodic and it repeats itself at every round-trip of the light inside the resonator.

We can use the laws of ray optics [162], to determine the conditions of confinement of light rays between two spherical mirrors of different radii $r_c^{(1)}$ and $r_c^{(2)}$. Light rays that bounce back and forth between the spherical mirrors of a resonator experience a periodic focusing action. The effect on the rays is the same as in a periodic series of lenses [163], which can be used as an optical transmission line (lens waveguide) (figure 5.6). Since reflection on a mirror of radius r_c can be described as the effect given by a thin lens with focal distance $f = r_c/2$, the $ABCD$ matrix of the ray between two round trips is given by [163]:

$$\begin{pmatrix} A & B \\ C & D \end{pmatrix} = \begin{pmatrix} 1 & 0 \\ -\frac{1}{f_1} & 1 \end{pmatrix} \cdot \begin{pmatrix} 1 & d \\ 0 & 1 \end{pmatrix} \cdot \begin{pmatrix} 1 & 0 \\ -\frac{1}{f_2} & 1 \end{pmatrix} \cdot \begin{pmatrix} 1 & d \\ 0 & 1 \end{pmatrix}.$$

We want this matrix to leave the ray unchanged, except for a global phase, an eigenvalue of

the matrix. In the end one obtains:

$$0 \leq \left(1 - \frac{d}{2f_1}\right)\left(1 - \frac{d}{2f_2}\right) \leq 1$$

The boundaries of the confinement condition are given by the equalities, and they define the regions within which a resonator is stable, as shown in figure 5.7.

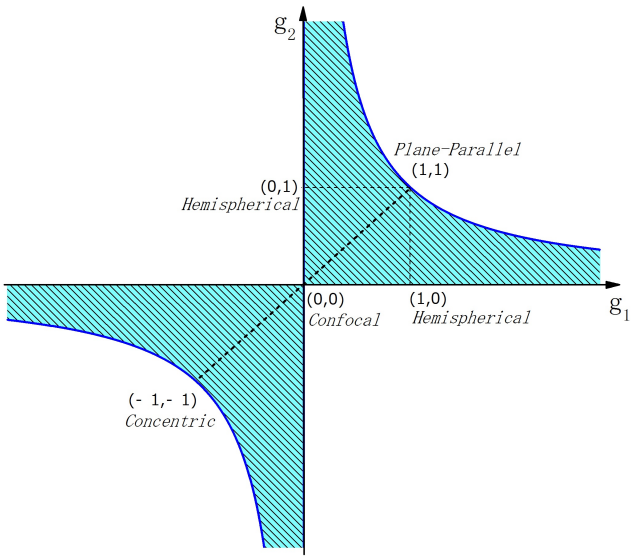

Figure 5.7: Resonator stability diagram with $g_1 = 1 - d/2f_1$ and $g_2 = 1 - d/2f_2$. The shaded area indicates the regions of stability, and various special configurations are indicated.

The stability diagram reproduced here shows particular different types of cavity configurations. In the case of same radius of curvature $r_c^{(1)} = r_c^{(2)} = r_c$, only the points on the line connecting concentric, confocal and plane-parallel configurations represent stability. Our cavity satisfies $r_c > d$ (where d is our cavity length L), so it lays in between the confocal and plane-parallel cases. This means that the beam inside the cavity will focus down by a certain amount at the cavity center (something that stops happening completely only when $r_c \to \infty$), defining the volume of the cavity, and therefore the optical potential depth (equation (4.9)), and optomechanical coupling (equation (4.33)). For the cavity used here, from the relation (8.30) of Appendix C, the cavity waist can be calculated to be $w_0 = 140.3 \pm 0.2\,\mu$m, bringing to a mode volume $V_c = \pi w_0^2 L \simeq 2.3 \times 10^{-9}\,\mathrm{m}^3$.

The choice of r_c and L is indeed important not just for light stability, but also for the prospect of trapping and cooling nanoparticles. Such parameters have been also chosen to guarantee enough space for the Paul trap which sits in the middle of the cavity, as described in section 5.5. At the same time, we wanted to test the behavior of the levitated system by using a low finesse first, given the facility of having off-the-shelf mirrors without any expensive custom mirror coating to be applied, and a less challenging Pound-Drever Hall locking implementation with a cavity linewidth which is not too small. In chapter 7 we will

see that our cooling results improve when using an higher finesse cavity with a smaller mode volume.

5.4.2 Cavity coupling

In the case of a real optical cavity we always need to take into account losses, given by the effects of absorption or scattering due to the imperfect surface of the cavity mirrors. We can lump these energy loss in a single coefficient l and write the mirrors reflectivities as $R = 1 - (T + l)$, where T is the mirror's transmittivity (see Appendix C). Because of this, together with the difficulty of completely fulfilling the mode matching conditions, even at resonance only a portion of the incident light will be coupled into the cavity. In this case the maximum total intensity transmitted by the cavity can be written:

$$I_T = I_0 \frac{T^2 (1 - 2l)}{(T + l)^2}, \tag{5.4}$$

where I_0 is the input intensity. To find the cavity coupling we can simply evaluate the ratio I_T/I_0, considering that the cavity finesse can be also defined [139]:

$$\mathcal{F} = \frac{\pi}{T + l},$$

so we obtain the expression:

$$I_T/I_0 = \varepsilon T^2 (1 - 2l) \left(\frac{\mathcal{F}}{\pi}\right)^2, \tag{5.5}$$

where a mode matching factor $0 \leq \varepsilon \leq 1$ is also introduced. As one can understand, the cavity coupling depends on the ratio between T and l. Having a reflectivity $R = 0.9998$, as in our case, means that the overall losses will be $(T + l) = 200\,\text{ppm}$. Unfortunately, T and l are not known separately, which means we cannot have a theoretical estimation of the maximum cavity coupling I_T/I_0 achievable. What we can do is to measure the experimental value, in the way explained further below in this section, once the alignment between the cavity and the input beams has been optimized.

What we know is that, when the mirrors parameters are such that on resonance no light is reflected from the input mirror, the resonator is said to be impedance matched [161]. The condition for impedance matching is simple: the input mirror intensity transmission T_1 must equal the sum of all other losses in the resonator, including the transmission of the other mirror as well as the total absorption and scattering losses of all the elements of the resonator:

$$T_1 = T_2 + l_1 + l_2. \tag{5.6}$$

Clearly, when the two mirrors are identical, this condition cannot be satisfied. The best one can do is to have mirrors with $l \ll T$, in which case the condition can be considered as satisfied.

The light power inside the cavity can be calculated from the input power P_{in} into the cavity (measurable with a power meter), which corresponds to an input intensity $I_0 = P_{\text{in}}/\pi w_{L/2}^2$. Here, $w_{L/2}$ is the beam radius at the input cavity mirror, being at a distance $x = L/2$ from the cavity waist, and expressed by equation (8.28) of Appendix C. We can then express the intracavity intensity:

$$I = I_0 \left(1 - \frac{\Delta_0/2\pi}{\text{FWHM}}\right) b \cdot C_p, \tag{5.7}$$

where $b = \mathcal{F}/2\pi$ is the number of bounces and C_p is the percentage of light coupled to the cavity. The latter can be measured experimentally looking at the light reflected by the cavity, as the laser is scanned across resonance, and calculate the ratio between the DC intensity level detected out of resonance, and the level reached by the intensity deep, visible every time the laser hits resonance. The cavity coupling depends on the mode matching (equation (5.5)), which we assume $\varepsilon \simeq 1$, and on the alignment between the laser beam and the cavity, so it can vary every time something in the setup gets changed or modified, and this implies realigning the cavity. The term in brackets, in equation (5.7), takes into account the detuning, which contributes as well to the level of intensity reached inside the cavity. Finally, the power circulating in the cavity, at the cavity waist, is:

$$P_c = I\pi w_0^2. \tag{5.8}$$

5.4.3 Thermal instabilities

When operating a cavity at high circulating intensities, another factor to take into account is the heating of the mirrors. The absorption loss from the cavity mirrors causes a heating effect at the dielectric-coated surface [137, 138]. The radius of curvature of the mirrors may change because of the thermal stress, affecting the cavity geometry and reducing its stability. First, the risk of damaging the mirrors has been studied in Ref. [138], and the incident intensity threshold for low-loss, high-reflectivity mirrors has been found to be higher than $100\,\text{MW/cm}^2$. Then, accurate measurements of the mirrors' radius of curvature were made by monitoring the FSR and the transverse mode range of the cavity, showing that the radius of curvature increases with the intensity on mirrors at a rate of $\simeq 105\,\mu\text{m}/(\text{MW/cm}^2)$, for ~ 6000 finesse cavity, in air. The main consequence of such an effect is a change in the cavity length with intracavity intensity, yielding to fluctuations in the resonance frequency. In order to keep the laser locked to resonance, one would need to provide a compensating

voltage through the cavity's PZT servo to keep the cavity length at a constant. In our experiment, a feedback control on the laser frequency, through both the PZT and thermal tuning ports, is used to lock the laser to the cavity resonance. This is able to compensate also for the slow frequency drifts that might be given by cavity length variations via heating of the mirrors.

5.4.4 Finesse measurements

To measure the finesse of our optical cavity we can use three different methods. Here we present an example of low finesse ($\mathcal{F} \sim 5,000$), taken from the earliest stages of the experiment, which allowed us to test and compare the three methods of measurement.

5.4.4.1 Sidebands technique

A simple procedure we can use to evaluate the finesse of the Fabry-Perot cavity is to use equation (8.26) of Appendix C, knowing the free spectral range of the cavity, and measuring its linewidth as the full width at half maximum of a transmitted intensity peak. In this example, we made use only of the weak beam, monitoring the light transmitted by the cavity with the help of a fast photodiode. By sending a voltage ramp to the fast tuning port of the laser, we can scan the laser frequency around a cavity mode of resonance (TEM_{00} in this case), and see in transmission a series of Airy peaks, as described in Appendix C, separated in time at a rate given by the ramp. The weak beam is also modulated in frequency by the EOM at 26.6 ± 0.2 MHz, for Pound-Drever-Hall, and this produces sidebands around each transmission peak. We can use the sideband separation to calibrate the timescale given by our oscilloscope, and then measure the FWHM of the main peak by performing a Lorentzian fit, as shown in figure 5.8.

For a sideband separation of 10.93 ms we have:

$$C = \frac{2 \times 26.6 \pm 0.2\text{MHz}}{10.93\text{ms}} = 4.786 \pm 0.001\ {}^{\text{MHz}}/_{\text{ms}}.$$

The Lorentzian fit represented in figure 5.8 gives a value FWHM(s) $= 143.32 \pm 0.04\,\mu$s, which corresponds to FWHM(Hz) = FWHM(s) $\times\, C = 0.697 \pm 0.006$ MHz. From here, the value of finesse results:

$$\mathcal{F} = \frac{\text{FSR}}{\text{FWHM}} = \frac{4.02 \pm 0.05\,\text{GHz}}{0.697 \pm 0.006\,\text{MHz}} = 5,762 \pm 80.$$

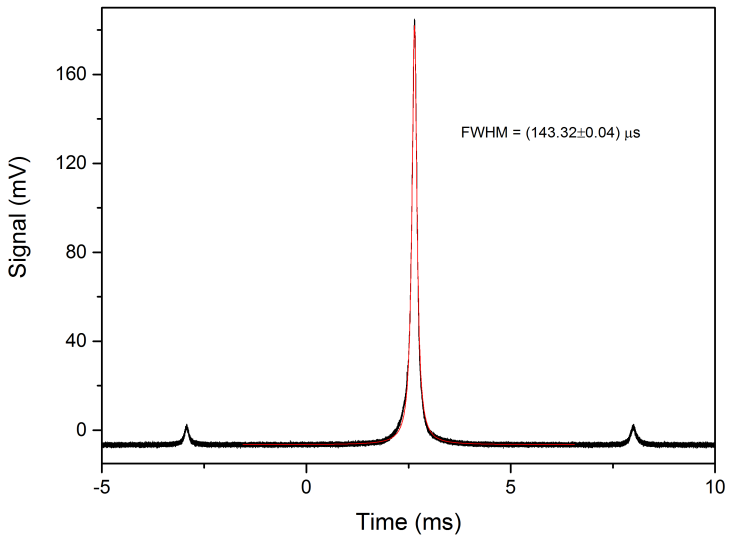

Figure 5.8: Lorentzian fit of the cavity transmission peak from the weak beam.

5.4.4.2 Ringdown

Probing the linewidth of the cavity transmission can be easily done if the optical resonator linewidth is much broader than the linewidth of the probe laser; if not, a direct measurement of the cavity decay is preferred. We can define the decay time of the cavity as [142]:

$$\tau = \frac{\mathcal{F}L}{\pi c}, \tag{5.9}$$

where L is the cavity length, $\mathcal{F}$ the cavity finesse and c the speed of light. The cavity decay can be measured by use of the decay or ring-down of the field inside the resonator. In the standard ring-down scheme [140] an electromagnetic field pulse is stored in the empty cavity, and the subsequent decay of the field is monitored in time. The duration of this excitation pulse should be much shorter than the cavity decay time, so that the excitation can be considered to be a delta function. One prepares the excitation field from a laser field by turning a shutter, which is often an acousto-optic modulator, on and off. Initially the shutter is opened, and the cavity is permitted to drift slowly toward resonance. At resonance a field builds up quickly in the cavity. When the cavity transmission signal reaches a certain threshold, the acousto-optic modulator is switched off, and the subsequent field decay is measured as a function of time. In [141, 142] they report a simpler and more powerful ring-down technique that requires neither a shutter nor a trigger circuit to turn the probe laser on and off at the right moment. Instead, they point out that if the cavity is quickly scanned, it is resonant with the probe for only a brief moment. This short resonance time effectively simulates a delta-function excitation. Now, the ringing effect that is obtained

is represented by an amplitude modulation in the decay curve that depends on the scan speed. In [141], the origin of this modulation is explained as the interference between the probe laser and the intracavity field. Since one of the mirrors is moving, the intracavity field, which built up when the cavity was resonant with the probe field, continuously shifts in frequency owing to the Doppler effect while its amplitude decays. Although the probe laser is no longer resonant with the cavity in a steady-state sense, it can still interact with the cavity field because of the finite transmittance of the mirror that it is incident upon. Since the probe and intracavity field have slightly different frequencies, a beating ensues. The exact same effect can be obtained if one scans the laser frequency instead, while keeping the cavity mirrors fixed. This is equivalent to modulating the cavity length, and for scan frequencies high enough a ring-down measurement can be performed.

To measure the decay time of our cavity we send a 20 kHz signal ramp to the fast tuning port of the laser, which allows us to see the ringing effect on each intensity peak of the transmitted weak beam, and to evaluate the decay time by fitting an exponential curve, as shown in figure 5.9.

Having a time decay $\tau = 0.207 \pm 0.006\,\mu$s, and making use of the relation (5.9), we find the value of the finesse:

$$\mathcal{F} = \pi \frac{\tau c}{L} = 5,230 \pm 150$$

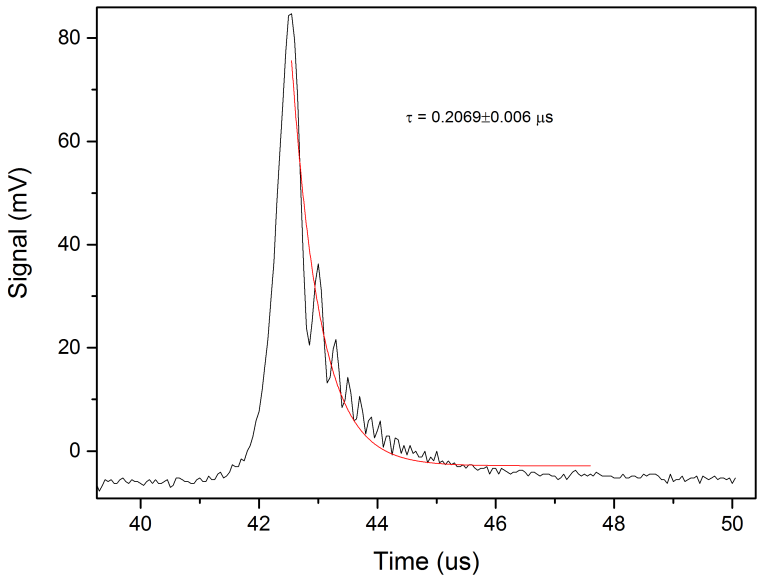

Figure 5.9: Intensity transmitted by the cavity from the weak beam, showing the ringing effect as the laser frequency is scanned around cavity resonance at 20 kHz. The decay time of the cavity can be measured via an exponential fit.

5.4.4.3 Scanning technique

In the third method we use to measure the cavity finesse, the laser is kept locked to the cavity resonance, and we make use of both the weak and the strong beam. While the former is locked via the PDH to the TEM_{00} cavity mode, the strong beam is scanned manually around resonance, by changing the voltage going to AOM_2, as described in section 5.3. By means of relation (5.2), we obtain the values of detuning, and we measure the corresponding values of the DC level of the intensity transmitted by the cavity (for the strong beam), and detected by a photodiode. For detuning $\Delta_0 = 0$ we have maximum transmission, and by moving to the blue ($\Delta_0 > 0$) or the red ($\Delta_0 < 0$) side of resonance we get the intensity Lorentzian profile, from which we extract the cavity linewidth (figure 5.10).

We fit the points with a Lorentzian function:

$$y = y_0 + \left[\frac{2A}{\pi} \frac{\text{FWHM}}{4\left(x - x_0\right)^2 + \text{FWHM}^2} \right], \tag{5.10}$$

which gives the value FWHM $= 766 \pm 6\,\text{kHz}$, and from here the finesse results: $\mathcal{F} = 5,248 \pm 70$.

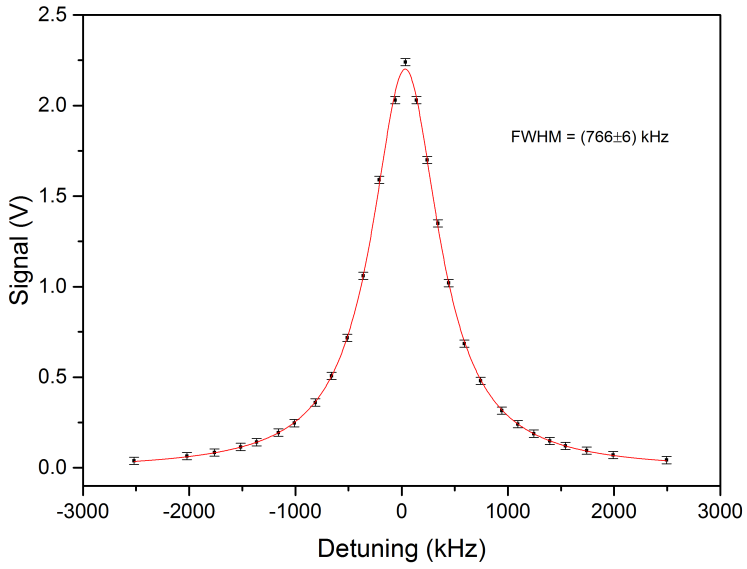

Figure 5.10: Intensity transmission signal as a function of the laser detuning. Red line represents the Lorentzian fit, from which the full width at half maximum of the cavity can be extracted.

During the course of the experiments, all three different methods have been used and interchanged, to check the consistency of the finesse obtained. We found that, according to the values of the finesse itself, some of the methods were more reliable than the others. In the case of low-medium finesse $(5,000 - 50,000)$ the ringdown method is the less precise, as

the ringing effect, and the cavity decay curve, are not easily observed. This is because the ringdown effect to be visible requires a high frequency signal modulating the laser, to beat the short decay time of the cavity, and this inevitably reduces the amount of signal detected in transmission by the photodiode. As a result, the exponential fit doesn't give an accurate value for τ. In the case of high finesse instead ($\gtrsim 50,000$), the Lorentzian peaks obtained with the sideband and the scanning methods show asymmetries, which can limit the precision of the Lorentzian fit. In the sideband technique case, one cannot often fully resolve the transmission peak when the cavity linewidth becomes too narrow. Furthermore, high circulating intensities attainable in a high finesse cavity cause thermal instabilities, due to the cavity mirror heating as already explained in section 5.4.3. In the scanning method this effect can affect the finesse measurement, as detuning variations, which bring to intracavity intensity variations, change the resonance condition such that the transmitted intensity is no longer symmetric around the initial value of resonance.

5.5 Paul trap structure

In our experiment, the Paul trap is a needle trap [143, 144] consisting of two metallic needles surrounded by a grounded electrode structure. In such traps, the curvature and distance between the needles crucially determine the confinement and the potential depth in both the radial and axial planes [143]. The advantage of a needle trap over 3D linear traps is the very open geometry. This means that high optical access is available for efficient interaction with a laser field, as well as collection of light scattered by the trapped particles. In our experiment, this feature is particularly useful as we want to couple the particle's motion to a cavity field, and at the same time monitor the particle's oscillations.

In theoretical investigations carried out prior to the presented work, 2D cross-sectional designs of the needle trap used in our experiment were made in SIMION. The potential and the electric field created at every point are generated and saved in PA (potential arrays) files.

Figure 5.11 shows a contour plot of the electric field in between the electrodes of our needle trap, by setting a voltage of 600 V peak to peak, and setting the distance between the electrodes to 1 mm, after importing the PA files to Mathematica. Clearly, the result looks different from the electric field contour proper of an ideal 3D Paul trap (see for instance [130]), where the hyperbolic electrode geometry gives rise to the exact quadrupole potential, presented in section 4.1.

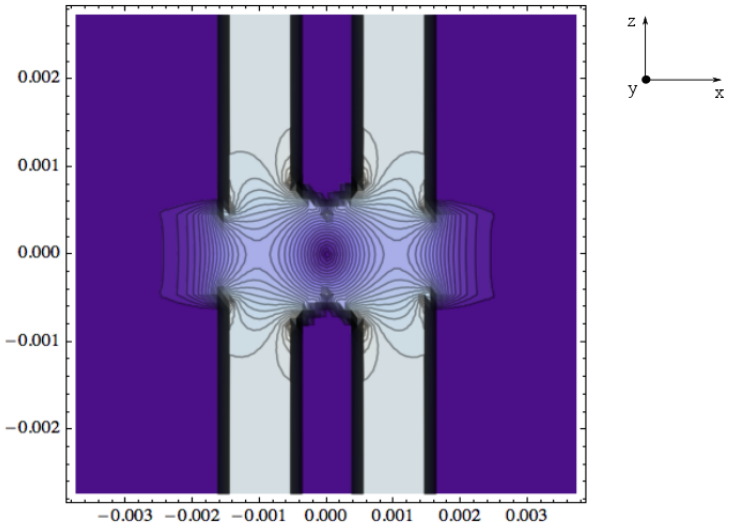

Figure 5.11: Contour plot of the electric field inside the needle trap used in this work, for a peak-to-peak setting of 600 V. Both the vertical separation (between the two pin electrodes) and the horizontal one (between each electrode and the corresponding cylindrical shield) are set to 1 mm.

To better see the difference between a pure parabolic potential and the potential given by our needle trap, we can plot in Mathematica the electric potential given by the SIMION simulation, to obtain the curves shown in figure 5.12. In both the x and z directions the potential deviates from the simple relation $V \propto x^2$ (and $V \propto z^2$), becoming wider as the nanosphere reaches larger excursions from its centre.

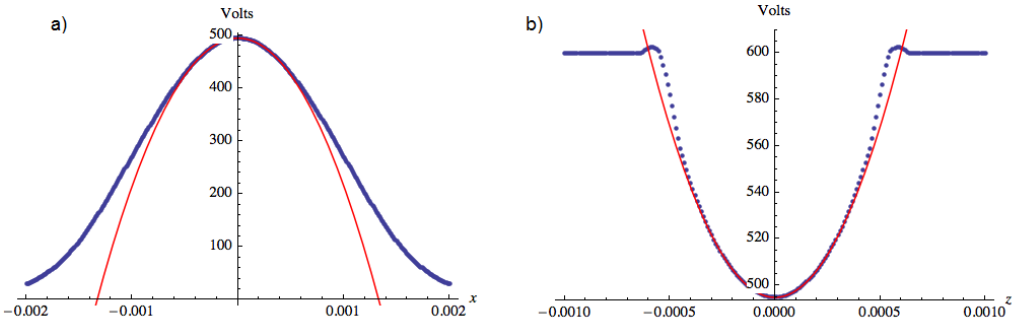

Figure 5.12: a) Model for the potential due to the Paul trap electrodes as a function of the displacement in the x-direction for a peak to peak voltage $V = 600\,\mathrm{V}$. The function $V(x) = 494.858 - 2.79384x^2$ is the fit that better represents the potential in this direction b) Paul trap potential as a function of displacement in the z-direction for a peak to peak voltage $V = 600\,\mathrm{V}$. The best fitting function in this case is $V(x) = 494.842 + 2.94176z^2$.

In literature [143, 144] normally an efficiency factor η, which ranges from $0.1 - 1$ in different traps, is introduced to account for the reduction in the trap confinement as compared to an analogous quadrupole trap with hyperbolic electrodes. η represents the ratio between the voltage required to obtain a given secular frequency, relative to the ideal Paul trap, and absorbs uncertainties in the effective trap dimension parameter r_0. In this way, the secular frequencies $\omega_s = \beta\frac{\omega_d}{2}$ (with β as in equation (4.7)), considering $a_u = 0$, true in our case,

become:

$$\omega_{\mathrm{s}}^{(u)} \propto \frac{QV_0\eta}{\mathrm{M}\omega_{\mathrm{d}}r_0^2} \tag{5.11}$$

The value of Q that can be inferred from ω_{s}, as it will be shown in section 5.7, is an effective charge for a trap where the efficiency is not accurately known.

5.5.1 Paul trap components

The needle Paul trap presented in this thesis consists of two electrodes formed by two rounded rods of 1.0 ± 0.1 mm in diameter, and angled ends, with a tip angle of $\simeq 110°$, enclosed by grounded cylindrical shields of 5.0 ± 0.1 mm in diameter and 1.0 ± 0.1 mm thick walls. The separation between each pin electrode and the corresponding shield is 1 mm, and they are isolated from one another with the help of a macor holder (figure 5.13). The two electrodes are held in place, facing each other at a distance of 1 mm, on an aluminum cylinder, as shown in figure 5.14.

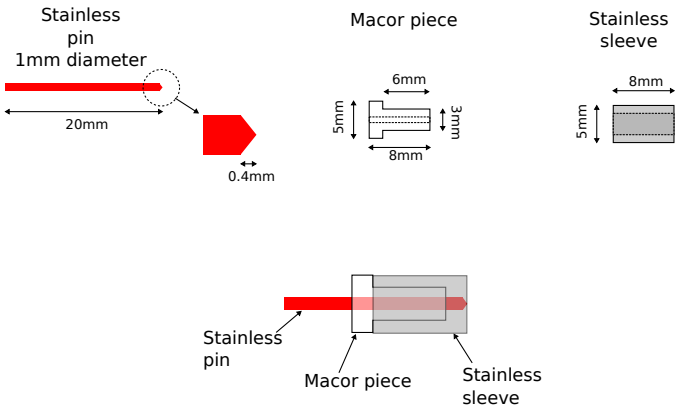

Figure 5.13: Schematic representation of the needle trap electrode components. A 1 mm thick stainless pin is enclosed by a cylindrical shield (sleeve), isolated with a macor piece and grounded to the rest of the chamber.

An rf voltage of $V_0 \cos(\omega_{\mathrm{d}} t)$, where V_0 is the amplitude of the time-varying signal ranging from $300 - 900$ V and $\omega_{\mathrm{d}} = 2\pi \times 1500$ Hz is its frequency, is applied to the electrodes. The 1.5 kHz sinusoidal signal is sent from a signal generator to a high voltage amplifier (Trek 2220), whose output reaches the inside of the vacuum chamber, where the Paul trap is located, via a feedthrough, and sent to the electrodes using two kapton insulated wires. One of the wires is then connected to the back of both rods, and the other one to the platform where the cylindrical holder sits on, for ground.

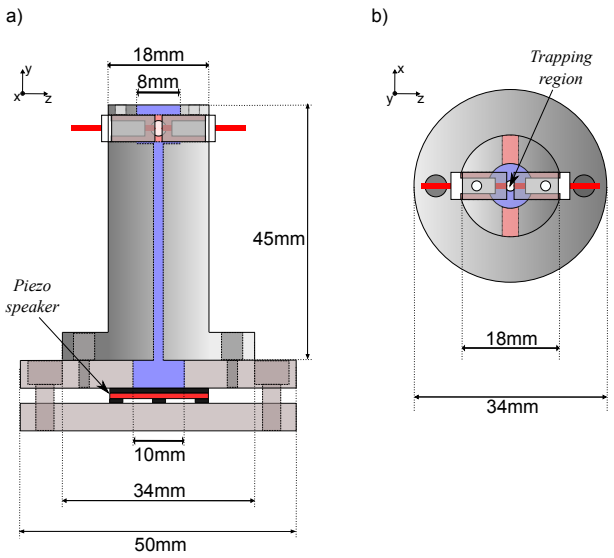

Figure 5.14: a) Side view of the Paul trap cylindrical holder. A 2 mm bore allows particles to travel from the bottom, where the speaker is located, to the trapping region at the top of the cylinder (see also figure 5.15). b) Top view of the Paul trap. The two pin electrodes are separated by a distance of 1 mm, and the laser light can travel through along the x direction.

5.5.2 Loading the Paul trap

To load the trap, a solution of nanoparticles (Corpuscular Inc.) and methanol is first sonicated using an ultrasonic bath for at least one hour to prevent clumping, and then slowly poured onto a 20 mm diameter piezo-disk speaker (VSB50EW-0301B Murata), placed underneath the Paul trap holder, as shown in figure 5.14a and figure 5.15. This transducer has a resonance frequency ranging between 800 Hz to 1 kHz, depending on how it is mounted, and a maximum voltage of 30 V. Two rubber rings are glued around the speaker's annulus, on both sides, and the speaker is placed and centered in between two aluminum plates at the bottom of the Paul trap cylindrical holder. Then, a few drops of solution can be poured from the 10 mm hole at the centre of the top plate. Once the methanol evaporates, the Paul trap holder is screwed on top, connecting in this way the particle reservoir to the trapping region at the top of the cylinder, via a 2 mm bore that goes all the way through the centre. The speaker is driven at about 1 kHz from a signal generator; this allows particles to be introduced into the trap, normally at a pressure of $\sim 5 \times 10^{-1}$ mbar. This pressure is chosen so that it is low enough that the trap voltages do not break down the remaining air between the electrodes (see section 5.6.1) , and high enough that the particles experience damping that allows them to be trapped. Despite sonication, as many particles are released by the piezo speaker at every attempt, often more than one sphere is trapped at the same time; an information that can be inferred from the relative intensity of the light scattered from the trapped spheres and also by the reduced stability of the particles in the trap when more than one particle is trapped.

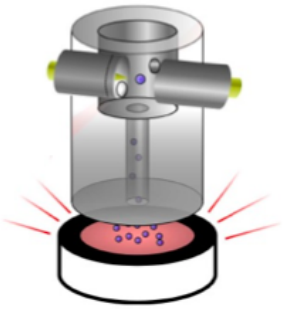

Figure 5.15: Schematic drawing of the loading process. A 20 mm diameter piezo transducer is covered in 200 nm nanoparticles in solution with methanol. When the latter evaporates, piezo is driven at $800 - 1000$ Hz with a signal generator, at a voltage of 20 V. This is enough to shake particles off the piezo's surface at pressures of $\sim 10^{-1}$ mbar, and let them reach the Paul trap, via the bore at the centre of the trap holder.

We found that by carefully reducing the amplitude of the voltage applied to the electrodes we are able to decrease the strength of the trap until only one sphere is left. We studied the trapping capabilities of our system for a long time before understanding the delicate equilibrium between the Paul trap voltage and frequency, surrounding pressure, and intracavity light intensity.

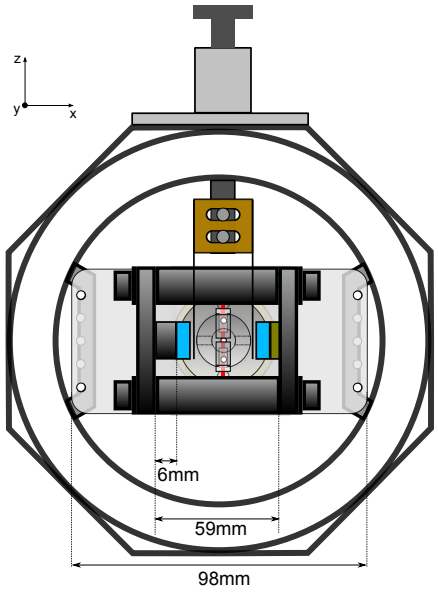

Figure 5.16: Top view representation of the trap. The optical cavity sits on an aluminum platform surrounding the Paul trap holder. To protect the mirror surfaces while loading the Paul trap, a copper shield can be pulled in and out via a linear positioner from the outside of the chamber.

To protect the mirrors from the particles sticking on their surface during loading, and prevent the cavity finesse to inevitably drop to low values, we use a copper shield, folded around the arm of a linear positioner (Lesker, KLPD series), as represented in figure 5.16. The shield, 69 mm long, can be controlled by hand from the back of the vacuum chamber, and it fits in between the mirrors and the Paul trap cylinder, at $\simeq 0.5$ mm distance from each side of the latter. A thin sheet of glass is also glued on top of the cylinder.

5.5.3 Positioning the trap

In order to avoid the cavity light field being blocked by the Paul trap holder, or clipped by the electrodes, the Paul trap structure is mounted on a remotely-controllable, vacuum compatible x-y-z translation stage. This is used to align it relative to the optical axis of the cavity. A fine control over the position of the Paul trap will also allow us to optimize the overlap between the electric and the optical field, to center the particle within the cavity waist, and eventually facilitate the optical capture by the cavity. Figure 5.17 represents a side view of the set-up, where the Paul trap is mounted on a translation stage at the bottom (Newport 6091 series), and it can be moved in the x-y-z directions by three actuators (Newport 8353-V, 0.5 in. picomotors), controlled via computer through a picomotor driver (New Focus 8742).

Figure 5.18 shows two photographs of the apparatus already described.

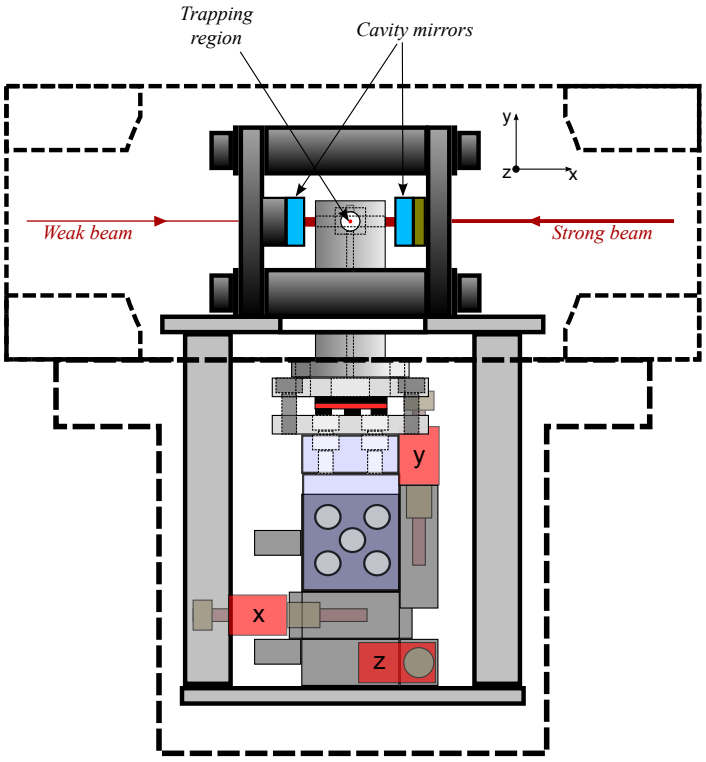

Figure 5.17: Side view representation of the trap structure inside the vacuum chamber. The cavity sits on a platform which surrounds the Paul trap holder, resting on two Viton feet glued on the two bottom rods. The Paul trap can be moved respect to the cavity axis in all three directions, by three picomotors controlled via software.

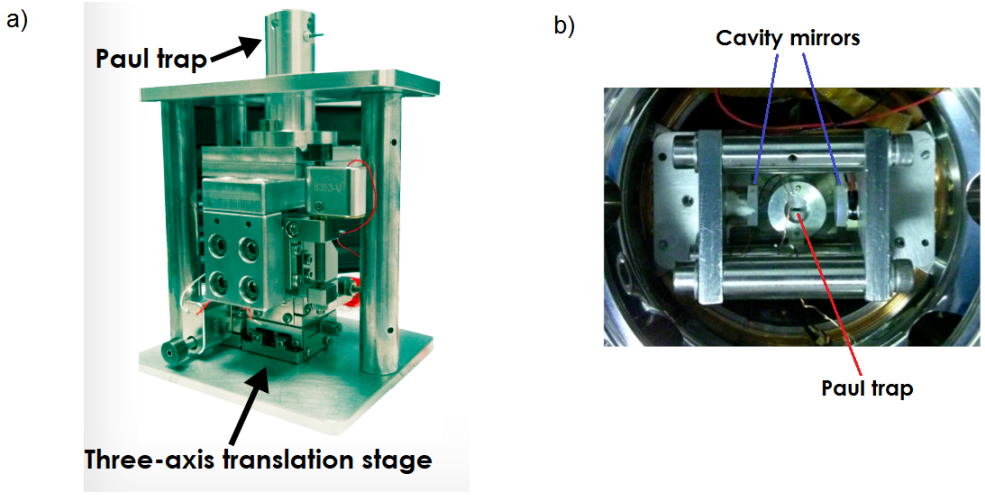

Figure 5.18: Two photographs of the experiment. a) Paul trap holder, mounted on a three axes translation stage, driven by three picomotors. An aluminum platform is fixed to the structure basis by three 12.7 mm long rods, fitting around the trap holder. b) Top view of the optical cavity, resting on the platform, with the Paul trap in the middle.

5.6 Vacuum system and stability

The optical cavity has been mounted inside a vacuum chamber for more than one reason. First of all, we want to improve as much as possible the mechanical quality factor of the nanoparticle. If we reduce the presence of air around the system, we limit the energy loss, usually suffered by a damped oscillator. Secondly, the refractive index of air, and so the optical length of the cavity, can change in time because of thermal agitation, creating fluctuations in the optical index and modifying the interference conditions inside the cavity. Furthermore, external acoustic noise could reduce the stability of the laser locking conditions, by perturbing the position of the two mirrors. Finally, we need to ensure an environment where dust will not be present to limit the performance of the optical components of the cavity.

The vacuum system that we use in our experiment is created by an automatic turbo pump station (Pfeiffer Vacuum HiCube 80 Eco) which consists of a roughing pump and a turbo. The former is a diaphragm pump (MVP-015-2), which operates from atmospheric pressure down to the fore-vacuum pressure (typically around 1mBar), at which the turbomolecular pump takes over. The ultimate pressure for the system we use is reported by manufacturers to be $< 1 \times 10^{-7}$ mbar.

The simple vibration from the turbo pump, which is directly connected to the vacuum chamber, is able to unlock the cavity, which can't be relocked without kicking the particle

away from the trap, unless the input power from the strong beam is kept low enough ($\lesssim$ 100 mW, depending on the pressure). This effect has been reduced by introducing a vibration damper (Pfeiffer PM006800X), and a valve that can isolate the system from the pump at the desired pressure, allowing it to always run at nearly 100% speed, where vibrational frequencies are high enough to leave locking unperturbed.

Not only light intensity, but also the voltage applied to the Paul trap can't be varied without taking into account the values of pressure, given the risk of air breakdown (see next section). Only below $\simeq 10^{-1}$ mbar voltages can be increased above 800 V. Knowing all these features, the system finally showed a very stable and consistent behavior, allowing us to even turn off the Paul trap and transferring particles to a pure optical trap, provided a stable locking, until pressures of 4.6×10^{-1}mbar.

5.6.1 Air breakdown

Application of an electric field of strength E between two electrodes can cause an electric discharge, i.e. a sudden presence of electric current in the system. This is also known as the point of electrical breakdown. In 1889 Friedrich Paschen published what is known as the Paschen's Law [145, 146], to describe the breakdown process:

$$V_{\mathrm{B}} = \frac{Bpd}{\ln(Apd) - \ln(\ln(1 + 1/\gamma))}. \tag{5.12}$$

The breakdown voltage V_{B} between two electrodes is a function of pd, the product of the pressure p inside the chamber and the distance d between the electrodes. The key parameters in the breakdown process are the electron-neutral cross section σ, the ionization potential V_i, and the secondary electron emission coefficient γ. In equation (5.12) the first two parameters are contained in the constants $A = \frac{\sigma}{k_B T_n}$ and $B = AV_i$, where T_n is the temperature of the neutral atoms and k_B is the Boltzmann constant.

To understand the physical process behind the Paschen's Law consider a vacuum chamber in which breakdown has not yet occurred. There may be several free electrons in the chamber due to the external ionizing sources such as cosmic rays. If a voltage is applied to the electrodes, a free electron will begin to accelerate towards the anode. If the gas is sufficiently dense, the electron may collide with a neutral atom, causing ionization. The resulting positive ion accelerates towards the cathode: when it collides with the electrode, there is a finite probability (γ) that a secondary electron will be emitted. This secondary electron may in turn ionize more neutrals: the positive ions that result will stream towards the cathode. If each electron, on average, creates enough ions to release at least one additional secondary electron from the cathode, the process becomes self-sustaining, and breakdown occurs. For

$A = 1.5\,\mathrm{mTorr}^{-1}\,\mathrm{m}^{-1}$, $B = 36\,\mathrm{V/mTorr}\times\mathrm{m}$ and $\gamma = 0.02$, which are typical values of air at room temperature using stainless steel electrodes, equation (5.12) leads to the plot shown in figure 5.19.

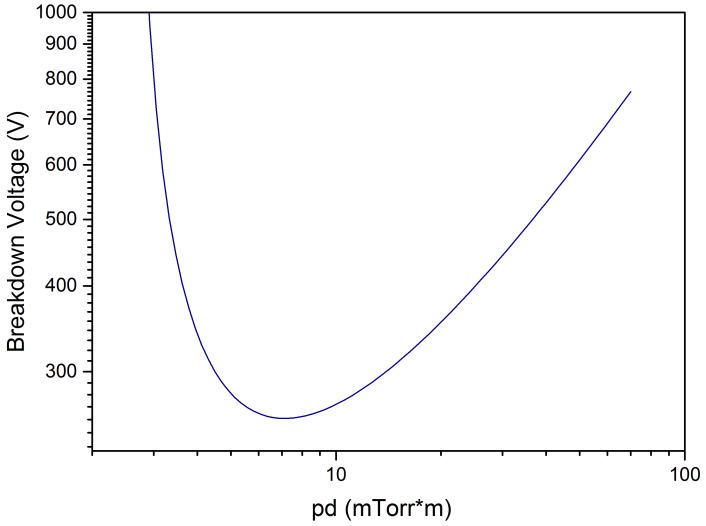

Figure 5.19: Paschen curve for typical values in air: $A = 1.5\,\mathrm{mTorr}^{-1}\mathrm{m}^{-1}$, $B = 36\,\mathrm{V/mTorr}\times\mathrm{m}$ and $\gamma = 0.02$.

To the left of the minimum, the breakdown voltage decreases with increasing *pd*. Here the gas is not very dense or the electrodes are very close; thus, even if a large number of secondary electrons are emitted, there is a low probability that any will collide with neutral atoms during the journey from the cathode to the anode. As *pd* increases, collisions are more likely, and therefore breakdown voltage is lower; thus the Paschen curve has a negative slope in this region. When *pd* increases beyond the curve minimum, collisions may be too frequent rather than too rare. In this regime, an electron on its way to the anode may collide so frequently that a larger input voltage is required for it to build up enough energy to ionize a neutral atom. The electron-neutral collision frequency and thus the voltage required increases with *pd*, explaining the positive slope of the Paschen curve at large *pd*.

The above discussion describes the breakdown process generally obtained using a uniform DC electric field. In our experiment though, we use an AC electric field to drive the Paul trap, and the driving frequency is also a variable that we might need to take into account in the gas discharge process. As we keep the driving frequency always constant, together with the electrodes separation, what we are interested in for the purpose of this thesis is the relation between the amplitude V_0 of the voltage that we can apply to the electrodes and the pressure inside the vacuum chamber, in order to avoid air breakdown. For a complete description of the similarities and differences between high-frequency field discharges and the DC-type of breakdown the reader can refer to [147].

In figure 5.20 we plot the values of the voltage amplitude V_0 sent to the Paul trap electrodes,

that generate breakdown inside the chamber, as a function of the pressure (values are reported in table 5.1). Each value of the breakdown voltage corresponds in our experiment to a visible distortion of the signal sent to the Paul trap, and shown by the oscilloscope. This was found to be the critical event that makes our nanoparticles to be lost by the trap, and that we need to avoid. The theoretical curve used for the data fit is of the form:

$$y = \frac{B(x+C)}{\ln(Ax+C)}, \tag{5.13}$$

where the distance between the electrodes is constant, $d = 1\,\text{mm}$.

Pressure (mbar)	Breakdown voltage amplitude (V)
0.0083	2000
0.03	830
0.064	560
0.34	400
0.74	370
1.4	340
2.5	350
6.3	370
7.4	400

Table 5.1: Values of the voltage amplitude applied to the Paul trap electrodes, generating breakdown, as a function of the pressure inside the chamber.

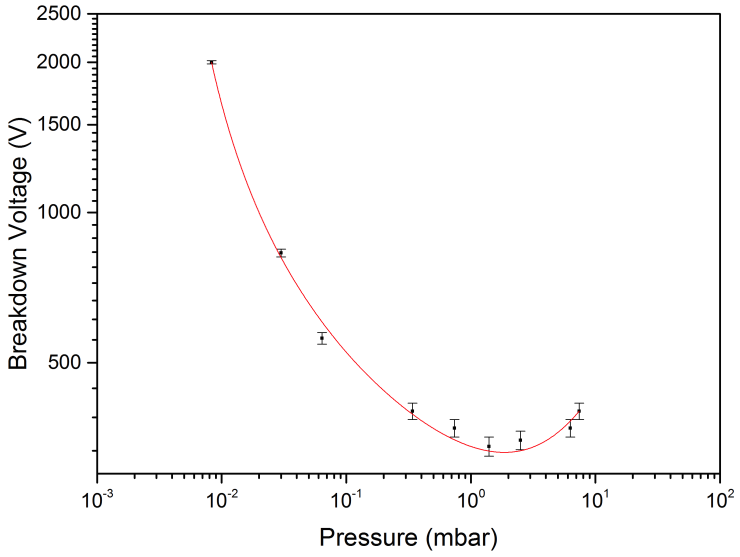

Figure 5.20: Breakdown voltages as a function of the pressure inside the vacuum chamber. Red curve represents the Paschen law, as written in equation (5.13).

The main information we are interested in is the maximum amplitude voltage that we can apply to avoid breakdown while a particle is trapped. In particular, near the pressure normally used for loading the trap ($10^{-1}\,\text{mbar} < p < 10^{0}\,\text{mbar}$) we found that the amplitude must always be $V_0 \leq 300\,\text{V}$.

5.7 Particles detection

To check if any particle has been loaded into the Paul trap, we can illuminate the cavity with one or both laser beams and collect the scattered light using a CMOS camera (Thorlabs DCC1645C), placed on top of a zoom macro lens (Navitar Zoom 7000) or a microscope (Navitar Zoom 6000), looking from the top window of the vacuum chamber, as explained in section 5.1. The ability to move the Paul trap in 3 dimensions respect to the cavity axis allows us to optimize the position of the particle respect to the cavity waist and maximize the amount of light scattered by the bead. Furthermore, the zoom is mounted on a translational stage, to center the camera on the particle and collect all of the scattered signal. Figure 5.21 shown an example of two different particles trapped.

In figure 5.21a one can clearly see the Paul trap electrodes with a particle levitating in the middle, and part of the Paul trap holder. The image in figure 5.21b) instead, was taken with a tighter zoom, using the microscope, and shows the particle inside the Paul trap, oscillating along the cavity axis.

To monitor the motion of the nanosphere in time, we replace the camera with an amplified photodiode (InGas temperature controlled PDA10DT-EC) and send the scattered signal S to the oscilloscope.

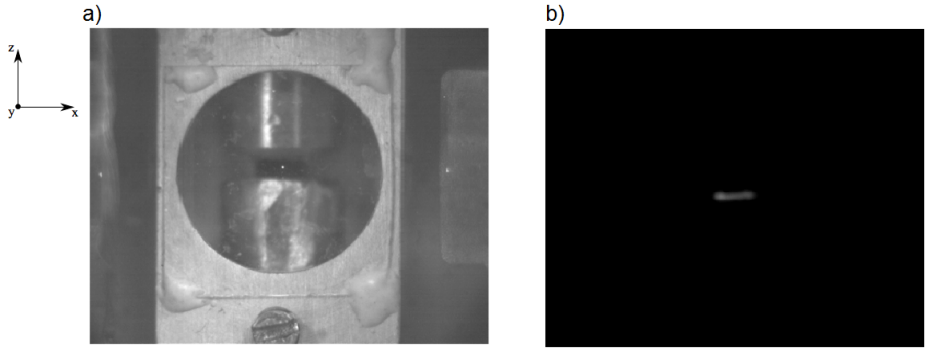

Figure 5.21: Photos of two particles trapped. a) Levitated particle appears as a white dot in the middle of the Paul trap electrodes, and it is illuminated by the intracavity light from both beams locked on resonance, at a pressure $p \sim 10^{-1}$ mbar. One of the cavity mirrors is also visible on the right side of the Paul trap. b) Photo of a nanoparticle oscillating along the cavity axis at pressure $p \simeq 4 \times 10^{-2}$ mbar, taken with the microscope.

5.7.1 Secular and micromotion

We can use only one laser beam (the weak beam) locked to the TEM_{00} mode of resonance to analyze the scattered signal, and characterize the motion of the particle in the Paul trap potential. The amount of circulating power inside the cavity is evaluated by using equations (5.7) and (5.8): for an input power $P_{\mathrm{in}} = 5\,\mathrm{mW}$, a finesse $\mathcal{F} \simeq 15,000$, and a measured cavity coupling $C_p \simeq 50\%$, the intracavity power is $P_{\mathrm{c}} \simeq 4\,\mathrm{W}$.

For the experimental parameters obtained above, the light scattered by the particle at a pressure $p = 6 \times 10^{-4}$ mbar, and collected with the photodiode, through the microscope, is the one represented in figure 5.22. A 5 seconds trace has been recorded with the oscilloscope (figure 5.22a), and it shows a rapid modulation given by the particle's oscillations in the trap. By taking the Fourier transform of that signal two main peaks, related to the secular motion, can be observed (figure 5.22b). At the same time, the micromotion at 1.5 kHz can be detected, along with a series of sidebands corresponding to the secular frequencies.

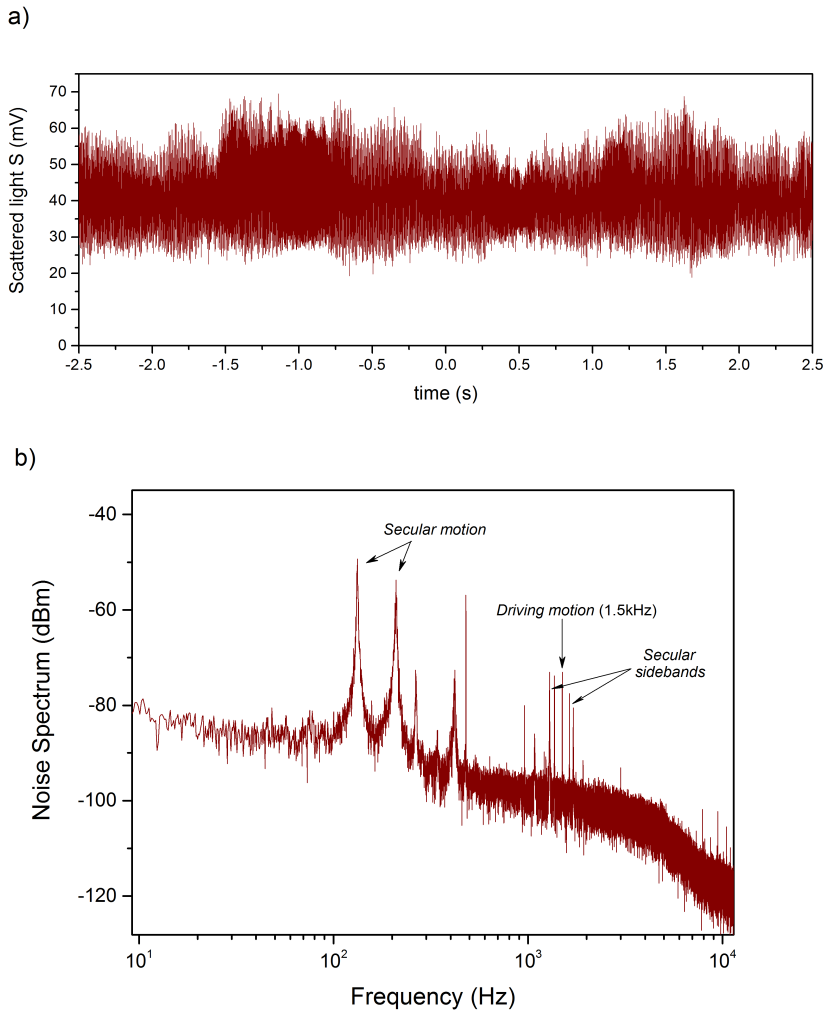

Figure 5.22: a) Time series of the light from the weak beam, scattered by a nanoparticle oscillating in the Paul trap. b) Corresponding power spectrum, in logarithmic scale, showing peaks associated to the Paul trap secular and driving motions.

We can better analyze the spectral features by moving to a linear scale, converting the dBm values on the y-axis into Volts, using the definition:

$$y\,[\mathrm{dBm}] = 10\log_{10}\frac{Power}{1\mathrm{mW}} = 10\log_{10}\frac{V_{rms}^2/50\Omega}{1\mathrm{mW}}, \tag{5.14}$$

where V_{rms} is quadratic mean of the voltage, and $50\,\Omega$ the input impedance of the oscilloscope. We also want the resulting data to be normalized in frequency, since the average

value of the total noise power is measured within a certain resolution bandwidth, which determines how close in frequency two different signals can be, and still be resolved into two separate peaks. Thus, we essentially move to the power spectral density (PSD), which is simply average noise power per unit of bandwidth. To do this, we divide our dBm data by the frequency separation between two adjacent points of the frequency axis. We thus perform the unit conversion, using equation (5.14):

$$y\left[\mathrm{V}^2/\mathrm{Hz}\right] = 0.05 \cdot 10^{\frac{y[\mathrm{dBm/Hz}]}{10}}. \tag{5.15}$$

From figure 5.23 we can measure the values of the two secular frequency components $\omega_{\mathrm{s}}^{(x,y)} = 2\pi \times 130\,\mathrm{Hz}$, and $\omega_{\mathrm{s}}^{(z)} = 2\pi \times 209\,\mathrm{Hz}$. In the same way, they can be evaluated in figure 5.23b, as they appear as a set of sidebands, centered around the driving frequency $\omega_{\mathrm{d}} = 2\pi \times 1.5\,\mathrm{kHz}$.

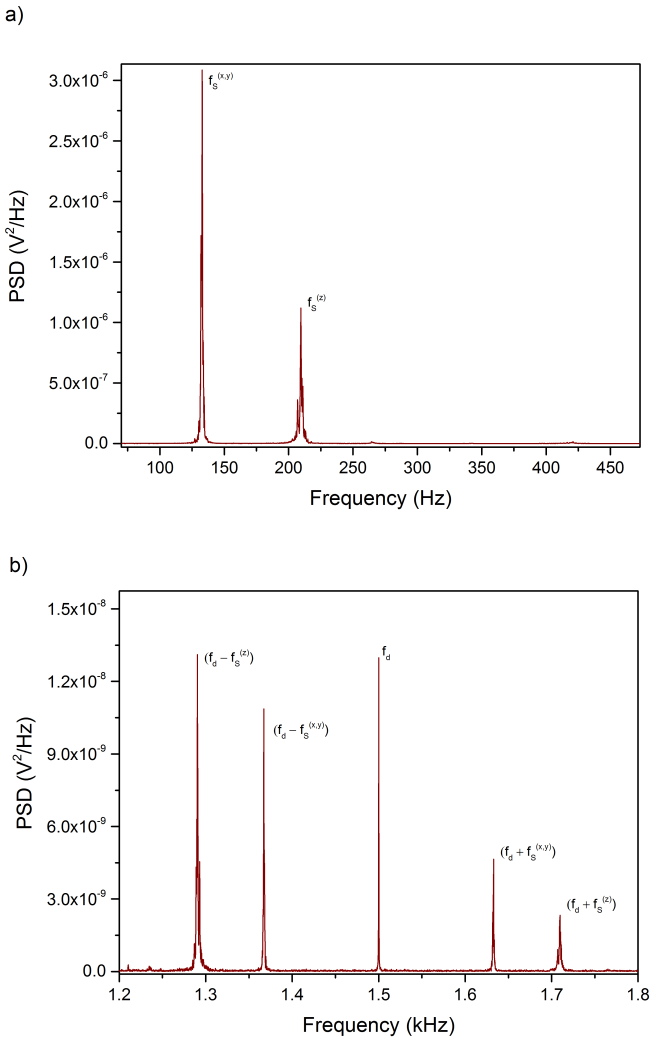

Figure 5.23: Linear spectrum of the particle's motion in the Paul trap. a) (x,y) and z components of the secular motion. b) Secular frequencies, appearing as sidebands of the driving frequency peak.

5.7.1.1 Secular frequencies vs Voltage

It is interesting to observe how the secular frequency peaks, shown in figure 5.23, shift as a function of the voltage amplitude sent to the Paul trap electrodes. Following the definitions given in section 4.1, and recalling that in our experiment $U_0 = 0$ (and therefore $a_u = 0$), we can express the secular frequencies in terms of voltage amplitude V_0 and driving frequency:

$$\begin{aligned} \omega_{\mathrm{s}}^{(x,y)} &= \frac{\omega_{\mathrm{d}}}{2}\sqrt{\frac{\left(q_{x,y}\right)^2}{2}} = \frac{2}{\sqrt{2}}\frac{QV_0}{\mathrm{M}\omega_{\mathrm{d}}r_0^2}, \\ \omega_{\mathrm{s}}^{(z)} &= \frac{\omega_{\mathrm{d}}}{2}\sqrt{\frac{\left(-2q_{x,y}\right)^2}{2}} = \frac{4}{\sqrt{2}}\frac{QV_0}{\mathrm{M}\omega_{\mathrm{d}}r_0^2}, \end{aligned} \tag{5.16}$$

where the mass of the particle $\mathrm{M} = \rho \cdot V = 7.36 \times 10^{-17}\,\mathrm{kg}$ (with density of silica $\rho = 2198\,\mathrm{kg/m^3}$, and volume of the nanosphere $V = 3.35 \times 10^{-20}\,\mathrm{m}^3$), and $r_0 = 0.5\,\mathrm{mm}$. In table 5.2 we report the different values of the secular frequencies as a function of the voltage amplitude. The first two values of the $\omega_{\mathrm{s}}^{(z)}$ component are missing as the corresponding peaks are masked by noise and not clearly visible in the spectrum.

V_0 (V)	$\omega_{\mathrm{s}}^{(x,y)}/2\pi$ (Hz) ($\pm$2Hz)	$\omega_{\mathrm{s}}^{(z)}/2\pi$ (Hz) ($\pm$2Hz)
134	59.6	/
200	72	/
304	105	144
400	130	209
508	156.5	260
598	182	320
720	221	420

Table 5.2: Values of the secular frequencies as a function of the voltage amplitude in the Paul trap. The driving frequency is constant, $\omega_{\mathrm{d}} = 2\pi \times 1.5\,\mathrm{kHz}$.

Nonetheless, we can plot the values as a function of V_0, and fit the data with the lines given by equations (5.16), from which we can extract the value for the charge Q. Figure 5.24 shows the linear behavior of the x and z components, with a resulting value of the charge $Q \simeq 2.24 \times 10^{-19}\,\mathrm{C}$ for the first one, and $Q \simeq 2.6 \times 10^{-19}\,\mathrm{C}$ for the second one, which can be approximated as a number of free charges on the nanosphere $Q/e \sim 1$.

The errors in the charge value given by the fit don't take into account the possible deviations from the theoretical values of M and r_0 (given by the electrodes distance), but those can be included in the efficiency factor η introduced in equation (5.11). The latter can be evaluated in average, using the experimental measurements presented, from the ratio between each voltage V_0 used, and each value of the ideal voltage $V_{ideal} = \omega_{\mathrm{s}}\omega_{\mathrm{d}}\mathrm{M}r_0^2/\sqrt{2}Q$ needed to obtain the measured secular frequencies, where we assume $Q/e = 1$, meaning $Q \simeq 1.6 \times 10^{-19}\,\mathrm{C}$. The result we obtain is $\eta = V_0/V_{ideal} \simeq 0.6$.

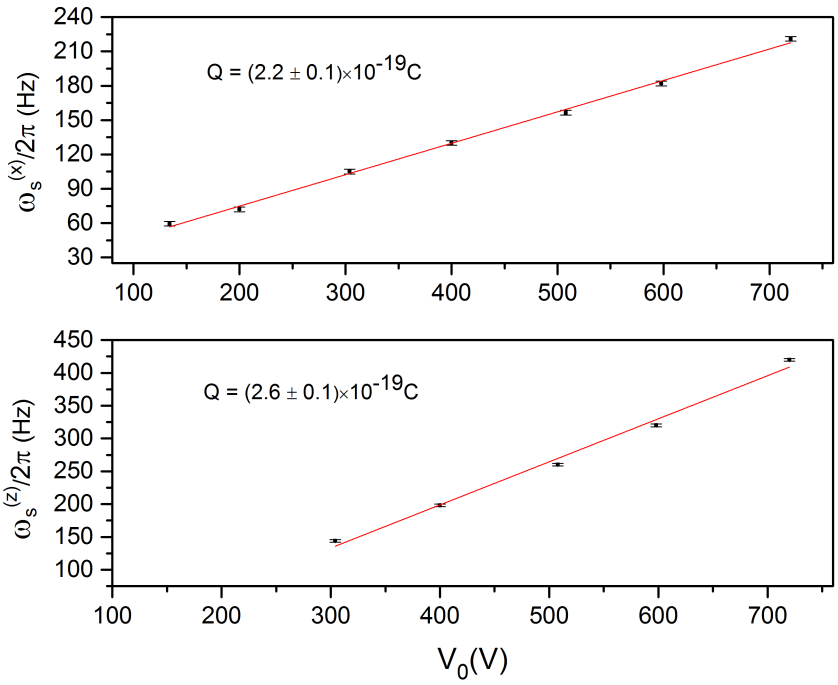

Figure 5.24: First and second components of the secular motion as a function of the voltage amplitude. The values of the charge given by the linear fits suggest a number of free charges $Q/e \sim 1$.

5.7.1.2 Secular frequencies vs Driving frequency

In the same way as previous paragraph, we can observe the behavior of the secular frequency, keeping a constant voltage and varying the driving frequency. Data are fitted once again using equations (5.16), with a fixed voltage $V_0 = 400$V, and we expect now a trend $\omega_s \sim 1/\omega_d$. We report on table 5.3 the value of the secular components as a function of $\omega_d/2\pi$.

$\omega_d/2\pi$ (Hz)	$\omega_s^{(x,y)}/2\pi$ (Hz) ($\pm$2Hz)	$\omega_s^{(z)}/2\pi$ (Hz) ($\pm$2Hz)
1200	159	290
1300	149.9	260
1400	140.5	231
1500	132	210
1600	125	190
1700	121	174
1800	115	160
1900	111	148

Table 5.3: Values of the secular frequencies as a function of the driving frequency in the Paul trap. Voltage is kept constant at $V_0 = 400$ V.

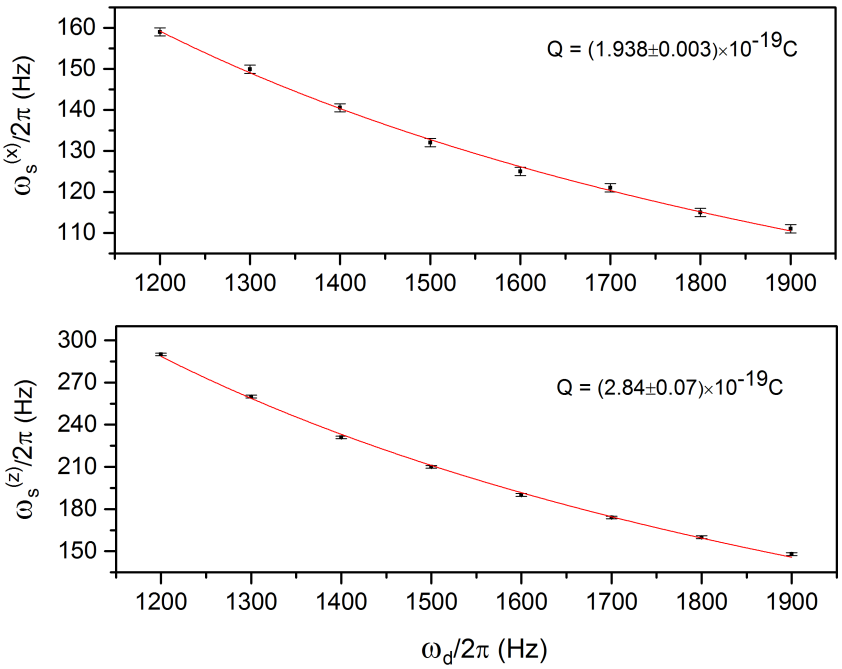

Figure 5.25: First component of the secular motion, as a function of the driving frequency.

Plots are given in figures 5.25, showing that both components follow the trend of equations (5.16). Considering the voltage used and the different values of the secular frequencies, the same result is obtained for the efficiency factor $\eta \simeq 0.6$.

5.8 Heating rates of particle's motion

In this section we show how to evaluate the nanoparticle's response to heating due to an on-resonant beam, at low pressures. To this purpose, we make use of the weak beam, locked via the PDH method to the fundamental cavity TEM_{00} mode, where the input power has been reduced to $P_{\mathrm{in}} = 0.2\,\mathrm{mW}$. The Paul trap's voltage amplitude and frequency are kept at constant values of $V_0 = 300\,\mathrm{V}$ and $\omega_{\mathrm{d}}/2\pi = 1.5\,\mathrm{kHz}$. In such a configuration, any heating that occurs in the particle's motion is mainly due to recoil effects and absorption and scattering of light by the nanosphere.

In order to make measurements of the heating of the nanosphere as a function of time, a microscope has been attached to the top of the vacuum chamber, allowing for video recording of the nanosphere's motion. These measurements consisted of allowing the on-resonant laser beam to enter the cavity and consecutively initializing the video recording. This allows one to directly see the nanosphere's orbit in the hybrid trap growing in displacement from the centre of the trap, until it reaches a point of instability and leaves the trap. Using MATLAB's image processing tools, the increase in displacement from near-equilibrium can be directly

found as a function of heating time. Lines of maximum excursion can nicely be detected using Hough transformations, which present themselves as a valuable tool for this kind of measurement [148]. This type of analysis has been carried out with the help of a UCL student, during his Master's project in our laboratory.

Two sets of data have been taken at pressures $p = 5 \times 10^{-5}$ mbar and $p = 4.6 \times 10^{-6}$ mbar, and in both cases the plots shown in figures 5.26 and 5.27 clearly exhibit that the heating rates are exponential. The best fits are summarized in table 5.4.

Pressure (mbar)	Time constant (s)	Heating rate (Hz)
5.0×10^{-5}	51.0 ± 5	0.0196 ± 0.0022
4.6×10^{-6}	17.9 ± 0.4	0.0559 ± 0.0012

Table 5.4: Heating rates of the nanosphere's motion for heating processes induced by the weak PDH laser beam at two different pressures. They correspond to the exponential fits in graphs 5.26 and 5.27 respectively.

When the pressure in the vacuum chamber is low, the damping due to the surrounding gas is less significant than at higher pressures. This prediction is clearly shown in the heating rates determined by the exponential fits, as heating is 35.4% faster at the pressure of 4.6×10^{-6} mbar than at one order of magnitude higher.

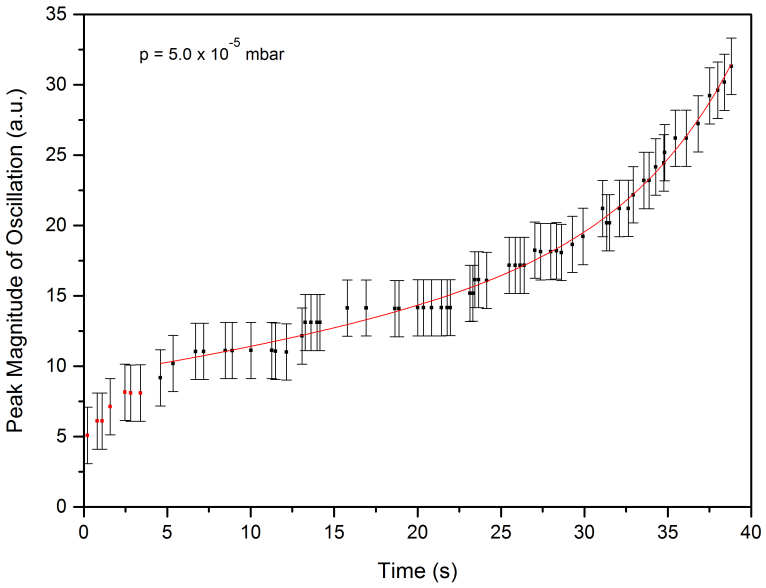

Figure 5.26: Heating of nanosphere using the weak PDH beam at a power of 0.2 mW and a vacuum chamber pressure of 5.0×10^{-5} mbar. The exponential function $f(t) = Ae^{\frac{t}{\tau_1}} + Be^{\frac{t}{\tau_2}}$ is fitted with parameters $A = 9.25$ a.u., $\tau_1 = 51.0$ s, $B = 0.0192$ a.u. and $\tau_2 = 6.11$ s. The points where $0 < t < 5$ have been excluded from the fit.

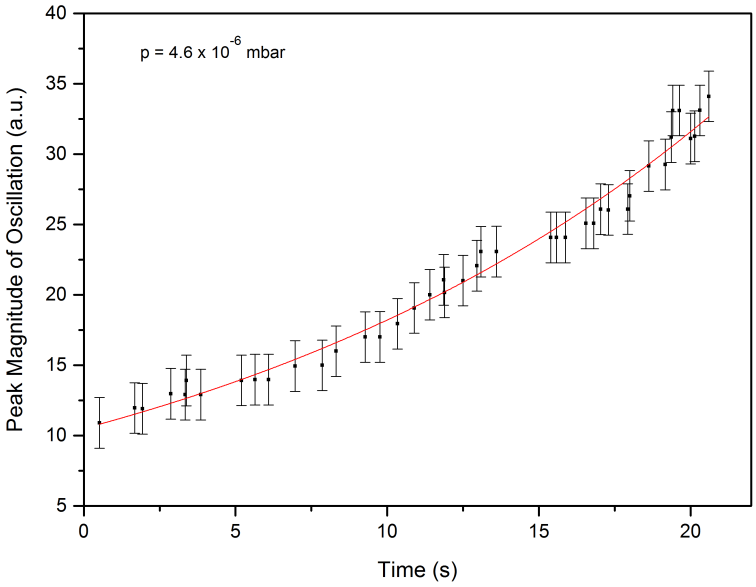

Figure 5.27: Heating of nanosphere using the weak PDH beam at a power of 0.2 mW and a vacuum chamber pressure of 4.6×10^{-6} mbar. The exponential function $f(t) = Ae^{\frac{t}{\tau}}$ is fitted with parameters $A = 10.5$ a.u. and $\tau = 17.9$ s.

5.9 Mechanical damping rates of particle's motion

In a standard optomechanical system, the mechanical resonator can be approximated as a damped harmonic oscillator, interacting with a thermal bath, as described in section 3.1.2. In this case, a mechanical peak of frequency ω_M can be observed in the power spectrum of the signal describing the position of the oscillator over time (i.e. light scattered by the object in the case of a levitated nanoparticle, or the light transmitted by the optical cavity after interacting with the mechanical resonator). Having a Lorentzian peak as the one in figure 3.2, means that one can evaluate the mechanical damping rate Γ_M by measuring the FWHM of the peak, and from there find the mechanical quality factor Q, from the relation (1.2).

In the hybrid system presented in this thesis, the periodic excursions in the mechanical motion given by the Paul trap, as described in section 4.3, lead to broadening of the mechanical frequencies, in a way that will become clear in next chapter. This fact prevents us from estimating the mechanical damping rate in the way described above, and another method for the experimental determination of Γ_M, and hence Q-factor, has to be devised.

In order to make a measurement of the gas damping rate, the nanosphere is heated up using a heating process similar to the ones studied in section 5.8. Once the oscillation has grown to approximately its maximum from the centre of the cavity, the path of the laser beam has then been blocked and unblocked at five different time intervals to see the evolution of

its oscillation. It is important to note that this measurement has been conducted with the on-resonant strong beam at a power of 1 mW. The weak beam's mode has been changed to the TEM_{10} mode, such that it does not feel the modulation by the nanosphere, and it is therefore only used as the frequency reference for the strong beam through the PDH locking and phase-locking schemes (the latter will be the subject of section 8.3).

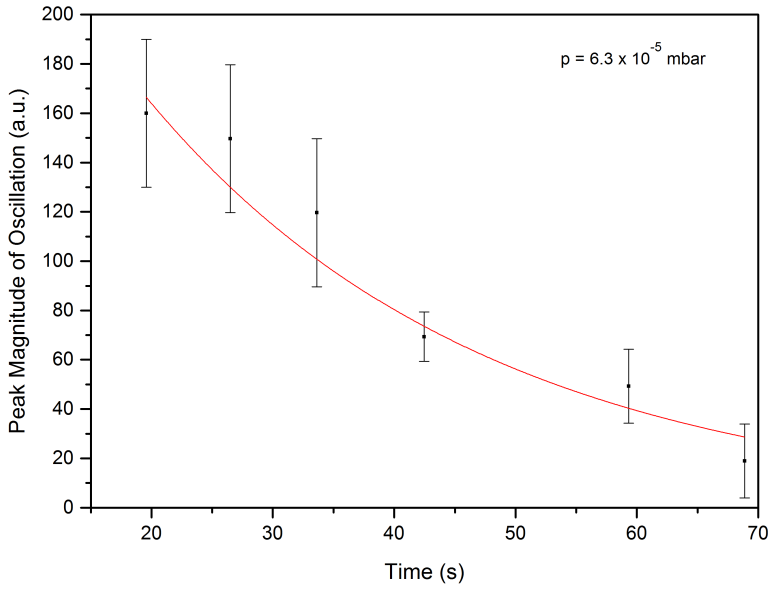

Figure 5.28: Peak-to-peak amplitude of oscillation as a function of time at the pressure of 6.3×10^{-6} mbar. The nanosphere's motion is naturally decaying due to background gas damping. The exponential function $f(t) = Ae^{-\frac{t}{\tau}}$ with parameters $A = 334.7$ a.u. and $\tau = 29.8$ s has been found as the best fit.

From figure 5.28 we can determine a value of the damping rate and mechanical Q-factor of the system. The time constant of the decay has been found to be $\tau_M = (29.8 \pm 6.2)$ s, which corresponds to a damping rate of $\Gamma_M = (0.034 \pm 0.007)$ Hz. To find the reference value of the central mechanical frequency $\bar{\omega}_M$, we can red-detune the strong beam by $\Delta_0 \simeq \kappa/2$ using the same input power $P_{in} = 1$ mW, and let the particle cool and localize on a single optical well. The value for the mechanical frequency is found to be $\bar{\omega}_M \simeq 2\pi \times 13$ kHz. Using this, the mechanical Q-factor at the pressure of 6.3×10^{-6} mbar is found to be $Q \approx (2.4 \pm 0.5) \times 10^6$. The accuracy and precision of this measurement are very limited, since the strong beam heats the nanosphere in a matter of a few seconds, in the same way observed for the weak beam in previous section. Thus, every time the laser probes the nanosphere in order to make it visible to the microscope and camera, the nanosphere gains a fraction of energy from the light. Therefore the uncertainties on the values found in this section must be larger than given by the fitting errors of around 20%. In order to check how accurate the fit really is, the fitting can be done separately for all consecutive points in figure 5.28, which,

in theory, should be the same. By doing this, the systematic uncertainty that arises from the laser giving some energy to the nanosphere every time the beam is unblocked to take the measurement should be eradicated. This is done by applying the following equation for an exponential decay time constant to successive points $(t_i, f(t_i))$ and $(t_{i-1}, f(t_{i-1}))$:

$$\tau_i = \frac{t_i - t_{i-1}}{\ln\left(\frac{f(t_{i-1})}{f(t_i)}\right)}. \tag{5.17}$$

Table 5.5 shows the individual exponential decay parameters of the individual points. The first two values that have been extracted using the first three points of figure 5.28 have been omitted as the uncertainties were too large. The uncertainties are relatively large as these points have been extracted manually from the video images, rather than using the previously employed Hough transformation techniques in MATLAB.

Time constant (s)	Damping rate (Hz)
9.54 ± 2.74	0.105 ± 0.030
25.6 ± 13.3	0.039 ± 0.020
11.0 ± 3.6	0.091 ± 0.030

Table 5.5: Exponential damping parameters for the damping rate measurement at a pressure $p = 6.3 \times 10^{-6}$ mbar for consecutive points in figure 5.28. The first two sets of parameters are not shown as the uncertainty is too high for a conclusive result, therefore only three sets are displayed.

These can be averaged to give values of $\tau_{\mathrm{M}} = (15.4 \pm 4.7)\,\mathrm{s}$ and $\Gamma_{\mathrm{M}} = (0.065 \pm 0.020)\,\mathrm{Hz}$. The corresponding Q-factor for a mechanical frequency of $\omega_{\mathrm{M}} = 2\pi \times 13\,\mathrm{kHz}$ is $\mathrm{Q} = (1.3 \pm 0.4) \times 10^6$ at $p = 6.3 \times 10^{-6}\,\mathrm{mbar}$. These values are more reasonable than the ones found by the direct fit in figure 5.28, as the heating effect of the laser has been compensated for. Considering equation (2.1), the theoretical value one obtains for the mechanical damping, at room temperature and pressure $\sim 10^{-6}\,\mathrm{mbar}$, is $\Gamma_{\mathrm{M}}^{(theo)} \simeq 0.015\,\mathrm{Hz}$. Therefore, the experimental value $\Gamma_{\mathrm{M}} = (0.065 \pm 0.020)\,\mathrm{Hz}$ obtained in our measurement appears to be a sensible result at a pressure of $6.3 \times 10^{-6}\,\mathrm{mbar}$.

The unwanted heating effects of the laser while probing the nanosphere for this measurement made the method used inaccurate. An alternative option for future measurements of greater precision would be to turn off the Paul trap and have the nanosphere trapped purely by the laser beams during optomechanical cooling. This would lead to a much more well-defined mechanical frequency peak in the signal's power spectrum, allowing for a direct measurement of the mechanical damping rate.

Chapter 6

Cavity cooling in the hybrid trap

This chapter presents the cooling results obtained by using the experimental setup described in chapter 5. To observe the dynamics and characterize the cooling of a single particle, we measure the scattered light S as the nanosphere passes through the standing wave field. This provides a measurement of particle position as a function of time. Free motion of the particle produces a rapid modulation as the particle moves through many antinodes of the standing wave cavity field. Here, the trajectory of the nanoparticle is well parametrized by the Paul trap secular and micromotion frequencies. However, when a particle is trapped and cooled it oscillates around a single antinode, as described in chapter 4, with a mechanical frequency $\omega_{\mathrm{M}} \simeq 2\pi \times 18\,\mathrm{kHz}$.

Analyzing the power spectral density of the particle's motion, we demonstrate a factor of 100 cavity-cooling when the laser light is detuned by a value of the order of the cavity linewidth, $\Delta_0 \simeq -\kappa$, with a cooling rate $\Gamma_{\mathrm{opt}} \approx 30\,\mathrm{Hz}$.

6.1 Particle's motion via scattered light

The full dynamics described in section 4.3 can be observed experimentally when using both the weak and strong beam, and when a detuning between them is applied. Free motion and captured motion are very well distinguishable as we measure the nanoparticles position as a function of time, by detecting the scattered light S coming from the strong beam. Cooling or heating of the nanoparticles motion are also observed depending on the value of the detuning, and the pressure inside the vacuum chamber.

The effect of two different detunings on the dynamics of a trapped nanoparticle is shown in figure 6.1. The red trace is taken for light that is red detuned by approximately the value of the cavity linewidth ($\Delta_0 \simeq -\kappa$), at a pressure of $7.4 \times 10^{-3}\,\mathrm{mbar}$. This trace clearly shows an interchange between periods of free motion in the Paul trap, and regions where

the nanosphere is captured in the optical potential (marked by the arrows). The latter are characterized by an increase in the mean scattered light, as the particle is localized near an antinode of the cavity standing wave. Captures can last up to 0.3 s. After this time they escape the optical potential due to noise in the light field, which is sufficient to kick them out of the well (a situation we have confirmed with simulations), as both the optomechanical coupling G_1 and the optical potential $A\hbar\,|a|^2$ (see section 4.2) are very weak. On the other hand, for blue detuned light ($\Delta_0 \simeq \kappa$) at the same pressure, the trace doesn't show any capture, with a constant mean scattered light intensity, as this detuning leads to heating of the particles motion.

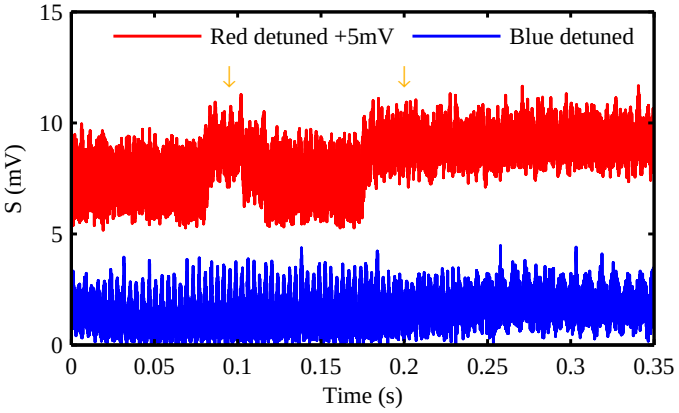

Figure 6.1: The effect of detuning Δ_0 from the cavity resonance on the nanospheres motion scattered light signal S, at a pressure of 7.4×10^{-3} mbar with $\Delta_0 \simeq \pm\kappa$, where κ is the cavity linewidth [36]. When the light is red detuned from the cavity resonance (upper red trace, signal offset for clarity) there are periods of free motion in the Paul trap, and regions where the nanosphere is captured in the optical potential (marked by arrows), with a cooling rate depending upon the location within the optical standing wave. The nanosphere is not captured by the optical potential when the light is blue detuned from the cavity resonance (lower blue trace).

A clear difference in the behavior of a single particle in the case of blue and red detuning could also be seen using the camera, as shown in figure 6.2. To have a clear view on the particle's motion, normally the zoom and the focus on the microscope were changed respect to the photodiode case. By properly adjusting the camera parameters, such as the frame rate, we were able to see a continuos growth of the nanoparticle's oscillations for the blue detuned case, visible in particular along the cavity axis (figure 6.2a). This trend would only be counteracted by the surrounding gas damping, leading in a matter of a few seconds to either a constant amplitude, or to sudden particle loss at lower pressures ($\lesssim 10^{-4}$mbar). In the red detuned case (figure (6.2b) the photo is taken at a moment of optical capture, where the particle looks well localized and the amount of scattered light is higher compared to the blue detuning case. Both photos represent the same particle, trapped at a pressure of 4×10^{-2}mbar.

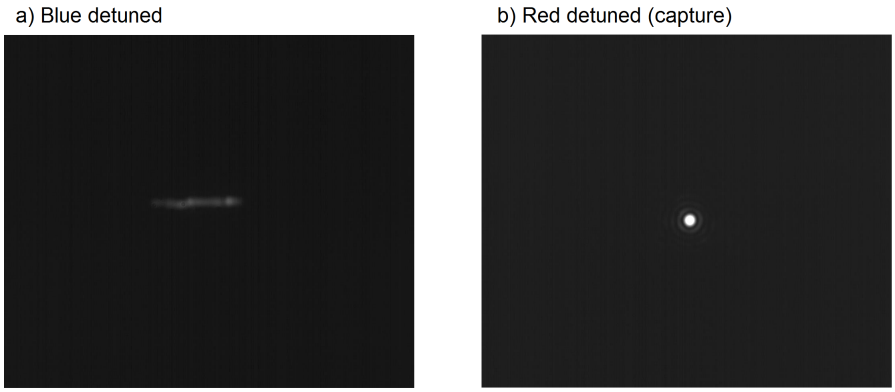

Figure 6.2: Comparison between blue and red detuning, in the case of a particle trapped at a pressure of 4×10^{-2}mbar.

6.2 Blue detuning

When light is blue-detuned, the motion of the nanosphere is heated by the optical cavity field. With an optical field alone the particle would be driven out of the optical trap. Although the nanoparticle is driven out of the optical field it is still trapped by the Paul trap potential. The nanoparticle is heated along the cavity axis x, and this motion is also coupled to the radial directions y,z. There is a strong modulation in S due to the motion in the y,z directions, as the particle is driven entirely out of the optical field, and then brought back into the optical field by the Paul trap. This type of motion is observed in the experiment, as shown in figure 6.3, with a frequency at twice the secular frequency ω_s, and confirmed by our simulations.

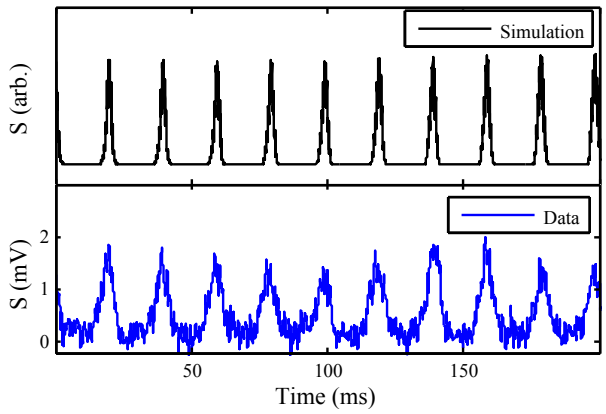

Figure 6.3: Simulated and measured modulation of the light scattered by the levitated nanosphere, when the light is blue detuned by $\sim \kappa/2$ from the cavity resonance. The nanosphere is heated out of the optical field by the light, and periodically driven back into the light field by the Paul trap with a frequency set by the secular frequency ω_s.

6.3 Red detuning and cooling

By looking in more detail at the free motion (fig. 6.4a) we see how a rapid modulation in the scattered light S, as the particle passes through many antinodes of the standing wave cavity field, alternates with turning points of motion (marked by arrows). The power spectral density of the nanosphere's motion in this regime (fig. 6.4b) shows how the trajectory can be well parametrized by the Paul trap secular $\omega_s = 2\pi \times f_s$ and micromotion $\omega_d = 2\pi \times f_d$ frequencies, despite the presence of the optical field.

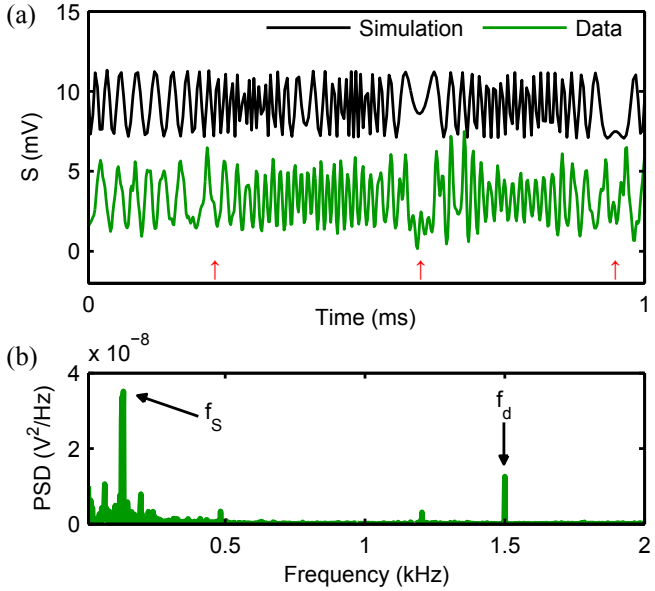

Figure 6.4: Free motion in the Paul trap. a) The scattered signal S as the Paul trap drives the nanosphere across the optical standing wave, with a simulation showing the predicted dynamics. b) The corresponding power spectral density showing a secular frequency at $\sim 100\,\mathrm{Hz}$ and the micromotion frequency at $1.5\,\mathrm{kHz}$. Measurement of f_s allows readout of the charge, in this case just a single charge $Q/e = 1$ [36].

Figure 6.5 instead, shows the capture and initial cooling process for a nanosphere at a pressure of $4.6 \times 10^{-4}\,\mathrm{mbar}$. In this trace the initial rapid modulation is followed by a dip in intensity as the particle is trapped. The particle then starts to undergo a well defined motion in the optical well, showing period doubling as the Paul trap causes asymmetric oscillations about the optical antinode. The average scattered light intensity increases as the nanosphere is cooled towards the optical antinode. In this case the motion from the Paul trap is still present and marked by arrows.

As explained in section 4.3, to quantify the cavity cooling we consider the motion of the nanoparticle within one well of the optical potential $x'(t) = x(t) - x_N$. Within the optical potential a mechanical frequency ω_M can be defined, which depends upon the depth of the optical potential, $A\hbar\,|\alpha|^2$, and which well, N, of the standing wave the particle is confined to.

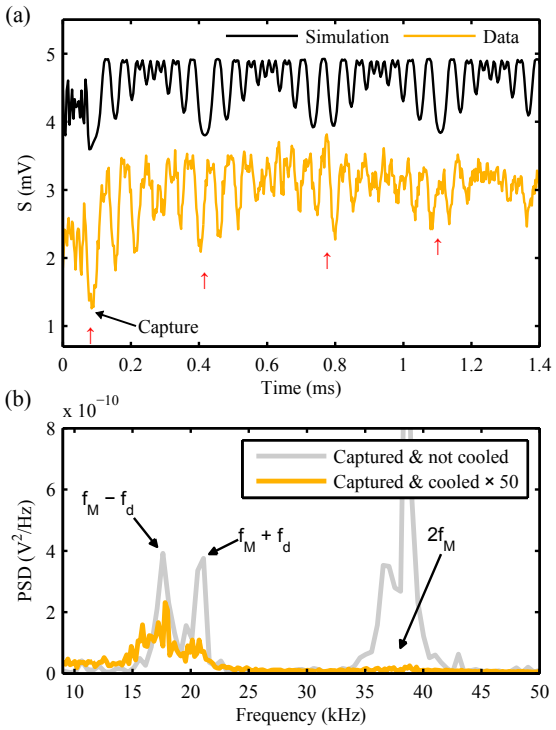

Figure 6.5: Capture and optomechanical cooling of a nanosphere. a) The scattered signal S once the nanosphere has been captured, at a pressure of 4.6×10^{-4} mbar, and a simulation of the process. b) Corresponding power spectral density (in V^2/Hz units) showing peaks at the mechanical frequency $f_\mathrm{M} \pm f_\mathrm{d}$ and doubled frequency $2f_\mathrm{M}$. At a pressure of 7.4×10^{-3} mbar (grey line) mechanical damping from the background gas dominates and the nanoparticle is not cooled, as shown by the unsuppressed peak at $2f_\mathrm{M}$. At a lower pressure of 4.6×10^{-4} mbar (orange line), the doubled frequency is heavily suppressed. [36].

Since $\omega_\mathrm{M} \gg \omega_\mathrm{s}, \omega_\mathrm{d}$ the motions due to the optical and Paul trap potentials are adiabatically separable; as $t \to \infty$ we approximate the motion along the optical axis by $x'(t) \sim X_\mathrm{d} \sin(\omega_\mathrm{d} t) + X_\mathrm{M}^\infty \cos(\omega_\mathrm{M} t)$ (equation (4.26)). The drive amplitude X_d is largely undamped. X_M^∞ is the steady-state amplitude of the mechanical motion; initially $X_\mathrm{M}(t)$ decays as $\sim e^{-\Gamma_\mathrm{opt} t}$ but tends to a steady-state value determined by noise heating processes.

By analyzing the Fourier spectrum of the captured nanosphere motion one finds, to leading order, frequencies at $\omega_\mathrm{M} \pm \omega_\mathrm{d}$ with amplitude A_1, and a single peak at $2\omega_\mathrm{M}$ with amplitude A_2. This will be further explained in the next section, 6.4. These amplitudes are related to the amplitude of the motion of the nanosphere, such that, in the limit of small amplitude oscillations:

$$\frac{A_2}{A_1} \to \frac{X_\mathrm{M}^\infty}{X_\mathrm{d}}.$$

Thus, the relative amplitudes of the Fourier peaks A_1, A_2 provide a means to estimate the steady state amplitude X_M^∞ and thus enable an estimate of the equilibrium temperature of the nanosphere. In particular, if there is strong cooling, we have $X_\mathrm{M}^\infty / X_\mathrm{d} \to 0$, resulting in the suppression of the second harmonic ($2\omega_\mathrm{M}$) peak in the spectrum. Thus we expect that those traces for which the second peak is weak or nearly absent correspond to the strongest

cooling. In this case, we estimate the reduction in temperature from:

$$\frac{T_{\rm eq}}{T_{\rm int}} \sim \left[\frac{X_{\rm M}^{\infty}}{X_{\rm M}(t=0)}\right]^2,$$

where $T_{\rm int}$ corresponds to an initial temperature which we can choose to define either as the height of the optical well or of a bath at $T = 300\,\mathrm{K}$, while $T_{\rm eq}$ is our final equilibrium temperature. The motion of the nanoparticle is cooled to $\sim 10\,\mathrm{K}$, which represents a factor of ~ 100 reduction in energy from the well depth $A\hbar\left|\alpha\right|^2$. Figure 6.5 b) also shows that at a pressure of $7.4\times10^{-3}\,\mathrm{mbar}$ (grey line) the damping due to the background gas is $\Gamma_{\rm M} \sim \Gamma_{\rm opt}$, hence no cooling is evident and $A_2 > A_1$. At a pressure of an order of magnitude lower, where $\Gamma_{\rm opt} > \Gamma_{\rm M}$ (orange line), both the capture and subsequent cooling are dominated by optomechanical damping and there is a significant reduction in the size of A_2. The width of peaks is due to the excursion of the nanosphere into the anharmonic regions of the optical potential.

Finally, provided one allows for slow excursions in the equilibrium point, the optomechanical damping rate $\Gamma_{\rm opt}$ can be evaluated using equation (4.31):

$$\Gamma_{\rm opt} = \bar{G}_1^2\kappa\left[S(\omega_{\rm M}) - S(-\omega_{\rm M})\right],$$

where $\bar{G}_1$ represents the optomechanical coupling strength, as derived in section 4.4.1, and $S(\omega) = \left[(\Delta_{x_0} - \omega)^2 + \kappa^2/4\right]^{-1}$. For the case of the levitated system investigated here, the effective optomechanical coupling is such that, for the experimental parameters used in figure 6.5 ($\mathcal{F} \simeq 15000$, $\Delta_0/2\pi = 288\,\mathrm{kHz}$, intracavity power $P = 14\,\mathrm{W}$, $\omega_s = 2\pi\times100\,\mathrm{Hz}$), we find $\Gamma_{\rm opt} \approx 20 - 30\,\mathrm{Hz}$, where the capture is at a well position $\mathrm{N} = kx_{\rm N}/\pi \sim 600 - 700$. The mechanical damping is $\Gamma_{\rm M} \simeq 1\,\mathrm{Hz}$, at $4.6\times10^{-4}\,\mathrm{mbar}$ pressure, thus the expected equilibrium temperature (from equation (3.36)) is:

$$T_{\rm eq} = \frac{\Gamma_{\rm M}}{\Gamma_{\rm M}+\Gamma_{\rm opt}}T \sim 10\,\mathrm{K}. \tag{6.1}$$

6.4 Analysis of the experiment

The intensity of the scattered light field from a point particle is proportional to the term $S = \cos^2\left(kx'(t)\right)\mathcal{L}(y,z)$. The experiment uses spheres of radius $\mathrm{R} \simeq 200\,\mathrm{nm}$. For the transverse motion, the sphere dimensions are small relative to the beam waist $w_0 \simeq 130\,\mu\mathrm{m}$ so a point particle approximation is quite reasonable. However, this is not the the case in the axial direction given the standing wave potential for $\lambda/2 = 532\,\mathrm{nm}$. A previous study of the effect of the particle size on the optical coupling parameter A [70] showed that the

behavior R = 200 nm remains qualitatively similar to a point dipole particle. Nevertheless, for accuracy, here we convolve the scattering function with a sphere of finite size in our simulations and calculate for our scattering function [36]:

$$S(t) = \bar{S}(t)\mathcal{L}\left(y(t), z(t)\right), \tag{6.2}$$

where:

$$\begin{aligned} \bar{S}(t) &= \frac{1}{2} - \frac{3}{16\left(k\mathrm{R}\right)^3}\cos\left(2kx'(t)\right)\left[2k\mathrm{R}\cos\left(2k\mathrm{R}\right) - \sin\left(2k\mathrm{R}\right)\right] \\ &= \frac{1}{2} + C\left(k\mathrm{R}\right)\cos\left(2kx'(t)\right). \end{aligned} \tag{6.3}$$

The Fourier transform of the scattered field, yielding the frequency spectrum of scattered radiation, allows us to extract the characteristic frequencies of the motions. $\mathcal{L}\left(y(t), z(t)\right)$ is modulated at the lowest frequencies (of order 100 Hz) by the transverse secular frequencies $\omega_{\mathrm{s}}^{(y)}$ and $\omega_{\mathrm{s}}^{(z)}$; Fourier transforms of traces of the order of several seconds show these clearly, as in figures 5.22 and 6.4.

We focus now on Fourier transforms of the trapped regions, dominated by the mechanical and drive frequencies. The scattered signal in frequency space may be calculated using equations (4.26) and (6.3), and is given by:

$$\bar{\mathbf{S}}(\omega) = C(k\mathrm{R})\sum_{(m,n)}(-1)^l J_m\left(2kX_{\mathrm{M}}^{\infty}\right)J_n\left(2kX_{\mathrm{d}}\right)\delta\left[\omega - (m\omega_{\mathrm{M}} + n\omega_{\mathrm{d}})\right], \tag{6.4}$$

where $m + n = 2l$, $l \in \mathbb{Z}$, while peaks with $m + n = 2l + 1$ are absent from the spectrum. The relative amplitude of the peaks (m, n) and (m', n') in the spectrum is:

$$\mathcal{A}_{rel} = \frac{J_{m'}\left(2kX_{\mathrm{M}}^{\infty}\right)J_{n'}\left(2kX_{\mathrm{d}}\right)}{J_m\left(2kX_{\mathrm{M}}^{\infty}\right)J_n\left(2kX_{\mathrm{d}}\right)}.$$

If $X_{\mathrm{M}}^{\infty} \ll X_{\mathrm{d}} \lesssim (1/k)$ then $\mathcal{A}_{rel} \sim \frac{\Gamma(m+1)}{\Gamma(m'+1)}\left(kX_{\mathrm{M}}^{\infty}\right)^{m'-m}$, leading to an exponential reduction of higher order peaks (here Γ is the Gamma function).

Inspection of equation (6.4) shows that the dominant terms in the spectrum involving the mechanical frequency are:

$$C(k\mathrm{R})^{-1}\bar{\mathbf{S}}(\omega) \sim \bar{\mathbf{S}}_1^{+}(\omega) + \bar{\mathbf{S}}_1^{-}(\omega) + \bar{\mathbf{S}}_2(\omega)$$

where:

$$\bar{\mathbf{S}}_1^{\pm}(\omega) \simeq \mp J_1\left(2kX_{\mathrm{M}}^{\infty}\right)J_{\pm 1}\left(2kX_{\mathrm{d}}\right)\delta\left(\omega - \omega_{\mathrm{M}} \pm \omega_{\mathrm{d}}\right)$$

and

$$\bar{\mathbf{S}}_2(\omega) = -J_0\left(2kX_\mathrm{d}\right) J_2\left(2kX_\mathrm{M}^\infty\right) \delta(\omega - 2\omega_\mathrm{M}).$$

The first terms $\bar{\mathbf{S}}_1^{\pm}(\omega)$ predicts a pair of peaks of similar amplitude centered at frequencies $\omega_\mathrm{M} \pm \omega_\mathrm{d}$. The second term $\bar{\mathbf{S}}_2(\omega)$ produces a peak at the second harmonic (i.e. at double the mechanical frequency). We find that both these features are a common feature of Fourier transforms in the trapped regime although the experimental peaks are broadened due to the spread in ω_M as well as other thermal broadening effects.

An important point is that the relative amplitudes of these peaks provide a means to estimate the steady state amplitudes X_M^∞ and thus enable an estimate of the equilibrium temperature of the nanosphere. In particular, if there is strong cooling:

$$\left| \frac{J_0\left(2kX_\mathrm{d}\right) J_2\left(2kX_\mathrm{M}^\infty\right)}{J_{\pm 1}\left(2kX_\mathrm{d}\right) J_1\left(2kX_\mathrm{M}^\infty\right)} \right| \sim \frac{X_\mathrm{M}^\infty}{X_\mathrm{d}} \to 0,$$

resulting in the suppression of the second harmonic ($2\omega_\mathrm{M}$) peak in the spectrum. Thus we expect that those traces for which the second peak is weak or nearly absent correspond to the strongest cooling. In this case, we estimate the reduction in temperature from $\frac{T_\mathrm{eq}}{T_\mathrm{in}} \sim \left[\frac{X_m^\infty}{X_\mathrm{M}(t=0)}\right]^2$ where T_in corresponds to an initial temperature, while T_eq is our final equilibrium temperature.

Chapter 7

Nonlinear dynamics and strong cavity cooling

This chapter reports on the improvements obtained in the detection of the particles mechanical motion and cooling performance, of the hybrid electro-optical trap. Increasing the finesse of the optical cavity and reducing its mode volume, as described in section 7.1, raises the optomechanical coupling and permits a detectable modulation of the cavity field, coming from the trapped particle's oscillations. We show that, by looking at the cavity output power spectral density, cooling rates $\Gamma_{\rm opt}$ in the $1000\,{\rm s}^{-1}$ range are obtained. The cavity output offers readout of linear-in-position and quadratic-in-position (nonlinear) couplings between the levitated particle and the intracavity field, and it shows that we are able to tune the linear to non-linear ratio ($G_1 : G_2$) to reach $G_1 \sim 0$, isolating the true nonlinear dynamics (as seen in section 4.4.1). Further, due to the dynamic nature of this experiment, we are able to observe the damping, in time, of cavity field modulations driven by nonlinear coupling. This has not been previously observed, and G_2 effects have not been previously detected in any levitated system. Finally, we identify a previously unobserved shift of the Paul trap secular frequencies due to the optical cavity (section 7.4) which enables readout of key parameters, such as the nanoparticle charge and mean number of photons in the cavity.

7.1 New cavity

In chapter 6 we saw how the nanospheres were confined within an optical well for a time of the order of 0.3 s, after which they tend to escape the optical potential. The optomechanical coupling $\bar{G}_1$ and optical potential $A\hbar\left|\bar{\alpha}\right|^2$ were weak, so that the noise in the light field was sufficient to kick the nanospheres out of the well. Once the spheres were lost from the optical well they are recaptured by the Paul trap and returned to the cooling cycle. To solve the

problem of loss from the optical potential a higher finesse optical cavity can be employed, as this allows us operation in the sideband-resolved regime $-\Delta_0 \simeq \omega_{\rm M} \gtrsim \kappa$, which yields maximum cooling. Also, having a cavity with smaller mode volume V_c increases the value of the optomechanical coupling, since $\bar{G}_1^2 \propto V_c^{-2}$, and the optical potential depth $A \propto V_c^{-1}$. This allows longer capture times in the optical wells and higher optomechanical damping rates. For example, for a cavity finesse $\mathcal{F} = 100,000$, and a cavity waist $w_0 = 60\,\mu$m, cooling rates of $\sim 10\,$kHz are possible.

We reduced the length of the cavity, and used mirrors with a smaller radius of curvature and a higher reflectivity, to obtain a higher finesse. The dependences of the cavity waist on the mirror's radius of curvature and cavity length are expressed in equation (8.30) of Appendix C. They are plotted separately in figure 7.1. The new cavity will have the same structure described in section 5.4, but we reduced the length of the invar rods to $28.5 \pm 0.1\,$mm, and employed mirrors with radius of curvature of $r_c = 25\,$mm and thickness $3 \pm 0.1\,$mm. Their nominal reflectivity is $R = 0.999984$, which gives in theory a finesse of $\mathcal{F} \simeq 200,000$. The new length of the cavity $L = 13.5 \pm 0.2\,$mm, gives a cavity waist $w_0 = 61.3 \pm 0.1\,\mu$m, and a new free spectral range of FSR $= 11.1 \pm 0.1\,$GHz.

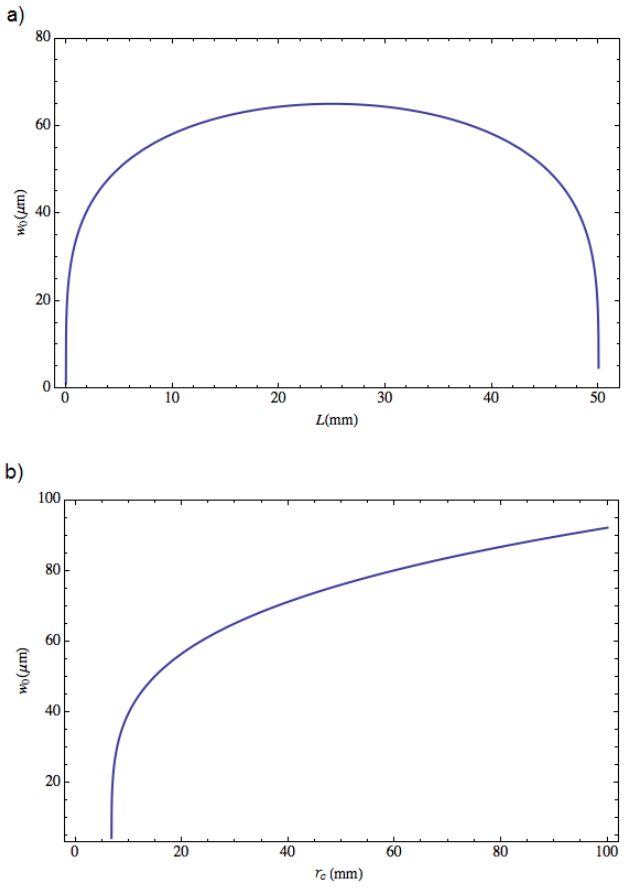

Figure 7.1: Cavity waist as a function of the cavity length L, and mirror's radius of curvature r_c. In (a) the radius of curvature of the mirrors is kept fixed at $r_c = 25\,$mm, while in (b) the cavity length is constant, $L = 13.5\,$mm. Fixing both values leads to a cavity waist $w_0 \simeq 61.3\,\mu$m

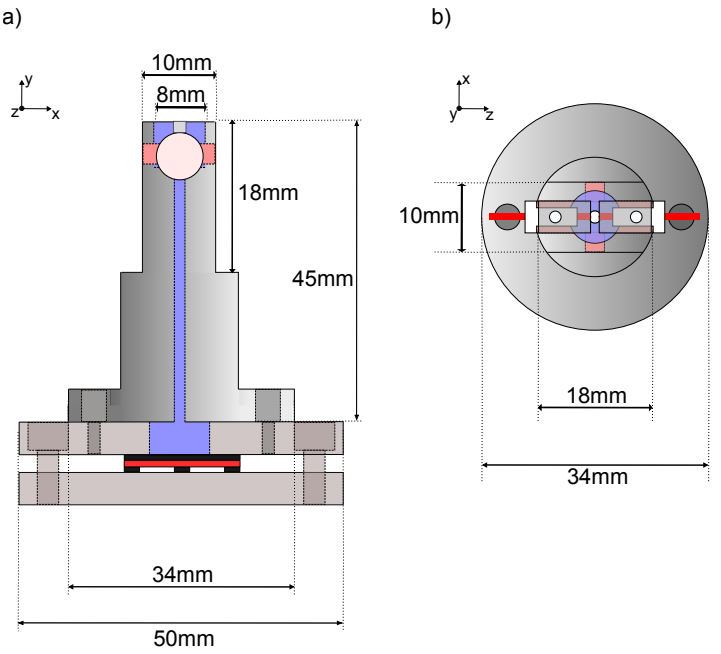

Figure 7.2: Side view representation of the new ion trap holder, with thickness along the cavity axes (x) of 10 mm, leaving enough space for the new, shorter cavity which sits around it (see also figure 7.3)

Using the new shorter cavity, required a reduction in the diameter of the Paul trap holder along the direction of the cavity axes (x) down to 10 mm, as shown in figure 7.2. Everything else in the Paul trap was kept unchanged, including the electrode separation and the loading mechanism. We also employed a new, thinner shield, which is now $\simeq$ 10.5 mm wide, and fits in between the Paul trap holder and the cavity mirrors, at a distance from the latter of $\simeq$ 1.5 mm on each side.

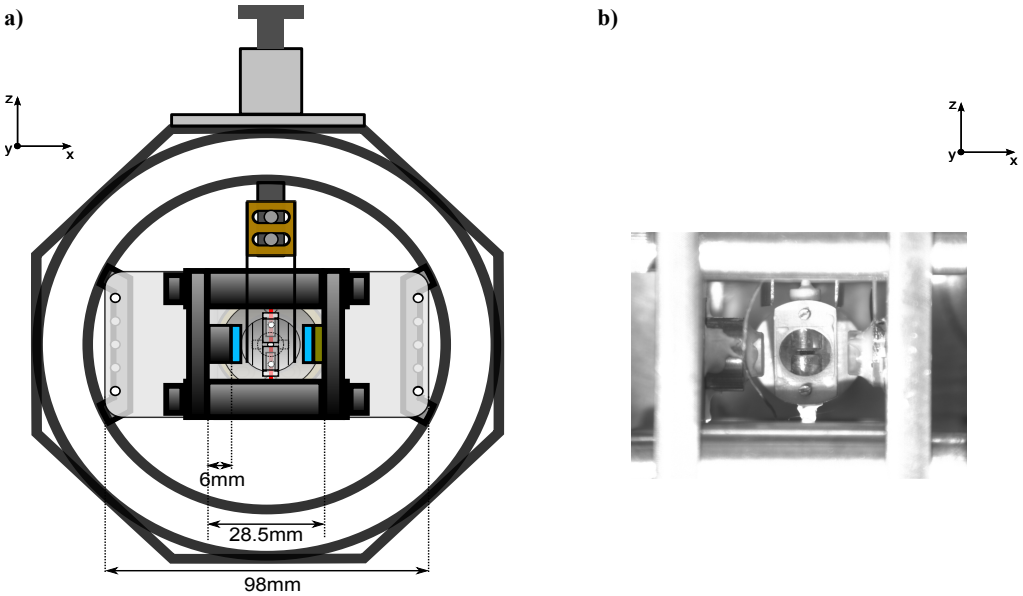

Figure 7.3: a) Top view representation of the new, shorter cavity sitting around the Paul trap structure. b) Photo of the apparatus taken with CMOS camera from the top window of the vacuum chamber.

Figure 7.3 shows a representation of the hybrid trap with the new cavity dimensions, as well as a photo of the setup. Given the small size and the compactness of the system, handling the mirrors and the cavity structure for alignment becomes a very delicate procedure, due to the risk of scratching the mirror's surfaces, hence decreasing the reflectivity. After reaching a cavity coupling of $\sim 10\%$ for both the weak and the strong beam, we check the cavity finesse.

7.1.1 Cavity finesse

To measure the finesse of the new cavity we use the scanning technique described in section 5.4.4.3, but this time we drive the AOMs using a two output function generator (Le Croy Wave Station 3162) to provide a more stable frequency source to the AOMs, with respect to the drivers employed before (see Appendix B for a comparative test between the drivers used). The function generator allows us to perform a frequency sweep of its output, going to AOM_2, so that we can set the detuning range and make an automatic scan across resonance. While driving AOM_1 at fixed 80 MHz with one output, we set the sweep limits for the signal going to AOM_2, from 76 MHz to 84 MHz, in 1ms sweep time. The function generator and the oscilloscope are triggered from the same external signal, so that the beginning of the scan corresponds to 0 ms in time scale.

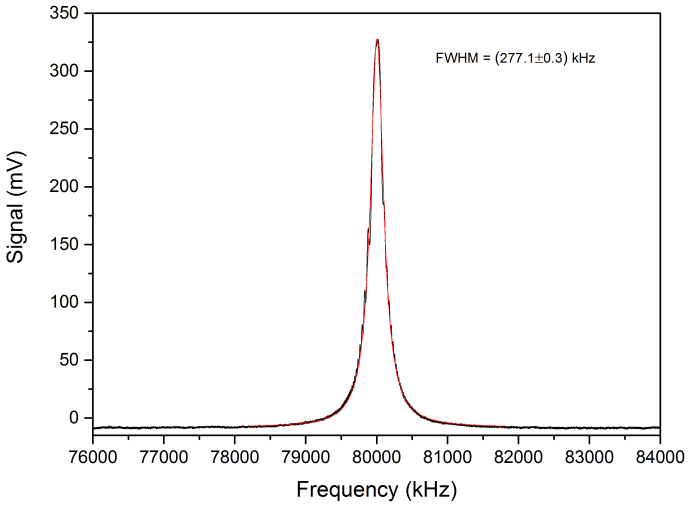

Figure 7.4: Cavity transmission signal as a function of the AOM_2 frequency. Both AOMs are driven with a two output function generator, keeping AOM_1 frequency at 80MHz and sweeping the signal going to AOM_2 across resonance [76 MHz − 84 MHz] in 1 ms sweep time.

The horizontal axes of our oscilloscope can then be related to the AOM_2 frequency:

$$\rho_2 = \frac{(76-84)\,\mathrm{MHz}}{1\,\mathrm{ms}} t + 76\,\mathrm{MHz}$$

where t is the time variable, going between 0 and 1 ms. The resulting resonance peak obtained at the output of the cavity is shown in figure 7.4. The Lorentzian fit gives a cavity linewidth FWHM $\simeq 277$ kHz, corresponding to a finesse $\mathcal{F} = \text{FSR/FWHM} = 48900 \pm 400$. The latter is lower than the theoretical value predicted ($\mathcal{F} \simeq 200,000$), probably due to some dirt deposited on the mirrors during the glueing and cavity assembling processes.

We will see in the following sections that with such a cavity we obtain a significant increase in the optomechanical coupling rates, with respect to the results shown in chapter 6 (where the finesse was $\mathcal{F} \simeq 15,000$), and the system now allows trapping for indefinite periods of times, at a vacuum of $\sim 10^{-6}$ mbar. In addition, a non-trivial coupled dynamics is evidenced by detectable modulations of the cavity field, by linear and nonlinear coupling contributions.

7.2 Heterodyne detection of cavity output

Besides the new $\sim 50,000$ finesse cavity, the rest of the optical apparatus remains mainly unchanged, as shown in figure 7.5. This time though, the trapped particle stays permanently localized on a cavity antinode as the pressure is reduced to the current limit of the vacuum chamber at $\approx 10^{-6}$ mbar, and the mechanical motion can be observed from the heterodyne spectrum of the recorded time series, for the cavity output signal.

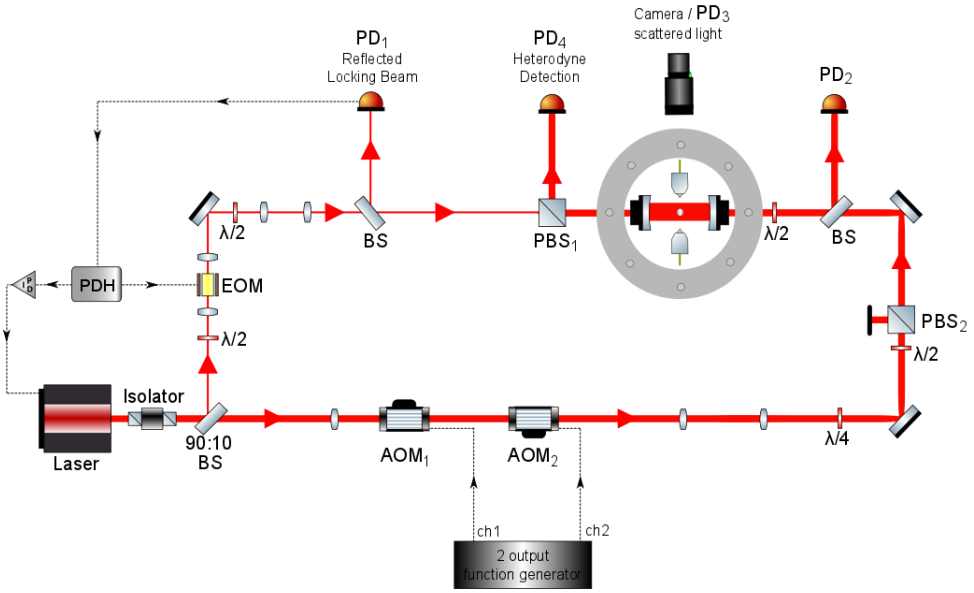

Figure 7.5: Optical scheme for cavity output detection: A single beam is split into two beams. One is passed through an EOM to provide sidebands for a Pound-Drever-Hall locking scheme that locks the laser to the cavity resonance. The second beam, which drives the cooling/trapping, passes through two AOMs to provide a beam with a tunable downshifted frequency ($\Delta_0/2\pi$) of up to 200 kHz to the on resonance beam. Interference between these two beams produces a heterodyne signal that is centered at frequency $\Omega = -\Delta_0$, and recorded on a photodiode (PD_4).

Rotating the polarization of the weak beam appropriately, a portion of the resonant light reflected from the cavity gets reflected at PBS_1 and is coincident on a detector (PD_4) with the transmitted light from the strong beam. The latter is red-detuned by $-\Delta_0/2\pi = 50-100\,\mathrm{kHz}$ via the AOMs, driven at different frequencies by a two output function generator. This leads to a beat signal on PD_4 with heterodyne frequency $\Omega = -\Delta_0$.

The mechanical frequencies ($\omega_M = 2\pi\times 10-40\,\mathrm{kHz}$ typically) appear as heterodyne sidebands around this peak in the spectrum at $\Omega \pm \omega_M$ due to the G_1 coupling and at $\Omega \pm 2\omega_M$ due to G_2 coupling. There are also peaks at ω_M and $2\omega_M$ due to the direct modulation of cavity transmission by the particle. These features are clearly illustrated in figure 7.6, which shows plots of the recorded heterodyne spectrum $\left(\mathrm{PSD}^{1/2}\right)$ for a nanoparticle trapped near the centre of the optical potential. Also simulations are included for comparison. For these low N the nonlinear contribution evidenced by strong modulation at $\approx 2\omega_M$ dominates. When visible, the mechanical frequency shows the splitting $\omega_M \pm \omega_d$ given by the Paul trap drive.

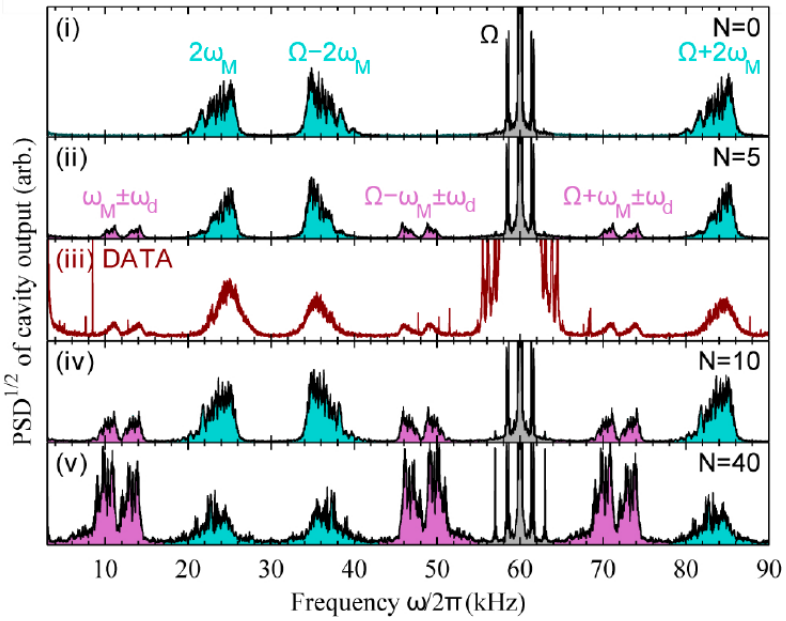

Figure 7.6: Comparison in the simulations of the nonlinear stochastic dynamics (panels i,ii,iv,v) and an experimental spectrum corresponding to trapping in low $N \simeq 5$ (iii). $\sqrt{\mathrm{PSD}}$ of the steady state heterodyne spectra are shown on a linear scale. All spectra show the strong beat frequency component at $\Omega/2\pi = 60\,\mathrm{kHz}$ which is the detuning between the on-resonance locking beam and the red detuned cooling beam. The mechanical motion can be observed as sidebands around this peak at $\Omega \pm \omega_M$ due to G_1 coupling and at $\Omega \pm 2\omega_M$ due to G_2 coupling. There are also peaks at ω_M and $2\omega_M$ due to the direct modulation in cavity transmission of the particle. Pressure is $p = 10^{-2}\,\mathrm{mbar}$, input power $P_{in} = 0.07\,\mathrm{mW}$ and particle charge $Q = 2$.

In the presence of optomechanical damping, the axial motion $x(t) \simeq x(0)e^{-\Gamma_{\mathrm{opt}}t/2}$ is damped by the varying radiation pressure. In the presence of sufficiently strong coupling, the cavity field amplitude and phase fluctuations can provide an indirect means to detect the particle motion. The nanoparticle's motion causes a change in the resonant frequency of the cavity,

represented by a change in the effective detuning:

$$\Delta_0 \to \Delta_0 + A\cos^2\left(kx(t)\right). \tag{7.1}$$

Since (neglecting noise terms), the intracavity field $a(t)$ is :

$$a(t) \approx \frac{\varepsilon}{(i\Delta_0(t) + \kappa/2)}, \tag{7.2}$$

where ε is the laser drive amplitude and $a(t) \equiv \bar{\alpha} + \delta a(t)$, where $\delta a(t)$ is the fluctuating part of the intracavity field. The heterodyne detection signal:

$$|s(t)| \simeq \left|\sqrt{\kappa}\left(\bar{\alpha} + \delta a(t)\right) + A_p e^{i\Omega t}\right|^2, \tag{7.3}$$

is obtained by beating the transmitted cavity field with a reference beam (the weak beam) of amplitude A_p, shifted (relative to the laser) by frequency Ω. The heterodyne signal includes terms $S_\phi(t) \propto (\delta a(t) + e^{i\phi}\delta a^*(t))$ where ϕ determines which quadrature is detected. At present ϕ is not controlled. Nevertheless, examination of equation (7.2) we can show that regardless of ϕ,

$$S_\phi(t) \propto \cos^2\left(kx(t)\right). \tag{7.4}$$

For the usual optomechanical set-ups, the phase quadrature (ideally obtained by homodyne detection) $S_\pi(\omega) \propto x(\omega)$ directly follows the motion. In contrast, the form in equation (7.4), results in a far more complex cavity output: even if the $|x(\omega)|$ spectrum is sharply peaked around $\omega \simeq \pm\omega_{\mathrm{M}}$, one finds a much more complex form for $|S_\pi(\omega)|$. There are sideband peaks near both $\omega \simeq \omega_{\mathrm{M}}$ as well as $\omega = 2\omega_{\mathrm{M}}$. The $\omega \simeq \omega_{\mathrm{M}}$ sidebands are split into multiple peaks due to the Paul trap. While this potentially complicates attempts to infer $|x(\omega)|$ from the heterodyne signal, we show that this additional fine-structure provides new means of analysis, offering a distinct sideband “fingerprint" for different dynamical regimes. As a detail, the heterodyne detection provides a duplicated sideband structure as there are a set of $|S_\pi(\omega)|$ sidebands centered on $\omega = \Omega$ and a further set of sidebands centered on $\omega = 0$. Provided $A_p \simeq \sqrt{\kappa}\bar{\alpha}$, these sidebands are of similar heights; while not dynamically very significant, this duplicate structure becomes useful where a particular peak is obscured by instrumental noise. Finally, in some cases, like in figure 7.6, there are instances where we do not plot the PSD of the output $\left\langle |S_\phi(\omega)|^2 \right\rangle$. Instead we show $\mathrm{PSD}^{1/2} \equiv \sqrt{\left\langle |S_\phi(\omega)|^2 \right\rangle}$. The advantage is to emphasize dynamically interesting, but small, spectral features. However, this also emphasizes noise, whether instrumental noise in the experiment or from the single-trajectory stochastic Langevin dynamics needed to simulate the rapidly changing sideband structure as the particle cools in time.

7.2.1 Estimating N from sideband structure

In the same way as described in section 4.3, the axial motion of the captured nanoparticle is approximately separable into its classical and thermal motions:

$$x(t) \approx x_0(t) + \triangle x(t) \approx X_{\rm d} \sin(\omega_{\rm d} t) + \triangle x(t=0) e^{-\Gamma_{\rm opt} t/2} \cos(\omega_{\rm M} t)\,, \tag{7.5}$$

with $X_{\rm d} \approx -\frac{\omega_{\rm T}^2}{\omega_{\rm M}^2}\frac{\lambda}{2}{\rm N}$ and disregarding any phase between the drive and mechanical oscillation. $\triangle x(t)$ is the thermal motion, initially strongly damped and its amplitude decays exponentially. The classical drive $x_0(t)$ instead is not cooled and its amplitude remains constant. The thermal fluctuations eventually reach a steady state value $\triangle x(t) \to \overline{\triangle x}$ where heating (mainly from background gas) and optomechanical cooling are in balance. Here, the steady-state, asymptotic variance $\left(\overline{\triangle x}\right)^2 \sim \Gamma_{\rm M}/\Gamma_{\rm opt} \left(\triangle x(T_B)\right)^2$ where $\triangle x(T_B)$ is the variance obtained in the absence of any optomechanical cooling, when the thermal motion is in equilibrium with the $T_B = 300\,{\rm K}$ thermal noise bath. Since the variance may be related to an equilibrium temperature, we can use the expression:

$$T \approx \frac{\Gamma_{\rm M}}{\Gamma_{\rm opt}} T_B, \tag{7.6}$$

to estimate the temperature scale (as opposed to an accurate temperature measurement) of the cooled particle in the experiments, provided we can estimate $\Gamma_{\rm opt}$.

In the case of low N we can write:

$$x(t) \approx X_{\rm d} \sin(\omega_{\rm d} t) + \overline{\triangle x} \cos(\omega_{\rm M} t)\,. \tag{7.7}$$

Then, the frequency spectrum of $S_\phi(t)$, has dominant contributions from:

$$\begin{aligned} S_\phi(\omega) \quad &\sim \quad J_1\left(2k\overline{\triangle x}\right) J_1\left(2kX_{\rm d}\right) \left[\delta\left(\omega - (\omega_{\rm M} + \omega_{\rm d})\right) + \delta\left(\omega - (\omega_{\rm M} - \omega_{\rm d})\right)\right] + \\ &+ \quad J_2\left(2k\overline{\triangle x}\right) J_0\left(2kX_{\rm d}\right) \left[\delta\left(\omega - 2\omega_{\rm M}\right)\right]. \end{aligned} \tag{7.8}$$

Thus there are peaks of equal height at $\omega = \omega_{\rm M} \pm \omega_{\rm d}$, but no peak actually at the mechanical frequency itself; there is however a peak at $\omega = 2\omega_{\rm M}$. We note that if one detects the x motion via scattered light as in chapter 6 and [36], then a relation like equation (7.4) still holds: since the scattered light probes the fringe structure of the standing wave, it also $\propto \cos^2(kx(t))$, hence the basic sideband structure of the particle in the low cooling regime described is similar. However, the underlying physics is quite different; in the present case the cavity field is an active participant in the dynamics so at very low pressures and for low phonon occupancy consideration of back-action effects will become essential to understand-

ing the output spectra.

The situation for high N is different; the excursion in $x_0(t)$ is large enough to cause an oscillation in $\omega_{\rm M}$, since $\omega_{\rm M} \equiv \omega_{\rm M}(x_0(t))$. In this case,

$$x(t) \approx x_0(t) + \overline{\triangle x} \cos\left(\omega_{\rm M}(x_0)t\right), \tag{7.9}$$

since

$$\mathrm{M}\omega_{\rm M}^2 = 2\hbar k^2 A \left|\bar{\alpha}\right|^2 \cos\left(2kx_0\left(t\right)\right). \tag{7.10}$$

The result is not, in fact, to broaden the Fourier peak, but rather to cause a change in the relative height of the $\omega = \omega_{\rm M} \pm \omega_{\rm d}$ side bands. Thus the change from a double-peaked structure to a single dominant peak in the cavity output is the hallmark of capture in an optical well with high N. In Appendix A and in [149] we elucidate more clearly the relation between the transmitted light sidebands and the displacement spectra.

7.3 Cooling

The initial optomechanical damping as well as the steady state behavior after cooling, were investigated in the experiment. For each dataset the cavity resonance width κ was measured. It was used to estimate the finesse using the usual expression $\kappa = \pi c/\mathcal{F}L$ (assuming total losses from the cavity correspond to losses at the mirrors). $\mathcal{F} = 40,000 - 55,000$ corresponds to $\kappa/2 = 2\pi \times (85-115)\,\mathrm{kHz}$. The input power may be estimated from the intracavity photon number given by mechanical and secular frequencies, as presented in next section (7.4), using the relation $\mathrm{n} = \left|\bar{\alpha}\right|^2 = \varepsilon^2/\left(\Delta_{x_0}^2 + \kappa^2/4\right)$, since $\mathrm{n} \simeq \frac{P_{\rm in}}{\hbar\omega_l}\frac{\kappa/2}{\kappa^2/4+\Delta_{x_0}^2}$. The damping rate from the background gas is assumed to be as the one expressed in equation (2.1), and it varies linearly with the pressure, as the path length of air molecules $\gg$ the particle size [68], as confirmed by previous measurements with levitated particles [105]. Thus, for example, a pressure of $p = 10^{-5}\,\mathrm{mbar}$ corresponds to $\Gamma_{\rm M} = 0.11\,\mathrm{s}^{-1}$.

For the data shown in figures 7.6, the mechanical frequencies $\omega_{\rm M} \simeq 2\pi \times 12.5\,\mathrm{kHz}$ and the low values of $P_{\rm in} \simeq 0.07 - 0.08\,\mathrm{mW}$ means that the depth of the optical potential $\hbar A|\bar{\alpha}|^2 \sim 400\,\mathrm{K}$ cannot support particles much hotter than room temperature. For the pressures of $10^{-2}\,\mathrm{mBar}$ of the experiment, stochastic simulations find that optical trapping occurs only for $\mathrm{N} \lesssim 20$, mainly because for increasing N the well height becomes much lower than the maximum, over part of the cycle of the trap oscillation (see inset of figure 4.5), thus a particle cannot become trapped in high N unless there is strong cooling. The advantage of the lower N is that the quadratic component is clearly visible. Then from equation (7.8),

the ratio Υ, of the heights of the quadratic peak to the linear peaks shown in figure 7.6 is:

$$\Upsilon \simeq \frac{J_2\left(2k\overline{\triangle x}\right) J_0\left(2kX_{\rm d}\right)}{J_1\left(2k\overline{\triangle x}\right) J_1\left(2kX_{\rm d}\right)}. \tag{7.11}$$

For low N, then $X_{\rm d}$ is small. $\triangle x$ is not necessarily very small for a hot particle, but we are only aiming to estimate a temperature scale, hence with small argument approximations:

$$\Upsilon \approx \frac{k\overline{\triangle x}}{kX_{\rm d}}, \tag{7.12}$$

thus with $kX_{\rm d} \approx \pi {\rm N}\frac{\omega_{\rm T}^2}{\omega_{\rm M}^2}$ and $k_B T \approx {\rm M}\omega_{\rm M}^2 \left(\triangle x\right)^2$ and also $\sqrt{2}\omega_{\rm d}\omega_{\rm s} \approx \omega_{\rm T}^2$ then, one can estimate the equilibrium temperature:

$$T \approx \left[\frac{2\pi^2 {\rm M}\omega_{\rm d}^2}{k_B k^2}\right]\left[\frac{\omega_{\rm s}}{\omega_{\rm M}}\right]^2 \Upsilon^2 {\rm N}^2 \simeq 0.106\times 10^4 \left[\frac{\omega_{\rm s}}{\omega_{\rm M}}\right]^2 \Upsilon^2 {\rm N}^2 \simeq 60\,{\rm K}, \tag{7.13}$$

since we have $\omega_{\rm s}/2\pi = 120\,{\rm Hz}$ while $\omega_{\rm M}/2\pi = 12.5\,{\rm kHz}$ so $\left[\omega_{\rm s}/\omega_{\rm M}\right]^2 \approx 10^{-4}$, while $N \approx 5$ and $\Upsilon \approx 5$ for the data in figure 7.6. Thus this data corresponds to quite modest cooling, sufficient to stably trap, but not to significantly reduce the temperature.

The next two data sets are the ones represented in figures 7.7 and 7.8. They both correspond to higher mechanical frequencies $\omega_{\rm M} \simeq 2\pi\times 35-40\,{\rm kHz}$ and hence higher $P_{\rm in} \simeq 0.5-0.7\,{\rm mW}$. The factor of ten increase in well-depth relative to data set discussed above (figure 7.6) makes trapping in high N possible. We note that, according to simulations, ${\rm N} \sim 300-500$ is not uncommon since trapping usually occurs at the turning points of the secular motion, thus near the extrema (in x) of the trajectory, where the nanoparticle is moving slowest.

For the initial cooling stage, it was not possible to directly measure the exponential damping of individual mechanical oscillations, as we cannot simply observe the curve $x(t) = x(0)e^{-\Gamma_{\rm opt}t/2}$. In the experiment, one infers the mechanical motions indirectly, from the heterodyne output fluctuations $S(t)$ and corresponding spectra $|S(\omega)|$. In addition, there is higher frequency instrumental noise which masks individual oscillations. Instead, after capture, the particle was abruptly disturbed from steady state. This has been done by applying a modulation to the signal from the function generator, going to $\rm AOM_2$, using a 400 mHz ramp whose depth can be selected. As the particle cooled, the temporal evolution of the heterodyne spectrum was obtained by evaluating a series of spectra $|S(\omega, \langle t\rangle)|$, using a sequence of narrow time windows, centered on time $= \langle t\rangle$. Figure 7.7 shows how the heterodyne spectrum changes as the particle is cooled at a fixed pressure $p = 3\times 10^{-4}\,{\rm mbar}$. The heterodyne spectra are averaged over a 2.4 ms period separated in time by 0.2 ms. Although the spectral features are broadened and not fully resolved due to the ms duration of the time interval of the recorded time series, there is good agreement between experiment and theory. Both cases

show the $2\omega_M$ nonlinear coupling/frequency-doubled sidebands which can only be detected in the first few milliseconds as they are rapidly cooled. Cooling of the linear sidebands at ω_M occurs more slowly over a timescale $\sim 10\,\mathrm{ms}$. We obtain a cooling rate of $\Gamma_{opt} \sim 400\,\mathrm{s}^{-1}$ from equation (4.31). From the standard expression $T \simeq 300\,\mathrm{K} \times \Gamma_M/(\Gamma_{opt} + \Gamma_M)$ this would imply $T \approx 0.3\,\mathrm{K}$ at steady state. Using this method, cooling rates on $1000\,\mathrm{s}^{-1}$ scales (still much lower than possible in sideband resolved regimes) were seen. Finally, this method illustrates also the more rapid cooling of the G_2 peak due to quadratic coupling.

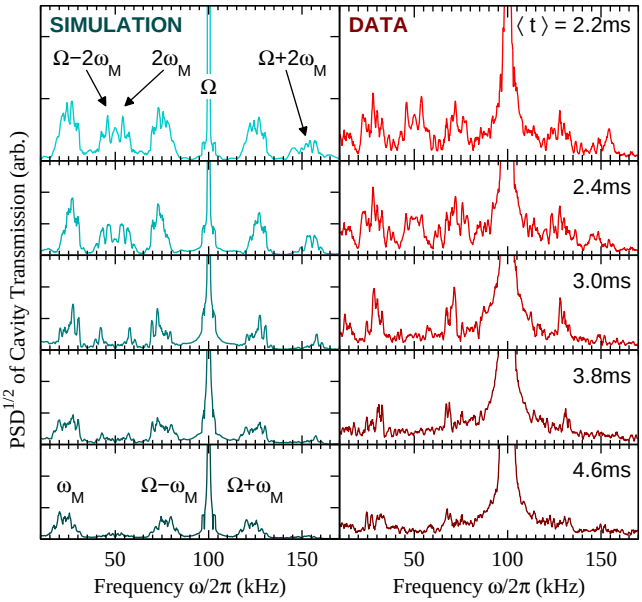

Figure 7.7: Cooling dynamics of a particle which is first captured in a high (N ≈ 450) well. From steady-state, it is perturbed so its cooling and re-equilibration may be observed. The (expected) much faster damping of the G_2 sidebands at $\omega = 2\omega_M$, $\Omega \pm 2\omega_M$ relative to the G_1 sidebands at $\omega = \omega_M$, $\Omega \pm \omega_M$ is clearly seen. Both experimental data and non- linear stochastic simulations show reductions in G_1 sideband heights which indicate cooling on ms timescales and hence $\Gamma_{opt} \sim 1000\,\mathrm{s}^{-1}$. $\sqrt{\mathrm{PSD}}$ of heterodyne spectra are shown on a linear scale. Pressure $p = 3 \times 10^{-4}\,\mathrm{mbar}$, input power $P_{in} = 0.5\,\mathrm{mW}$, and charge $Q = 1$. We set $= \Omega = -\Delta_0 = 2\pi \times 100\,\mathrm{kHz}$. From these values and equation (4.31) we obtain $\Gamma_{opt} \sim 400\,\mathrm{s}^{-1}$, in broad agreement with the observed ms cooling timescales.

Figure 7.8a) represents the steady state heterodyne spectra of a particle located at high optical well, and trapped indefinitely at all pressures, which were lowered to the minimum achievable with the current pump ($\sim 10^{-6}\,\mathrm{mbar}$). The absence of any double peak structure in the steady state data suggests $\mathrm{N} \gtrsim 300$; the unusually high secular frequency 237 Hz that was detected, indicates a highly charged bead ($Q = 3$), which also cools more effectively. Figure 7.8b) indicates that the variation of the area of the sidebands of the experimental cavity output data with pressure is consistent with a linear dependence on pressure, wherever a strong peak is observed above the noise floor of the data. Each PSD is an average of 15 sets of 1 second duration data and are smoothed over 100 Hz. Also shown is a PSD without a trapped particle which shows the noise floor of the measurements. Due to the relatively high background noise, the steady state sidebands can only be clearly observed down to

$p \gtrsim 10^{-4}$ mbar even though we can clearly image the scattered light from the trapped particle on a CCD camera at 10^{-6} mbar. In this dataset no nonlinear sidebands were detected, since G_1 is large compared with G_2: thus the linear to nonlinear sideband ratio could not be used to estimate the temperature. The data was instead calibrated by assuming that for the higher pressures (5.4×10^{-1} mbar), there is little cooling and the particle temperature remains close to that of the surrounding gas (room temperature $T \sim 300\,\mathrm{K}$).

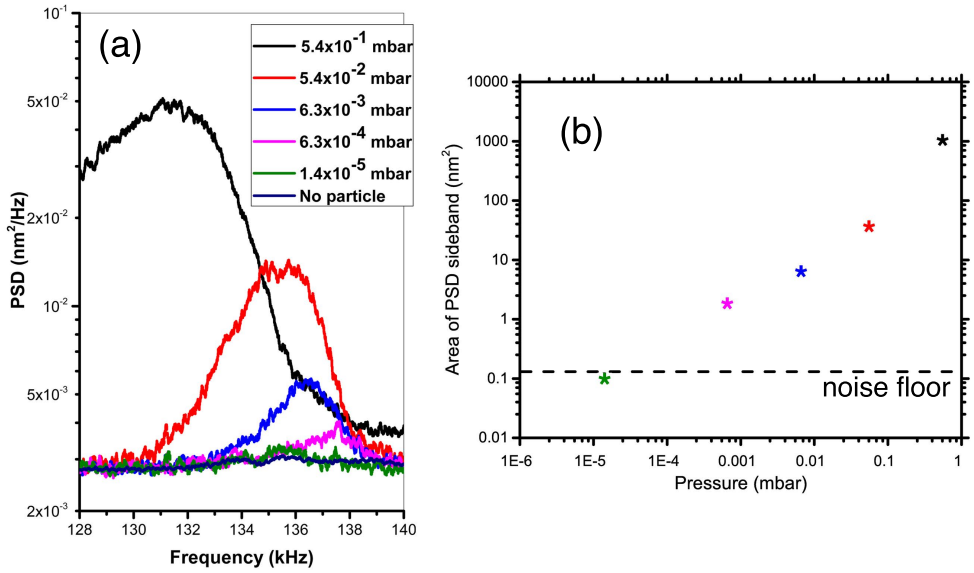

Figure 7.8: (a) Steady state data of a strongly cooled particle. The calibrated PSD spectra show single dominant peaks, indicating high N ($\sim 300-600$) trapping. Trapping occurred at a pressure $p = 0.5\,\mathrm{mBar}$ ($T \sim 300\,\mathrm{K}$) which was then gradually reduced to $p = 5\times10^{-6}\,\mathrm{mBar}$, the current limit of our apparatus. PSDs (y-axes) are plotted on a log scale. Also shown is a background PSD taken with no particle trapped. The peak heights and hence T, scale approximately with p. For $p \lesssim 10^{-5}\,\mathrm{mBar}$ it is no longer possible to detect the motional sidebands although it can be observed from the scattered light that the particle is still trapped. $\mathcal{F} = 50,000$ and $P_{in} = 0.6\,\mathrm{mW}$; for N ≈ 300 equation (4.31) predicts $\Gamma_{\mathrm{opt}} \approx 2000\,\mathrm{s}^{-1}$. (b) Change in area of the PSD as a function of pressure, demonstrating that we can measure a 1000 fold reduction in the area and thus the temperature, limited by the noise floor of the measurement.

As outlined in section 7.2, in the current experiments the phase of the heterodyne beat signal (and thus the corresponding quadrature of the cavity output) is not carefully controlled. Nevertheless, we can simply assume that the cavity output is proportional to the PSD of the position quadrature $y_{out} = a_{out} + a_{out}^*$, where the cavity output field $a_{out} = a_{in} - \sqrt{k}a$ and a is the intracavity field while a_{in} is incoming optical noise on the transmitted side of the cavity. Thus we assume:

$$S_{het}(\omega) = N S_{yy}(\omega), \tag{7.14}$$

where where $S_{het}(\omega)$ is in millivolts per Hz and N is a proportionality constant. For a typical optomechanical system the cavity output $y(\omega) \simeq G\eta(\omega)x(\omega)$ where $x(\omega)$ represents the mechanical displacement (and where G corresponds to $\bar{G}_1$ in our case). The function $\eta(\omega) =$

$\chi_0(\omega) - \chi_0^*(-\omega)$ is given in terms of optical susceptibilities $\chi_0(\omega) = [-i(\omega + \Delta_0) - \kappa/2]^{-1}$. Using the corrected value $\Delta_{x_0} = \Delta_0 + A\cos^2 kx_0 \simeq \Delta_0 + A \simeq 74\,\mathrm{kHz}$, the susceptibility function is approximately constant, for $\Delta_{x_0} \gg \omega_\mathrm{M}$. Here $|\eta(\omega)|^2 \simeq |\eta_0|^2 \simeq (7.5 - 8) \times 10^{-13}\,\mathrm{s}^2$. If we wish to consider, instead of y, a different quadrature, such as the phase quadrature, we may simply modify the value of η_0. The precise value is unimportant, we simply assume it is a constant. Within this approximation, we assume the area of the sidebands of the displacement spectrum to be related to the area of the sidebands of the PSD of the cavity output:

$$\int S_{yy}(\omega)d\omega = \bar{G}_1^2 |\eta_0|^2 \int S_{xx}(\omega)d\omega, \tag{7.15}$$

where the integrals above are over the areas of the respective sidebands.

Hence, although the hybrid trap cavity output normally exhibits a split-sideband structure, which is of different shape from $S_{xx}(\omega)$, a theoretical investigation [150], shows that, far from the quantum limit, the above relation between the sideband areas is preserved. In the data set examined here (figure 7.8), no splitting of the sidebands was apparent: at high N a single peak is dominant (see Appendix D and [149]) and any weaker structures were unresolved. Nevertheless, we use equation (7.15) to estimate a calibration constant. With $\mathrm{M}\omega_\mathrm{M}^2 \int S_{xx}(\omega)d\omega \simeq k_B T$, as described in section 3.1.3 (equation (3.16)), we may calculate the maximum sideband area, $A_{max} = \int S_{het}(\omega \approx \Omega + \omega_\mathrm{M})$ obtained by integrating the sideband of the heterodyne PSD centered on $\omega \approx \Omega + \omega_\mathrm{M}$ for data at highest pressure $p = 0.5\,\mathrm{mbar}$, and hence:

$$\frac{\mathrm{M}\omega_\mathrm{M}^2 A_{max}}{N\bar{G}_1^2 |\eta_0|^2} = k_B T. \tag{7.16}$$

Assuming $T = 300\,\mathrm{K}$, we estimate the calibration constant:

$$C \simeq \frac{300 k_B}{\mathrm{M}\omega_\mathrm{M}^2 A_{max}} \equiv \left[N\bar{G}_1^2 |\eta_0|^2\right]^{-1}, \tag{7.17}$$

which converts the heterodyne output to m^2/Hz.

Figure 7.8b) shows a plot of the integrated area of calibrated PSD $S_{het}(\omega)$ as a function of pressure when the noise floor shown has been subtracted from the data. As the area is proportional to the temperature we demonstrate that we can measure a change in the area, and thus temperature, by at least 1000, limited by the noise floor of the system.

7.4 The cavity shift

In section 4.1 we have defined the Paul trap potential as the sum of a DC static field and an AC component which oscillates with a drive frequency $\omega_{\rm d}$: $V_{\rm ion}(x,y,z,\omega t) = V^{\rm AC}(x,y,z,\omega_{\rm d} t) + V^{\rm DC}(x,y,z)$. The spatial form of the AC/DC components is similar with $V^{\rm DC} = \frac{1}{2}{\rm M}\omega_{\rm DC}^2\left(x^2+y^2-2z^2\right)$. The corresponding frequencies depend on the applied voltages V_0 and U_0 respectively; $\frac{1}{2}{\rm M}\omega_{\rm T}^2 = QV_0/r_0^2$ while $\frac{1}{2}{\rm M}\omega_{\rm DC}^2 = QU_0/r_0^2$ where $r_0 \simeq 0.5$mm for the present study. The x,y,z motions are separable and given by Mathieu equations (4.5), where we recall that the stability parameters are: $a_{x,y} = 8QU_0/{\rm M}\omega_{\rm d}^2 r_0^2$ and $q_{x,y} = 4QV_0/{\rm M}\omega_{\rm d}^2 r_0^2$, with $a_z = -2a_x$ and $q_z = -2q_x$. While the fast micromotion is characterized by oscillations at $\omega_{\rm d}$, the slower secular motion is given by:

$$\omega_{\rm s} = \frac{\omega_{\rm d}}{2}\sqrt{a_u + \frac{q_u^2}{2}}, \tag{7.18}$$

with $u = x,y,z$. Although in this study $U_0 = 0$, a new aspect of the stronger coupling A is that, provided transverse motions are of small amplitude relative to the beam waist w, the optical mode provides an approximate parabolic potential which in turn combines with the oscillating Paul trap field by introducing an effective DC parameter $a_z = a_y$ where:

$$a_{y,z} = \frac{16\hbar A{\rm n}}{{\rm M}\omega_{\rm d}^2 w^2}, \tag{7.19}$$

where n is the mean photon number in the cavity. Where $a_y \gg q^2$, the secular frequencies tend to the usual transverse optical frequencies; conversely, for low intensity of light (low n), they tend to the secular frequencies of the Paul trap. In the intermediate regime, the two fields combine non-trivially. In particular, since a_u is a stability parameter of the Mathieu equations, for larger q_u, the optical field can destabilize the particle, causing exponential growth in the transverse motions. This is suppressed once the trajectories sample the non-harmonic parts of the optical field, but can lead to unwanted growth in lateral motion for high q_u.

The main significance of equation (7.19) is that the secular motions now depend on both particle charge and cavity photon number n. Lack of certainty in the estimated coupling efficiency between the laser-drive and cavity is an additional uncertainty in estimating n. While n can also be inferred from the mechanical frequency, if both $\omega_{\rm M}$ and $\omega_{\rm s}$ are available and since both depend on n, this provides a more precise and robust way to measure n.

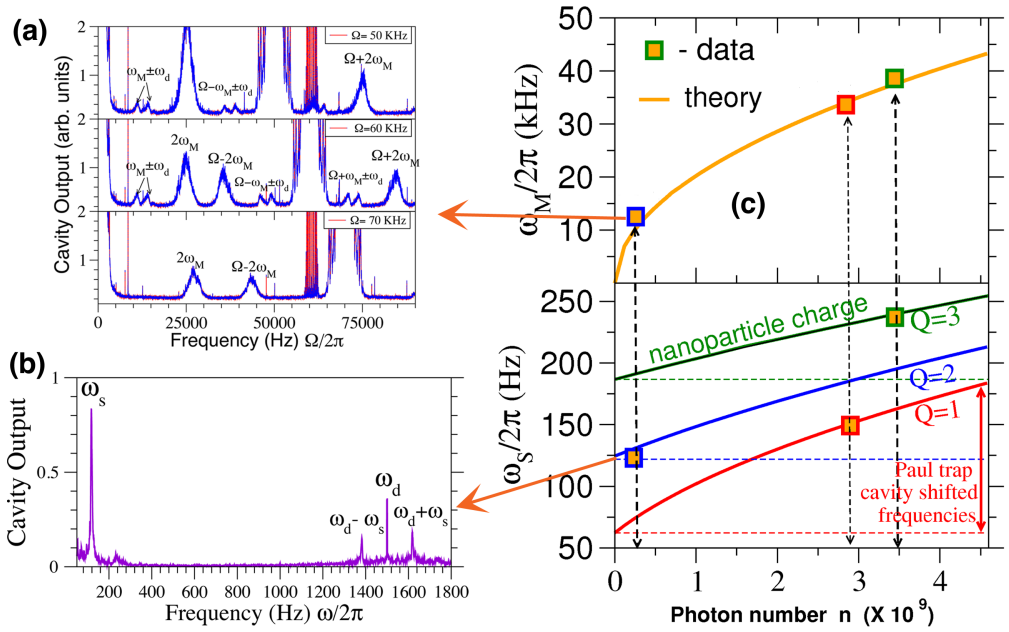

Figure 7.9: A new effect of the stronger light-matter coupling is a newly identified "cavity shift" of the Paul trap secular frequencies. This can be used to measure the charge on the nanosphere and the photon number in the cavity. (a) Shows three sets of experimental data (middle panel is the data discussed in figure 7.6) taken at different values of detuning $\Delta_0 = \Omega$. Red spikes represent instrumental noise, of no physical significance. Note the lowest panel shows data capture for N = 0 hence only the quadratic coupling peak at $2\omega_M$ can be seen. (b) Shows low frequency data, used to obtain the secular frequencies. (c) The Paul trap secular frequencies experience a significant shift due to their interaction with the cavity field. Since both ω_s and ω_M must correspond to the same photon number n this allows read-out of the charge on the nanosphere Q and of n: as shown in the graph, both frequencies must lie on the same vertical line.

In figure 7.9c) we show a plot of frequency against n, for three different trapped particles. Mechanical frequencies can be read from the heterodyne spectra like the ones of figure 7.9a). Here the heterodyne peak depends on the value of the detuning, and the middle panel corresponds to data in figure 7.6, where a a particle of charge $Q = 2$ was trapped. A low frequency spectrum of the same particle is shown in figure 7.9b). Because of the axial secular motion is fully suppressed, the lowest secular frequency is given by $q \equiv q_y$. Since both ω_M and ω_s must correspond to the same photon number n this allows read-out of the charge on the nanosphere and of n: as show in the graph both frequencies must lie on the same vertical line. As the optomechanical cooling rate $\Gamma_{opt} \propto nN^2Q^2$ for small oscillations, these are important parameters to be evaluated.

Another interesting aspect that we note from equations (2.6) and (7.10) is that both the mechanical frequency and $a_{y,z}$ are related to A/M, and thus are both proportional to the polarizability/mass ratio, hence $a_{y,z}, \omega_M^2 \propto \alpha/M$. Thus modulations at different length time scales ($\sim$ 100 Hz for $\omega_s/2\pi$ and $\sim$ 100 kHz for $\omega_M/2\pi$) provide an independent measurement of polarizability and mass. The cavity-induced stability parameter may be varied by

adjusting the cavity input power; the usual AC stability parameter can still be adjusted by varying the AC voltage applied to the Paul trap. Hence it is possible to operate the combined optical-ion trap such that information on either of the ratios Q/M and α/M, or both simultaneously is accurately provided. This means that the hybrid trap can act as a spectrometer which operates either destructively (as in the standard Q/M spectrometry by selective ejection of particles with the selected ratios), or non-destructively, by reading out the cavity induced shift of the secular frequencies.

Chapter 8

Experimental tests for future improvements

In this final chapter we will present some further experimental solutions that have been explored for improving the readout sensitivity and cooling performances of our apparatus. The first idea is to modify the optical setup to use only one laser beam, the strong beam for trapping and cooling the nanoparticles, locked to the cavity via side locking. Different solutions for the feedback loop implementation have been tested and compared, looking at the noise spectra of cavity output.

In the second part of the chapter we go back to a two-beams scheme, where two separate laser sources have been used. A new infrared laser is employed as the weak beam, and it is locked to the cavity via PDH. The strong laser can then be tuned to a different frequency, to hit a different cavity mode and doing so minimizing the interference between the two beams at the detection. The strong laser is phase locked to the weak one in order to maintain the frequency difference between the two always constant, as described in section 8.3.

In the last section we discuss about the cleaning method used for the cavity mirrors, which allowed to bring the finesse up to unexpected high values, useful to get the experiment close to the sideband resolved regime.

8.1 Side locking

Many implementations in high precision measurements in modern optics require an active control and stabilization of the lasers frequency. The free-running linewidth (or short term stability) and noise spectrum of different lasers can vary greatly depending on the stability and finesse of the resonator design, gain-medium characteristics, and other laser parameters.

To detect fluctuations in the laser frequency, a highly stable reference is needed for comparison. One common way in which this is achieved is by using a high-finesse Fabry-Perot cavity, constructed in such a way as to provide the necessary stability over the time scale of interest. The noise intrinsic to the laser can be characterized in terms of the linear spectral density of frequency fluctuations, defined as the RMS frequency fluctuations per square-root unit bandwidth [Hz/Hz$^{1/2}$].

We have already described the use of the PDH technique to lock the laser used in our experiment, to the optical cavity. Besides this, there are other ways to generate an error signal, resulting from the difference between the laser frequency and the cavity resonance, which is then fed back to the laser source. The simplest and most straightforward approach is to hold the laser frequency to one side of the cavity transmission fringe. In this way small changes in laser frequency would produce a strong proportional cavity response. The so called "side-fringe" locking technique uses the slope on either side of the transmission peak to convert frequency fluctuations of the laser into amplitude fluctuations, which are subsequently detected by a photodiode. Figure 8.1 shows the simple scheme of a side lock loop. Before locking, a photodiode detects the resonance transmission peaks from the cavity, and the signal is directly sent to a servo amplifier. Here, one can apply an offset to center the peaks at half height around zero (figure 8.1b). Once the loop is closed and the lock is on, any intensity variation around the zero value will be corrected in the laser frequency emission. The correction can be made in many ways, by acting on the laser piezo (as figure 8.1 suggests), by changing the cavity length, or by using an AOM in between the laser and the cavity.

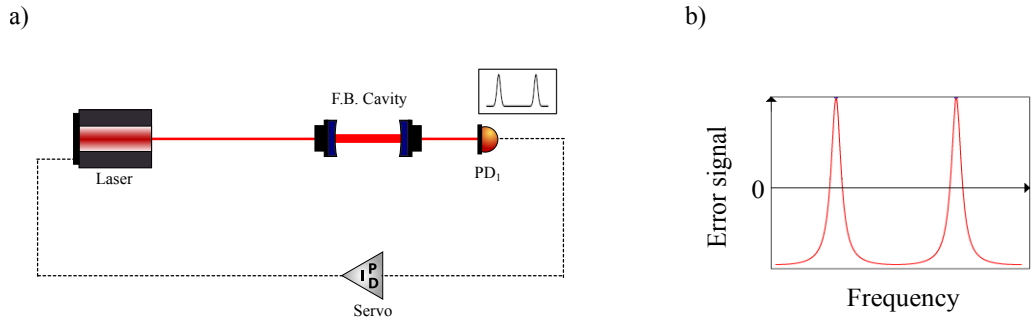

Figure 8.1: Schematic of a side lock. a) Light transmitted by the cavity is collected by a detector, whose signal is sent to a servo amplifier. The resulting error signal is fed back to the laser, to correct for frequency oscillations and instabilities. b) Error signal given by the cavity transmission peaks, centered at half height, where the intensity slope is maximum.

Although easy to implement, the side-of-fringe locking technique suffers from several drawbacks. First, amplitude modulation (AM) from the laser directly couples into the error signal; the feedback loop cannot tell the difference between frequency modulation (FM) and AM. Changes in the laser amplitude will therefore be "written" onto the laser frequency.

Secondly, due to the photon-lifetime of the Fabry-Perot cavity, fast frequency fluctuations of the laser will not be detected in transmission through the cavity. A final limitation is the narrow locking range. A small deviation from the locking point can cause the laser to unlock if the frequency momentarily shifts across the cavity transmission peak. The last two limitations present a particularly troubling tradeoff; high-finesse cavities are desirable so as to provide a narrow linewidth for laser stabilization, yet will simultaneously limit the bandwidth of the feedback loop and reliability of the lock.

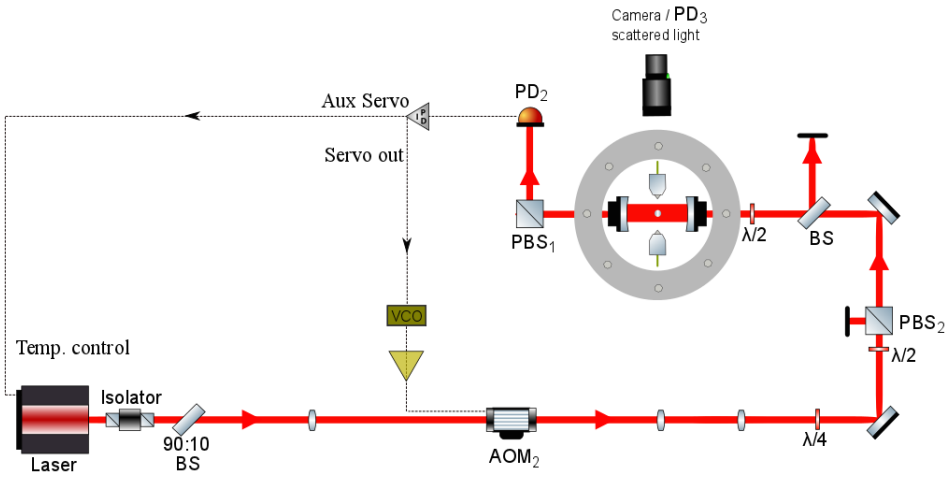

Figure 8.2: Side lock implementation for our experiment. The light transmitted by the cavity is detected by a photodiode (PD_2) and the signal is sent to a servo amplifier (Vescent D2-125). In the configuration represented here, the servo output controls the VCO which drives an AOM, for correcting the laser frequency. An auxiliary output is also employed as a slow correction acting on the laser's temperature, to compensate for slow frequency drifts.

In our experiment, the main advantage of such a setup is the fact that we can use just one laser beam to both lock to the cavity and apply optomechanical damping. Locking at half height of resonance means in fact being already red or blue detuned, by $\Delta_0 \simeq \pm\kappa/2$. The best way to find out which side is red and which is blue will be to trap a particle and look at the amplitude of its oscillations; only for the cooling case we will be able to see the bead localizing and getting optically trapped. Using only one laser beam means also that we are completely eliminating any unwanted beating effect happening between the weak and the strong beam at frequency $\Omega = \Delta_0$, as in the results of chapter 7. Hopefully in this way the cavity spectrum will present a lower noise floor and will offer a more sensitive readout of the mechanical motion around the region of interest $10 - 100\,\mathrm{kHz}$. On the other hand, the fact that we are using only the transmitted light, detuned from resonance, to detect the particle motion might actually reduce the sensitivity, respect to having an on-resonance lock, or a reference signal to use in heterodyne or homodyne detection. The main disadvantage of side lock is also the fact that we are not able to finely select the value of the detuning. The latter depends directly on the locking point, and any intensity fluctuation in the laser can change

it (although we can make the side lock intensity independent, as shown in section 8.1.1).

Figure 8.2 shows a representation of the side-lock implementation for the experiment. The strong beam goes through one AOM before entering the cavity, and the transmitted part of the beam is collected at PD_2. We use a servo amplifier (Vescent D2-125 Laser Servo) which contains a tunable PID filter loop that allows the input error signal to be fed back to the laser. The servo box has a main voltage output (servo output) and an auxiliary output, generated by integrating the servo output, and whose purpose is to drive the servo output to zero. We can use the latter to correct for slow frequency drifts by acting on the temperature control of the laser, while the main servo output goes to a VCO that controls the AOM. Alternatively, one can use the PZT laser control and keep the AOM frequency fixed, or try different combinations.

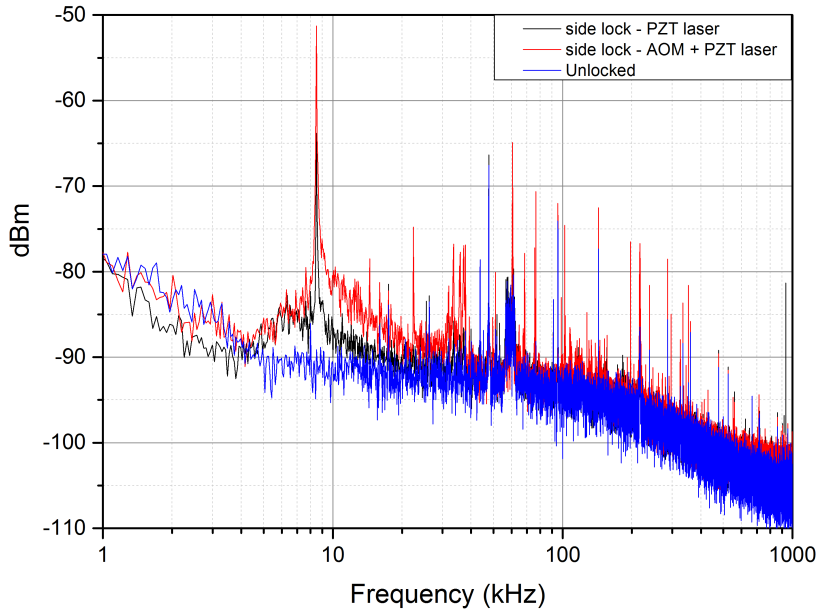

Figure 8.3: Power spectra of the empty cavity (no particles trapped) transmitted signal for the side lock. In one case (red curve) the servo output is sent to the VCO that controls the AOM, while a slower correction, from the auxiliary output, controls the temperature of the laser. The black curve represents the case of the laser source being controlled by both signals, and the AOM is kept at constant frequency. The blue curve is the signal detected when no lock is on.

The power spectrum of the transmitted cavity light that we obtain by locking with such a scheme is reported in figure 8.3. Here three different spectra are compared, in the case of empty cavity (no particles present): the red one is obtained by using the AOM to control the laser's frequency, while the auxiliary output is sent to the laser's temperature (as in figure 8.2). The black spectrum instead, corresponds to the servo output acting on the PZT laser control, and the AOM is not modulated. The blue curve is the noise spectrum of the unlocked signal. The main peak at $\simeq 8.5\,\mathrm{kHz}$ is a common feature of all the locked

signals (also visible with the Pound-Drever-Hall locking) and indicates a particular mode of vibration of the cavity structure. Although the two locking options look very similar from the spectra of figure 8.3, the use of the laser piezo as the main feedback control seems to offer a slightly lower floor respect to the use of the VCO and AOM, around the mechanical frequencies region ($10 - 100\,\mathrm{kHz}$). In addition, the former method gives a more durable stability of the lock, which is always preferable.

8.1.1 Balanced detection

One main difficulty of the side lock scheme as presented in the last section is the fact that we need to keep the input intensity fixed at all times, to keep the locking point fixed and ensure a constant detuning. This prevents us from changing the input power at PBS_2 (useful control over the trapped particles) without modifying the cooling conditions. One way to make the side lock intensity independent is to take the error signal as the difference between the signal coming from the cavity and a reference signal from the laser. If they have same amplitude, any change in the laser intensity won't affect the relative difference between the DC reference and the cavity transmission, keeping in this way the locking point always constant.

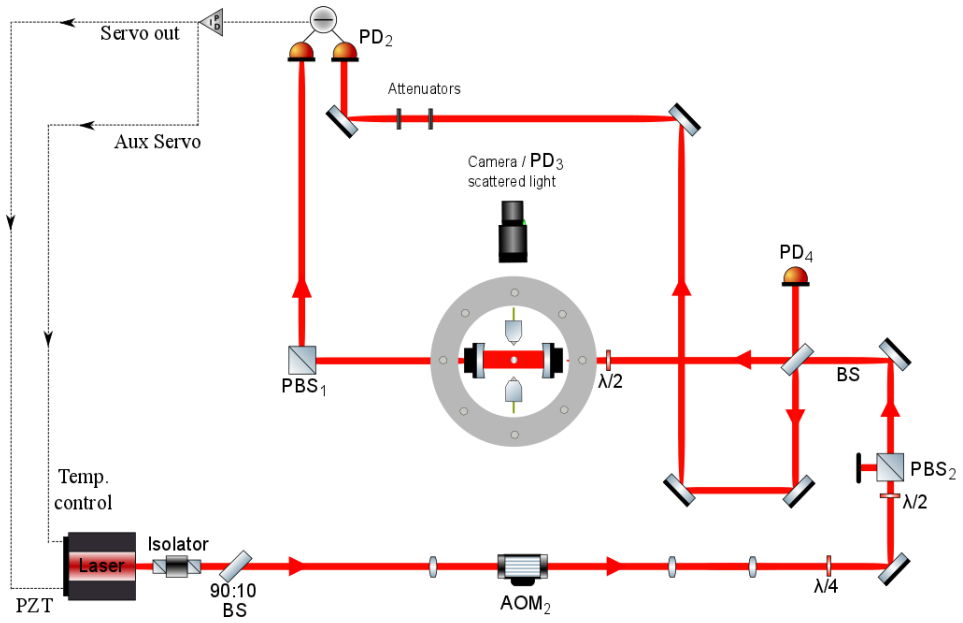

Figure 8.4: Scheme of side lock with balanced detection. The light transmitted by the cavity is subtracted to the laser signal picked up after PBS_2, and before entering the cavity. The difference signal is now used as the error signal to be fed back to the laser.

Figure 8.4 shows how the optical scheme has been modified to implement intensity independent side locking. We use a balanced amplified detector (Thorlabs PDB210C) at PD_2 where we collect at the same time the transmitted signal from the cavity and a portion of

the laser beam, before entering the cavity. The latter can be attenuated by using neutral density filters before the beam reaches the photodiode. The balanced detector subtracts the two optical signals from each other, resulting in the cancellation of common mode noise. The resulting signal will be independent from the laser intensity changes, which happen on both beams at the same time. Also in this case, the servo output is sent to the laser piezo, and the slow control goes to the laser temperature.

To compare the sensitivity of the balanced signal to the previous case, we look at the frequency spectrum. To go from dBm to $\mathrm{Hz}^2/\mathrm{Hz}$ we first pass to Volts squared per units of bandwidth, as already explained in section 5.7 (equation (5.15)). To obtain frequency units, we then need the FWHM (Hz) of the cavity, and divide that by the measured amplitude of the transmission peaks at the detector, A_d (Volts), to have a factor $c = (\mathrm{FWHM}/A_d)^2$. The conversion to be performed then is:

$$y\left[\mathrm{Hz}^2/\mathrm{Hz}\right] = c \cdot 0.05 \cdot 10^{\frac{y[\mathrm{dBm/Hz}]}{10}} \tag{8.1}$$

Figure 8.5 shows two different spectra taken before and after implementing the balanced detection for the side lock. Between 10 and 100 kHz the curves appear to have a different sensitivity and the noise floor for the balanced case is lower by a factor of 10.

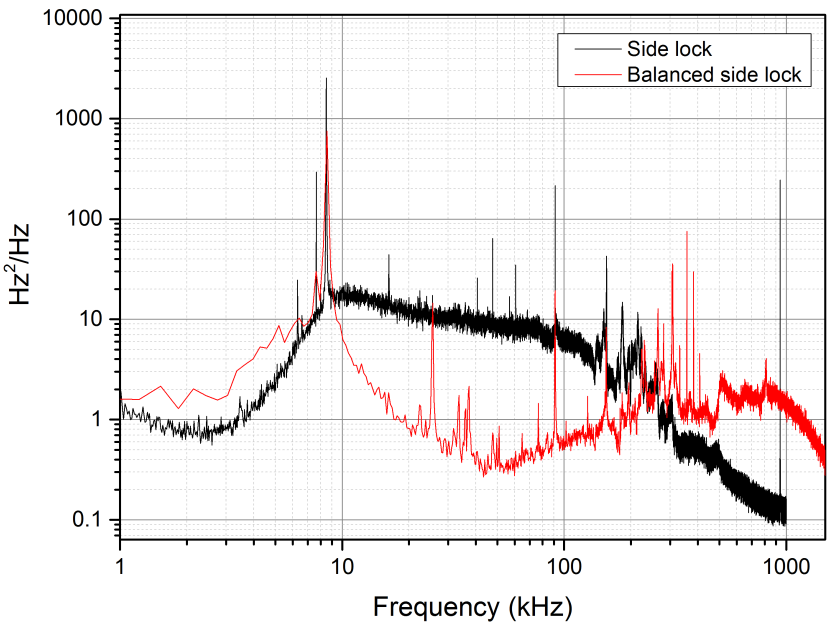

Figure 8.5: Comparison between the frequency spectra taken for side locking with (red) and without (black) balanced detection. The former shows a higher sensitivity around the region of interest ($10 - 100$ kHz). The laser power entering the vacuum chamber for the simple side lock case is 40 mW, while for the balanced case it is $\simeq 20$ mW.

Using the balanced side locking on the red side of resonance, particles are stably trapped

and one can look at the characteristic mechanical features of their hybrid motion in the power spectrum of the error signal (i.e. cavity transmission). An example is reported in figure 8.6, where the PSD, in units of V^2/Hz , was obtained by subtracting a background PSD taken with no particle trapped to the ones containing the mechanical motion of the nanosphere. The signal has been recorded for three different values of pressure and for all of them both the linear component $\omega_M \pm \omega_d$ and the quadratic one $2\omega_M$ are clearly visible. This means that with side locking the trapping of the particle can be very stable even at low pressures (here the cavity finesse is $\simeq 40,000$), but at the same time cooling is difficult to optimize, due to the uncertainty over the values of the detuning, and that is why no significant damping is observed as a function of the pressure.

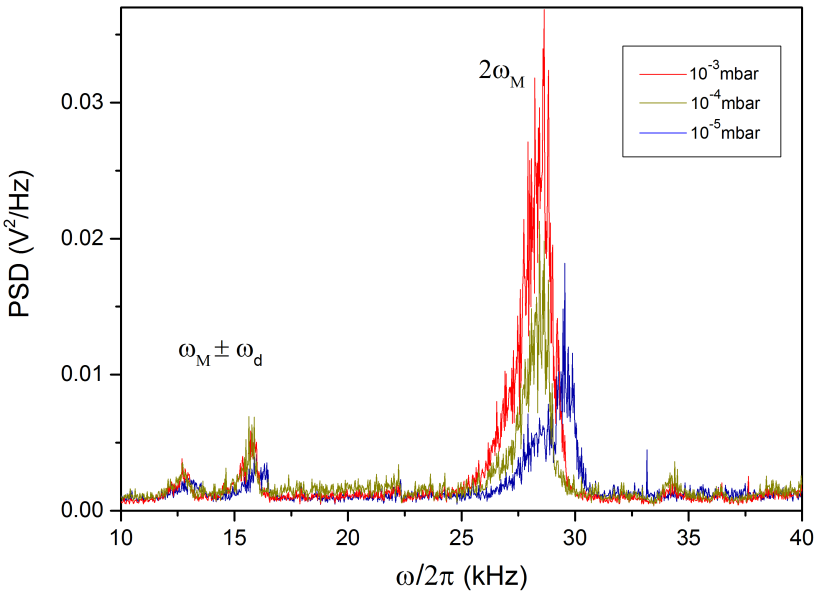

Figure 8.6: Steady state spectrum of a trapped particle using balanced side locking. The linear and quadratic components of the mechanical motions are visible down to the lowest pressure reached (10^{-5} mbar). Background noise coming for a PSD taken after loosing the particle has been subtracted to all three spectra. Despite the red detuned locking no significant damping is visible, due to the difficulty in optimizing the value of the detuning.

8.2 Second laser

Two laser beams can also be used to lock the cavity. The probe beam must be locked to a cavity resonance, and a second beam is required to cool the particles motion. We still need to eliminate beating effects happening at the detuning to decrease the level of noise around the mechanical frequency peaks. This can be done by having the two laser beams operating on different cavity modes, which are going to be separated in frequency by a few GHz. Any beating will now occur at very high frequencies with respect to the $10 - 100$ kHz range that

we are interested in observing. As such a big frequency difference for two beams coming from the same laser source is difficult to achieve, two separate sources, independently tuned around the cavity resonances, can be employed.

In our case, the frequency separation between two different cavity transverse modes can be calculated using equation (8.27) of Appendix C, for a cavity length $L = 13.5 \pm 0.2\,\text{mm}$ and radius of curvature of the mirrors $r_c = 25\,\text{mm}$. The difference between the fundamental cavity mode TEM_{00} and the first higher order mode TEM_{10} (or TEM_{01}) is $(\nu_{1,1,0} - \nu_{1,0,0}) = 3.86 \pm 0.3\,\text{GHz}$. One could then use one laser to lock onto the TEM_{10} mode and a second one to hit the TEM_{00} for the cooling. The technique employed to lock both lasers to the two respective cavity modes is described in section 8.3.

We employ a 1064 nm single mode solid state laser (Lighwave electronics M101-1064-V70), which has a bandwidth of 5kHz and maximum output power of 5 mW, as the weak beam that is locked to the TEM_{10} mode. To be able to tune the laser around the desired cavity mode, and apply the feedback from the PDH, we bonded a thin piezoelectric disk to the monolithic crystal of this laser, as shown in the photo of figure 8.7.

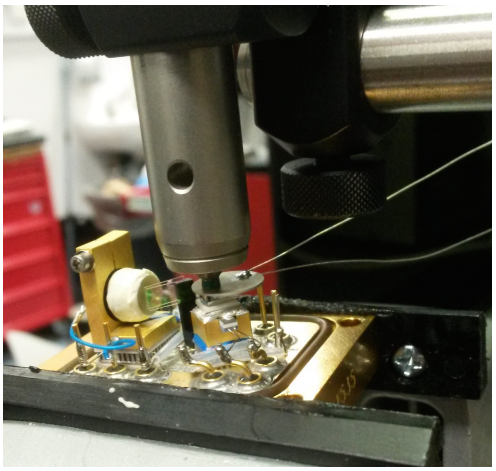

Figure 8.7: A picture of the glueing process carried out to bond the piezo element onto the laser crystal. After applying epoxy in between the piezo and the laser crystal we keep pressure on the piezo from the top, and let the glue dry for a few hours. Two wires have been soldered to the sides of the piezo to apply the voltage needed for frequency modulation.

The piezoelectric element is a 0.25 mm thick plate of diameter 5 mm, and it was glued with vacuum epoxy to the non-optical face of the monolithic resonator. Two wires have been soldered onto the two sides of the piezo, and attached to a BNC connector to receive the voltage signal from the outside, for frequency modulation.

To check the sensitivity of the piezo element we test it using a confocal Fabry Perot cavity (Thorlabs SA200 9A) which has a free spectral range of 1.5 GHz. We use a spectrum analyzer controller to generate a sawtooth wave voltage, required to repetitively scan the length of the FP cavity in order to sweep through one FSR of the interferometer. After aligning the

laser to the cavity we see the resonance peaks appearing on the oscilloscope, the distance between two adjacent ones being $\simeq 4.64\,\mathrm{ms}$, which corresponds to one FSR. When we then apply a voltage to the piezo mounted to the laser we see the peaks shifting by $5\,\mu\mathrm{s}$ per Volt. This means that the tuning sensitivity is $\simeq 1.6\,\mathrm{MHz/V}$.

It is now essential to know the waist of the new laser in order to choose the coupling lenses to be used in the experiment for the mode matching which maximize the cavity coupling. We maintain the same path used so far for the weak beam (see for example figure 5.1), and we perform the waist measurement by placing a CMOS camera on a translational stage along the beam path, close to one of the regions where we know the beam is focalizing, namely where the EOM normally sits. Here, we take pictures of the beam profile at different distances from a set point, corresponding to the focusing lens placed before the EOM. The images have been subsequently analyzed on Matlab to evaluate the width of the beams Gaussian profile, knowing the camera resolution ($5.2\,\mathrm{pixels}/\mu\mathrm{m}$). The measured values are plotted in figure 8.8.

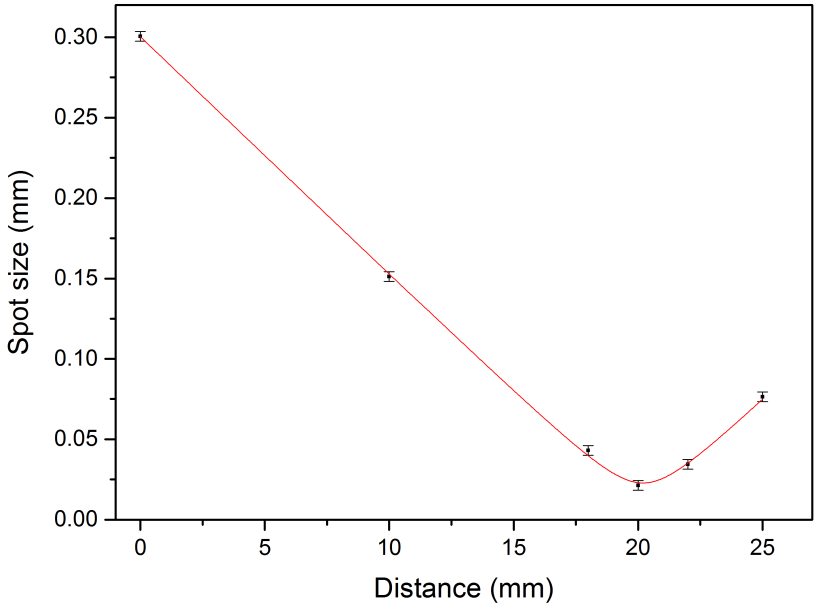

Figure 8.8: Waist measurement for the weak laser. The different spotsizes have been evaluated by analyzing images of the beam's transverse intensity profile, taken with a CMOS camera. The distances on the x-coordinate are taken from an initial distance x_0 to a reference point, represented by a focusing lens along the beam's path.

The fitting function corresponds to the relation (8.28) as expressed in Appendix C:

$$w(x) = \sqrt{w_0 \left[1 + \left(\frac{\lambda\,(x - x_0)}{\pi w_0^2}\right)^2\right]}, \tag{8.2}$$

where x_0 is the initial distance from the focusing lens, at which the first picture is taken, and

w_0 is the laser waist that we can extract from the fit, and we obtain $w_0 = 22.84 \pm 0.2\,\mu$m.

8.3 Optical phase locking

In order to keep the weak and the strong lasers at the same frequency difference and have them both locked to the cavity, on the TEM_{00} and TEM_{10} modes, we employ an optical phase-locked loop (OPLL) [151, 152]. In electronics, a phase-locked loop (PLL) is a negative feedback control system that drives the phase of an oscillator to track the phase of a reference oscillator. For a simple sinusoidal signal we define phase the signal:

$$\phi = A\cos\left(\omega t + \theta\right), \tag{8.3}$$

where A is the signal's amplitude, ω is the angular frequency and θ is the phase offset. An electronic PLL usually consists of four essential elements: a phase detector, a loop filter, a voltage-controlled oscillator (VCO), and a reference oscillator. The VCO is controlled by a voltage input and generates an output signal with frequency $\omega_0(t)$ and phase $\phi_0(t)$. The reference oscillator provides a known stable frequency signal to which the PLL can phase lock, with frequency $\omega_{\mathrm{ref}}(t)$ and phase $\phi_{\mathrm{ref}}(t)$. VCO and reference signals are compared at the phase detector, which outputs an error voltage based on the phase difference between the two inputs given by:

$$\phi_e(t) = \phi_{\mathrm{ref}}(t) - \phi_0(t). \tag{8.4}$$

The error voltage is then processed by the loop filter to become the control voltage of the VCO, thus closing the feedback loop. The negative feedback causes the control voltage to modulate the VCO center frequency, adjusting $\phi_e(t)$ to a constant. Since frequency is the time derivative of phase, phase tracking also means that $\omega_0(t) = \omega_{\mathrm{ref}}(t)$. The loop is considered locked when the average frequency of the VCO, is equal to the average frequency of the reference oscillator.

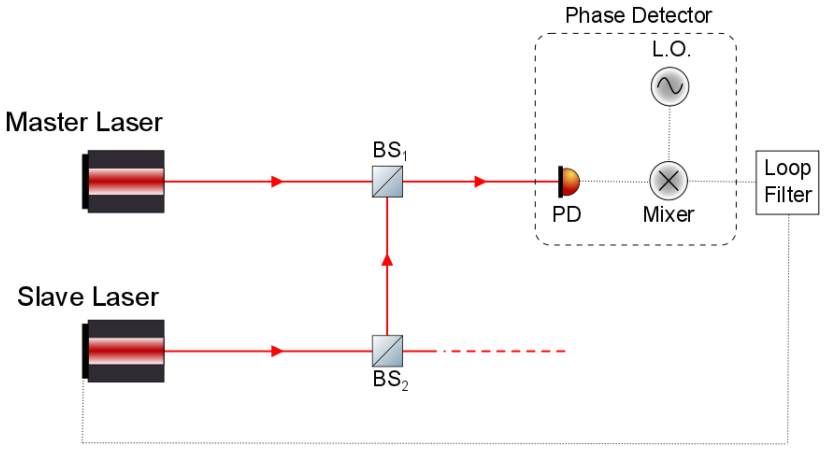

Figure 8.9: Schematic for an optical phase-locked loop: a master and a slave laser are overlapped at BS_1, and the resulting beat-note is detected by a photodiode (PD). The PD signal carries the information about the frequency and the phase difference between the lasers and is compared to a reference signal from a local oscillator (L.O.). The output is then sent to a loop filter and finally fed back to the slave laser to control the frequency of the beat note.

Optical phase locking is a natural extension of PPLs, and it can be used to phase lock two lasers. As shown in figure 8.9, an OPLL is composed of four main parts: a master laser, a slave laser, a phase detector, and a loop filter. The master laser serves as the frequency and phase reference for the slave. In order to obtain information on the frequency and phase difference between the lasers, the master and the slave are mixed with a beam splitter and the beat signal detected with a photodiode which serves as the phase detector. The resulting beat-note signal contains the relevant information about the frequency and phase difference between the lasers, thus providing the error signal needed by the feedback loop to compensate for any deviations in frequency and phase between the lasers. If it is necessary for the lasers to operate at different frequencies, then a local oscillator must be used to mix down the beat-note signal from the photodiode. In this case, the local oscillator will determine the frequency difference between the two lasers and can be used to tune the frequency of the slave relative to the master laser.

In our experiment we use an offset phase servo (Vescent D2-135) which locks the frequency and the phase of an input beat-note to a reference frequency signal (the local oscillator mentioned above), which can be sourced internally from a VCO, or externally from a user-input frequency reference. By adjusting the latter, the frequency difference between the lasers can be adjusted from 250 MHz to 10 GHz. This feature gives us the possibility to carefully tune the frequency offset between the weak and the strong laser and have fine control (depending on the precision of the reference source) over the detuning of the cooling laser. A complete scheme of the experimental setup is represented in figure 8.10.

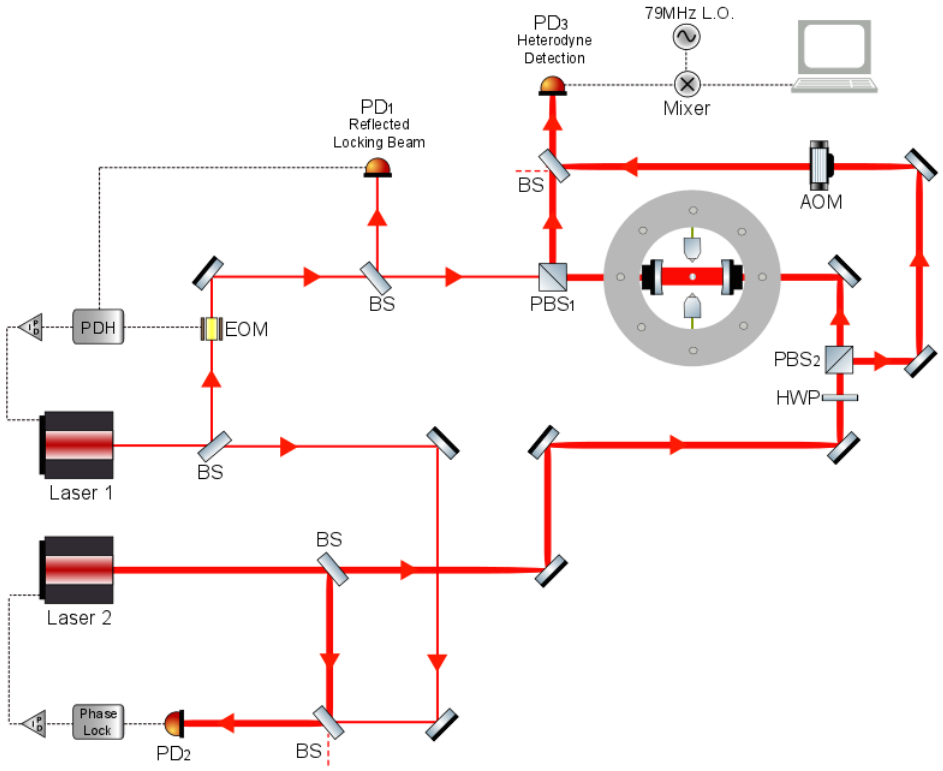

Figure 8.10: Experimental setup: Light from two solid state lasers enters the optical cavity from opposite directions, at two different powers and frequencies, resonating inside the cavity at two different transverse modes. The weaker laser is tuned around the TEM_{10} mode and kept locked to the cavity via the Pound-Drever-Hall method (PD_1). The stronger laser is instead phase-locked to the weak one, by constantly monitoring the beating between the two at PD_2, and hits the TEM_{00} mode inside the cavity. Red or blue detuning can be obtained by shifting the frequency of the phase lock. An heterodyne detection is performed on PD_3, between the signal transmitted by the cavity and a portion of the strong laser beam, shifted by 80MHz with an AOM. The detected signal is then mixed down to 1 MHz and sent to an oscilloscope.

The weak beam (Laser 1) is used to keep the laser locked to the cavity on the TEM_{10} mode of resonance, via the Pound-Drever-Hall, by collecting the cavity reflected signal on PD_1, while the stronger beam (Laser 2) is used for trapping and cavity cooling. The latter is locked in phase to the weak laser, measuring their frequency difference through the beat-note signal obtained by superimposing the two laser beams on a fast photodiode PD_2. In this way, the strong beam sits on the fundamental cavity mode TEM_{00}, and its frequency can then be shifted with respect to the cavity resonance, to attain the desired detuning, by adjusting the externally-sourced reference frequency of the phase lock. The mechanical frequencies of the particle can be observed from the heterodyne spectrum of the recorded time series after the particle is trapped. The transmitted cooling light from the cavity is heterodyned with a portion of the strong beam, from PBS_2, which is not sent into the cavity, and it is frequency shifted by 80 MHz using an acousto-optic modulator (AOM). The resulting beat note signal at 80 MHz, detected on PD_3, is finally mixed with a local oscillator at 79 MHz,

to obtain a beat frequency of $\Omega = 1\,\mathrm{MHz}$ which can be observed on the oscilloscope. The mechanical motion is observed as heterodyne sidebands around this peak in the spectrum at $\Omega \pm \omega_\mathrm{M}$ due to G_1 coupling and at $\Omega \pm 2\omega_\mathrm{M}$ due to G_2 coupling. At this stage of the experiment, the cavity finesse has been increased to $\mathcal{F} \simeq 250,000$ (which means a cavity linewidth $\kappa \simeq 45\,\mathrm{kHz}$), by cleaning the cavity mirrors (see section 8.4).

Figure 8.11 shows an example of the noise spectrum obtained for a trapped particle at pressure $p = 5 \times 10^{-2}\,\mathrm{mbar}$, while having the strong beam locked on resonance (detuning $\Delta_0 = 0$). Traces of the particle's mechanical motion are visible on the right hand side of the heterodyne peak $\Omega = 1\,\mathrm{MHz}$. A symmetric double sideband centered on the mechanical frequency $\omega_\mathrm{M} \simeq 18\,\mathrm{kHz}$, with splitting $\pm\omega_\mathrm{d}$ given by the micromotion from the Paul trap is visible, as well as a dominant single peak at $2\omega_\mathrm{M}$. Based on what described in section 7.2, for the case in figure 8.11 we can estimate a well number $\mathrm{N} \sim 5 - 10$.

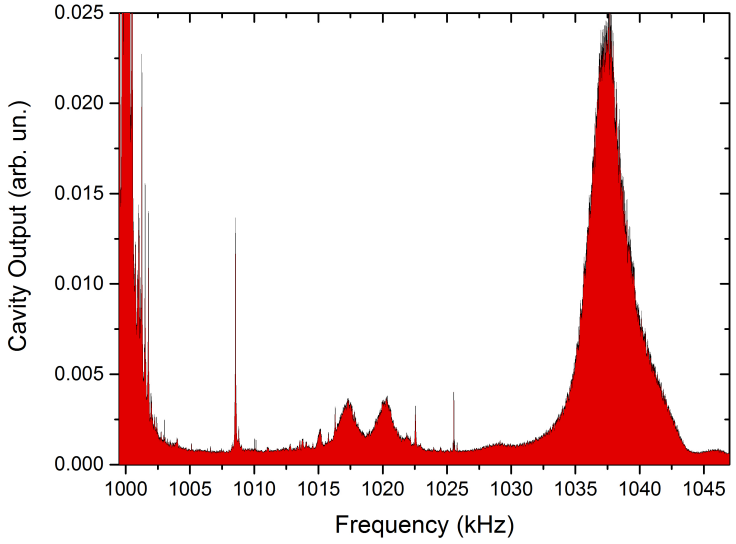

Figure 8.11: Spectrum of the heterodyned cavity output as the particle is optically captured in a low well $\mathrm{N} \sim 5 - 10$, where, G_2-driven $\gtrsim$ G_1-driven modulations of the intracavity field. The G_2 modulations are frequency doubled $2\omega_\mathrm{M}$ peaks, where ω_M is the mechanical frequency. The G_1 modulations are at $\omega_\mathrm{M} \pm \omega_\mathrm{d}$ where ω_d is the driving frequency of the Paul trap. Here mechanical frequencies appear as sidebands of the $\Omega = 1\,\mathrm{MHz}$ heterodyne peak, at $\Omega + (\omega_\mathrm{M} \pm \omega_\mathrm{d})$ and $\Omega + 2\omega_\mathrm{M}$. Pressure is $p = 5 \times 10^{-2}\,\mathrm{mbar}$, and we have a cavity finesse $\mathcal{F} \simeq 250,000$. Here no optomechanical cooling is applied yet, as the strong beam is kept locked on resonance ($\Delta_0 \simeq 0$).

In figure 8.12, we show how the non-linear motion, represented by the G_2 peak at frequency $\Omega + 2\omega_\mathrm{M}$, responds to changes in the pump laser detuning, obtained by shifting the reference frequency of the phase lock. Particle was stably trapped within an optical well $\mathrm{N} = 5 - 10$, at fixed pressure of $5 \times 10^{-2}\,\mathrm{mbar}$. At this pressures, background gas is the main source of noise heating and prevents the particle to be cooled as much as already observed in chapter 7.

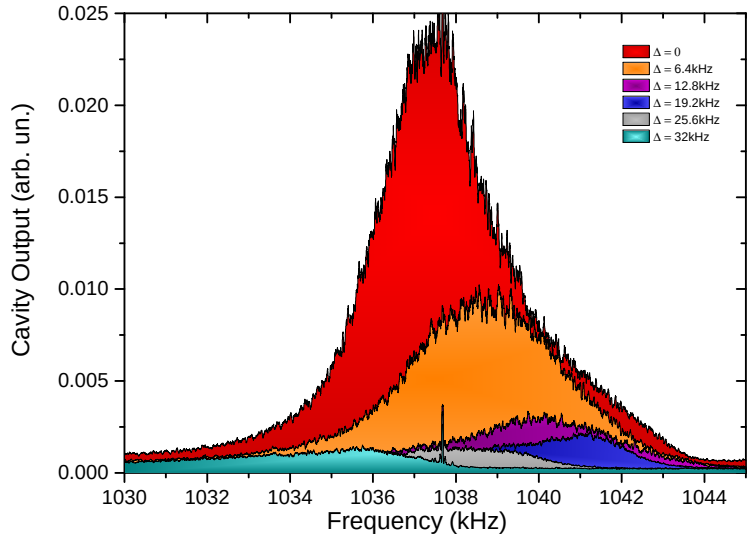

Figure 8.12: Cooling of the quadratic part of the motion, represented by the $\Omega + 2\omega_{\mathrm{M}}$ peak, as a function of the laser detuning. Particle was trapped in a low optical well ($\mathrm{N} = 5 - 10$) at a pressure of 5×10^{-2} mbar.

Nonetheless, a reduction in the area under the peaks is clearly visible, as the pump laser frequency is red detuned in steps from cavity resonance ($\Delta_0 = 0$) to $\Delta_0/2\pi = -32\,\mathrm{kHz}$, which is beyond half of the cavity linewidth. By measuring the area under the different peaks, whose values are plotted in figure 8.13, we obtain a factor of 20 decrease.

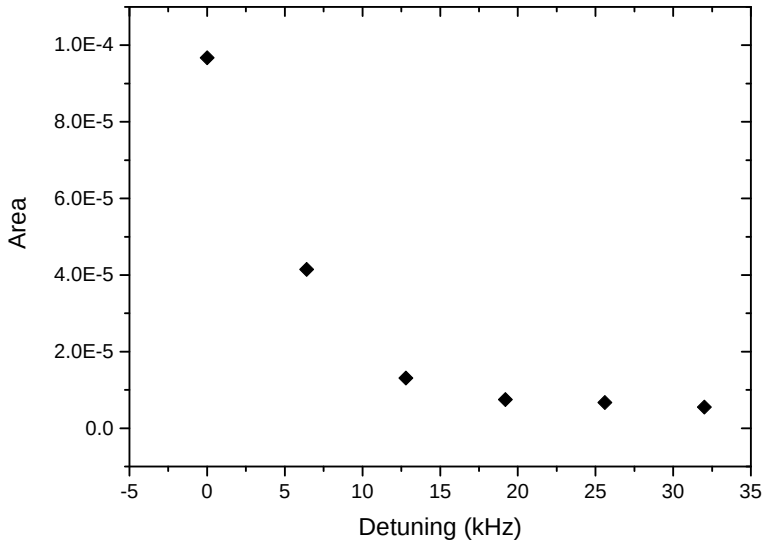

Figure 8.13: Decrease in the area under the $\Omega + 2\omega_{\mathrm{M}}$ peaks, as a function of the detuning. Its value is reduced by a factor of 20, going from resonance ($\Delta_0 = 0$) to a detuning $\Delta_0/2\pi = 32\,\mathrm{kHz}$.

8.4 Mirror cleaning

During the course of our experiments we observed many variations in the cavity finesse value, due to the amount of particles that were loaded and then lost by the trap, ending up sticking on the mirrors surfaces and decreasing their reflectivity. Despite the presence of the copper shield, used during every loading attempt, once particles were trapped the risk of loosing them and having them hit and stick on the mirrors was always present. Because of this, we had to replace the cavity mirrors at least twice, every time going through the assembly process described in section 5.4.

Cleaning high reflectivity mirrors can be a very delicate process as well, since most of the well known cleaning methods for optics [153, 154] could damage, scratch or remove part of the surface coating. With a mechanical cleaning technique for example, where a piece of lens cleaning tissue is folded, wet in acetone and swept with a tweezer from the center to the border of the mirror, can be dangerous since it is possible to produce additional scratches by dragging particles over the surface. A different option could be bathing in acetone or methanol: the mirror is placed into warm acetone or methanol of ultra high purity. After about 5 minutes the mirror is taken out holding the surface vertical such that no liquid drop can stay on the surface. If some liquid dried out on the surface, it would leave the dissolved dirt behind. One can even think about an ultrasonic bath, where the mirrors are placed into a small vessel filled with pure acetone and put into an ultrasonic bath for about 5 minutes. This device is filled with water and produces ultrasonic vibrations of the liquid which remove particles from the surface. However this is not something that can be done without taking the mirrors off the cavity first, and the risk of damaging them is high.

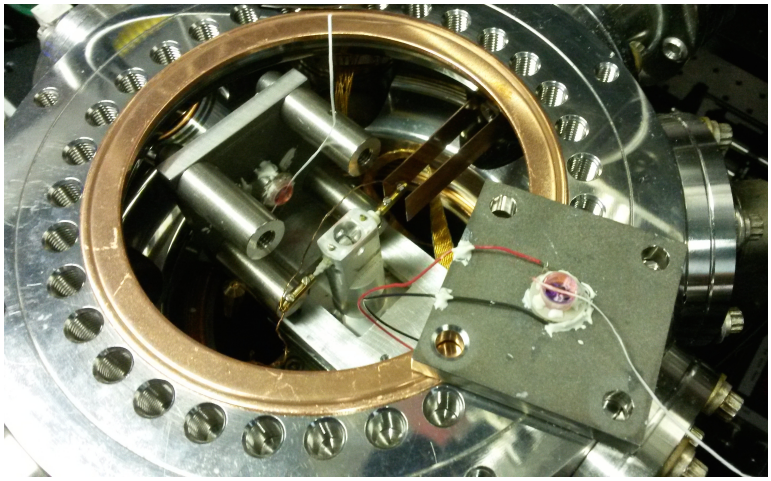

Figure 8.14: Picture of the experimental apparatus while cavity mirrors are being cleaned. The cavity structure can be temporarily unmounted to access the two mirrors more easily. The cleaning polymer is applied on the mirrors surfaces and dental floss is placed on top, to create a "handle" for pealing the polymer off, after letting it dry. For a better result, both cavity ends can be extracted from the chamber and rested on their external faces; having the mirrors facing up guarantees a more even distribution of the polymer on their surfaces.

The best option for us is cleaning with polymer film: a droplet of special polymer (polypropylene or polyetheretherketone) solution is poured, brushed or sprayed on the surface of the mirrors. The polymer flows over the surface as a homogeneous layer and embeds the particles. As the polymer dries to a film, organic compounds are dissolved and particulates are encapsulated by the polymer. Peeling off the polymer film reveals a pristine optic surface that is as clean as or cleaner than new. Several repetitions of the procedure might be needed to guarantee the removal of all particles. In rare cases the polymer can stick to the side of the mirror if too much was used, this residue has then to be removed with acetone. In general, using the polymer is fast and safe, since there is almost no risk of damaging the surface.

We decided to go for the last method, applying a few drops of red colored polymer solution (First Contact, Photonic Cleaning Tech.) on each mirror, and placing a short bit of unwaxed dental floss on top (an additional drop of polymer can be added to glue the floss down). After the solution dries up (30 - 40 minutes) we can carefully pull the exposed end of floss to peel off the polymer. As shown in the photo of figure 8.14 we can perform the cleaning of the two cavity mirrors separately, by separating the two ends of the cavity structure. Once the polymer is removed, and the cavity has been realigned, we can check the cavity finesse.

The example in figure 8.15 shown the ringdown effect visible at the cavity output after cleaning the mirrors, by scanning the strong laser at 2kHz. The decay time measured, $\tau = 6.35 \pm 0.1\,\mu$s, suggest that a finesse $\mathcal{F} = 440,000 \pm 9000$ has been reached.

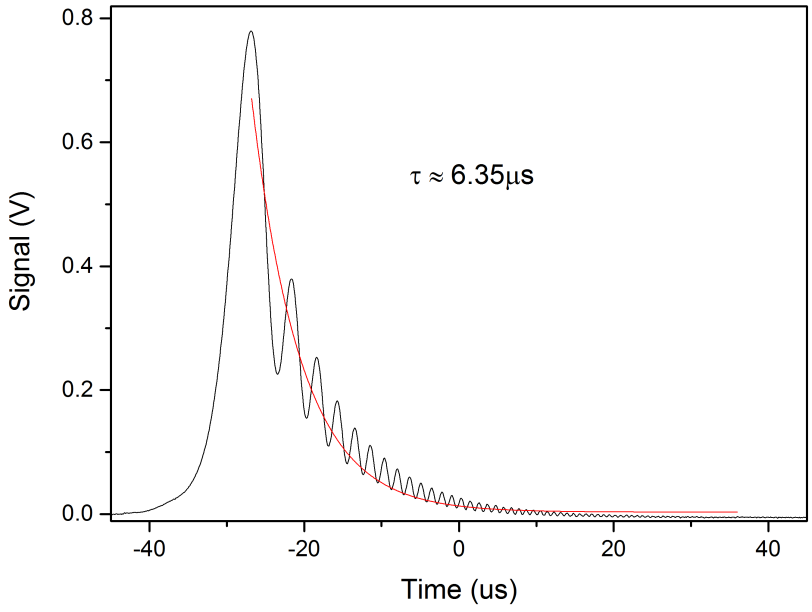

Figure 8.15: Ringdown measurement obtained by scanning the laser frequency at 2 kHz. The exponential fit gives a decay time $\tau \simeq 6.35\,\mu$s, corresponding to finesse $\mathcal{F} \simeq 400,000$.

8.5 Future perspectives

The hybrid electro-optical system presented in this thesis already demonstrated cavity cooling by a factor of $\sim 10^4$, of the centre-of-mass motion of levitated silica nanospheres in high vacuum. We believe that ground state cooling is within reach with this system at this stage, where the only main limitation has been identified to be the lack of sensitive means to read-out the particles motion, as they are even too cold for reliable temperature measurement. To overcome this problem, further technical improvements, consisting on a state-of-the-art homodyne detection, are being currently implemented. Such a technique involves bringing the light beam transmitted by the cavity to interfere with a local oscillator of same frequency, and split the resulting signal into two equal portions, that will be collected with a balance detection. The signal difference obtained will be a null-average, sinusoidal function of the path difference between the two beams. Such signal can be used as the error signal of a feedback loop that locks the phase of the two beams, by acting on an electromagnetically driven mirror along the local oscillator optical path. This type of detection seems attractive as it is barely sensitive to laser power fluctuations, and it allows specific read out of a specific phase quadrature of the cavity light, where the information on the particle's motion is maximum.

At the same time, a noise budget analysis has to be carried out to find the main sources of noise in the system, and if possible reduce them. Substrate vibrational noise, electronic noise and laser noise will have to be controlled at a level comparable to the photon shot noise, in order to have a displacement sensitivity able to reveal motional temperatures in the μK range, that, for mechanical frequencies of $10 - 100\,\mathrm{kHz}$, correspond to a thermal occupation $n_{th} \lesssim 1$. In this sense, possibly a new cavity structure will have to be designed, such to offer high finesse for sideband resolved cooling, and better mechanical stability to reduce vibrations.

As far as the Paul trap is concerned, as we have seen it is instrumental to achieve low pressure, but it introduces a higher degree of complexity in the dynamics of the particles. An important step will be to modify the Paul trap such that, after the particle has been initially cooled, we can turn off the AC field and to add a constant voltage. In this way nanoparticles can be levitated in an optical field with only a constant DC field applied, and it will be possible to shift them from a cavity antinode allowing a fine control on the ratio between linear and quadratic coupling, and maximize optomechanical cooling. Alternatively, additional cooling in the Paul trap could be implemented [155]. In particular, one can implement an active feedback cooling mechanism, by detecting the secular motion of the particle and feed the signal back to the Paul trap electrodes. This would be used to damp the motion of the particle in the radial directions, while the cavity cools down the

axial motion.

The technical steps towards cooling to low phonon numbers, including the suppression of conventional sources of noise (e.g. parametric heating from lasers, blackbody radiation, background gas), offer not only a future quantum technology but also allows laboratory tests of models postulated to account for the rapid collapse of macroscopic quantum superpositions (see section 2.1). To isolate the contribution given by the continuous spontaneous localization (CSL), which acts as an additional (non-conventional) source of noise from the standard decoherence predicted in the framework of quantum mechanics, a specific protocol for the hybrid trap has been proposed in [83]. The basic idea relies on the simple technique of parametric heating of the trapped nanosphere in high vacuum once the particle has been cooled to a low phonon number. The heating due to the noise sources in the system is allowed to act for a period of time after the cavity cooling has been turned off. After waiting for a fixed period of time the increased position/energy of the oscillator is measured via a cavity homodyne measurement. The final phonon number is then compared with predictions obtained with and without CSL. This approach has two appealing aspects. First, by levitating the particle only with the Paul trap it is possible to remove the major heating process, that is, optical scattering. Second, ground state cooling in the Paul trap potential is not strictly necessary. Experimentally, we can see two potential issues. First, the center of the Paul trap potential needs to be accurately aligned with the antinode where the nanoparticle is localized otherwise when the cooling beam is shut off the particle will acquire additional momentum thus increasing the phonon number in the Paul trap. Second, a measurement strategy needs to be devised to determine the final occupation number after the evolution in the Paul trap alone. An intriguing possibility towards the solution of both issues is to trap highly charged particles so that the trapping potential is dominated by the Paul trap while the cavity field is exploited for cooling and measurement. Injection of highly charged particles is already being investigated by the our group.

Clearly, all possible sources of noise generating decoherence have to be reduced as much as possible, to make the CSL effects more visible. One characteristic that many schemes for collapse test have in common (see for example [84]) is the requirement of a cryogenic environment in order to minimize blackbody recoil heating. Implementing the described protocol will then require the development of a new dedicated setup and to adapt current technology of the hybrid trap for operation in a cryogenic environment. However, an important step will be the experimental demonstration of the viability of the technique at room temperature.

Summary and conclusions

This thesis has presented a hybrid optical and quadrupole electric trap for both confining and optomechanically cooling charged levitated dielectric nanoparticles in high vacuum. We use a Paul trap to electrodynamically levitate charged silica nanospheres while the field from a high finesse optical cavity further confines and cools them.

In our system, a silica nanosphere, typically with a 1-3 elementary charges on the surface, is first trapped within the Paul trap. The latter consists of two opposing cylindrical electrodes of diameter 1mm on which a high voltage ($600 - 800\,\mathrm{V}$) at audio frequencies ($1.5\,\mathrm{kHz}$) is applied. The electrodes, when combined with concentric grounded shield electrodes, provide a well defined, near quadrupole trap with excellent optical access. The intracavity optical field passes through the centre of the Paul trap producing an overlapping optical and electrical potential suitable for cavity cooling. The optical cavity is formed by two plano-concave mirrors, attached to the two opposite ends of a unique invar structure, holding them at a fixed distance, and where one of the mirrors is glued to a piezoelectric disk for tuning the cavity resonance, via cavity length modulation. The optical cavity is placed within a vacuum chamber which can be pumped to $10^{-6}\,\mathrm{mbar}$ using a turbo molecular pump. The Paul trap is mounted on a x-y-z translation stage, and it is placed within the centre of the cavity. The stage allows the particle trapped in the Paul trap to be centered within the cavity field. A long working-distance microscope with camera is used to image the trap region, from the top of the vacuum chamber. The camera can be replaced by a amplified InGaAs diode to detect the scattered light from the particle as function of time. A single frequency Nd:YAG laser is used to produce the cavity field. The Pound-Drever-Hall scheme, which applies feedback to a piezoelectric actuator in the laser, is used to lock the laser onto the TEM_{00} cavity resonance. The laser beam is split into two components, with a weak beam used for locking, and the other shifted in frequency using two AOMs, to provide red-detuned light for cooling. The weak beam is at a low enough intensity that it does not significantly perturb the motion of the trapped particle, while the cooling beam is 50 times more intense, and in all experiments is detuned to the red by half of the cavity linewidth, $\kappa/2$. Nanospheres of radius $209\,\mathrm{nm}$ are introduced into the trap at a pressure of approximately $0.1\,\mathrm{mbar}$ using a piezoelectric

speaker that is driven by a signal generator. To prevent clumping of the particles they are sonicated in a methanol solution for greater than 1 hour before being deposited to dry on the piezoelectric speaker. To prevent accumulation of the nanoparticles on the mirrors, movable shields are placed in front of each mirror while the particles are loaded into the Paul trap. After $\approx 1\,\mathrm{s}$ of continuous loading, the piezoelectric speaker is turned off and the shields are removed. The weak laser beam is then locked onto resonance, and cooling occurs within the field of the stronger red-detuned beam that counter-propagates to the locking beam. The vacuum chamber is then pumped down to a low enough pressure that damping due to cavity cooling dominates over damping due to residual gas, which corresponds to a pressure of approximately $10^{-4}\,\mathrm{mbar}$.

In the first part of the thesis, we investigated the dynamics of the nanoparticles in the hybrid trap, which result from the combination of the particles motion in the Paul trap potential and its simultaneous interaction with the cavity standing wave. The deep, but spatially broad, potential of the Paul trap is modulated by the periodic potential of the standing-wave optical field, and cooling occurs when the nanoparticle has low enough energy to be trapped and localized within a single antinode of the standing wave. Once optically captured, the particle undergoes a relatively complicated motion which consists of a combination of harmonic motion in the optical potential (with mechanical frequencies ω_{M} of $\sim 10\,\mathrm{kHz}$) and a lower frequency motion due to the Paul trap (with driving frequency $\omega_{\mathrm{d}} = 1.5\,\mathrm{kHz}$). We note that the motion induced by the Paul trap acts to periodically pull the particle away from the centre of the antinode, where cooling becomes inefficient. For this reason, the optomechanical cooling rate is modulated in time by the Paul trap micromotion, and it depends on which optical well the particle is trapped in.

When looking at the light scattered by the particle, in the red-detuned regime, the signal showed periods of free motion, characterized by the secular and micromotion oscillations in the Paul trap, and periods of captured motion, always corresponding to an average increase in the scattered light. Here, the motion was dominated by mechanical oscillations within one antinode, along the cavity axis, but we note that the low-frequency secular motion could be still observed, due to motion in the radial direction of the cavity light field. Indeed, a range of frequencies was visible in the scattered signal's power spectrum; in particular the mechanical motion is characterized by components at $\omega_{\mathrm{M}} \pm \omega_{\mathrm{d}}$, as well as $2\omega_{\mathrm{M}}$. The relative heights of these components could be used to calculate the cooling rate of the nanoparticle's motion.

The first results reported in this thesis were obtained using a cavity with finesse $\mathcal{F} \simeq 15,000$, and an intracavity power $P = 14\,\mathrm{W}$. At a pressure of $10^{-4}\,\mathrm{mbar}$ we found an optomechanical cooling rate $\Gamma_{\mathrm{opt}} \approx 20 - 30\,\mathrm{Hz}$, bringing the centre-of-mass temperature of the nanoparticle

from 300 K to a final value of ~ 10 K. We found that the nanospheres were confined within an optical well for a limited period of time (of order 200 ms), still far longer than the time needed to attain a steady state temperature (of order 10 ms). Due to a weak optomechanical coupling and optical potential, particles used to escape from the optical well and were recaptured by the Paul trap, restarting their cooling cycle.

To solve the problem of loss from the optical potential and improve the cooling performances, we decided to employ an higher finesse optical cavity with a smaller mode volume. This was indeed the subject of the second portion of the thesis, where we have described the modifications in the experimental setup, using a shorter cavity with finesse $\mathcal{F} \simeq 50,000$, which brought to 20-fold increase in the optomechanical coupling rate. The latter became strong enough to permit detectable modulation of the cavity field by the levitated particles. We could start detecting and analyzing the light transmitted by the cavity, which showed traces of both linear (G_1) and quadratic (G_2) optomechanical coupling. We showed that the signature of quadratic coupling in the levitated system was a cavity response at twice the mechanical frequency, as the cavity field is modulated by an x^2 term, as well as an x term (linear term). The ratio between the G_1 and G_2 contributions in the spectra depended on the optical well number, and we could estimate the value of N from the observed sideband structure. Given the dynamic nature of the experiment, we were able to observe the damping, in time, of the cavity modulations driven by the nonlinear coupling. Moreover, by reducing the environmental pressure to 10^{-4} mbar we measured a reduction in the area under the steady-state linear spectral components (proportional to the centre-of-mass temperature) by 1000. Due to the relatively high background noise, for pressures $\lesssim 10^{-5}$ mbar it was no longer possible to detect the motional sidebands, although it could be observed from the scattered light that the particle was still trapped.

Furthermore, we identified a previously unobserved shift of the Paul trap secular frequencies due to the optical cavity, which enables readout of key parameters, such as the nanoparticle's charge and the number of photons in the cavity. The effective cavity-induced stability parameter in the Paul trap selects polarizability to mass ratios rather then charge to mass ratios, and it can be varied by adjusting the cavity input power. This means that the combined ion trap high-finesse cavity setup could be used as a spectrometer that permits more complete characterization and sizing of nanoparticles, including biological samples such as viruses.

Finally, in the last chapter of this thesis, we reported some of the possible implementations that were carried out in order to improve the detection of the nanoparticle's motion, by reducing the noise floor of the system. Among those, we described a side locking scheme, where using only the strong laser beam, locked to one side of cavity resonance, and the

optical phase locking, where a second laser has been introduced in the apparatus. In the first case, the system showed stable trapping and motional sidebands were clearly visible even at 10^{-5} mbar, but cooling was limited by the lack of control in the detuning values. In the second case, we obtained excellent control over the detuning Δ_0, being able to observe a reduction in the area under the frequency peaks as a function of Δ_0. In the case examined though, experiments were carried out at relative high pressures ($\sim 10^{-2}$ mbar), as the locking scheme revealed itself not to be enough stable, eventually leading to particle's loss as the pressure was lowered.

In the near future, the hybrid system presented in this work could allow cooling of the nanoparticles to their ground state of motion, provided one can work with higher cavity finesses, allowing to operate in sideband resolved regime, which leads to maximum cooling, and higher input powers (leading to both higher cooling and higher mechanical frequencies). Ground state cooling would also require achieving pressures below 10^{-7} mbar, where the damping from the background gas becomes negligible compared to the optomechanical dampings achievable, and the motional sidebands would be detectable with sensitive balanced homodyne detection.

Appendix A

Modulated Optomechanics

In optomechanics, readout of the temperature of a mechanical oscillator can be achieved by detection of the motional sidebands of the cavity output, which offer ultrasensitive probes of the oscillator's dynamic [50, 51]. In particular, an important development was the detection of an asymmetry in the two frequency peaks (sidebands) of the output power of a probe beam detuned to the positive and negative side of the cavity resonance [156, 157]. Here, observations mirror an underlying asymmetry in the motional spectrum: an oscillator in its ground state $n_{th} = 0$ can absorb a phonon and down-convert the photon frequency (Stokes process), but it can no longer emit any energy and up-convert a photon (anti-Stokes process). Sideband asymmetry has become an important tool in optomechanics and has now been used to establish cooling limited by only quantum backaction [158].

In the case of the hybrid trap presented in this thesis, we have shown that the experimentally observed sidebands of the cavity light have a peculiar spectral profile. The distinguishing features of the cavity spectrum are pairs of peaks at $\omega \simeq (\omega_{\rm M} \pm \omega_{\rm d})$ and $\omega \simeq -(\omega_{\rm M} \pm \omega_{\rm d})$, where $\omega_{\rm M}$ is the mechanical frequency and $\omega_{\rm d}$ is the driving frequency of the oscillating Paul trap. Here we explain the split-sideband spectra, and in particular the N-dependent asymmetric splitting observed experimentally, by using a theoretical quantum model based on linearized dynamics, which considers slow modulations of the optomechanical coupling $g(t)$ and mechanical frequency $\omega_{\rm M}(t)$ [149]. This can be applied to any optomechanical setup where the spring constant and g are both modulated, but in the case of the hybrid trap such modulations arises automatically from the periodic variations of the mean position of the particle, given by the Paul trap. Furthermore, such model shows that, when the system is taken down to the quantum backaction limit, the shape of the split sideband is altered, and it can offer a signature of quantum noise limited dynamics, within a single motional sideband.

In chapter 4 we have shown that:

$$\sin 2kx_0(t) = 2kX_{\rm d} \sin \omega_{\rm d} t, \text{ where } 2kX_{\rm d} = -\frac{\omega_{\rm T}^2}{\omega_{\rm M}^2} 2\pi {\rm N}, \tag{8.5}$$

and that, with the $x_0(t)$ excursion, the optomechanical parameters are given by:

$$g(x_0) = kA\bar{\alpha} \sin 2kx_0(t), \tag{8.6}$$

$$\Delta_0(x_0) = \Delta_0 + A \cos^2 kx_0(t), \tag{8.7}$$

$$\omega_{\rm M}^2(x_0) = \bar{\omega}_{\rm M}^2 \cos 2kx_0(t). \tag{8.8}$$

Since $\omega_{\rm d} \ll \omega_{\rm M}$, however, $x_0(t)$ varies slowly on the scale of the mechanical oscillation allowing separate considerations of the motions; thus we can use the instantaneous values of $x_0(t)$, and substitute values from (8.5) into the above equations. Substitutions of (8.5) into (8.6) gives the optomechanical coupling in terms of N:

$$g(\mathrm{N}, t) = \frac{\omega_{\rm T}^2}{\bar{\omega}_{\rm M}^2} 2\pi k A \bar{\alpha} \mathrm{N} \sin \omega_{\rm d} t. \tag{8.9}$$

A consequence of high-N catch is that the Paul trap pulls the nanosphere away from the antinode and towards the linear region of the optical well, thereby modulating $\omega_{\rm M}$ as well. We square (8.5) and (8.8), add them, and then solve for $\omega_{\rm M}(t)$:

$$\omega_{\rm M}(t) = \bar{\omega}_{\rm M} \left[1 - (2kX_{\rm d})^2 \sin^2 \omega_{\rm d} t\right]^{1/4}. \tag{8.10}$$

Expanding up to the second order in $\Theta \equiv \frac{\pi^2}{2} \frac{\omega_{\rm T}^4}{\bar{\omega}_{\rm M}^4}$, we obtain:

$$\omega_{\rm M}(\mathrm{N}, t) \approx \bar{\omega}_{\rm M}(\mathrm{N}) + 2\omega_2(\mathrm{N}) \cos 2\omega_{\rm d} t, \tag{8.11}$$

where:

$$\bar{\omega}_{\rm M}(\mathrm{N}) \approx \left(1 - \Theta \mathrm{N}^2 - \frac{9}{2}\Theta^2 \mathrm{N}^4\right) \bar{\omega}_{\rm M}, \tag{8.12}$$

$$\omega_2(\mathrm{N}) \approx \frac{1}{2}\left(\Theta \mathrm{N}^2 + 3\Theta^2 \mathrm{N}^4\right) \bar{\omega}_{\rm M}. \tag{8.13}$$

Note that the $g, \omega_{\rm M}$ modulations are out of phase, in the sense that when the mechanical frequency is maximum, the magnitude of coupling strength between motion and the cavity field is a minimum, and vice-versa. Equation (8.11) underlines the non-trivial, two-way interaction between the cavity and the Paul trap: the mechanical frequency is shifted and modulated by the Paul trap, while the secular frequencies of the Paul trap acquire a "cavity-shift" from the optical field (see section 7.4).

For a generic optomechanical system, the quantum dynamics is given by the linearized quantum Hamiltonian:

$$\hat{H}/\hbar = \Delta \hat{a}^\dagger \hat{a} + \omega_{\rm M}\left(\hat{p}^2 + \hat{\mathrm{x}}^2\right) + g\left(\hat{a}^\dagger + \hat{a}\right)\hat{x}, \tag{8.14}$$

where $\hat{x} \equiv \left(\hat{b} + \hat{b}^\dagger\right)$ in appropriately scaled units. The corresponding equations of motions are solved in frequency space [14], and may be written in terms of quadrature operators

$\hat{y}(\omega) = \frac{1}{\sqrt{2}}\left(\hat{a}^\dagger(\omega) + \hat{a}(\omega)\right)$:

$$\hat{y}(\omega) = ig\eta(\omega)\cdot\hat{x}(\omega) + \sqrt{\kappa}\hat{Y}_{th}(\omega), \tag{8.15}$$

where $\eta(\omega) = \chi_0(\omega) - \chi_0^*(-\omega)$ and $\hat{Y}_{th}(\omega) = \chi_0(\omega)\hat{a}_{in} + \chi_0^*(-\omega)\hat{a}_{in}^\dagger$, which contain the optical susceptibility $\chi_0(\omega) = \left[-i\left(\omega+\Delta\right) + \frac{\kappa}{2}\right]^{-1}$. In this well known form, the first term of (8.15) represents the back-action of the mechanical motion on the cavity field, the second the cavity-filtered incoming quantum noise. The measurable, cavity output spectrum is then obtained from input-output theory [14] $\hat{a}_{out} = \hat{a}_{in} - \sqrt{\kappa}\hat{a}(\omega)$ by considering the interference with the incoming imprecision noise (typically shot noise from the laser), so $\hat{y}_{out}(\omega) = \frac{1}{\sqrt{2}}\left(\hat{a}_{out}^\dagger(\omega) + \hat{a}_{out}(\omega)\right)$.

If we include the modulation of $g(t)$ we obtain instead:

$$\hat{y}(\omega) = \bar{g}\eta(\omega)\cdot[\hat{x}(\omega+\omega_{\rm d}) - \hat{x}(\omega-\omega_{\rm d})] + \sqrt{\kappa}\hat{Y}_{th}(\omega), \tag{8.16}$$

where $\bar{g} \equiv \frac{\omega_{\rm T}^2}{\bar{\omega}_{\rm M}^2}\pi k A\bar{\alpha}$N. The notable difference between the standard case and the modulated optomechanics is that in equation (8.16) the optical field does not probe the displacement spectrum $\hat{x}(\omega)$ but rather is sensitive to the interference between shifted spectra at $\omega_{\rm M}\pm\omega_{\rm d}$. For a small modulation ($X_d \ll \lambda$), $\omega_2 \approx 0$ and only g is appreciably modulated. In this case, the minus sign in equation (8.16) is not significant: the shifted spectra do not interfere appreciably. The result is a cavity field fluctuation spectrum characterized by a "twin peaks" structure, as illustrated in figure 8.16(b). The green trace represents $\hat{x}(\omega)$, and is peaked at $\omega = \omega_{\rm M}$. In contrast, cavity intensity modulations (blue trace) are peaked at $\omega_{\rm M}\pm\omega_{\rm d}$.

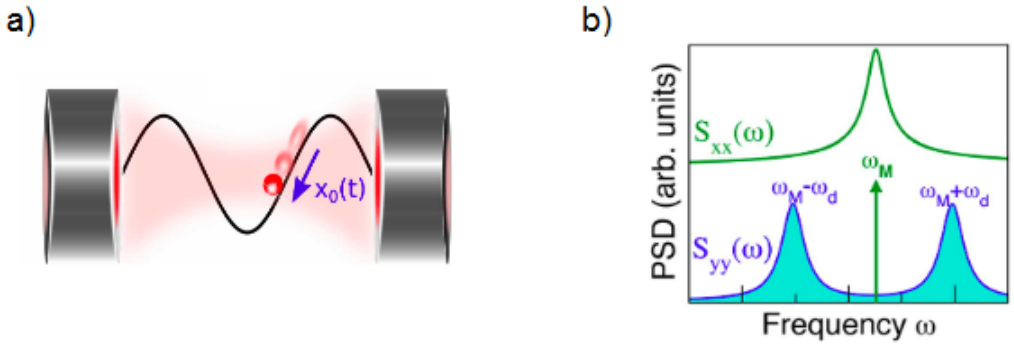

Figure 8.16: a) In electro-optical traps, a slow oscillation is induced such that $x_0(t) = X_{\rm d}\sin\omega_{\rm d}t$, which pulls the centre of mass oscillations of particles away from $x_0 = 0$, enabling cooling. For small oscillations, this corresponds to an effective modulation of the optomechanical coupling $g(t) = 2\bar{g}\sin\omega_{\rm d}t$ and a simultaneous, out-of-phase, modulation of the mechanical frequency $\omega_{\rm M}(t) = \bar{\omega}_{\rm M} + 2\omega_2\cos(2\omega_{\rm d}t)$. b) For a small ($X_{\rm d} \ll \lambda$) modulation, $\omega_2 \approx 0$ and only g is appreciably modulated. In that case, while the power spectral density (PSD) of the displacement spectrum, $S_{xx}(\omega) \equiv \left\langle|\hat{x}(\omega)|^2\right\rangle$, is still peaked at $\pm\omega = \omega_{\rm M}$, the cavity spectrum, $(S_{yy}(\omega))$ exhibits a characteristic structure of 'twin peaks' at $\pm\omega = \omega_{\rm M}\pm\omega_{\rm d}$ (figure from [149]).

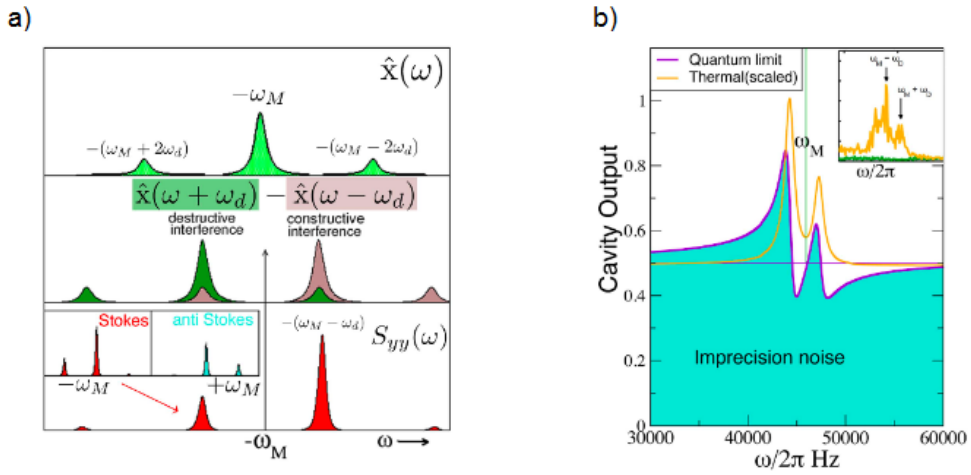

Figure 8.17: (a) For a generic system where both $g(t) = 2\bar{g}\sin\omega_{\rm d}t$ and $\omega_{\rm M}(t) = \bar{\omega}_{\rm M} + 2\omega_2\cos(2\omega_{\rm d}t)$ are modulated, figure illustrates schematically how the spectrum of the cavity field ($S_{yy}(\omega)$), arises from the spectrum of the mechanical motion. Top panel illustrates the $\hat{x}(\omega)$ spectrum: the effect of $\omega_2 > 0$ is to produce additional $\pm 2\omega_{\rm d}$ side-peaks. Middle panel: unlike the typical optomechanical case, the cavity field now follows $\hat{x}(\omega+\omega_{\rm d}) - \hat{x}(\omega-\omega_{\rm d})$ rather than $\hat{x}(\omega)$. The interference of the individual $\hat{x}(\omega \pm \omega_{\rm d})$ components (shown in brown/green) yields constructive enhancement near $\omega \simeq \pm(\omega_{\rm M} - \omega_{\rm d})$, and destructive cancellation near $\omega \simeq \pm(\omega_{\rm M} + \omega_{\rm d})$. Instead of the 'twin peak' structure seen in figure 8.16 for $\omega_2 \approx 0$, the resultant cavity output sidebands display a pair of peaks of asymmetric heights (lower panel). For small g , the ratio between peaks $r \approx (2\omega_{\rm d} - \omega_2)^2 / (2\omega_{\rm d} + \omega_2)^2$, so the $\omega_{\rm M} + \omega_{\rm d}$ peak is strongly suppressed for $\omega_2 \sim 2\omega_{\rm d}$ ($r \approx 0$). This asymmetry is distinct from the usual Stokes/antiStokes sideband asymmetry at $\pm\omega \simeq \omega_{\rm M}$, which is still present. Lower panel shows the Stokes peaks (red). (b) In thermal regimes, the ratio r is insensitive to $\Gamma_{\rm M}$; however, as $\Gamma_{\rm M} \to 0$ and the backaction limit is attained, correlations between back-action and incoming noise alters the relative heights of the peaks, mainly since ponderomotive squeezing lowers the height of the $\omega_{\rm M} + \omega_{\rm d}$ peak relative to the imprecision floor. For incoming quantum shot noise, significant changes in r arise only if the oscillator is near the ground state. Inset shows experimental data, similar to figure 6.5, illustrating asymmetries in experimental sidebands, in the scattering of light out of the cavity, which supports the modulated optomechanics model (figure from [149])

For larger modulations, however, the effect of $\omega_{\rm M}(t) = \bar{\omega}_{\rm M} + 2\omega_2\cos 2\omega_{\rm d}t$ is to cause $\hat{x}(\omega)$ to develop sidebands at $\bar{\omega}_{\rm M} \pm 2\omega_{\rm d}$. This effect cause the two main peaks of the shifted spectra $\hat{X}^{\pm}(\omega) = \hat{x}(\omega+\omega_{\rm d}) - \hat{x}(\omega-\omega_{\rm d})$ to interfere with each other's sidebands (figure 8.17a)). In this case the minus sign in (8.16) (and the out-of-phase nature of the modulations) implies that one peak grows by constructive interference, while the other one diminishes.

This can be understood if, for modest backaction ($\bar{g}$ small), we write $\hat{X}^{\pm}(\omega)$ in the form:

$$\hat{X}^{\pm}(\omega) \approx \sqrt{\Gamma_{\rm M}}\left[\hat{X}_{th}(\omega+\omega_{\rm d}) - \hat{X}_{th}(\omega-\omega_{\rm d})\right] + \bar{g}\hat{Y}_{BA}(\omega) - i\omega_2\sqrt{\Gamma_{\rm M}}\hat{X}_{\omega_2}(\omega) - i\omega_2\bar{g}\hat{Y}_{BA}^{(\omega_2)}(\omega), \tag{8.17}$$

where $\hat{X}_{th}$ terms represent incoming thermal noises and $\hat{Y}_{BA}$ represents the back-action terms driven by imprecision noise. The last two terms are corrections to account for the modulation of $\omega_{\rm M}$: the first comprises thermal effects, the second the corresponding back-action effects. For $\omega_2 = 0$ and neglecting backaction, the shifted spectra arise mainly from incoming thermal noises $\hat{X}_{th}(\omega) = \chi_{\rm M}(\omega)\hat{b}_{in} + \chi_{\rm M}^*(-\omega)\hat{b}_{in}^\dagger$, weighted by the

mechanical susceptibility $\chi_{\rm M}(\omega) = \left[-i\left(\omega-\omega_{\rm M}\right)+\frac{\Gamma_{\rm M}}{2}\right]^{-1}$. The anti-Stokes sideband for example, is primarily due to the weighted thermal noise operators $\chi_{\rm M}(\omega\pm\omega_{\rm d})\hat{b}_{in}(\omega\pm\omega_{\rm d})$. The susceptibilities $|\chi_{\rm M}(\omega\pm\omega_{\rm d})|$ are sharply peaked at frequencies $\omega\mp\omega_{\rm d}$ (since $\Gamma_{\rm M}$ is small), yielding to the "twin peak" structure since the ratio of the twin peak weights $r = |\chi_{\rm M}(\omega-\omega_{\rm d})|^2 / |\chi_{\rm M}(\omega+\omega_{\rm d})|^2 = 1$.

The main effect of ω_2 is to introduce the extra correction from the $\hat{X}_{\omega_2}$ term which means replacing the thermal weights:

$$\chi_{\rm M}(\omega\pm\omega_{\rm d}) \rightarrow \chi_{\rm M}(\omega\pm\omega_{\rm d})\left[1-i\omega_2\chi_{\rm M}(\omega\mp\omega_{\rm d})\right]. \tag{8.18}$$

Evaluating the corrections (the terms in square brackets) near the frequency peaks of the noise, we find they are $\approx (2\omega_{\rm d}\pm\omega_2)/2\omega_{\rm d}$, so the ratio of the peaks in the power spectral density would be:

$$r \approx \left(2\omega_{\rm d}-\omega_2\right)^2 / \left(2\omega_{\rm d}+\omega_2\right)^2, \tag{8.19}$$

predicting a full cancellation for $2\omega_{\rm d}\sim\omega_2$.

We then take $\Gamma_{\rm M}\rightarrow 0$, which, for cooling parameters (red detuned light), takes the system down to the quantum back action, where the heating is limited by quantum shot noise, $n_{th} \equiv n_{BA} \approx \left(\frac{\kappa}{4\omega_{\rm M}}\right)^2$ [158]. By calculating the PSD for $\hat{X}^{\pm}(\omega)$, $S_{X^{\pm}X^{\pm}}$ (see [149] for details), one finds that it differs very little from the thermal spectrum. This indicates that even for $\Gamma_{\rm M}=0$, a regime where the oscillator motion is completely driven by optical imprecision noise, r and the shape for $S_{X^{\pm}X^{\pm}}$ don't change. However, for $S_{y_{out}y_{out}}(\omega)$, this is not the case: the sideband shape is unchanged for the thermal regime but changes significantly in the quantum backaction limit (figure 8.17b)). The underlying reason for this change can be understood as follows: the total backaction in equation (8.17), $\bar{g}\hat{Y}_T(\omega) = \bar{g}\left[\hat{Y}_{BA}(\omega) - i\omega_2\hat{Y}_{BA}^{(\omega_2)}(\omega)\right]$, which by itself still leads to a ratio r, develops correlations with the incoming imprecision terms $\hat{Y}_{imp}(\omega) = \hat{a}_{in}+\hat{a}_{in}^{\dagger}-\sqrt{\kappa}\hat{Y}_{th}$. The key difference between $S_{X^{\pm}X^{\pm}}$ and $S_{y_{out}y_{out}}(\omega)$ in the quantum limit arises because:

$$\left\langle\left|\bar{g}\hat{Y}_T(\omega)\right|^2\right\rangle \neq \left\langle\left|\frac{\hat{Y}_{imp}(\omega)}{\sqrt{\kappa}}-\bar{g}\hat{Y}_T(\omega)\right|^2\right\rangle. \tag{8.20}$$

Ponderomotive squeezing originates from such correlations [159, 160] between backaction and incoming noise and, in the standard optomechanical case, it leads to Fano-like line experimental profile [159, 160] and (an often small) dip where the output light spectrum lies below the imprecision floor. However, in the present case, the height of the $\omega_{\rm M}+\omega_{\rm d}$ is lowered as it overlaps with a poderomotive squeezing dip of the stronger peak, leading to a change in r: the sideband structure is more reshaped and the $\Gamma_{\rm M}$ invariance of r is

lost. Although poderomotive squeezing does require a ground state oscillator, for quantum shot-noise limited spectra a change in r only becomes appreciable if $n_{th} \to n_{BA}$, leading to a noticeable decrease in height of the $\omega_{\rm M} + \omega_{\rm d}$ peak above the imprecision noise level.

As a final remark, we note that, in the case $\kappa \gg \omega_{\rm M}$ (fast cavity limit), we can assume the fluctuations of the cavity field $a(t)$ follow the mechanical motion with no delay. For optical trapping however $a(t) \propto \cos^2 2kx(t)$, and light scattered from the cavity has a similar dependance. In turn, $x(t)$ combines the slow $x_0(t)$ motion with the fast mechanical motion $x_{\rm M}(t) \simeq X_{\rm M} \cos \Phi_{\rm M}(t)$, where $X_{\rm M}$ is the variance of the thermal motion, the phase being $\Phi_{\rm M}(t) = \int_0^t \omega_{\rm M}(t')dt' = \int_0^t (\bar{\omega}_{\rm M} + 2\omega_2 \cos 2\omega_{\rm d} t')dt'$. Hence, $x(t) \simeq X_{\rm d} \sin(\omega_{\rm d} t) + X_{\rm M} \cos\left(\bar{\omega}_{\rm M} t + \frac{2\omega_2}{2\omega_{\rm d}} \sin 2\omega_{\rm d} t\right)$. The Fourier transform of $\cos^2 2kx(t)$ using this ansatz gives reasonable approximation of the split-sideband spectrum for a fast cavity. More importantly, it describes also scattering of light out of the cavity (illustrated in inset of figure 8.17b)) which illustrated suppression of the $\omega_{\rm M} + \omega_{\rm d}$ sideband. While not a full demonstration, this classical-regime data does demonstrate the coherent relative phase accumulation and interplay between the slow and fast motions; it indicates that in combination with homodyne or heterodyne detection, split sideband asymmetries may be investigated experimentally once quantum-limited regimes are attained.

Appendix B

The AOMs drivers

One of the reasons for particle loss from the optical trap has been identified in the frequency instabilities given by the VCO that drives AOM_2, which generates noise on the trapping light field inside the cavity. For this reason, we decide to drive both AOMs with a more stable signal (respect to the drivers described in section 6.4) coming from a tunable function generator (Le Croy Wave Station 3162), that can reach a maximum output of 160 MHz. Before doing that, we test the stability of the two drivers used previously, by mixing the output signals of each one of them with a 79.998 MHz reference signal (local oscillator LO) coming from a crystal controlled oscillator (MODA80 AA Opto-Electronic). By using two directional couplers (Minicircuit ZMCD-30-1+) we can pick up a portion of the driving signals going to the AOMs, for the mixing. As shown in the schemes of figure 8.18, the mixed output is sent to a 1.9MHz low pass filter (MiniCircuit ZX05-1L-S+), to isolate the low frequency component $(\rho_1 - \rho_2)$ and measure its bandwidth on an oscilloscope.

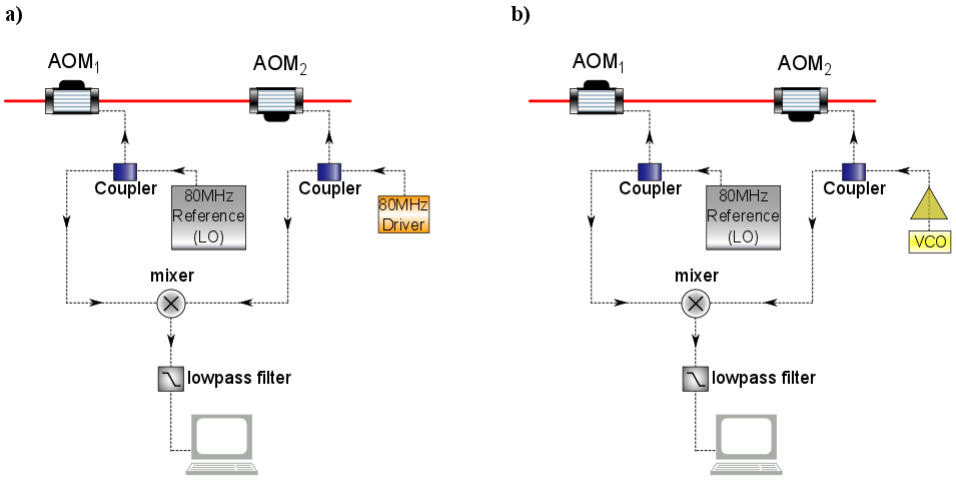

Figure 8.18: Representations of the connections made to test and compare the stability of the two drivers used in chapters 5 and 6, for the AOMs. a) A portion of the reference signal from a crystal controlled oscillator (LO), with a fixed frequency $\rho_1 = 79.998$ MHz (measured with a frequency counter), is mixed with the signal coming from the driver 1080 AF-AIFO 2.0, used in this case to drive the second AOM at $\rho_2 \simeq 80$ MHz$\pm$0.1%. b) The same local oscillator is mixed with the signal from the VCO.

In the case represented by figure 8.18a) the signal difference $(\rho_1 - \rho_2)$ going to the oscilloscope has a non-zero value $(\rho_1 - \rho_2) \simeq 25.3$ kHz and a bandwidth FWHM $\simeq 100$ Hz, as shown in the linear spectrum reported in figure 8.19.

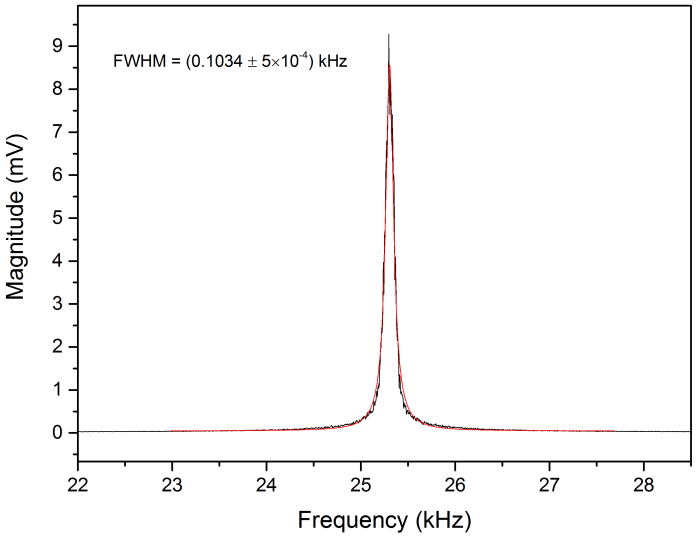

Figure 8.19: Linear spectrum of the frequency difference signal, for the two drivers described in figure 8.18a.

In the case of the VCO (figure 8.18b)), we can tune the input voltage such that the central value of the mixed signal is $(\rho_1 - \rho_2) \simeq 25.3\,\text{kHz}$, as the one above. By looking at its bandwidth, FWHM $\simeq 4\,\text{kHz}$ in figure 8.20, it becomes clear that, for the Voltage Controlled Oscillator case, the frequency oscillations are much broader, and this gives an idea of the limits one gets in the detuning stability, by using the VCO as a AOM driver.

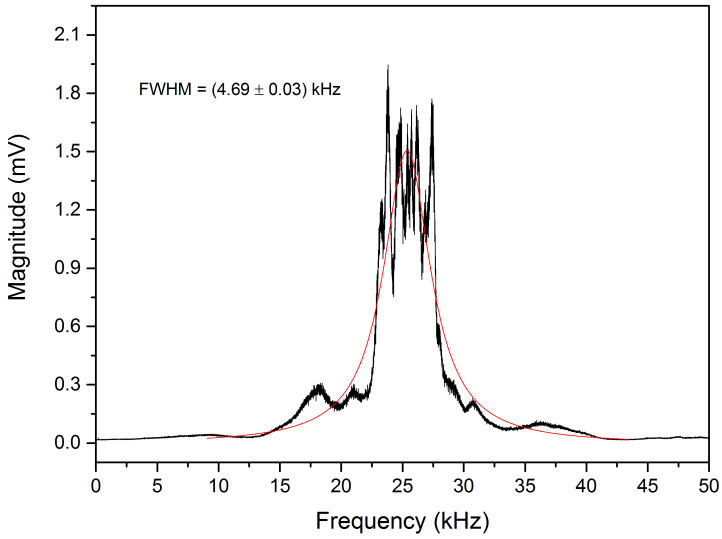

Figure 8.20: Linear spectrum of the frequency difference signal, for the two drivers, one of them being the VCO, described in figure 8.18b.

We can now try and drive the two AOMs using a two output function generator (Le Croy Wave Station 3162), as in figure 8.21, keeping the first channel fixed at $\rho_1 = 80\,\text{MHz}$, and

setting the second one at $\rho_1 = 80.01\,\text{MHz}$, to visualize their frequency difference on the oscilloscope (a peak at 10 kHz) and measure the signal's bandwidth.

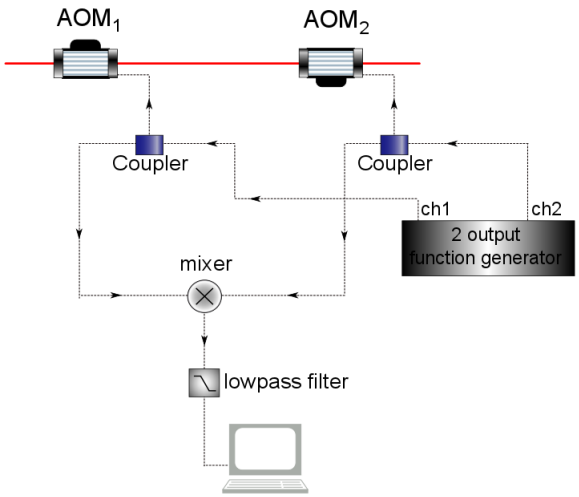

Figure 8.21: Testing the frequency stability of the tunable function generator driving the AOMs. Outputs from channels 1 and 2 are kept fixed at $\rho_1 = 80\,\text{MHz}$ and $\rho_2 = 80.01\,\text{MHz}$ respectively.

Figure 8.21 shows a peak at 10 kHz containing the same amount of points as figures 8.19 and 8.20, and this now prevents an accurate frequency measurement, being the pick much narrower than the previous two cases. Nonetheless, the bandwidth is now FWHM $\sim$ Hz, which implies a much higher stability than the drivers used up to now.

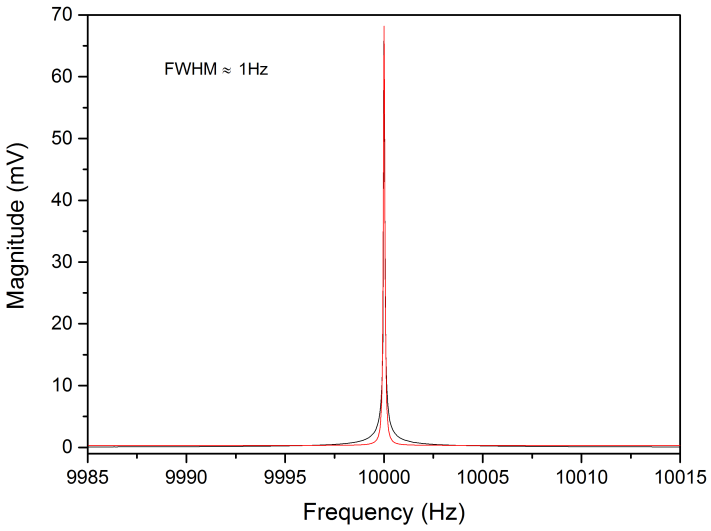

Figure 8.22: Linear spectrum of the frequency difference signal, between the two channels of the function generator, as described in figure 8.18a.

Appendix C

The Fabry-Perot cavity

The interferometer devised by C. Fabry and A. Perot in 1899 is a simple example of one-dimensional optical resonator [161], consisting of two flat (or spherical) partially reflecting plates of glass or quartz, between which light is repeatedly reflected and confined at certain resonance frequencies. The frequency selectivity, which makes an optical resonator useful as optical filter or spectrum analyzer, comes from the multiple-beam interference mechanism [162], which can be described as follows.

The most common method of producing a large number of mutually coherent beams is by division of amplitude. The division occurs by multiple reflections between two parallel, partially reflecting surfaces, like two semitransparent mirrors, which for simplicity are considered to be infinitely thin (figure 8.23). The primary ray, with amplitude E_0, is partially transmitted and partially reflected at the first surface. Provided that there is no absorption, all the subsequent rays can be written in terms of E_0, by adding the coefficient of reflection r and the coefficient of transmission t.

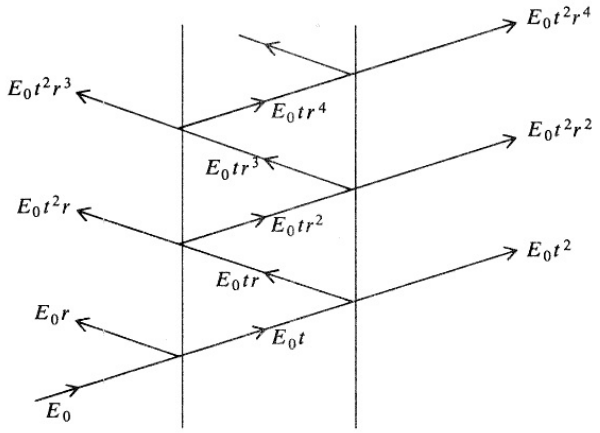

Figure 8.23: Paths of light rays in multiple reflection between two parallel mirrors (figure from [162]).

The phase difference between any two successive rays can be calculated considering their path difference (figure 8.24):

$$\delta = k \cdot (\overline{BC} + \overline{CD} - \overline{OA}) = \frac{2\pi}{\lambda}(2\overline{BC} - \overline{OA}),$$

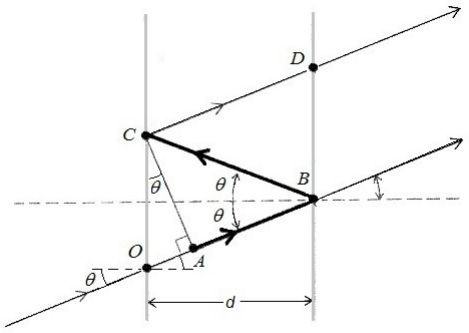

Figure 8.24: Diagram showing the path difference between two successive rays (figure from [162].)

which can be written as:

$$\delta = 2\pi \frac{2d\cos\theta}{\lambda},$$

where λ represents the light wavelength. Knowing that the condition for constructive interference is given by $\delta = 2n\pi$ (with $n = 1, 2, 3..$), we now understand why resonance is obtained for a cavity length equal to $n \cdot \lambda/2$ (supposing an angle of incidence of $\theta = 90°$).

The total transmitted amplitude will be given by taking into account this phase difference and summing the amplitudes of all the transmitted rays:

$$E_T = E_0 t^2 + E_0 t^2 r^2 e^{i\delta} + E_0 t^2 r^4 e^{2i\delta} + ... = \frac{E_0 t^2}{1 - r^2 e^{i\delta}}.$$

From this, the intensity reads:

$$I_T = |E_T|^2 = I_0 \frac{|t|^4}{|1 - r^2 e^{i\delta}|^2},$$

where $I_0 = |E_0|^2$ is the intensity of the incident beam. We also know that a phase change may occur on reflection, hence r will be, in general, a complex number $r = |r|e^{i\delta_r/2}$. Defining the reflectance $R = |r^2|$ and the transmittance $T = 1 - R = |t|^2$ of one surface, one finally obtains:

$$I_T = I_0 \frac{T^2}{|1 - Re^{i\Delta}|^2}, \tag{8.21}$$

where $\Delta = \delta + \delta_r$ is the total phase difference of two successive beams. The denominator in equation (8.21) can be modified to:

$$|1 - Re^{i\Delta}|^2 = 1 - R\left(e^{i\Delta} + e^{-i\Delta}\right) + R^2 = (1 - R)^2 \left[1 + \frac{4R}{(1 - R)^2} \sin^2 \frac{\Delta}{2}\right]. \tag{8.22}$$

Considering the definition given for $T = 1 - R$, we get:

$$I_T = I_0 \frac{1}{1 + F \sin^2 \frac{\Delta}{2}}, \tag{8.23}$$

where $F = 4R/(1-R)^2$ is called "coefficient of finesse". Maxima and minima of intensity in equation (8.23) are given by:

$$I_T^{max} = I_0 \quad \text{for} \quad \Delta = 2n\pi,$$

$$I_T^{min} = \frac{I_0 T^2}{(1+R)^2} \quad \text{for} \quad \Delta = (2n+1)\pi.$$

We note that maxima are always constant and correspond to the incident beam intensity (figure 8.25), while minima depend on reflectance and, therefore, on the coefficient of finesse. F can be then defined as a measure of the sharpness of the interference fringes.

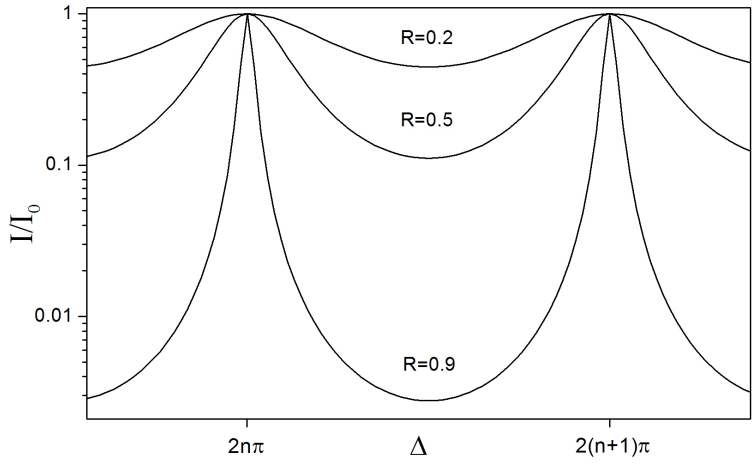

Figure 8.25: Intensity distribution of fringes in multiple beam interference.

The intensity of the light confined between the two surfaces can be found with the same method to be:

$$I = I_0 \frac{1}{(1-R)} \frac{1}{1 + F \sin^2 \frac{\Delta}{2}}.$$

So, its maximum value correspond to $I = I_0/(1-R)$. In this case, the value depends on R, and can also be a lot higher than I_0, showing that, differently from other interferometers, inside a Fabry-Perot cavity with high finesse, light intensity is enhanced.

The separation between adjacent orders of interference in a Fabry-Perot instrument is defined as the free spectral range (FSR). Clearly, in terms of the cavity length d, this distance is

simply $\lambda/2$. In terms of the parameter Δ instead, the free spectral range corresponds to:

$$\Delta_{\mathrm{FSR}} = \Delta_{n+1} - \Delta_n = 2\pi$$

We can express the free spectral range also in terms of mode frequency of the FP interferometer:

$$\nu_n = n \cdot \frac{c}{2d\cos\theta}, \tag{8.24}$$

such that:

$$\mathrm{FSR} = \Delta\nu = \nu_{n+1} - \nu_n = \frac{c}{2d\cos\theta} \tag{8.25}$$

Furthermore, the intensity peaks have a full with at half maximum (FWHM) which, can be expressed as:

$$\mathrm{FWHM} = \frac{\mathrm{FSR}}{\mathcal{F}} \tag{8.26}$$

where $\mathcal{F} = \frac{\pi}{2}\sqrt{F}$, is the cavity finesse.

Optical modes

Although the ray optical approach is useful for determining the geometrical conditions under which rays are confined, it cannot be used to describe the modes of the resonator, i.e., the resonance frequencies and wavefunctions of the optical waves that exist self-consistently within the resonator. For this purpose, one needs to use wave optics, which of course is able to confirm our previous results, but also gives information concerning the spread of the field distribution and the losses suffered by the light beam. To reproduce the stability condition we need to look for field distributions that repeat their shape on each lens of the guide except for a phase factor γ:

$$\Psi_2 = \gamma\Psi_1$$

This is an eigenvalue problem that can be solved with the help of Kirchoff-Huygens diffraction integral in the Fresnel approximation [163], and brings to the general solution:

$$\Psi(x,y,z) = \frac{w_0}{w(x)} H_q\left(\frac{\sqrt{2}y}{w(x)}\right) H_l\left(\frac{\sqrt{2}z}{w(x)}\right) \cdot \\ \cdot \exp\left\{-i\left[kx - (q+l+1)\arctan\left(\frac{\lambda x}{\pi w_0^2}\right) + \frac{\pi(y^2+z^2)}{\lambda\Upsilon(x)}\right]\right\} e^{-\left(\frac{y^2+z^2}{w^2(x)}\right)}$$

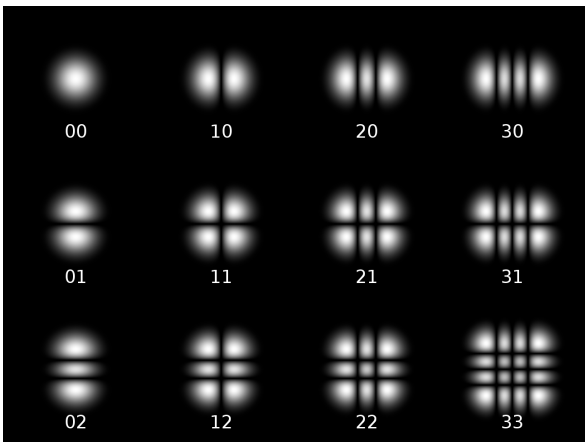

Figure 8.26: Different Hermite-Gaussian tranverse mode spatial intensities for a spherical-mirror resonator. Numbers represent different dependences on the spatial transverse coordinates y, z.

which represents the so called Hermite-Gaussian mode amplitudes (where H are the Hermite polynomials). The latter form a complete system of orthogonal functions; it is thus possible to express every wave field as a series expansion in terms of these modes. The indices (q, l) label different spatial dependences on the transverse coordinates y, z. Modes with different (q, l) are called transverse modes, TEM_{ql} (see figure 8.26)

In this context, it is useful to remark that different transverse modes in a stable resonator will have different resonance frequencies. From the resonance condition, the frequencies of the axial-plus-transverse modes can be written [164]:

$$\nu_{nql} = \left[n + (q + l + 1) \frac{\cos^{-1}\left(\pm\sqrt{g_1 g_2}\right)}{\pi} \right] \frac{c}{2d} \tag{8.27}$$

with $g_1 = 1 - \frac{d}{r_c^{(1)}}$ and $g_2 = 1 - \frac{d}{r_c^{(2)}}$, where $r_c^{(1,2)}$ are the radii of curvature of the two cavity mirrors.

Gaussian beam

The fundamental mode TEM_{00} corresponds to the case when the Hermite polynomials are equal to 1, and it is referred to simply as the Gaussian mode. This is characterized by a symmetric wave whose energy is confined about its axis of propagation (the x axis) and whose wavefront normals are paraxial rays.

The beam width $w(x)$ increases in both directions from its minimum value w_0 at the beam waist ($x = 0$), and it is given by the relation:

$$w^2(x) = w_0^2 \left[1 + \left(\frac{\lambda x}{\pi w_0^2} \right)^2 \right]. \tag{8.28}$$

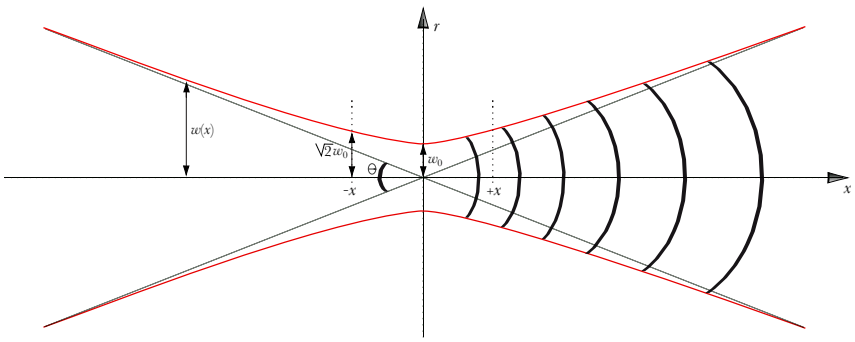

Figure 8.27: Representation of a Gaussian beam.

We also define x_0 as the Reyleigh length, the distance at which the beam waist increases to a factor $\sqrt{2}w_0$. The radius of curvature of the wavefronts is:

$$\Upsilon(x) = x\left[1 + \left(\frac{\pi w_0^2}{\lambda x}\right)^2\right]. \tag{8.29}$$

For $x \gg x_0$ we can approximate $\Upsilon(x) \sim x$, which implies $w(x) \sim w_0 x/x_0$, and the beam half angle θ will be given by the expression:

$$\theta \sim \frac{w(x)}{x} = \frac{\lambda}{\pi w_0}.$$

A Gaussian beam reflected from a spherical mirror will retrace the incident beam if the radius of curvature of its wavefront is the same as the mirror radius. Thus, if the radii of curvature (Υ) of the wavefronts of a Gaussian beam at planes separated by a distance d match the radii r_c of two mirrors (considering the same r_c for both of them here) separated by the same distance d, a beam incident on the second mirror will reflect and retrace itself to the first mirror, where it once again will reflect and retrace itself back to the second mirror, and so on. The beam can then exist self-consistently within the spherical-mirror resonator, and it's said to be a mode of the spherical mirror resonator.

We can thus calculate the beam radius w_0 in the center of the resonator using equation (8.29) with $x = d/2$:

$$w_0 = \sqrt{\frac{\lambda}{2\pi}\left[d\left(2r_c - d\right)\right]^{\frac{1}{2}}} \tag{8.30}$$

Mode matching

The output of a good, single mode laser is itself a pure Gaussian beam, since it is the result of radiation escaping an optical cavity. So, if we want to insert a laser mode into a spherical mirror resonator in the most efficient way, we need to face the problem of matching Gaussian beams to each other. One or more lenses can be used to transform a laser beam

in order to make it of suitable diameter and phase-front curvature for injection into a given optical structure. The two parameters in question, $w(x)$ and $\Upsilon(x)$, can be combined into the complex parameter q [165, 166]:

$$\frac{1}{q(x)} = \frac{1}{\Upsilon(x)} - i\frac{\lambda}{\pi w^2(x)}.$$

Calling the complex beam parameter at a point x_1 on the optical axis q_1, and designating by q_2 its value at a later point, allows us to accomplish a general beam transformation in free space using the $ABCD$ matrix [163]:

$$q_2 = \frac{Aq_1 + B}{Cq_1 + D}. \tag{8.31}$$

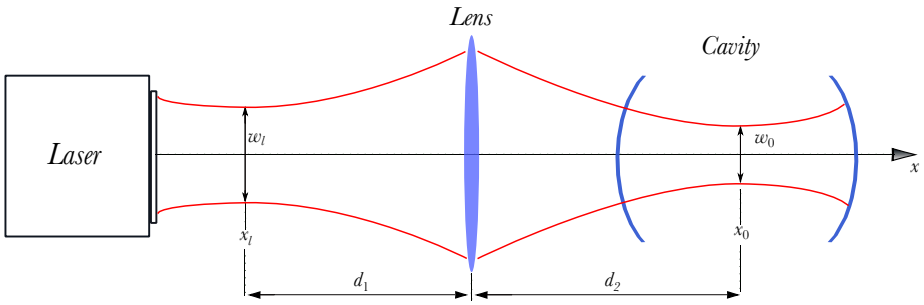

Figure 8.28: Mode matching of a Gaussian beam by means of a lens.

In particular, using the same matrix formalism already introduced in section 5.4.1, if we consider the sequence (d_1) drift - lens - (d_2) drift between the laser waist w_l at $x = x_l$, and the cavity waist w_0 at $x = x_0$ (as shown in figure 8.28), the matrix will assume the form:

$$\begin{pmatrix} A & B \\ C & D \end{pmatrix} = \begin{pmatrix} 1 & d_2 \\ 0 & 1 \end{pmatrix} \cdot \begin{pmatrix} 1 & 0 \\ -\frac{1}{f} & 1 \end{pmatrix} \cdot \begin{pmatrix} 1 & d_1 \\ 0 & 1 \end{pmatrix} = \begin{pmatrix} 1 - \frac{d_2}{f} & d_1 + d_2 - \frac{d_1 d_2}{f} \\ -\frac{1}{f} & 1 - \frac{d_1}{f} \end{pmatrix}.$$

Then equation (8.31) becomes:

$$q_2 = \frac{(1 - d_2/f)q_1 + (d_1 + d_2 - d_1 d_2/f)}{-(q_1/f) + (1 - d_1/f)}. \tag{8.32}$$

The complex beam parameters at the laser and cavity waist are purely imaginary since $\Upsilon(x_l), \Upsilon(x_0) \to \infty$; they are:

$$q_1 = i\frac{\pi w_l^2}{\lambda}, \qquad q_2 = i\frac{\pi w_0^2}{\lambda}.$$

If one inserts these expressions for q_1 and q_2 into equation (8.32) and equates the imaginary

parts and the real parts, one obtains:

$$\frac{d_1 - f}{d_2 - f} = \frac{w_l^2}{w_0^2}, \qquad (d_1 - f)(d_2 - f) = f^2 - f_0^2.$$

Combining the last two relations we obtain the matching formulas:

$$d_1 = f \pm \frac{w_l}{w_0}\sqrt{f^2 - f_0^2}, \quad d_2 = f \pm \frac{w_0}{w_l}\sqrt{f^2 - f_0^2} \tag{8.33}$$

where f_0 is a characteristic length of the system, defined by the two beams: $f_0 = \pi w_l w_0/\lambda$. Any lens with focal distance $f \geq f_0$ can be used to perform the matching transformation. Note also that the sign on the right hand sides of equations (8.33) must either both be positive or both negative; it is thus possible to satisfy the mode matching condition in two different ways.

Although the presented procedure was devoted to the simple case of one thin lens, it is also applicable to more complex systems, since the transmission of Gaussian beams through a succession of free space elements and lenses can be described by the successive multiplication of the corresponding matrices.

Concerning higher order modes of oscillations we need to keep in mind that a Hermite-Gaussian beam of order (q, l) has the same wavefronts as a Gaussian beam, although its amplitude distribution differs. So, the design of a resonator that matches a given beam (or the design of a beam that "fits" a given resonator) is therefore the same as in the Gaussian beam case, regardless of (q, l).

Appendix D

The Pound-Drever-Hall method

In order to have a stable intracavity power for trapping and cooling, as well as measuring with high precision the displacements of the mechanical oscillator, we need to keep the laser beam resonant with the optical cavity. If we assume the cavity length to be fixed, we only have to worry about the possible laser frequency fluctuations, generally caused by vibration, stress, and changes in temperature, as sources of instability. To solve this problem, one could measure these fluctuations using the Fabry-Perot cavity as a frequency reference at ω_c, and then construct a feedback loop that uses the results to continuously tune the laser, to maintain the condition $\omega_l = \omega_c$. In principle, this could be done simply by using the intensity of the light transmitted by the cavity. As we know in fact, the cavity acts as a filter, and a small change in laser frequency would produce a proportional change in the transmitted intensity. Thus, we could measure the latter and feed the signal back to the laser to hold this intensity (and so the laser's frequency) constant. Unfortunately this approach suffers from one main problem: the system cannot distinguish between fluctuations in the laser's frequency, which changes the intensity transmitted through the cavity, and fluctuations in the intensity of the laser itself. A better method would be to measure the intensity reflected by the cavity, and hold that to its minimum value (zero), decoupling in this way intensity and frequency noise. But there is still one difficulty: the intensity of the reflected beam is symmetric about resonance, and this means that, if the laser's frequency drifts out of resonance with the cavity, we can't tell just by looking at the reflected intensity whether the frequency needs to be increased or decreased to bring it back onto resonance.

The solution is represented by measuring the first derivative of intensity $dI/d\omega$, which is instead antisymmetric about resonance. If we vary the frequency and we compare these variations with the reflected intensity variations, we can now tell which side of resonance we are on. Once we have a measurement of the derivative of the reflected intensity with respect to frequency, we can feed this measurement back to the laser to hold it on resonance. This is the basic operational concept of the Pound-Drever-Hall method [147, 167], which was conceived by Ron Drever, based on similar microwave techniques used by R. V. Pound, and it is now the most popular laser-locking method currently in use.

Figure 8.29 shows a basic setup that is capable of implementing such a scheme. In practice, it is often easier to modulate the phase of the output laser beam, instead of the frequency, but the results are essentially the same, since by definition the instantaneous frequency $\omega(t)$

of an electromagnetic wave is given by:

$$\omega(t) = \frac{d\varphi}{dt}$$

So, if we modulate the phase such that:

$$\varphi(t) = \omega_0 t + A\sin(\Omega t + \phi)$$

with Ω angular frequency of modulation, an equivalent result is obtained for the frequency:

$$\omega(t) = \frac{d}{dt}\left[\omega_0 t + A\sin(\Omega t + \phi)\right] = \omega_0 + B\cos(\Omega t + \phi)$$

Therefore, the laser beam passes through a phase modulator (EOM in our setup) driven by some local oscillator. It then passes through the cavity, and the reflected beam is picked off with a beam splitter and sent to a photodetector, whose output is compared with the local oscillator's signal via a mixer. The latter can be seen as a device that performs the product of its inputs, so its output will contain signals at both DC, or very low frequency, and twice the modulation frequency. A low pass filter on the output of the mixer isolates this low frequency signal, that is proportional to the derivative of the reflected intensity, and it is then fed into a servo amplifier to appropriately adjust the laser frequency and lock the laser to the cavity resonance (figure 8.29). Note that the same result can be instead obtained by feeding the output signal to an actuator stuck at the back of the far mirror of the cavity, to control the cavity length.

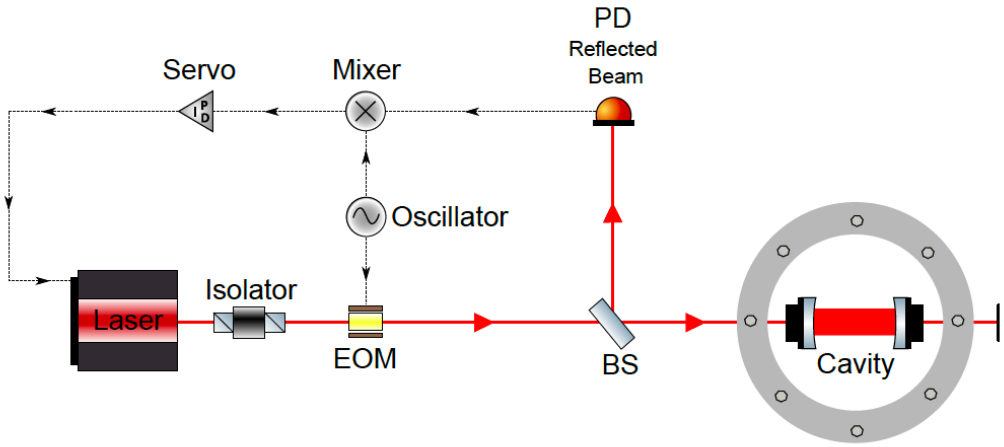

Figure 8.29: Basic Pound-Drever-Hall locking scheme.

Quantitative model

The transition from frequency to phase modulation and extraction of the error signal is not necessarily intuitive, but is obvious in the mathematics. The beam that reflects from a Fabry-Perot cavity is the coherent sum of two different beams: The promptly reflected beam, which bounces off the first mirror and never enters the cavity, and the leakage beam, which is the small part of the standing wave inside the cavity that leaks back through the first mirror, which is never perfectly reflecting. Examining the phases of each component, the prompt reflection has a phase shift of π . The leakage beam consists of multiple phase components, the first round-trip component having a phase shift of $-2L\omega/c$ from its travel along the cavity. With the same approach used in Appendix C for multiple beam interference, one can evaluate the electric field of the reflected beam E_{ref}, and if we write the magnitude of the incident electric field as $E_{inc} = E_0 e^{i\omega t}$, we obtain the reflection coefficient of the cavity:

$$F(\omega) \equiv \frac{E_{ref}}{E_{inc}} = \frac{r\left(e^{i\omega/\mathrm{FSR}} - 1\right)}{1 - r^2 e^{i\omega/\mathrm{FSR}}} \tag{8.34}$$

where r is the amplitude reflection coefficient of each mirror. When the cavity is resonating perfectly, i.e. $L = n\lambda/2$, it's easy to see that the above quantity goes to zero, corresponding to the fact that light is totally transmitted. As a matter of fact, the promptly reflected beam and the leakage beam have the same amplitude and are exactly 180° out of phase, so in this case the two beams interfere destructively. If the cavity is not quite perfectly resonant then the phase difference between the two beams will not be exactly 180° and they will not completely cancel each other out. Some light gets reflected off the cavity and its phase tells us which side of resonance the laser is on.

Now, if we modulate the incident electric field at an angular frequency Ω we obtain:

$$\begin{aligned} E_{inc} &= E_0 e^{i(\omega t + \beta \sin \Omega t)} \\ &\simeq E_0 \left[J_0(\beta) + 2iJ_1(\beta)\sin \Omega t\right] e^{i\omega t} \\ &= E_0 \left[J_0(\beta)e^{i\omega t} + J_1(\beta)e^{i(\omega+\Omega)t} - J_1(\beta)e^{i(\omega-\Omega)t}\right] \end{aligned}$$

where the first expression has been expanded using Bessel functions J , supposing the modulation depth β to be small. We note that after phase modulation, there are really three different frequency components in the beam: a carrier, with angular frequency ω, and two sidebands with frequencies $\omega \pm \Omega$. Once this phase-modulated beam reaches the cavity and reflects, each frequency component can be treated independently and multiplied by the

reflection coefficient at the appropriate frequency:

$$E_{ref} = E_0 \left[F(\omega) J_0(\beta) e^{i\omega t} + F(\omega+\Omega) J_1(\beta) e^{i(\omega+\Omega)t} - F(\omega-\Omega) J_1(\beta) e^{i(\omega-\Omega)t} \right]$$

What we really measure with a photodetector is the power of the reflected field:

$$\begin{aligned} P_{ref} &= |E_{ref}|^2 = P_c |F(\omega)|^2 + P_s \left\{ |F(\omega+\Omega)|^2 + |F(\omega-\Omega)|^2 \right\} \\ &+2\sqrt{P_c P_s} Re \left[F(\omega) F^*(\omega+\Omega) - F(\omega) F^*(\omega-\Omega) \right] \cos \Omega t \\ &+2\sqrt{P_c P_s} Im \left[F(\omega) F^*(\omega+\Omega) - F(\omega) F^*(\omega-\Omega) \right] \sin \Omega t \\ &+ \left(\mathcal{O} \left[2\Omega \right] \right) \end{aligned}$$

where P_c and P_s are the power of the carrier and sideband components, respectively. The Ω terms arise from the interference between the carrier and the sidebands, while the 2Ω terms come from sidebands interfering with each other. To retrieve the phase information, we need to separate one of the two terms oscillating at the modulation frequency, the sine term or the cosine term. For a reasonably fast modulation frequency ($\Omega \gg FSR/\mathcal{F}$) near resonance, the $\sin(\Omega t)$ term with the imaginary component of $F(\omega)$ will be dominant. This is true because when the carrier is near resonance and the modulation frequency is high enough that the sidebands are not, we can assume that the sidebands are totally reflected $F(\omega \pm \Omega) \approx -1$. Then:

$$F(\omega) F^*(\omega+\Omega) - F^*(\omega) F(\omega-\Omega) \approx -i2\mathrm{Im} \left\{ F(\omega) \right\}$$

becomes purely imaginary. To extract this sine term we use the mixer, which multiplies the signal $P_{ref} \propto \sin(\Omega t)$ from the photodetector with $\sin(\Omega t)$ from the oscillator, giving a DC component and a $\cos(2\Omega t)$ term (this comes from the fact that the product of two sine waves is: $\sin \Omega t \sin \Omega' t = \frac{1}{2} \left\{ \cos \left[(\Omega - \Omega') t \right] - \cos \left[(\Omega + \Omega') t \right] \right\}$, and in our case $\Omega' = \Omega$). The first one is isolated via a low pass filter, and the Pound-Drever-Hall error signal will be then:

$$\epsilon = -2\sqrt{P_c P_s} \mathrm{Im} \left\{ F(\omega) F^*(\omega+\Omega) - F(\omega) F^*(\omega-\Omega) \right\}$$

whose plot is shown in figure 8.30.

On the contrary, at slow modulation frequencies, $F(\omega)F^*(\omega+\Omega) - F(\omega)F^*(\omega-\Omega)$ is purely real, and only the cosine term survives. In this case we need to match the phases of the two signals going into the mixer, if we don't want the DC signal to be zero. Turning a sine into a cosine is a simple matter of introducing a 90° phase shift, which can be simply done with a phase shifter.

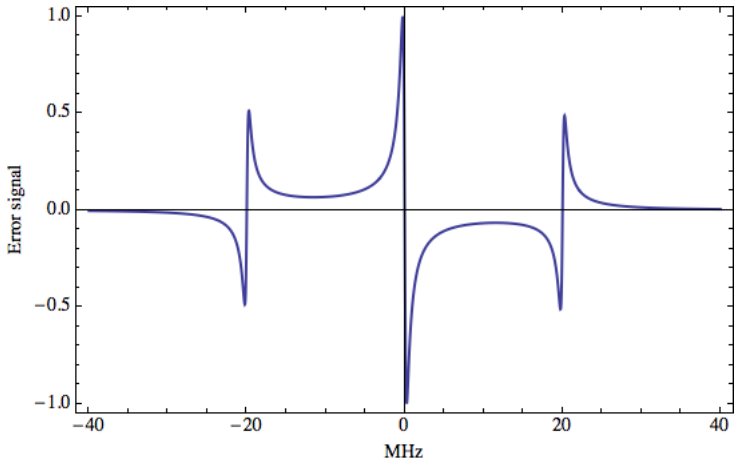

Figure 8.30: The normalized PDH error signal $\epsilon/2\sqrt{P_c P_s}$, for a modulation frequency simulated to be $\Omega = 20$MHz.

Bibliography

[1] A. Einstein, "Approximative integration of the field equations of gravitation", Sitzungsber Preuss Akad Wiss Berlin, 688-696 (1916)

[2] LIGO Scientific and Virgo Collaborations (B. P. Abbott, *et al.*) "Observation of gravitational waves from a binary black hole merger", Phys. Rev. Lett. **116**, 061102 (2016)

[3] J. Kepler, "De Cometis" (1619)

[4] J. C. Maxwell, "A treatise on electricity and magnetism", Vol. **2,** Clarendon Press, Oxford (1873)

[5] V. B. Braginsky, F. Y. A. Khalili, "Quantum Measurements", Cambridge University Press (1995)

[6] V.B. Braginsky, A.B. Manukin, M.Y. Tikhonov, "Investigation of dissipative ponderomotive effects of electromagnetic radiation", Soviet Journal of Experimental and Theoretical Physics, **31**, 829 (1970)

[7] N. Schlosser, G. Reymond, I. Protsenko, P. Grangier, "Sub-poissonian loading of single atoms in a microscopic dipole trap", Nature **411**, 1024-1027 (2001)

[8] A. Ashkin, J. M. Dziedzic, T. Yamane, "Optical trapping and manipulation of single cells using infrared laser beams", Nature **330**, 769 - 771 (1987)

[9] D. J. Wineland, Wayne M. Itano," Laser cooling of atoms", Phys. Rev. A **20**, 1521–1540 (1979)

[10] W, M. Itano, D. J. Wineland, "Laser cooling of ions stored in harmonic and penning traps", Phys. Rev. A **25**, 35–54 (1982)

[11] William D. Phillips, "Laser cooling and trapping of neutral atoms", Rev. Mod. Phys. **70**, 721 (1998)

[12] M. H. Anderson, J. R. Ensher, M. R. Matthews, C. E. Wieman, E. A. Cornell, "Observation of Bose-Einstein condensation in a dilute atomic vapor", Science **269**, 198-201 (1995)

[13] T.J. Kippenberg, K.J. Vahala, "Cavity Opto-Mechanics", Optics Express, **15**, 17172-17205 (2007)

[14] M. Aspelmeyer, T. J. Kippenberg, F. Marquardt, "Cavity optomechanics", Rev. Mod. Phys. **86**, 1391 (2014)

[15] F. Marquardt and S. M. Girvin, "Optomechanics", Physics **2**, 40 (2009)

[16] M. Pinard, C. Fabre, A. Heidmann, "Quantum-nondemolition measurement of light by a piezoelectric crystal", Phys. Rev. A **51**, 2443 (1995)

[17] S. Bose, K. Jacobs, P. L. Knight, "Preparation of nonclassical states in cavities with a moving mirror", Phys. Rev. A **56**, 4175-4186 (1997)

[18] S. Mancini, P. Tombesi, "Quantum noise reduction by radiation pressure", Phys. Rev. A **49**, 4055 (1994)

[19] S. Mancini, V. I. Man'ko, P. Tombesi, "Ponderomotive control of quantum macroscopic coherence", Phys. Rev. A **55**, 3042 (1997)

[20] K.C. Schwab, M.L. Roukes, "Putting Mechanics into Quantum Mechanics", Physics Today **58**, 7, 36 (2005)

[21] F. Marquardt, "Optomechanics: "Push towards the quantum limit", Nature Physics **4**, 513 - 514 (2008)

[22] A. Schließer, P. Del'Haye, N. Nooshi, K. J. Vahala,T. J. Kippenberg, "Radiation Pressure Cooling of a Micromechanical Oscillator Using Dynamical Backaction", Physical Review Letters **97**, 243905 (2006)

[23] P. F. Cohadon, A. Heidmann, M. Pinard, "Cooling of a mirror by radiation pressure", Phys. Rev. Lett. **83**, 3174 (1999)

[24] M. Vogel, C. Mooser, K. Karrai, and R. J. Warburton, "Optically tunable mechanics of microlevers", Appl. Phys. Lett. **83**, 1337 (2003)

[25] J. D. Teufel, T. Donner, Dale Li, J. W. Harlow, M. S. Allman, K. Cicak, A. J. Sirois, J. D. Whittaker, K. W. Lehnert, R. W. Simmonds, "Sideband cooling of micromechanical motion to the quantum ground state", Nature **475**, 359–363 (2011)

[26] J. Chan, T. P. Mayer Alegre, A. H. Safavi-Naeini, J. T. Hill, A. Krause, S. Gröblacher, M. Aspelmeyer, O. Painter, "Laser cooling of a nanomechanical oscillator into its quantum ground state", Nature **478**, 89–92 (2011)

[27] P. F. Barker, M. N. Shneider, "Cavity cooling of an optically trapped nanoparticle", Phys. Rev. A **81**, 23826 (2010)

[28] D. E. Chang, C. A. Regal, S. B. Papp, D. J. Wilson, J. Ye, O. Painter, H. J. Kimble, P. Zoller, "Cavity optomechanics using an optically levitated nanosphere", Proc. Natl. Acad. Sci. USA **107**, 1005-1010 (2010)

[29] O. Romero-Isart, M. L. Juan, R. Quidant, J. I. Cirac, "Optically levitating dielectrics in the quantum regime: Theory and protocols", New J. Phys. **12**, 033015 (2010)

[30] S. Singh, G. A. Phelps, D. S. Goldbaum, E. M. Wright, P. Meystre, "All-optical optomechanics: an optical spring mirror", Phys. Rev. Lett. **105**, 213602 (2010)

[31] O. Romero-Isart, A. C. Pflanzer, F. Blaser, R. Kaltenbaek, N. Kiesel, M. Aspelmeyer, J. I. Cirac, "Large Quantum Superpositions and Interference of Massive Nanometer-Sized Objects", Phys. Rev. Lett. **107**, 020405 (2011)

[32] J. Bateman, S. Nimmrichter, K. Hornberger, Hendrik Ulbricht, "Near-field interferometry of a free-falling nanoparticle from a point-like source", Nat. Commun. **5**, 4788 (2014)

[33] D. Goldwater, M. Paternostro, P. F. Barker, "Testing wave-function-collapse models using parametric heating of a trapped nanosphere", Phys. Rev. A **94**, 010104 (2016)

[34] M. Bahrami, M. Paternostro, A. Bassi, H. Ulbricht, "Proposal for a noninterferometric test of collapse models in optomechanical systems", Phys. Rev. Lett. **112**, 210404 (2014)

[35] Andrew A. Geraci, Scott B. Papp, John Kitching, "Short-range force detection using optically cooled levitated microspheres", Phys. Rev. Lett. **105**, 101101 (2010)

[36] J. Millen, P. Z. G. Fonseca, T. Mavrogordatos, T. S. Monteiro, P. F. Barker, "Cavity cooling a single charged levitated nanosphere", Phys. Rev. Lett. **114**, 123602 (2015)

[37] P. Z. G. Fonseca, E. B. Aranas, J. Millen, T. S. Monteiro, P. F. Barker, "Nonlinear dynamics and strong cavity cooling of levitated nanoparticles", Phys. Rev. Lett. **117**, 173602 (2016)

[38] G. S. Landsberg, "Optics", Vol. **1**, Nauka, Moskow (1976)

[39] S. Gasiorowicz, "Quantum Physics", J. Wiley & Sons, New York, (1985)

[40] G. Anetsberger, R. Rivière, A. Schliesser, O. Arcizet, T. J. Kippenberg, "Ultralow-dissipation optomechanical resonators on a chip", Nat. Phot. **2**, 627-633 (2008)

[41] C. Zener, "Internal friction in solids II. General theory of thermoelastic internal friction", Phys. Rev. **53**, 90 (1938)

[42] A. A. Kiselev, G. J. Iafrate, "Phonon dynamics and phonon assisted losses in Euler-Bernoulli nanobeams", Phys. Rev. B **77**, 205436 (2008)

[43] L. D. Landau, E. M. Lifshitz, "Statistical Physics", Course of Theoretical Physics **5** (1980)

[44] D. F. Walls, G. J. Milburn, "Quantum Optics", Springer (1993)

[45] G. Grynberg, A. Aspect, C. Fabre, "Introduction to quantum optics: from the semi-classical approach to quantized light", Cambridge University Press (2010)

[46] C. Gardiner, P. Zoller, "Quantum Noise, a handbook of markovian and non-markovian quantum stochastic methods with applications to quantum optics", Springer (2004)

[47] O. Arcizet, P. F. Cohadon, T. Briant, M. Pinard, A. Heidmann, J. M. Mackowski, C. Michel, L. Pinard, O. Français, L. Rousseau, "High-sensitivity optical monitoring of a micromechanical resonator with a quantum-limited optomechanical sensor", Phys Rev Lett. **97**, 133601 (2006)

[48] T. Corbitt, D. Ottaway, E. Innerhofer, J. Pelc, N. Mavalvala, "Measurement of radiation-pressure-induced optomechanical dynamics in a suspended Fabry-Perot cavity", Phys. Rev. A **74**, 021802(R) (2006)

[49] A. Schliesser, R. Rivière, G. Anetsberger, O. Arcizet, T. J. Kippenberg, "Resolved Sideband Cooling of a Micromechanical Oscillator", Nature Physics **4**, 415-419 (2008)

[50] F. Marquardt, J. P. Chen, A. A. Clerk, S. M. Girvin, "Quantum theory of cavity-assisted sideband cooling of mechanical motion", Phys. Rev. Lett. **99**, 093902 (2007)

[51] I. Wilson-Rae, N. Nooshi, W. Zwerger, T. J. Kippenberg, "Theory of Ground State Cooling of a Mechanical Oscillator Using Dynamical Backaction", Phys. Rev. Lett. **99**, 093901 (2007)

[52] Phillip C.D. Hobbs, "Reaching the Shot Noise Limit", Optics & Photonic News **2**, 17-23 (1991)

[53] S. Schreppler, N. Spethmann, N. Brahms, T. Botter, M. Barrios, Dan M. Stamper-Kurn, "Optically measuring force near the standard quantum limit", Science, **344**, 1486-1489 (2014)

[54] T.J. Kippenberg and K.J. Vahala, "Cavity Optomechanics: Back-Action at the Mesoscale", Science, **321**, 1172-1176 (2008)

[55] O. Arcizet, "Mesure optique ultrasensible et refroidissement par pression de radiation d'un micro-résonateur mécanique", Université Pierre et Marie Curie (2006)

[56] A. D. O'Connell, M. Hofheinz, M. Ansmann, Radoslaw C. Bialczak, M. Lenander, Erik Lucero, M. Neeley, D. Sank, H. Wang, M. Weides, J. Wenner, John M. Martinis, A. N. Cleland, "Quantum ground state and single-phonon control of a mechanical resonator", Nature **464**, 697-703 (2010)

[57] S. Gröblacher, J.B. Hertzberg, M.R. Vanner, G.D. Cole, S. Gigan, K.C. Schwab, and M. Aspelmeyer, "Demonstration of an ultracold micro-optomechanical oscillator in a cryogenic cavity", Nature Physics **5**, 485-488 (2009)

[58] O. Arcizet, P. F. Cohadon, T. Briant, M. Pinard, A. Heidmann, "Radiation-pressure cooling and optomechanical instability of a micro-mirror", Nature **444**, 71-74 (2006)

[59] T. Corbitt, Y. Chen, E. Innerhofer, H. Müller-Ebhardt, D. Ottaway, H. Rehbein, D. Sigg, S. Whitcomb, C. Wipf, N. Mavalvala, "An all-optical trap for a gram-scale mirror", Phys. Rev. Lett. **98**, 150802 (2007)

[60] D. Kleckner, D. Bouwmeester, "Sub-kelvin optical cooling of a micromechanical resonator", Nature **444**, 75-78 (2006)

[61] A. Schliesser, T. J. Kippenberg, "Cavity optomechanics with whispering-gallery-mode optical micro-resonators", Advances In Atomic, Molecular, And Optical Physics **58**, 207-323 (2010)

[62] B. M. Zwickl, W. E. Shanks, A. M. Jayich, C. Yang, A. C. Bleszynski Jayich, J. D. Thompson, J.G.E. Harris, "High quality mechanical and optical properties of commercial silicon nitride membranes" Appl. Phys. Lett. **92**, 103125 (2008)

[63] Y. Tsaturyan, A. Barg, E. S. Polzik, A. Schliesser, "Ultracoherent nanomechanical resonators via soft clamping and dissipation dilution", Nature Nano. (2017)

[64] M. Eichenfield, R. Camacho, J. Chan, K.J Vahala, O. Painter, "A picogram-and nanometre-scale photonic-crystal optomechanical cavity", Nature **459**, 550-555 (2009)

[65] M. H. Schleier-Smith, I. D. Leroux, H. Zhang, M. A. Van Camp, V. Vuletić, "Optomechanical Cavity Cooling of an Atomic Ensemble", Phys. Rev. Lett. **107**, 143005 (2011)

[66] C. A. Regal, J. D. Teufel, K. W. Lehnert, "Measuring nanomechanical motion with a microwave cavity interferometer", Nat. Phys. **4**, 555-560 (2008)

[67] M. Aspelmeyer, P. Meystre, K. Schwab, "Quantum optomechanics", Physics Today **65**, 7, 29 (2012)

[68] Z. Yin, A. A. Geraci, T. Li, "Optomechanics of Levitated Dielectric Particles", Int. J. Mod. Phys. B **27**, 1330018 (2013)

[69] G. A. T. Pender, P. F. Barker, F. Marquardt, J. Millen, T. S. Monteiro, "Optomechanical cooling of levitated spheres with doubly-resonant fields" Phys. Rev. A **85**, 021802 (2012)

[70] T. S. Monteiro, J. Millen, G. T. A. Pender, F. Marquardt, D. Chang, P. F. Barker, "Dynamics of levitated nanospheres: towards the strong coupling regime" New J. Phys. **15**, 015001 (2013)

[71] O.Romero-Isart, M. L. Juan, R. Quidant, J. I. Cirac, "Toward quantum superposition of living organisms" New J. Phys. **12**, 033015 (2010)

[72] A. I. Lvovsky, H. Hansen, T. Aichele, O. Benson, J. Mlyneky, S. Schillerz, "Quantum state reconstruction of the single-photon Fock state", Phys. Rev. Lett. **87**, 050402 (2001)

[73] O. Romero-Isart, "Quantum superposition of massive objects and collapse models", Phys. Rev. A **84**, 052121 (2011)

[74] R. Kaltenbaek, G. Hechenblaikner, N. Kiesel, O. Romero-Isart, K. C. Schwab, U. Johann, M. Aspelmeyer, "Macroscopic quantum resonators (MAQRO). Testing quantum and gravitational physics with massive mechanical resonators", Exp. Astron. **34**, 123-164 (2012)

[75] A. Bassi, G. Ghirardi, "Dynamical reduction models", Physics Reports **379**, 257–426 (2003)

[76] G. C. Ghirardi, A. Rimini, T. Weber, "Unified dynamics for microscopic and macroscopic systems", Phys. Rev. D **34**, 470 (1986)

[77] G. C. Ghirardi, P. Pearle, A. Rimini, "Markov processes in Hilbert space and continuous spontaneous localization of systems of identical particles", Phys. Rev. A **42**, 78 (1990)

[78] L. Diósi, "A universal master equation for the gravitational violation of quantum mechanics", Phys. Lett. A **120**, 377 (1987)

[79] S. Nimmrichter and K. Hornberger, "Macroscopicity of mechanical quantum superposition states", Phys. Rev. Lett. **110**, 160403 (2013)

[80] S. Gerlich, S. Eibenberger, M. Tomandl, S. Nimmrichter, K. Hornberger, P. J. Fagan, J. Tüxen, M. Mayor, M. Arndt, "Quantum interference of large organic molecules", Nat. Com. **2**, 263 (2011)

[81] S. Gerlich, L. Hackermüller, K. Hornberger, A. Stibor, H. Ulbricht, M. Gring, F. Goldfarb, T. Savas, M. Müri, M. Mayor, M. Arndt, "A Kapitza–Dirac–Talbot–Lau interferometer for highly polarizable molecules", Nature Physics **3**, 711 - 715 (2007)

[82] M. Bahrami, M. Paternostro, A. Bassi, H. Ulbrich, "Proposal for a noninterferometric test of collapse models in optomechanical systems", Phys. Rev. Lett. **112**, 210404 (2014)

[83] D. Goldwater, M. Paternostro, P. F. Barker, "Testing wave-function-collapse models using parametric heating of a trapped nanosphere", Phys. Rev. A **94**, 010104 (2016)

[84] J. Li, S. Zippilli, J. Zhang, D. Vitali, "Discriminating the effects of collapse models from environmental diffusion with levitated nanospheres", Phys. Rev. A **93**, 050102 (2016)

[85] J. D. Thompson, B. M. Zwickl, A. M. Jayich, Florian Marquardt, S. M. Girvin, J. G. E. Harris, "Strong dispersive coupling of a high-finesse cavity to a micromechanical membrane", Nature **452**, 72-75 (2008)

[86] A. M. Jayich, J. C. Sankey, B. M. Zwickl, C. Yang, J. D. Thompson, S. M. Girvin, A. A. Clerk, F. Marquardt, J. G. E. Harris, "Dispersive optomechanics: a membrane inside a cavity", Nwe J. Phys. **10**, 095008 (2008)

[87] V. B. Braginsky, Y. I. Vorontsov, K. S. Thorne, "Quantum Nondemolition Measurements", Science **209**, 547 (1980)

[88] C. Doolin, B. D. Hauer, P. H. Kim, A. J. R. MacDonald, H. Ramp, J. P. Davis, "Nonlinear optomechanics in the stationary regime", Phys. Rev. A **89**, 053838 (2014)

[89] W. Nie, Y. Lan, Y. Li, S. Zhu, "Effect of the Casimir force on the entanglement between a levitated nanosphere and cavity modes", Phys. Rev. A **86**, 063809 (2012)

[90] E. Fischbach, C. Talmadge, "The search for non-Newtonian gravity", Springer-Verlag, New York (1999)

[91] A. Arvanitaki, Andrew A. Geraci, "Detecting High-Frequency Gravitational Waves with Optically Levitated Sensors", Phys. Rev. Lett. **110**, 071105 (2013)

[92] A. Ashkin, "Acceleration and trapping of particles by radiation pressure", Phys. Rev. Lett. **24**, 156, (1970)

[93] A. Ashkin, J. M. Dziedzic, "Stability of optical levitation by radiation pressure", Appl. Phys. Lett. **24**, 586 (1974)

[94] A. Ashkin, J. M. Dziedzic, "Optical levitation in high vacuum", Appl. Phys. Lett. **28**, 333 (1976)

[95] A. Ashkin, J. M. Dziedzic, J. E. Bjorkholm, S. Chu, "Observation of a single-beam gradient force optical trap for dielectric particles", Opt. Lett. **11**, 288-290, (1986)

[96] R. Omori, T. Kobayashi, A. Suzuki, Observation of a single-beam gradient-force optical trap for dielectric particles in air", Opt. Lett. **22**, 816-818, (1997)

[97] W. H. Wright, G. J. Sonek, M. W. Berns, "Parametric study of the forces on microspheres held by optical tweezers", App. Opt. **33**, 1735-1748, (1994)

[98] L. Novotny, B. Hecht, "Principles of Nano-Optics", Cambridge University Press (2006)

[99] Y.Harada, T.Asakura, "Radiation forces on a dielectric sphere in the Rayleigh scattering regime", Opt. Comm. **124**, 529 (1996)

[100] Timo A. Nieminen, "Optical manipulation: Trapping ions", Nature Photonics **4**, 737–738 (2010)

[101] V. Vuletić, S. Chu, "Laser cooling of atoms, ions, or molecules by coherent scattering", Phys. Rev. Lett. **84**, 3787 (2000)

[102] V. Vuletić, H. W. Chan, A. T. Black, "Three-dimensional cavity Doppler cooling and cavity sideband cooling by coherent scattering", Phys. Rev. A **64**, 033405 (2001)

[103] P. Horak, G. Hechenblaikner, K. M. Gheri, H. Stecher, H. Ritsch, "Cavity-Induced Atom Cooling in the Strong Coupling Regime", Phys. Rev. Lett. **79**, 4974 (1997)

[104] J. Dalibard, C. Cohen-Tannoudji, "Laser cooling below the Doppler limit by polarization gradients: simple theoretical models", J. Opt. Soc. Am. B **6**, 2023-2045 (1989)

[105] N. Kiesel, F. Blaser, U. Delic, D. Grass, R. Kaltenbaek, M. Aspelmeyer, "Cavity cooling of an optically levitated submicron particle", Proc. Natl Acad. Sci. USA **110**, 14180 (2013)

[106] P. H. Jones, O. M. Maragò, G. Volpe, "Optical Tweezers: principles and applications", Cambridge University Press (2015)

[107] A. Ashkin, "Optical trapping and manipulation of neutral particles using lasers," Optics & Photonics News **10**, 41 (1999)

[108] J. Millen, T. Deesuwan, P. F. Barker, J. Anders, "Nanoscale temperature measurements using non-equilibrium Brownian dynamics of a levitated nanosphere", Nature Nano. **9**, 425 (2014)

[109] C. J. Price, T. D. Donnelly, S. Giltrap, N. H. Stuart, S. Parker, S. Patankar, H. F. Lowe, D. Drew, E. T. Gumbrell, R. A. Smith, "An in-vacuo optical levitation trap for high-intensity laser interaction experiments with isolated microtargets", Rev. of Sc. Ins. **86**, 033502 (2015)

[110] J. Gieseler, B. Deutsch, R. Quidant, L. Novotny, "Subkelvin Parametric Feedback Cooling of a Laser-Trapped Nanoparticle", Phys. Rev. Lett. **109**, 103603 (2012)

[111] V. Jain, J. Gieseler, C. Moritz, C. Dellago, R. Quidant, L. Novotny, "Direct measurement of photon recoil from a levitated nanoparticle", Phys. Rev. Lett. **116**, 243601 (2016)

[112] T. Li, S. Kheifets, M. G. Raizen, "Millikelvin cooling of an optically trapped microsphere in vacuum", Nature Physics **7**, 527–530 (2011)

[113] T. Li, S. Kheifets, D. Medellin, M. G. Raizen, "Measurement of the instantaneous velocity of a Brownian particle", Science **328**, 5986 (2010)

[114] C. Genes, D. Vitali, P. Tombesi, S. Gigan, M. Aspelmeyer, "Ground-state cooling of a micromechanical oscillator: Comparing cold damping and cavity-assisted cooling schemes", Phys. Rev. A **77**, 033804 (2008)

[115] M. Paternostro, S. Gigan, M. S. Kim, F. Blaser, H. R. Böhm, M. Aspelmeyer, "Reconstructing the dynamics of a movable mirror in a detuned optical cavity", New J. Phys. **8** (2006)

[116] C. K. Law, "Interaction between a moving mirror and radiation pressure: a Hamiltonian formulation", Phys. Rev. A **51**, 2537 (1995)

[117] G. W. Ford, J. T. Lewis, R. F. O'Connell, "Quantum Langevin equation", Phys. Rev. A **37**, 4419 (1988)

[118] V. Giovannetti, D. Vitali, "Phase-noise measurement in a cavity with a movable mirror undergoing quantum Brownian motion", Phys. Rev. A **63**, 023812 (2001)

[119] P. Asenbaum, S. Kuhn, S. Nimmrichter, U. Sezer, M. Arndt, "Cavity cooling of free silicon nanoparticles in high vacuum", Nature Commum. **4**, 2743 (2013)

[120] F. Marquardt, J. G. E. Harris, S. M. Girvin, "Dynamical multistability induced by radiation pressure in high-finesse micromechanical optical cavities", Phys. Rev. Lett. **96**, 103901 (2006)

[121] C. Metzger, M. Ludwig, C. Neuenhahn, A. Ortlieb, I. Favero, K. Karrai, F. Marquardt, "Self-induced oscillations in an optomechanical system driven by bolometric backaction", Phys. Rev. Lett. **101**, 133903 (2008)

[122] A. A. Clerk, Florian Marquardt, and J. G. E. Harris, “Quantum measurement of phonon shot noise”, Phys. Rev. Lett. **104**, 213603 (2010)

[123] A. Nunnenkamp, K. Børkje, J. G. E. Harris, and S. M. Girvin, “Cooling and squeezing via quadratic optomechanical coupling”, Phys. Rev. A **82**, 021806(R) (2010)

[124] K. Børkje, A. Nunnenkamp, J. D. Teufel, and S. M. Girvin, “Signatures of nonlinear cavity optomechanics in the weak coupling regime”, Phys. Rev. Lett. **111**, 053603 (2013)

[125] K. Jacobs, L Tian, J. Finn, “Engineering superposition states and tailored probes for nanoresonators via open-loop control”, Phys. Rev. Lett. **102**, 057208 (2009)

[126] K. Fujii, “Introduction to the Rotating Wave Approximation (RWA) : two coherent oscillations”, arXiv:1301.3585 (2014)

[127] W. Paul, "Electromagnetic Traps for Charged and Neutral Particles". Rev. Mod. Phys. **62**, 531 (1990)

[128] M. Tona, M. Kimura,“Parallel-plate ion trap useful for optical studies of microparticles”, Rev. Sci. Instrum. **75**, 2276 (2004)

[129] R. E. March, “An introduction to quadrupole ion mass trap spectrometry”, Journal of Mass Spectrometry, **32**, 351-369 (1997)

[130] F. G. Major, V. N. Gheorghe, G. Werth, “Charged Particle Traps: Physics and Techniques of Charged Particle Field Confinement”, Springer 2015

[131] S. Schlemmer, J. Illemann, S. Wellert, D. Gerlich, “Nondestructive high-resolution and absolute mass determination of single charged particles in a three-dimensional quadrupole trap”, J. Appl. Phys. **90**, 5410 (2001)

[132] R. F. Wuerker, H. Shelton, R. V. Langmuir, “Electrodynamic containment of charged particles”, J. Appl. Phys. **30**, 342-349 (1959)

[133] P. E. Kloeden, E. Platen, “Numerical solution of stochastic differential equations”, Springer-Verlag (1992)

[134] https://www.coherent.com/lasers/laser/diode-pumped-solid-state-lasers/mephisto-mephisto-s

[135] A. Yariv, “Quantum electronic”, J.Wiley & Sons, third edition (1989)

[136] T. L. Floyd, “Electronics fundamentals: circuits, devices, and applications”, Pearson/Prentice Hall (2007)

[137] N. Uehara, K. Ueda, "Accurate measurement of the radius of curvature of a concave mirror and the power dependence in a high-finesse Fabry–Perot interferometer", Appl. Opt. **34**, 5611-5619 (1995)

[138] L. S. Meng, J. K. Brasseur, D. K. Neumann, "Damage threshold and surface distortion measurement for high-reflectance, low-loss mirrors to 100+ MW/cm^2 cw laser intensity", Opt. Exp. **13**, 25, 10085-10091 (2005)

[139] Christina J. Hood, H. J. Kimble, Jun Ye, "Characterization of high finesse mirrors: loss, phase shifts and mode structure in an optical cavity", Phys. Rev. A **64**, 033804 (2001)

[140] G. Rempe, R. J. Thompson, H. J. Kimble, "Measurement of ultralow losses in an optical interferometer", Opt. Lett. **17**, 363 (1992)

[141] K. An, C. Yang, R. R. Dasari, M. S. Feld, "Cavity ring-down technique and its application to the measurement of ultraslow velocities", Opt. Lett. **20**, 1068-1070 (1995)

[142] J. Poirson, F. Bretenaker, M.Vallet, A. Le Floch, "Analytical and experimental study of ringing effects in a Fabry–Perot cavity. Application to the measurement of high finesses", J. Opt. Soc. Am. B, **14**, 11, 2811-2817 (1997)

[143] T. Delord, L. Nicolas, L. Schwab, G. Hétet, "Electron spin resonance from NV centers in diamonds levitating in an ion trap", New J. Phys. **19** (2016)

[144] L. Deslauriers, S. Olmschenk, D. Stick, W. K. Hensinger, J. Sterk, and C. Monroe, "Scaling and suppression of anomalous heating in ion traps", Phys. Rev. Lett. **97**, 103007 (2006)

[145] F. Paschen, Wied. Ann. **37**, 69–96 (1889)

[146] V. A. Lisovskiy, S. D. Yakovin, V. D. Yegorenkov, "Low-pressure gas breakdown in uniform dc electric field", J. Phys. D: Appl. Phys. **33**, 2722–2730 (2000)

[147] M. A. Herlin, S. C. Brown, "Breakdown of a gas at microwave frequencies", Phys. Rev. **74**, 291 (1948)

[148] R. O. Duda, P. E. Hart, "Use of the Hough transformation to detect lines and curves in pictures", Comm. ACM **15**, 11 (1972)

[149] E B Aranas, P Z G Fonseca, P F Barker and T S Monteiro, "Split-sideband spectroscopy in slowly modulated optomechanics", New J. Phys. **18** 113021 (2016)

[150] E. B. Aranas, P. Z. G. Fonseca, P. F. Barker and T. S. Monteiro, "Thermometry of levitated nanoparticles in a hybrid electro-optical trap", Journal of Optics **19**, 3 (2017)

[151] A. M. Marino, C. R. Stroud Jr., "Phase-locked laser system for use in atomic coherence experiments", Rev. Sc. In. **79**, 013104 (2008)

[152] F. Friederich, G. Schuricht, A. Deninger, F. Lison, G. Spickermann, P. Haring Bolívar, H.G. Roskos, "Phase-locking of the beat signal of two distributed-feedback diode lasers to oscillators working in the MHz to THz range", Opt Express **18**, 8 (2010)

[153] https://www.newport.com/n/how-to-clean-optics

[154] https://www.edmundoptics.com/resources/application-notes/optics/cleaning-optics

[155] W. M. Itano, J. C. Bergquist, J. J. Bollinger, D. J. Wineland, "Cooling methods in ion traps", Physica Scripta, **59**, T59 (1995)

[156] A. H. Safavi-Naeini, J. Chan, J. T. Hill, T. P. Mayer Alegre, A. Krause, O. Painter, "Observation of quantum motion of a nanomechanical resonator", Phys. Rev. Lett. **108**, 033602 (2012)

[157] F. Y. Khalili, H. Miao, H. Yang, A. H. Safavi-Naeini, O. Painter, Y. Chen, "Quantum back-action in measurements of zero-point mechanical oscillations", Phys. Rev. A **86**, 033840 (2012)

[158] R. W. Peterson, T. P. Purdy, N. S. Kampel, R. W. Andrews, P. L. Yu, K. W. Lehnert, C. A. Regal, "Laser cooling of a micromechanical membrane to the quantum backaction limit", Phys. Rev. Lett. **116**, 063601 (2016)

[159] A. H. Safavi-Naeini, S. Gröblacher, J. T. Hill, J. Chan, M. Aspelmeyer. O. Painter, "Squeezed light from a silicon micromechanical resonator", Nature **500**, 185–189 (2013)

[160] A. Pontin, C. Biancofiore, E. Serra, A. Borrielli, F. S. Cataliotti, F. Marino, G. A. Prodi, M. Bonaldi, F. Marin, D. Vitali, "Frequency-noise cancellation in optomechanical systems for ponderomotive squeezing", Phys. Rev. A **89**, 033810 (2014)

[161] Bahaa E. A. Saleh, Malvin Carl Teich, "Fundamentals of Photonics", John Wiley & Sons (1991)

[162] Grant R. Fowles, "Introduction to Modern Optics", Dover edition (1989)

[163] D. Marcuse, "Light Transmission Optics", Van Nostrand Reinhold (1972)

[164] A. E. Siegman, "Lasers", University Science Books (1986)

[165] G. Bardin, J-P. Jorda, "Mode matching of an optical cavity" (1997)

[166] H. Kogelnik, T. Li, "Laser Beams and Resonators", Applied Physics **5**, 10, 1550-1567 (1966)

[167] R. W. P. Drever, J. L. Hall, F. V. Kowalski, J. Hough, G. M. Ford, A. J. Munley, H. Ward, "Laser phase and frequency stabilization using an optical resonator", App. Phys. B **31**, 97-105 (1983)

[168] Eric D. Black, "An introduction to Pound–Drever–Hall laser frequency stabilization", Am. J. Phys. **69**, 79 (2001)